Transient Optical Phenomena Related to Point Defects in Pure and Doped Silica

Vincenzo de Michele

▶ **To cite this version:**

Vincenzo de Michele. Transient Optical Phenomena Related to Point Defects in Pure and Doped Silica. Optics [physics.optics]. Université de Lyon; Università degli studi (Palerme, Italie), 2021. English. NNT : 2021LYSES013 . tel-04675495

HAL Id: tel-04675495

https://theses.hal.science/tel-04675495v1

Submitted on 22 Aug 2024

HAL is a multi-disciplinary open access archive for the deposit and dissemination of scientific research documents, whether they are published or not. The documents may come from teaching and research institutions in France or abroad, or from public or private research centers.

L'archive ouverte pluridisciplinaire **HAL**, est destinée au dépôt et à la diffusion de documents scientifiques de niveau recherche, publiés ou non, émanant des établissements d'enseignement et de recherche français ou étrangers, des laboratoires publics ou privés.

N° d'ordre NNT : **2021LYSES013**

THESE de DOCTORAT DE L'UNIVERSITE DE LYON

opérée au sein de

Université Jean Monnet

et

Università degli Studi di Palermo

en cotutelle

Ecole Doctorale N° 488
Science, ingénierie, santé

Spécialité de doctorat :
Discipline : Optique, photonique, hyperfréquences

Soutenue publiquement le 01/04/2021, par :

Vincenzo De Michele

Transient Optical Phenomena Related to Point Defects in Pure and Doped Silica

---

Skuja, Linards	Leading Researcher/University of Latvia	Reviewer
Tomashuk, Alexander L.	Leading Researcher/A. M. Prokhorov GFI RAS	Reviewer
Garrelie, Florence	Professor/University of Lyon	President
Agnello, Simonpietro	Professor/University of Palermo	Examiner
Messina, Fabrizio	Professor/University of Palermo	Examiner
Ouerdane, Youcef	Professor/University of Lyon	Supervisor
Girard, Sylvain	Professor/University of Lyon	Supervisor
Cannas, Marco	Professor/University of Palermo	Supervisor
Boukenter, Aziz	Professor/University of Lyon	Invited
Marin, Emmanuel	Professor/University of Lyon	Invited

Acknowledgements

At the end of this long PhD, I would like to thank those who have helped and supported me during these three years. The time spent at the Laboratoire Hubert Curien and at the University of Palermo, with all the related opportunities offered, gave me a strong boost not only from a scientific point of view, but also for my personal growth.

I am immensely grateful to the professors that shared with me their time and wide experience. There are no words to express my sense of gratitude, so I will just say thank to: Sylvain Girard, Emmanuel Marin, Aziz Boukenter and Youcef Ouerdane from the Laboratoire Hubert Curien and Marco Cannas from the University of Palermo. They gave me the opportunity to broaden my education, not only during discussions related to my research topic, but also by giving me the opportunity to participate in different research missions, international conferences and summer schools. They have believed in me in these years, giving me the freedom to choose how to deal with the challenges related to my project, teaching me to have confidence in my abilities, but also to understand when I was wrong. I will always be grateful to them.

Special thanks go to Fabrizio Messina and Alice Sciortino: they introduced me to the fascinating world of the ultrafast spectroscopy, with rigor but also with a lot of sympathy, spending a lot of time with me during the period spent in Palermo, but also during long video calls. Thank you Fabrizio and Alice.

For all the people that I have mentioned up: do not worry, these acknowledgements will not substitute the beer I will offer you!

I would also like to thank the reviewers of my PhD thesis: thanks to their careful judgement, I am very proud of the final manuscript.

I will also express my gratitude to the two institutions which supported my project: the Laboratoire Hubert Curien and the University of Palermo.

I feel I must thank all the MOPERE members (present and past), as well as the LaBAM group in Palermo, who welcomed me even though I was from a different 'race'.

Special thanks are necessary also to Antonino Alessi, for the help given and for the always stimulating discussions.

Another important person to thank is Cosimo Campanella: dear friend, valuable colleague and shoulder to lean on. Hard moments become funny with him. Of course I would like to also thank Rossana for the funny moments spent together.

I am also grateful for this experience because I had the possibility to meet (other) wonderful people: Ciro D'Amico (also for the stimulating physics discussions on the way to home), Valentina Zantedeschi, Laure Bsawmaii, Benedetta Bartolini, Francesco Ansante and Nassu.

I would also like to thank some of my best friends and, in general, people who have encouraged me during these years:

Giuseppe Calvaruso, Riccardo Raspante, Gabriele Ricupati, Onofrio Buttitta, Pietro Tralongo, Marzia Viscuso, Eleonora Buttitta, Giuditta Lo Cascio, Rosellina Lisuzzo, Federica Buttitta, Diletta Nuzzo (especially for the funny video calls during the quarantine), Alessia Vecchio, Giulia Buttitta, Marta La Mantia, Marta Gigante, Amanda Ficano, Chiara Sciré, the GAP group, the professors Ciro Scianna, Sebastiano Grimaudo and Ornella Piazza (who have always believed in me and very important for my personal growth), my friends (and wonderful collegues from the times of my university) Gabriele Coniglio, Nino Madonia, Alessia Castellini, Nadia Milazzo, Marta Marchese and Gaetano Li Vecchi.

Thank you to my grandfather Totò and my grandmother Antonia, Padre Mazzola and Zia Maria: I am sure that you are celebrating this moment with me.

Last but not least, I thank my family: despite the distance, they were always close to me. Thank you mom, dad and sisters: I do not think I would have accomplished this result without you. It is also important to thank the member of the extended family: thank you Roberto Grimaudo and Giuseppe Pipitone.

To my family and Zia Maria

Table of Content

Introduction

Regarding the wide technological relevance of point defects embedded in transparent materials, the research community is continuously searching to improve our knowledge about their properties in such materials. Indeed, wide band-gap materials are particularly interesting for many technological applications as they present exceptional optical and mechanical properties, such as a high transparency, a low conductivity as well as low manufacturing costs. Among these materials, the amorphous silica (a-SiO_2) glass plays a key-role because of its good wide range transmission properties combined to a high radiation tolerance, explaining that the investigation of its optical properties remains one of the hot topics of solid state physics and more generally of the materials science [1], [2]. The exceptional properties of a-SiO_2 arise from the strong covalent bond between the silicon and the oxygen atoms and also by the topology of its glass network. Since most of the technological applications revolve around its highly transparency from the ultraviolet (UV) to the infrared (IR) domains, the study of the impact of point defects on it remains of major importance [1], [3], [4]. Point defects represent a structure, with the dimensions of the fundamental structural unit of the silica, which interrupts its ideal amorphous structure, resulting in interstitial sites, vacancies, dangling bonds, homopolar bonds and/or accommodating impurity atoms. Those defect sites, also called color centers, give rise to the appearance of new absorption bands where the "ideal" material should be transparent, degrading the performances of silica-based devices such as lenses or optical fibers. Therefore, color centers strongly influence the optical properties, in general, in wide band-gap materials, making the a-SiO_2 useful in the understanding of such media thanks to its simple and well-known structure.

For the above-mentioned reasons, a particular attention should be devoted on the structure, the electronic properties and also the generation mechanisms of point defects in silica. In this PhD thesis, we are interested to shed light into the transient defect's behavior, studying their generation and optical properties, as well as the whole photocycle which characterizes the involved defect. Basically, we are interested to characterize the induced color centers as the consequence of the interaction of photons with the silica, those photons originating from either ionizing irradiation as

X-rays or from high intensity femtosecond lasers. In order to evaluate the impact of the defect generation in the material, two different classes of samples, with crucial technological importance, are investigated in the present manuscript through a variety of spectroscopic techniques.

The first case of study will be devoted to the investigation of the defect generation under X-rays in silica-based optical fibers (OFs) and their impact on their optical properties in the UV to IR domains. Nowadays OFs represent a crucial technology for our society, employed in many different technological fields from communications, sensing, medicine, even integrated as part of more complex devices and sensors such as diagnostics or autonomous vehicles [4]–[6]. One of the very interesting applications of such silica-based materials concerns their use as sensors or data links in harsh radiation-rich environments, such as those encountered in space or at nuclear power plants or high energy physics facilities. This explains that this research field remains very attracting for the research community despite decades of years of research and a lot of discoveries. In this framework, it is well-known that the exposure to radiation, such as γ-, X-rays, neutrons or protons, degrades the fiber transparency through the so-called Radiation-induced irradiation (RIA) and/or emission of parasitic light, called Radiation-induced emission (RIE) [1], [4]. These macroscopic phenomena are largely imputable to the radiation-induced point defects. It is then mandatory to investigate the basic mechanisms of generation and recombination to be able to evaluate the vulnerability of the fiber-based devices to the targeted environments and also to imagine mitigation procedures to design radiation hardened devices. In other words, the alternative solutions to the various problems generated by the irradiations can only be found through a detailed knowledge of the basic mechanisms evoked during the radiation/matter interaction. Notwithstanding the relevance of the point defects in the optical fiber's behavior exposed to ionizing irradiation, many lacunas and open questions are still present despite numerous successful studies, especially regarding the point defects in pure and doped optical fibers responsible of their degradation at telecommunication wavelengths. The main objective of this PhD thesis revolves around the possibility to increase our knowledge and understanding on the origin of the radiation induced defects in silicate glasses and fibers, with great attention not only on the stable defects generated during the irradiation, but also on the transient ones governing the responses of the glass during exposure.

The second case of study deals with the interaction between bulk silica and high intensity femtosecond lasers [7]–[9]. Indeed, the last decades were characterized by the development of new

laser technologies devoted to the generation of ultra-short high peak intensity femtosecond laser sources, opening the way to the three-dimensional processing of transparent dielectrics, as well as 2D-nano-modifications on surfaces, with unpredictable photonic applications. This success is basically due to the ultrashort duration of femtosecond laser pulses, allowing to concentrate the laser energy ($\sim \mu J/pulse$) to peak intensity values per single pulse of the order of tens of TW/cm^2. At these intensity levels, it is possible to excite and induce permanent structural modifications in wide-bandgap transparent materials through nonlinear mechanisms of energy deposition, rendering possible to induce permanent and controlled refractive index changes [7], [10]. Indeed, the absorption processes taking place on a few hundreds of femtoseconds involve primarily the electronic sub-system, occurring on a timescale much shorter than the energy deposition on the atomic network, involving the heat diffusion and/or thermo-elastic relaxation. The spectroscopic characterization of the exposed volume highlights the generation of point defects [11]–[14], driven by the high intensity pulses, making the investigation of these defects crucial in order to understand the wide possibilities offered by ultrafast photonic micromachining. Notwithstanding the wide possibilities in the application of such photonic devices, the relaxation path, after the excitation which leads to the new optical properties, is still unclear. Here we will investigate the laser wavelength effects on the waveguide's inscription, with particular attention on the generated stable defects, but also to those less stable and also generated during the femtosecond laser pulse exposition, in order to highlight the advantages of an in situ characterization of the induced defects, compared to a post-mortem one.

Finally, since we are interested to the general transient behavior of the point defects, rather than to study only the generation of such defects, we choose to investigate in depth the whole photocycle of two particular point defects in linear absorption conditions. Indeed, by transient absorption measurements based on a sub-picosecond pulse laser, it is possible to follow the defect's photocycle just after the laser pulse up to a few nanoseconds. However, pump-probe experiments in large bandgap insulators are particularly difficult as they imply to use tunable excitations in the UV range, which even today, remains a rather complex task from the experimental point of view. The goal of this section is to provide an innovative approach in addressing unresolved issues regarding color centers in wide band-gap solids that often dominate their optical response, through the study of stable defects in amorphous silica.

The PhD thesis manuscript is organized as follow.

Chapter 1 presents the silica glass structure, with its topology and electronic properties. Moreover, the notion of point defects will be introduced, with particular attention on their optical properties. An overview on the structure and electronic properties of intrinsic and extrinsic defects will be provided, in order to have a complete view about the variety of defects that will be discussed along the PhD thesis. The further section is related to the interaction between the amorphous silica and the radiation, starting with the optical properties of a-SiO_2 and going in deep in the defect generation under ionizing irradiation and through non-linear photoionization, explaining the phenomena linked to these various radiation exposures.

Chapter 2 is devoted to the concepts at the basis of the phenomena observed along this PhD thesis. It introduces the experimental techniques used to investigate the samples under test, such as optical absorption, the Radiation-induced attenuation, the photoluminescence, pump-probe spectroscopy, Raman and Rayleigh scattering and the phase contrast microscopy. Namely, since a large part of the present manuscript is related to the pump-probe transient absorption technique, and since this technique having a femto-picosecond resolution time remains very innovative to investigate solid system, this experimental technique will be particularly detailed.

Chapter 3 introduces both the different types of samples that will be studied during the thesis and also the different experimental facility/setup exploited along these three years of work. Even in this case, as already done for the chapter 2, a particular attention will be devoted to the pump-probe experimental setup. It is important to note, that part of my PhD project was devoted to the development and improvement of a pump-probe setup capable to measure the transient absorption signal of defects embedded in amorphous silica matrix. This goal was reached at the University of Palermo, in the framework of the joined co-supervision between the University of Palermo and the Laboratoire Hubert Curien, finding the best experimental conditions to investigate such system. The experience gained at the University of Palermo was fundamental in order to continue the research on this topic in Saint Etienne with a new and high-performance experimental setup thought in order to gain more and new information on point defects in amorphous silica. The two pump-probe experimental setups from University of Palermo and Laboratoire Hubert Curien will be presented in this chapter.

Chapter 4 reviews our investigation about the basic mechanisms at the origin of the radiation-induced attenuation in different classes of optical fibers. We studied the pulsed and steady state X-ray radiation response of so-called "canonical" optical fibers which are representative of the commercial ones except that thanks to the LabH6 Joint Research laboratory between LabHC and iXblue, we got access to all their composition and manufacturing process details. Samples under test are representative of the most spread types of optical fibers in data communication and dosimetry, such as Pure-Silica-Core (PSC), F-, Ge- and P-doped fibers. The radiation-induced absorption will be studied with particular attention of the defects responsible for the fiber darkening. In particular, we gain more information about the metastable defects mainly responsible of the fiber transient radiation responses. For this, we compared the RIA kinetics at both room temperature and liquid nitrogen temperature.

Chapter 5 focuses on our characterization of the interaction between amorphous silica and high intensity femtosecond laser pulses. The investigation was conducted by combining post mortem investigation of waveguides inscribed under different conditions with *in situ* characterization of the unstable defects bleached just after the irradiation. Even in this case, most of our attention will be devoted on the role of the defects in the optical properties of the inscribed waveguides, and on the relationship between their properties and the irradiation conditions.

The last chapter, chapter 6, presents a new and promising experimental approach to study the defect's photocycle under linear absorption conditions and with a sub-picosecond time resolution. Our method takes advantage from the possibility to tune, in a wide spectral range, the excitation wavelength in transient absorption (TA) measurements. Furthermore, being in linear absorption conditions, we are selectively exciting the color center of interest. As example of the benefit of this approach, here we report our study of TA measurements performed on the Non-Bridging-Oxygen-Hole-Center (NBOHC) and on the Germanium-Lone-Pair-Center (GLPC) under UV photo-excitation, following the femto-picosecond dynamics of these photoluminescent defects as a function of excitation wavelength in single-photon absorption conditions. The combination of the experiments allows clarification of the defect photocycle, highlighting how state-of-the-art TA measurements with tunable UV excitation could represent an innovative tool to investigate such amorphous systems and in general the solid state.

Finally, the conclusion summarizes the main experimental results and knowledge presented in the previous chapters, highlighting the future challenges to be overcome on this research topic and presenting how the present work could help into shedding light into these phenomena.

Introduction

Compte tenu de l'importance sur le plan technologique de la physique des défauts ponctuels présents dans les matériaux transparents, la communauté scientifique cherche continuellement à améliorer nos connaissances sur leurs propriétés dans ces matériaux. En effet, les matériaux à large bande interdite (large gap) sont particulièrement intéressants pour de nombreuses applications technologiques car ils présentent des propriétés optiques et mécaniques exceptionnelles, telles qu'une grande transparence, une faible conductivité ainsi que des coûts de fabrication faibles. Parmi ces matériaux, le verre de silice amorphe (a-SiO_2) joue un rôle prépondérant en raison de ses bonnes propriétés de transmission sur une large gamme spectrale combinées à une tolérance élevée aux radiations. Ceci explique que l'étude de ses propriétés optiques reste actuellement l'un des sujets phares de recherche de la physique des solides et plus généralement de la science des matériaux [1], [2]. Les propriétés exceptionnelles de la silice amorphe proviennent de la forte liaison covalente entre les atomes de silicium et d'oxygène, ainsi que de la topologie du réseau vitreux. Comme la plupart des applications technologiques tournent autour de sa grande transparence depuis le domaine ultraviolet (UV) jusqu'à celui de l'infrarouge (IR), l'étude de l'impact des défauts ponctuels sur ses propriétés reste d'une importance majeure [1], [3], [4]. Les défauts ponctuels représentent une structure, ayant des dimensions comparables à celles de l'unité structurelle fondamentale de la silice, qui interrompt la structure idéale du verre amorphe, entraînant la présence de sites interstitiels, de lacunes, de liaisons homopolaires et/ou d'impuretés. Ces sites de défauts, également appelés centres colorés, donnent lieu à l'apparition de nouvelles bandes d'absorption où le matériau "idéal" devrait être transparent, ce qui dégrade les performances des technologies à base de silice telles que les lentilles ou les fibres optiques. Par conséquent, les centres colorés influencent fortement les propriétés optiques des matériaux à large gap ; la silice amorphe est très utile pour comprendre la réponse de ces milieux grâce à sa structure simple et bien connue.

Pour les raisons susmentionnées, une attention particulière doit être accordée à la structure, aux propriétés électroniques et aux mécanismes de génération de défauts ponctuels dans la silice. Dans cette thèse de doctorat, nous nous intéressons au comportement des défauts transitoires, en

étudiant leurs mécanismes de génération et recombinaison, leurs propriétés optiques, ainsi que l'ensemble du photocycle qui caractérise le défaut en question. Globalement, nous nous intéressons à la caractérisation des centres colorés induits lors de l'interaction des photons avec la silice, ces photons provenant soit de radiations ionisantes (par exemple de rayons X), soit de lasers femtoseconde de haute intensité. Afin d'évaluer l'impact de la génération de défauts dans le matériau, deux catégories différentes d'échantillons, chacun d'une forte importance technologique, sont étudiées dans le présent manuscrit au moyen de diverses techniques spectroscopiques.

Le premier cas d'étude sera consacré à l'étude de la génération de défauts sous rayons X dans les fibres optiques à base de silice (OF) et leur impact sur leurs propriétés optiques dans les domaines de l'UV à l'IR. De nos jours, les FOS représentent une technologie cruciale pour notre société, utilisée dans de nombreux domaines technologiques différents tels que les communications, la détection, la médecine, voire intégrées dans des dispositifs et des capteurs plus complexes comme les diagnostics ou les véhicules autonomes [4]–[6]. L'une des applications très intéressantes de ces matériaux à base de silice concerne leur utilisation comme capteurs ou outils de communication dans des environnements complexes et radiatifs, comme ceux rencontrés dans l'espace, dans les centrales nucléaires ou les installations de physique des hautes énergies. Cela explique que ce domaine de recherche reste très attractif pour la communauté des chercheurs malgré des décennies d'années de recherche et de nombreuses découvertes passées. Dans ce cadre, il est bien connu que l'exposition à des radiations, telles que des rayons X ou γ, des neutrons ou des protons, dégrade la transparence des fibres à travers les phénomènes d'atténuation induite par irradiation (RIA) et/ou l'émission de lumière parasite, appelée émission induite par irradiation (RIE) [1], [4]. Ces phénomènes macroscopiques sont largement imputables aux défauts ponctuels créés par les radiations. Il est donc obligatoire d'étudier les mécanismes fondamentaux de leur génération et de leur recombinaison pour pouvoir évaluer la vulnérabilité des dispositifs à base de fibres aux environnements ciblés et ainsi pouvoir imaginer des procédures de mitigation afin de concevoir des dispositifs « durcis », résistants aux rayonnements. En d'autres termes, les solutions alternatives aux différents problèmes générés par les radiations ne peuvent être trouvées qu'à travers une connaissance détaillée des mécanismes fondamentaux de l'interaction rayonnement - matière. Malgré le rôle crucial des défauts ponctuels pour expliquer le comportement d'une fibre optique exposée aux radiations, diverses lacunes et questions ouvertes subsistent malgré de nombreuses études antérieures très poussées, notamment en ce qui concerne les défauts ponctuels

présents dans les fibres optiques à cœur de silice pure ou dopée et responsables de leur dégradation aux longueurs d'onde des télécommunications. L'objectif principal de cette thèse de doctorat tourne autour de la possibilité d'accroître nos connaissances et notre compréhension sur l'origine des défauts induits par les rayonnements dans les verres et les fibres de silice, avec une grande attention portée non seulement aux défauts stables générés pendant l'irradiation, mais aussi sur les défauts transitoires régissant la réponse du verre pendant son irradiation.

Le deuxième cas d'étude concerne l'interaction entre la silice massive et les lasers femtoseconde à haute intensité [7]–[9]. En effet, les dernières décennies ont été caractérisées par le développement de nouvelles technologies laser consacrées à la génération de sources laser femtoseconde pulsées à haute puissance, ouvrant la voie au traitement tridimensionnel des diélectriques transparents, ainsi qu'à la nano-structuration 2D de surfaces, amenant à de nombreuses applications photoniques. Ce succès s'explique essentiellement par la durée ultra-courte des impulsions laser femtosecondes, qui permet de concentrer l'énergie laser ($\sim \mu J/\text{impulsion}$) à des valeurs d'intensité crête par impulsion de l'ordre de dizaines de TW/cm^2. À ces niveaux d'intensité, il est possible d'exciter et d'induire des modifications structurelles permanentes dans les matériaux transparents à via des mécanismes non-linéaires de dépôt d'énergie, ce qui permet d'induire de manière controlée des changements d'indice de réfraction permanents [7], [10]. En effet, les processus d'absorption se déroulant sur quelques centaines de femtosecondes impliquent principalement le sous-système électronique, se produisant sur une échelle de temps beaucoup plus courte que le dépôt d'énergie sur le réseau atomique, impliquant la diffusion de chaleur et/ou la relaxation thermo-élastique. La caractérisation spectroscopique du volume irradié met en évidence la génération de défauts ponctuels [11]–[14], provoquée par les impulsions de haute intensité, ce qui rend l'étude de ces défauts cruciale pour comprendre les vastes possibilités offertes par le micro-usinage photonique ultra-rapide. Malgré les nombreuses possibilités d'application de ces dispositifs photoniques, les processus de relaxation consécutifs à l'excitation et conduisant aux nouvelles propriétés optiques, ne sont pas toujours clairs. Nous étudierons ici les effets de la longueur d'onde du laser sur l'inscription de guide d'onde dans le verre, en accordant une attention particulière aux défauts permanents générés, mais aussi à ceux moins stables et également générés par le laser femtoseconde, afin de mettre en évidence les avantages d'une caractérisation in situ des défauts induits, par rapport à une caractérisation post-mortem.

Enfin, comme nous nous intéressons au comportement transitoire général des défauts ponctuels, plutôt que d'étudier uniquement la génération de ces défauts, nous choisissons d'étudier en profondeur l'ensemble du photocycle de deux défauts ponctuels particuliers dans des conditions d'absorption linéaire. En effet, par des mesures d'absorption transitoire basées sur un laser à impulsion sub-picoseconde, il est possible de suivre le photocycle du défaut jusqu'à quelques nanosecondes après l'impulsion laser. Cependant, les expériences pompe-sonde dans des isolateurs à large gap sont particulièrement difficiles car elles impliquent d'utiliser des excitations accordables dans la gamme UV, ce qui, même aujourd'hui, reste une tâche assez complexe du point de vue expérimental. L'objectif de cette section est de fournir une approche innovante pour résoudre les problèmes relatifs aux centres colorés dans les solides à large gap qui dominent souvent leur réponse optique, grâce à l'étude des défauts stables dans la silice amorphe.

Le manuscrit de la thèse de doctorat est organisé comme suit.

Le chapitre 1 présente la structure du verre de silice, avec sa topologie et ses propriétés électroniques. En outre, la notion de défauts ponctuels sera introduite, avec une attention particulière sur leurs propriétés optiques. Un aperçu de la structure et des propriétés électroniques des défauts intrinsèques et extrinsèques sera fourni, afin d'avoir une vue complète concernant la variété des défauts qui seront discutés tout au long de la thèse de doctorat. La section suivante concerne l'interaction entre la silice amorphe et les radiations, en commençant par les propriétés optiques de la silice amorphe et en allant plus loin dans la génération des défauts sous irradiation ionisante et par photo-ionisation non-linéaire, expliquant les phénomènes relatifs à ces différentes expositions aux radiations.

Le chapitre 2 est consacré aux concepts à la base des phénomènes observés tout au long de cette thèse de doctorat. Il présente les techniques expérimentales utilisées pour étudier les échantillons testés, telles que l'absorption optique, l'atténuation induite par irradiation, la photoluminescence, la spectroscopie pompe-sonde, les diffusions Raman et Rayleigh et la microscopie à contraste de phase. En particulier, étant donné qu'une grande partie du présent manuscrit est liée à la technique d'absorption transitoire par sonde-pompe, et que cette technique ayant un temps de résolution femto-picoseconde reste très innovante pour étudier les systèmes solides, cette technique expérimentale sera particulièrement détaillée.

Le chapitre 3 présente à la fois les différents échantillons qui seront étudiés au cours de la thèse et les différents dispositifs expérimentaux exploités tout au long de ces trois années de travail. Même dans ce cas, comme déjà fait pour le chapitre 2, une attention particulière sera consacrée au dispositif expérimental pompe-sonde. Il est important de noter qu'une partie de mon projet de thèse a été consacrée au développement et à l'amélioration d'un dispositif pompe-sonde capable de mesurer le signal d'absorption transitoire des défauts présents dans la silice amorphe. Cet objectif a tout d'abord été atteint à l'Université de Palerme, dans le cadre de la co-supervision conjointe entre l'Université de Palerme et le Laboratoire Hubert Curien, en trouvant les meilleures conditions expérimentales pour étudier un tel système. L'expérience acquise à l'Université de Palerme a été fondamentale pour poursuivre les recherches sur ce sujet à Saint-Étienne avec un nouveau dispositif expérimental très performant, conçu pour obtenir de nouvelles informations sur les défauts ponctuels dans la silice amorphe. Les deux dispositifs expérimentaux pompe-sonde de l'Université de Palerme et du Laboratoire Hubert Curien seront présentés dans ce chapitre.

Le chapitre 4 passe en revue les résultats de nos travaux portant sur les mécanismes fondamentaux à l'origine de l'atténuation induite par irradiation dans différentes classes de fibres optiques. Nous avons étudié la réponse sous irradiation X pulsée et continue des fibres optiques dites "canoniques". Ces échantillons sont représentatifs des fibres commerciales, cependant grâce au laboratoire commun de recherche LabH6 entre le LabHC et iXblue, nous avons eu accès à tous les détails concernant leur composition et de leur procédé de fabrication. Les échantillons testés sont représentatifs des types de fibres optiques les plus répandus dans les télécommunications ou pour les applications de dosimétrie, tels que les fibres à cœur de silice pure (PSC), les fibres à cœur dopés F, G et P. L'absorption induite par irradiation sera étudiée avec une attention particulière pour les défauts responsables de la dégradation des fibres optiques. En particulier, nous obtiendrons plus d'informations sur les défauts métastables principalement responsables de leurs réponses transitoires. Pour cela, nous avons comparé les cinétiques de la RIA à la fois à température ambiante et à la température de l'azote liquide.

Le chapitre 5 porte sur la caractérisation de l'interaction entre la silice amorphe et les impulsions laser femtoseconde de haute intensité. L'étude a été menée en combinant l'investigation post mortem de guides d'ondes inscrits dans différentes conditions avec la caractérisation *in situ* des défauts instables guéris juste après l'irradiation. Même dans ce cas, l'essentiel de notre attention

sera consacré au rôle des défauts dans les propriétés optiques des guides d'ondes inscrits, et à la relation entre leurs propriétés et les conditions d'irradiation.

Le dernier chapitre, le chapitre 6, présente une approche expérimentale nouvelle et prometteuse pour étudier le photocycle du défaut dans des conditions d'absorption linéaire et avec une résolution temporelle inférieure à la picoseconde. Notre méthode tire parti de la possibilité d'accorder, dans une large gamme spectrale, la longueur d'onde d'excitation dans les mesures d'absorption transitoire (TA). De plus, en restant dans des conditions d'absorption linéaire, nous excitons sélectivement le centre coloré d'intérêt. Comme exemple de l'avantage de cette approche, nous présentons ici notre étude des mesures TA effectuées sur les défauts Non-Bridging-Oxygen-Hole-Center (NBOHC) et Germanium-Lone-Pair-Center (GLPC) sous photo-excitation UV. Nous suivons la dynamique femto-picoseconde de ces défauts photoluminescents en fonction de la longueur d'onde d'excitation dans des conditions d'absorption à un seul photon. La combinaison des expériences permet de clarifier le photocycle du défaut, et de montrer comment des mesures TA de pointe avec une excitation UV accordable pourraient représenter un outil innovant pour étudier ces systèmes amorphes et en général l'état solide.

Enfin, la conclusion résume les principaux résultats expérimentaux et connaissances présentés dans les chapitres précédents, en soulignant les défis futurs à relever sur ce thème de recherche et en présentant la manière dont les travaux actuels pourraient contribuer à faire la lumière sur ces phénomènes.

Introduzione

La rilevanza acquisita dai difetti di punto presenti nei solidi trasparenti, da un punto di vista technologico, spinge la comunità scientifica alla ricerca di nuove conoscenze riguardo questi materiali. Infatti, materiali ad alto bandgap sono particolarmente interessanti grazie alle molteplici applicazioni tecnologiche, in quanto presentano eccezionali peculiarià sia ottiche che meccaniche, come l'alta trasparenza, la bassa conduttività e i bassi costi di produzione. Tra questi materiali, la silice ricopre un ruolo fondamentale in quanto gode di ottime proprietà trasmissive, in un ampio intervallo spettrale, e alla buona tolleranza alla radiazione. Ciò spiega come mai lo studio delle sue proprietà ottiche è ancora un argomento di punta nella fisica dello stato solido e più in generale nelle science dei metariali. [1], [2]. Le sue eccezionali proprietà derivano dal forte legame covalente tra l'atomo di silicio e di ossigeno, oltre che dalla sua topologia. Dato che molte delle sue applicazioni in ambito tecnologico sono relative alla sua trasparenza nel dominio spettrale che va dall'ultravioletto (UV) all'infrarosso (IR), la ricerca dell'impatto dei difetti di punto sulla trasmissione è di fondamentale importanza [1], [3], [4]. I difetti di punto rappresentano strutture, caratterizzate da dimensioni dell'ordine della cella fondamentale della silice, le quali interrompono la struttura amorfa "ideale" del vetro, risultando in siti interstiziali, vacanze, legami omopolari e/o in presenza di impurità. Questi siti "difettosi", anche noti come centri di colore, danno luogo a nuove bande di assorbimento dove il materiale "ideale" sarebbe dovuto essere trasparente, riducendo le prestazioni dei dispositivi a base di sicile, come lenti o fibre ottiche. Pertanto, i centri di colore influenzano pesantemente le proprietà ottiche dei materiali ad alto bandgap e lo studio della silice permette di comprenderne il comportamento grazie alla sua ben nota e semplice struttura.

Per le ragioni sopra elencate, una particolare attenzione deve essere rivolta alla struttura, alle proprieta elettroniche e ai meccanismi di generazione dei difetti di punto nella silice. Lo scopo della presente tesi di dottorato è far luce sul comportamento transiente dei difetti, studiandone i meccanismi di generazione, le proprietà ottiche e anche il fotociclo che caratterizza certi difetti. Fondamentalmente, siamo interessati alla caratterizzazione dei centri di colore indotti dall'interazione di fotoni con la silice: sia i difetti generati come consequenza dell'esposizione alla

radiazione ionizzante, in questo caso raggi X, che a quelli indotti da laser al femtosecond ad alta intensità. Al fine di stimare l'impatto della generazione dei difetti sui materiali, nel presente manoscritto, sono studiate due diverse classi di campioni grazie all'ausilio di varie tecniche spettroscopiche.

Il primo caso di studio sarà relativo ai difetti indotti dall'esposizione ai raggi X in fibre ottiche e alla loro influenza sulle proprietà ottiche investigando in un dominio spettrale che va dall'UV all'IR. Le fibre ottiche rappresentano ormai una tecnologia di fondamentale importanza per la nostra società, essendo impiegate in molti campi: telecomunicazioni, sensoristica, medicina ed anche integrate come parte di dispositivi più complessi nella diagnostica o in veicoli autonomi [4]–[6]. Una delle applicazioni più interessanti relative a tali dispositivi a base di silice riguarda il loro impiego nella trasmissione di dati o come sensori in ambienti ad alta presenza di radiazione, come lo spazio, le centrali nucleari o strutture dedite alla fisica ad alte energie. Pertanto la comunità scienfitica è particolarmente interessata a tali studi, nonostante anni di ricerche e scoperte in questa direzione. È ben noto infatti che l'irraggiamento, sia esso dovuto a fasci γ, X, neutroni o protoni, riduce la trasmissione delle fibre mediante l'attenuazione indotta dall'irraggiamento (chiamata brevemente RIA) e/o dall'emissione di luce parassita, intesa come emissione anch'essa indotta dall'irraggiamento [1], [4]. Gran parte di questi fenomeni macroscopici sono causati dai difetti indotti dalla radiazione. È dunque necessario investigare i meccanismi alla base della loro generazione e ricombinazione così da stimare la vulnerabilità dei dispositivi basati su tecnologie a fibra ottica per il tipo di irraddiamento considerato e/o anche proporre protocolli e metodi per la progettazione di dispositivi più resistenti. In alter parole, soluzioni alternative ai diversi problemi generati dalla radiazione e che possono essere trovate solo attraverso la conoscenza dettagliata dei meccanismi microscopici che avvengono durante l'interazione con la radiazione. Nonostante la rilevanza dei difetti di punto e numerosi eccellenti studi sull'argomento, sono ancora presenti lacune nella comprensione della risposta delle fibre ottiche esposte alla radiazione, specialmente riguardo alla degradazione delle proprietà ottiche relativamente a fibre sia in silice pura che drogate, alle lunghezze d'onda utilizzate nelle telecomunicazioni. L'obbiettivo principale della presente tesi di dottorato è di apportare un contributo relativo alla comprensione sull'origine dei difetti di punto indotti dalla radiazione, focalizzando attenzione non solo sui difetti stabili, ma in particolare sui difetti transienti che influenzano il comportamento della silice durante l'esposizione alla radiazione.

Il secondo caso di studio riguarda l'interazione tra silica e laser al femtosecondo ad alta intensità [7]–[9]. Infatti gli ultimi decenni sono state caratterizzati dallo sviluppo di nuove tecnologie laser, dedicate alla generazione di sorgenti ad impulsi ultra brevi ad alta intensità, aprendo la strada alla fotonica tri- e bi-dimensionale di dielettrici, con imprevedibili applicazioni. Tale successo è fondamentalmente dovuto alla durata ultra breve dell'impulso dei laser al femtosecondo, che consente di concentrare l'energia del laser ($\sim \mu J/\mathrm{pulse}$) con valori di intensità di picco, per singolo impulso, dell'ordine di decine di $\mathrm{TW/cm^2}$. A questi ordini di grandezza, è possibile eccitare materiali ad alto bandgap ed indurre modifiche strutturali permanenti attraverso meccanismi non lineari di deposizione dell'energia della luce, rendendo possibile indurre cambiamenti permanenti e contrallati dell'indice di rifrazione del materiale irradiato [7], [10]. Infatti, i processi di assorbimento dei fotoni che avvengono entro centinaia di femtosecondi, coinvolgono principalmente il sottosistema degli elettroni, avendo luogo in una scala di tempo molto più corta di quella relativa alla deposizione di energia nei nuclei, non coinvolgendo la diffusione del calore e/o rilassamenti termo-elastici. La caratterizzazione spettroscopica del volume esposto evidenzia la generazione dei difetti di punto [11]–[14], causata dagli impulsi ad alta intensità, rendendo lo studio di questi difetti indotti cruciale al fine di comprendere le molte applicazioni offerte dalla microlavorazione fotonica. Nonostante le tante possibili applicazioni, la dinamica del rilassamento, successivo all'eccitazione che porta all'acquisizione di nuove proprietà ottiche, non è ancora del tutto chiaro. Nel presente studio, investighiamo l'effetto della scelta della lunghezza d'onda nella foto-iscrizione di guide d'onda, con particolare attenzione ai difetti stabili indotti, ma anche a quelli meno stabili, generati durante l'esposizione stessa al laser, così da evidenziare i vantaggi di una caratterizzazione *in situ* dei difetti indotti, rispetto all'analisi post-mortem.

Infine, dato che siamo interessati al comportamento transiente dei difetti di punto in generale, e non solo relativamente alla loro generazione, abbiamo scelto di studiare a fondo l'intero fotociclo di due particolari difetti di punto in condizione di assorbimento lineare. Infatti, attraverso misure di assorbimento transiente basato su impulsi al di sotto del picosecondo, è stato possibile seguire il fotociclo dei difetti appena dopo l'impulso laser fino a qualche nanosecondo. Tuttavia, esperimenti pump-probe in materiali ad alto bandgap sono particolarmente difficili in quanto necessitano dell'uso di una eccitazione tunabile nello spettro UV, che ancora oggi rappresenta una sfida dal punto di vista sperimentale. L'obbiettivo di questa sezione è quello di fornire un appoccio

sperimentale innovativo rivolto a risolvere problemi relativi ai centri di colore in solidi ad alto bandgap, che spesso dominano la loro riposta ottica, attraverso le studio di difetti stabili nella silice.

La tesi è organizzata come segue.

Nel capitolo 1 è presentata la struttura microscopica della silice, con la sua topologia e le sue proprietà elettroniche. Inoltre, sono introdotti e definiti i difetti di punto, con particolare attenzione alle loro proprietà ottiche. Verrà fornita una panoramica relativa alla struttura e alle proprietà elettroniche dei difetti intrinseci ed estrinseci, al fine di fornire una visione completa della varietà dei difetti che saranno discussi lungo questa tesi di dottorato. Le sessioni successive saranno rivolte all'interazione tra la silice e la radiazione, introducendone le proprietà ottiche, approfondendo i meccanismi di generazione di difetti sotto radiazione ionizzante e attraverso fotoionizzazione non lineare causata da laser ad alta intensità, presentando i vari fenomeni legati all'esposizione alla radiazione.

Il capitol 2 sarà dedicato ai concetti base dei fenomeni osservati lungo la tesi di dottorato. Saranno introdotte le basi relative alle tecniche sperimentali utilizzate per investigare i campioni studiati, come l'assorbimento ottico, lo studio della RIA, la fotoluminescienza, la spettroscopia pump-probe, lo scattering Raman e Rayleigh e la microscopia a contrasto di fase. In questo capitol verrà data particolare importanza alla tecnica dell'assorbimento transiente mediante pump-probe, poichè come tecnica spettroscopica ha una risoluzione temporale dell'ordine dei femto-picosecondi, risultando innovativa per studio dei sistemi solidi.

Il capitolo 3 introduce sia i diversi tipi di campioni che i diversi apparati spertimentali utilizzati durante questi 3 anni di lavoro. Anche in questo caso, come già detto per il capitol 2, particolare attenzione sarà rivolta alle misure di pump-probe. È importante sottolineare che parte del progetto di dottorato era finalizzato allo sviluppo e al miglioramento di un apparato sperimentale pump-probe capace di misurare l'assorbimento transiente relativo ai difetti di punto nella silice. Tale scopo è stato raggiunto all'Università di Palermo, nell'ambito della co-supervisione congiunta del progetto di dottorato, tra l'Università di Palermo ed il Laboratoire Hubert Curien (LabHC), trovando le migliori condizioni sperimentali per investigare tali sistemi. L'esperienza guadagnata all'Università di Palermo è stata fondamentale al fine di continuare la ricerca a Saint Etienne, utilizzando un nuovo e altamente performante apparato sperimentale pensato per ottenere nuove e

più profonde informazioni sui difetti di punto in silcie. I due apparati sperimentali per misure pump-probe, dell'Università di Palermo e del Laboratoire Hubert Curien, saranno presentati in questo capitolo

Nel capitol 4 sono riportati i risultati sui meccanismi base all'origine dell'attenuazione indotta dalla radiazione in diverse classi di fibre ottiche. Abbiamo infatti studiato la risposta di fibre ottiche "canoniche" alla radiazione X, sia pulsata che stazionaria. Tali fibre, dette "canoniche", sono rappresentative delle fibre ottiche commerciali, eccetto per il fatto che abbiamo accesso alla loro composizione chimica e ai dettagli di produzione, grazie al laboratorio comune LabH6 tra LabHC e l'iXblue. I campioni testati sono rappresentativi delle fibre ottiche più diffuse nel campo delle telecomunicazioni e della dosimetria, come le fibre ottiche in silice pura e le fibre dopate con fluoro, germanio e fosforo. L'attenuazione indotta dalla radiazione sara studiata con grande attenzione ai difetti responsabili dell'oscuramento della fibra. In particolare, abbiamo ottenuto nuove informazioni sui difetti metastabili, principali responsabili della risposta transiente delle fibre esposte alla radiazione. Per questo motive, abbiamo confrontato lo studio della RIA sia a temperatura ambiente che alla temperatura dell'azoto liquido.

Il capitolo 5 sarà focalizzato sulla caratterizzazione dell'interazione tra la silice e gli impulsi al femtosecondo ad alta intensità. Lo studio è stato condotto combinando la caratterizzazione post mortem delle guide d'onda inscritte sotto diverse condizioni sperimentali con misure in situ relative ai difetti instabili che decadono subito dopo l'irraggiamento. Anche in questo caso, la nostra attenzione si è rivolta al ruolo dei difetti nelle proprietà ottiche delle guide d'onda inscritte e alla relazione tra le loro proprietà ottiche e le condizioni di irraggiamento.

Nell'ultimo capitolo, viene presentato un nuovo e promettente approccio sperimentale per studiare il fotociclo dei difetti di punto in condizione di assorbimento lineare con una risoluzione sperimentale ad di sotto del picosecondo. Tale metodo sfrutta la possibilità di tunare, in un ampio intervallo spettrale, la lungezza d'onda di eccitazione per le misure di assorbimento transiente. Inoltre, essendo in condizioni di assorbimento lineare, siamo in grado di eccitare selettivamente il centro di colore di interesse. Come esempio delle potenzialità di tale approccio, nella presente tesi riportiamo lo studio dell'assorbimento transiente di due noti difetti di punto, il Non-Bridging-Oxygen-Hole-Center ed il Germanium-Lone-Pair-Center, sotto fotoeccitazione nell'UV, seguendone la dinamica in funzione della lunghezza d'onda di eccitazione ed in condizioni di

assorbimento lineare, in una scala temporale dell'ordine dei femto-picosecondi. La combinazione di questi esperimenti ha permesso di far luce sul fotociclo dei difetti coinvolti, evidenziando come le moderne misure di assorbimento transiente accoppiate con un'eccitazione UV tunabile rappresentino uno strumento innovativo per investigare sistemi amorfi ed, in generale, sistemi solidi.

Infine, le conclusioni riassumono i risultati presentati nei capitoli precedenti, evidenziando le sfide future relative a questo campo di ricerca e sottolineando come il presente lavoro contribuisce a far luce sui fenomeni osservati.

Chapter 1. Optical properties of amorphous silica and their evolution under irradiation

The present chapter aims to introduce the basic concepts needed to understand the amorphous silica (a-SiO_2) optical properties, in terms of point defects embedded in a solid amorphous matrix. Moreover, we will provide the theoretical background about the point defects electronic states, their generation and also light-SiO_2 interaction.

1.1. Silica structure

To define the point defects nature in SiO_2 and their relative optical properties, which are at the basis of the operation principle of many applications, it is necessary to point-out the ideal amorphous silica, its microscopic topology and electronic structure. In the following section, we will provide an overview of the important properties that make this glass so widely used in different technological fields and still one of the main studied material despite decades of studies [15].

1. 1.1 Topology

The fundamental structural unit of the amorphous silica is represented by a SiO_4 tetrahedron, depicted as a central silicon atom bound to four oxygen atoms at the corners (see Figure 1.1 a) [1], [2]. The bond is partially covalent and ionic, with an excess of negative charge on the oxygen atoms.

Nowadays, the 'ideal' a-SiO_2 topology is well represented by the Continuous Random Network (CRN) [16], the CRN approach being supported by both neutron and X-ray scattering measurements [17], [18]. The nature of the bonding between the oxygen and silicon atoms is analogous to the crystal counterpart one (quartz) [19], [20]. The main difference is based in their structural units linked together in a "random" organization forming a material without any long-

range order. Indeed, although the very rigid tetrahedron structures of the a-SiO_2 and of the quartz are similar, with $O - \widehat{Si} - O$ angle of ~109.5°, a $Si - O$ bond length of ~1.62 Å and the distance between two oxygen is ~2.62 Å, their lattice structures differ since the silica is a glass and the quartz a crystal [1], [2]. The main difference, giving rise to the CRN, is the wide variance of the angle defined by the connection between each pairs of SiO_4 tetrahedra, presenting different relative spatial orientations of the connected structural units. On the contrary, the quartz shows only a narrow angle distribution around ~144° (average value observed in a-SiO_2). As depicted in Figure 1.1 b) and Figure 1.1 c), amorphous silica network is characterized by a large distribution of the $Si - \widehat{O} - Si$ bridging angles, with values spreading between 120°÷180° [1]. The stochastic distribution of the bridging angle between two different adjacent tetrahedra entails the absence of translational symmetry and the loss of the long-range order, defining an amorphous material.

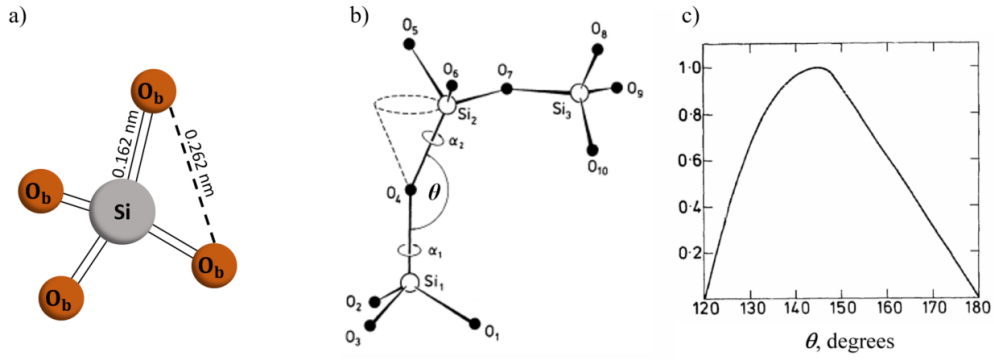

Figure 1.1. a) Model of the silica structural unit: the silicon atom is the grey sphere in the center and the oxygen atoms are the orange spheres at the corner of the tetrahedron. b) The representation of the $Si - \hat{O} - Si$ bridging angle between two SiO_4 tetrahedra, with c) the relative angle distribution in a- SiO_2 determined by X-ray diffraction. Figure adapted from [1].

To describe the topology of the silica network, the structural order has been divided in four ranges [1]. As already mentioned above, the ranges I and II are represented by the structural unit (Figure 1.1 a)) and the interconnection of adjacent structural units (Figure 1.1 b)), respectively. The most important parameters to characterize these spatial ranges are the $O - \widehat{Si} - O$ angle as well as the $Si - O$ bond length for the range I and the $Si - \widehat{O} - Si$ bridging angle and the two

torsion angles α_1 and α_2 (as shown in Figure 1.1 b), for the range II. The main disorder that characterizes the a-SiO_2 network arises at the range II.

The range III order is related to the intermediate range order for the amorphous network, shown in Figure 1.2. The range III is well described by the ring statistic, which counts the ring dimension taking every pairs of bonds on each atom finding the smallest sized ring (*expressed as number of tetrahedra*) in which both are contained. Indeed, the network could be described as a continuum of *n*-membered rings distribution. As supported by Raman and inelastic neutron scattering measurements, the silica ring statistic is dominated by 5-6 membered rings, but 4 and 3 membered rings are also present even at lower concentrations [1], [19], [21]–[23].

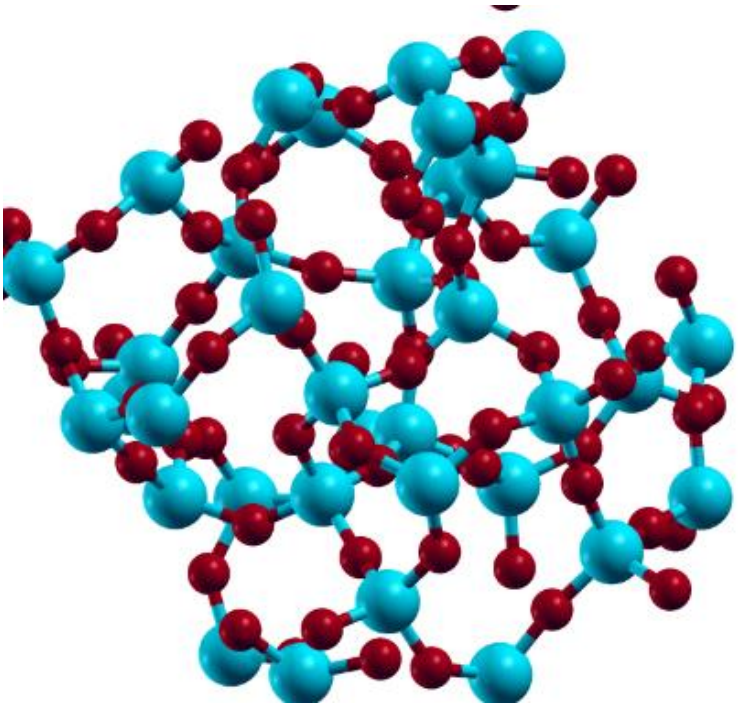

Figure 1.2. Representation of the silica range III order: silicon atoms are the blue spheres and the oxygen in red.

Although amorphous solids are characterized by the lack of the long-range order, it is nevertheless possible to observe long range density fluctuations that are described by the range IV order. This order gives rise to micro-heterogeneity over tens of angstrom length scale. It is possible to measure these fluctuations with respect to the silica average density through X-ray and neutron small angle scattering techniques [1].

1. 1.2 Bands structure

What characterizes the ideal silica is:

- No broken bonds or homopolar bonds;
- Each adjacent tetrahedra pair is connected by only one vertex;
- Chemically-ordered: each Si atom has four O neighbors tetrahedrally arranged in space and each O atom has two Si neighbors.

The deviation to these conditions defines a point defect, a concept that will be discussed in the next section. All the previous attributes would make the ideal pure silica totally transparent in a large spectral range, without considering nonlinear phenomena, from the near-infrared (NIR) to the ultraviolet (UV) light. In particular, amorphous silica and quartz share many macroscopic properties: they are both insulators, radiation tolerant, present good thermal and mechanical stabilities and they are both characterized by a wide band gap around 9 eV. In particular, since the band gap in solid arises from a periodic potential, it is evident that the above mentioned properties are linked with the short-range order periodicity, defined by the common a-SiO_2 structural unit and its crystal counterpart. Indeed, the most active optical transitions in silica are affiliated to the valence band (VB) and the conduction band (CB), constituted by a continuum of states. VB is fully occupied by electrons, while the CB is empty. On the contrary, the absorption coefficient $\alpha(E)$ comes to zero between these two electronic bands, establishing the band gap ($E_{gap} \sim 9$ eV), inside which no electronic state is present in 'ideal' vitreous silica. For a-SiO_2, the absorption coefficient $\alpha(E)$ (for direct and allowed transition), near the CB edge, is given by [24], [25]:

$$\alpha(E) \propto \sqrt{\hbar\omega - E_{gap}} \tag{1.1}$$

where $\hbar\omega$, with the reduced Planck constant $\hbar = 1.05 \cdot 10^{-34}$ Js $= 6.6 \cdot 10^{-16}$ eVs, is the energy of the incoming light and E_{gap} is the energy band gap.

The ideal silica is characterized by interband transition between a minimum ($\sim$9 eV) and a maximum energies, as shown in Figure 1.3, resulting in a continuous of absorption.

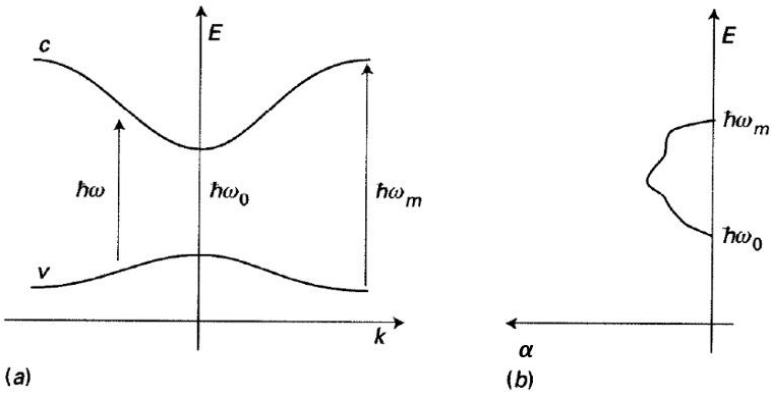

Figure 1.3. (a) Illustration of the conduction band (c) and the valence band (v) as function of the wave vector k in an insulator. (b) Absorption coefficient in an insulator: α differs from zero only between a minimum and a maximum energy values. Figure adapted from [26].

The electronic structure of the a-SiO_2 is illustrated in Figure 1.4 [27]. The VB is composed mostly by the 2p electronic states belonging to the oxygen lone pairs and by the electrons of the $Si-O$ bond [27], [28]. As depicted in Figure 1.4 the VB is composed of electronic states from -20 eV to 0 eV, for which the top of the band, from -5 eV to 0 eV is involved to the optical transition with point defects. 3s oxygen with p and d silicon electronic states contribute to the available CB states.

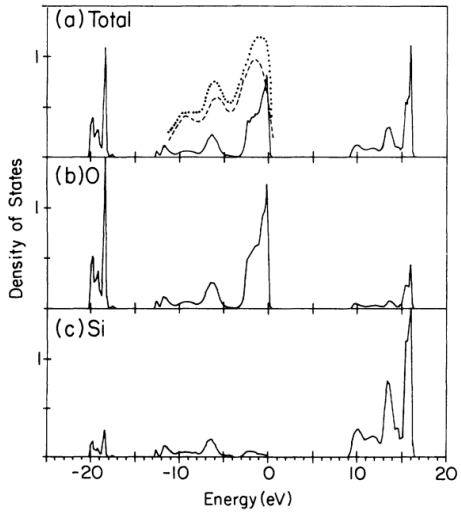

Figure 1.4. a) Calculated electronic density of states of silica (continuous line) overlapped with the states measured through photo-emission measurements (dotted and dashed lines). b) and c) are respectively the projections of the density of states on the oxygen (O) and silicon (Si) states. Figure adapted from [27].

1.2. Point defects

All the imperfections (defects) in the fused silica network, which could occur during the synthesis of the sample or be induced under laser or ionizing radiations, alter the properties of the glass, such as its thermal stability or its optical properties.

The defect importance lies on the many technological devices based on the exploitation of their optical and electronic properties, making the basic mechanisms study of their generation and their photocycle of primarily importance. In the following we will provide an overview of point defects usually observed in amorphous silica.

1. 2.1 Definition of point defects

All the deviations from the ideal silica structure as described in the previous section, have to be considered as defects. Along the present manuscript, we will focus on bulk defects embedded in the silica matrix, localized in a length scale comparable with the fundamental silica structural units, and for this reason, called point defects [1]–[3], [29]–[31]. Since the appearance of such structures modifies the optical properties of the transparent native material, the point defects are also sometimes called color centers. From the physical point of view, the presence of defects introduces molecular-like electronic levels inside the band gap creating new channels for optical transitions [1], [3], [26], [29]–[32]. The main absorption and luminescence bands known in pure SiO_2 are reported in Figure 1.5, assuming a Gaussian shape [32]. This profile is explained by the fact that the electrons linked to a defect cannot be described by a delocalized periodic wave function of the ideal solid, but from energy state typical of localized states. The presence of point defects allows optical transitions toward forbidden states (in the ideal silica), making not any more transparent the glass.

Basically, point defects could be divided into two categories: intrinsic and extrinsic centers. The former are composed by deformations involving O and Si atoms in the matrix. In particular, we are referring to homopolar bonds, double or broken bonds, trapped charges or under-

coordinated atoms. In the case of extrinsic defects other atom types are involved in addition to O and Si, such as the germanium (Ge), chlorine (Cl), other dopant kinds and alkaline impurities.

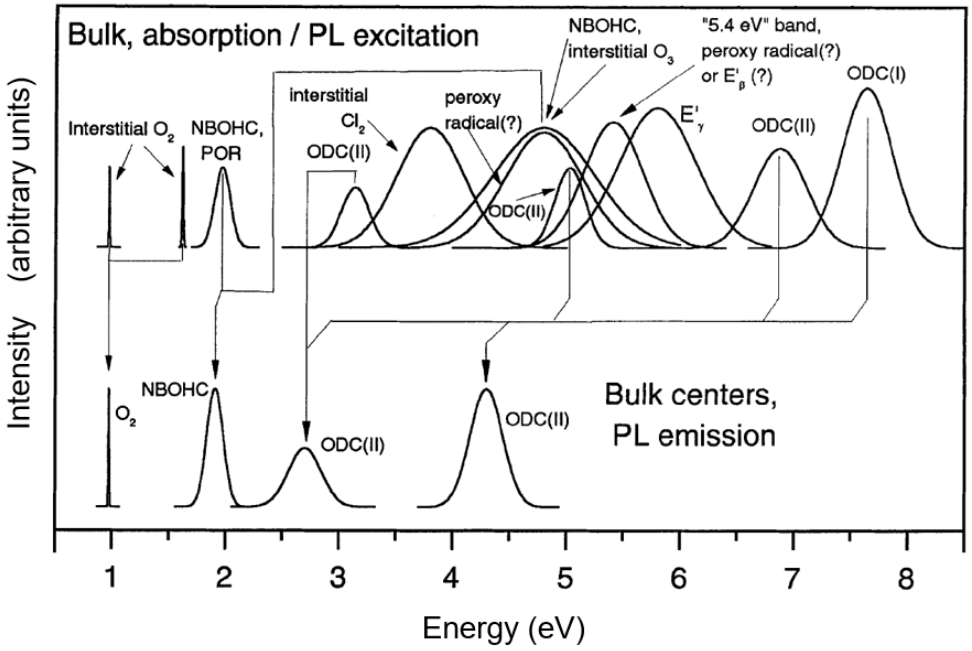

Figure 1.5. Absorption and photoluminescence bands of some intrinsic defects in a-SiO_2: the electronic defects lead the material to absorb and/or to emit light from the IR to the UV. Figure adapted from [32].

Because of their impact on the glass optical properties, point defects can be investigated through different experimental spectroscopic techniques. Indeed, the defects are generally associated with absorption bands, and could present radiative electronic relaxation. In this way it is possible to study the defect optical absorption (OA) spectra and photoluminescence (PL) properties. Furthermore, some defect types are also sensitive to Electron Paramagnetic Resonance (EPR) or characterized by Raman features.

The combination of several experimental techniques allows to gain more information and correlations on the defect features than a single experimental technique. For this reason, in the present manuscript, when it is possible, the investigation of point defects will be achieved by combining different spectroscopic techniques.

1. 2.2 Optical transition in point defects

The presence of point defects gives rise to emission and/or absorption bands, due to the transition between their molecular-like electronic levels. The difference in energy between the ground and the excited states is linked to the inhomogeneities in the defect surrounding and to the coupling between the electronic transition and phonons. In the amorphous silica case, the inhomogeneous broadening of the absorption bands is ~ 0.1 eV to be compared to $0.2 \div 1$ eV for the homogeneous one [3].

Color centers in bulk a-SiO_2 are embedded in the glass network, making the environment surrounding the defect crowded with several different atoms which affect the defect behaviours. Solving the Schrödinger equation to find the electronic states is particularly complex for such many-body problem. For this reason, in the following discussion, we will assume the defects as a single molecule interacting only with a small number of atoms, basically its nearer neighborhood [1], [3], [20]. Indeed, a color center strongly interacts with the host matrix and to have a reasonable description, it is not possible to treat the defect as a separate entity apart from the surrounding atoms. Since the defect electronic structure is largely influenced by the vibrational modes, via the electron-phonon coupling, we will consider the defect as a molecular complex including its interacting surrounding matrix and study the optical properties of the whole structure. The molecular complex involves N nuclei and n electrons which interact with the Coulomb force and the Hamiltonian could be written as [2], [3], [26], [33], [34]:

$$H = \frac{1}{2m}\sum_{i=1}^{n}\mathbf{p}_i^2 + \frac{1}{2}\sum_{l=1}^{N}\frac{\mathbf{P}_l^2}{M_l} + V(\mathbf{r},\mathbf{R}) \tag{1.2}$$

where m and M_l are the electron and nuclear mass of the l atom, respectively, $\mathbf{p}_i$ and $\mathbf{P}_l$ the electron and nuclei momentum and $V(\mathbf{r},\mathbf{R})$ the potential energy as function of the electron position ($\mathbf{r}$) and nucleus position ($\mathbf{R}$). The first two terms are linked to the kinetic energy of the electron and nuclei, respectively, while the third is the interaction potential, describing the electron/electron, nucleus/ nucleus and electron/nucleus interactions. The $V(\mathbf{r},\mathbf{R})$ term can be written as:

$$V(\mathbf{r},\mathbf{R}) = \frac{1}{2}\sum_i\sum_j \frac{e^2}{|\mathbf{r}_i - \mathbf{r}_j|} + \frac{1}{2}\sum_n\sum_m \frac{Z_n Z_m e^2}{|\mathbf{R}_n - \mathbf{R}_m|} - \frac{1}{2}\sum_i\sum_n \frac{Z_n e^2}{|\mathbf{R}_n - \mathbf{r}_i|} \quad (1.3)$$

where e is the electronic charge ($1.6 \cdot 10^{-19}$ C) and Z is the atomic number.

The solution of this many-body problem, through the Schrödinger equation

$$H\Psi(\mathbf{r},\mathbf{R}) = E\Psi(\mathbf{r},\mathbf{R}) \quad (1.4)$$

where $\Psi(\mathbf{r},\mathbf{R})$ is the eigenfunction (wave function) and $E(\mathbf{r},\mathbf{R})$ is the eigenvalue of the molecule, cannot be analytically solved. The procedure for this kind of problem requires the "Adiabatic Approximation" [3], [26], [33], [34], that according to the large ratio between the masses of the nuclei and the electrons ($M >> m$), considers the electron velocity much higher than the one of the nuclei. This observation could be represented from the electron point of view as if the nuclei positions are almost fixed, considering the value $\mathbf{R}_l$ as a static parameter, while for the nuclei point of view the electrons are spread around them, observing only an average potential. In this framework, the expectation value of the electrons energy, parameterized in the nuclei position and averaged over the all electron coordinates, with the nuclei potential, contribute to the effective potential (V_{eff}) felt by the nuclei [3], [33]:

$$V_{eff} = V_n + \langle K_e + V_e + V_{e-n} \rangle \quad (1.5)$$

where V_n is the nuclei/nuclei repulsion, K_e is the electrons kinetic energy, V_e the electrons repulsion and V_{e-n} is the electron-nuclei attraction. All these considerations form the so-called Born-Oppenheimer (or Adiabatic) approximation. In agreement with this picture, the molecule wave function can be factorized into an electronic $\varphi(\mathbf{r},\mathbf{R})$ and nuclear $\theta(\mathbf{R})$ wavefunctions:

$$\Psi(\mathbf{r},\mathbf{R}) = \varphi(\mathbf{r},\mathbf{R})\theta(\mathbf{R}) \quad (1.6)$$

where $\varphi(\mathbf{r},\mathbf{R})$ is expressed as a function of the electronic coordinates $\mathbf{r}$ and parametrized at the nuclear position $\mathbf{R}$, and $\theta(\mathbf{R})$ as function of the nuclear coordinates $\mathbf{R}$.

Proceeding in this way, the one equation problem becomes a two separated equations problem easier to handle. Indeed, by dividing the equation 1.4 by $\varphi(\mathbf{r},\mathbf{R})$ and $\theta(\mathbf{R})$, respectively, we obtain

$$[K_e + V_e(\mathbf{r},\mathbf{R}) + V_{e-n}(\mathbf{r},\mathbf{R})]\varphi(\mathbf{r},\mathbf{R}) = \varepsilon(\mathbf{R})\varphi(\mathbf{r},\mathbf{R}) \quad (1.7)$$

$$[K_n + V_n(\mathbf{R}) + \varepsilon(\mathbf{R})]\theta(\mathbf{R}) = E_n\theta(\mathbf{R}) \quad (1.8)$$

where K_e and K_n are the electronic and nuclear kinetic operators respectively, $V_e(\mathbf{r},\mathbf{R})$ and $V_{e-n}(\mathbf{r},\mathbf{R})$ represent the electron-electron repulsion and the electron-nuclei attraction, respectively, and depend on the nuclear position, $V_n(\mathbf{R})$ is the mutual repulsion between nuclei, E_n is the nuclear vibrational eigenvalue and $\varepsilon(\mathbf{R})$ it is the eigenvalue depending parametrically on the nuclear position **R**. Indeed, for different nuclear positions, the shape of the potential $V_e(\mathbf{r},\mathbf{R})$ changes, modifying even the eigenvalue $\varepsilon(\mathbf{R})$. In equation 1.7, because of the Born-Oppenheimer approximation, $K_n\varphi(\mathbf{r},\mathbf{R}) = \frac{1}{2}\sum_{l=1}^{N}\frac{\mathbf{P}_l^2}{M_l}\varphi(\mathbf{r},\mathbf{R}) = -\frac{1}{2}\sum_{l=1}^{N}\frac{\hbar^2}{M_l}\nabla_l^2\varphi(\mathbf{r},\mathbf{R}) \sim 0$. As it is evident from equation 1.8, the term $\varepsilon(\mathbf{R})$, in the framework of the adiabatic approximation, represents a correction of the potential felt by the nuclei including, in addition to the mutual repulsion, the contribution of nuclear interaction with the averaged electronic distribution.

Under the above-mentioned approximation, the total energy of the single molecule can be written as the sum of the two eigenvalues:

$$E_{tot} = \varepsilon + E_n \quad (1.9)$$

The resolution of the couple of equations 1.7 and 1.8 is very complex to handle in a 3D space, involving 3N dimensions. To simplify the problem, it is possible to describe the nuclear motion as a function of the nuclear displacement from the equilibrium position, which is characterized by a vibrational, or "configuration", coordinate Q. This configurational coordinate is easy to image in a diatomic molecule, as the distance between the two atoms, in n-atoms molecule, the configurational coordinate corresponds to the normal coordinate, expressed as a set of $\{Q_f\}$ nuclear normal coordinates. With this assumption, and under the hypothesis of harmonic vibrations (small vibrations compared to the equilibrium position Q_0), it is possible to write the nuclear wave function $\theta(\mathbf{Q})$, now as function of the normal coordinates, as a product of harmonic oscillator functions $\theta_f(Q_f)$ for each normal coordinate Q_f:

$$\theta(\mathbf{Q}) = \prod_{f=1}^{N_f} \theta_f(Q_f) \tag{1.10}$$

where N_f is the number of normal vibrational modes. The nuclear problem presents the following solution:

$$E_n(n_f) = \hbar\omega_f\left(n_f + \frac{1}{2}\right) \tag{1.11}$$

with $n_f = 0, 1, 2, 3$ ... is the vibrational quantum number and ω_f the frequency of the normal mode f. Since we have defined the effective potential energy V_{eff} of the system as the sum of the average electronic distribution and nuclear mutual repulsion, considering only one normal mode, in the harmonic approximation, the electronic potential $\varepsilon(Q_f)$ represents the minimum of the parabola described by the nuclear motion at the position Q_{f0}. V_{eff} could be expressed (Figure 1.6) as

$$V_{eff} = \varepsilon(Q_{f0}) + \frac{1}{2}A_f(Q_f - Q_{f0})^2 \tag{1.12}$$

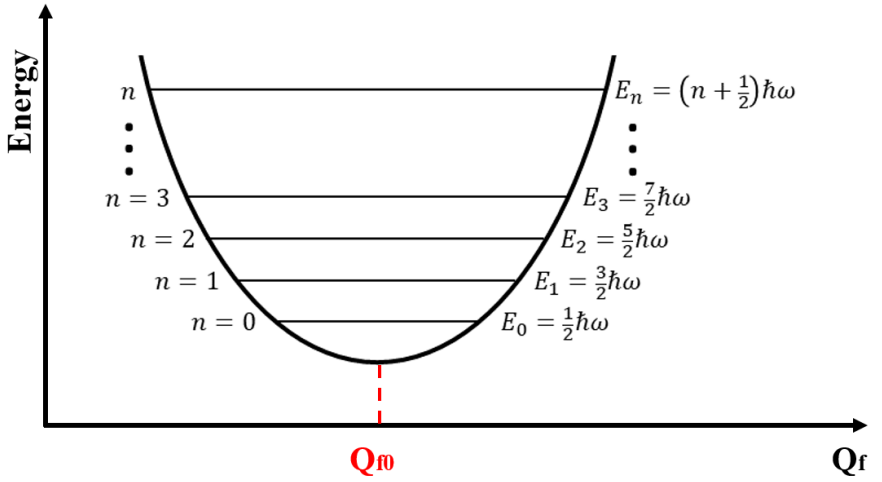

Figure 1.6. Energy of the molecule under the harmonic approximation as function of the generalized coordinate Q_f and the vibrational quantum number n.

By the second derivative with respect to Q_f, it is possible to obtain an expression of the curvature of the potential A_f [3]:

$$A_f = \frac{d^2 V_{eff}}{dQ_f{}^2} = \hbar^2 \omega_f{}^2 \tag{1.13}$$

Therefore, according to the equations 1.9, 1.11 and 1.12, the total energy of the system could be expressed by:

$$E_{tot} = \varepsilon^{eq} + \sum_{f=1}^{N_f} \hbar\omega_f \left(n_f + \frac{1}{2}\right) \tag{1.14}$$

where ε^{eq} represents the electronic eigenvalue when the nuclei are in the equilibrium position Q_{f0}.

When a molecule absorbs light in the vis-UV spectral range (optical absorption), it involves a transition between states at low energy (possibly ground state) to a higher energy level (excited state) of an electron. All vibrational levels are thermally populated following the Boltzmann distribution at a certain temperature T. Therefore, the optical transition could be seen as a transition from a vibrational level of the ground state to another vibrational level belonged to the excited electronic state. Generally, the equilibrium position of the ground state of normal coordinate Q_{f0} changes in the excited state: $Q'_{f0} = Q_{f0} + \Delta_f$, with a displacement Δ_f (linear coupling). The effective harmonic potentials of the ground (V_{gr}) and excited (V_{ex}) states could be written as:

$$V_{gr} = \varepsilon_{gr}^{eq} + \frac{\hbar^2}{2} \sum_{f=1}^{N_f} \omega_f{}^2 (Q_f - Q_{f0})^2 \tag{1.15}$$

$$V_{ex} = \varepsilon_{ex}^{eq} + \frac{\hbar^2}{2} \sum_{f=1}^{N_f} \omega_f{}^2 (Q_f - Q'_{f0})^2 = \varepsilon_{ex}^{eq} + \frac{\hbar^2}{2} \sum_{f=1}^{N_f} \omega_f{}^2 (Q_f - Q_{f0} - \Delta_f)^2 \tag{1.16}$$

where ε_{gr}^{eq} and ε_{ex}^{eq} represent the energies of the ground and excited electronic states, respectively, and of course, the energy of the system when the nuclei are in the equilibrium positions.

Assuming that the oscillation frequencies of the ground and excited state are the same (linear coupling approximation), the energies of the states are:

$$E_{gr} = \varepsilon_{gr}^{eq} + \sum_{f=1}^{N_f} \hbar\omega_f \left(n_f + \frac{1}{2}\right) \tag{1.17}$$

$$E_{ex} = \varepsilon_{ex}^{eq} + \sum_{f=1}^{N_f} \hbar\omega_f \left(m_f + \frac{1}{2}\right) \tag{1.18}$$

with n_f and m_f the vibrational quantum numbers of the two states. Considering that an electronic transition happens in a time window of ~10^{-15} s, while the nuclear vibrations are of the order of 10^{-12} s, it is reasonable to assume that the nuclear position and velocity do not change during the optical transition. This approximation is called Franck-Condon principle [34], which basically states that the optical absorption and luminescence (*radiative transition from the excited to the ground state*) could be described by a vertical transition between the ground and the excited state, in the normal coordinate system, as illustrated in Figure 1.7. Moreover, the electron remains in the excited state about ~10^{-9} s, before to decay newly to the ground state, having during this time the possibility to thermalize according to the Boltzmann distribution. The difference between the absorbed and emitted energies during the transition gives rise to the Stokes shift.

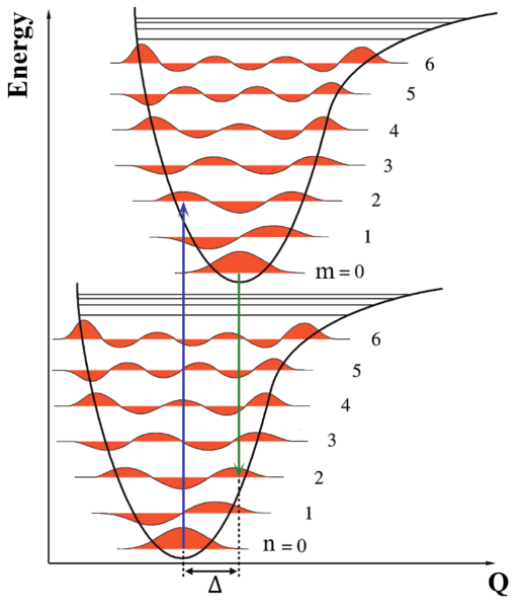

Figure 1.7. Illustration of the Frank-Condon principle: the optical transitions are represented as vertical transitions between the ground and the excited states in the normal coordinate system.

Considering only one normal coordinate, it is well known that the optical absorption transition rate $R_{gr\to ex}$, between the ground state at the $n-th$ vibrational state to the excited state at the $m-th$

vibrational state, is proportional to the square modulus of the quantum mechanical matrix element between the two states, resulting in the Dirac formalism as:

$$R_{gr\rightarrow ex} \propto \left|\langle \Psi_{ex}|e\mathbf{r}|\Psi_{gr}\rangle\right|^2 \tag{1.19}$$

where $e\mathbf{r}$ is the dipole moment due to the electronic charges. Considering equation 1.6, the electronic dipole moment operator will be applied only to the electronic wave function. In agreement with the Condon approximation, the dependence on the Q parameter of the $\varphi(\mathbf{r},\mathbf{Q})$ is weak, then we can substitute the normal coordinates by their averaged values in the electronic state $\varphi(\mathbf{r},\overline{\mathbf{Q}})$ (Q_{f0} and Q'_{f0} in our example). Proceeding with the above-mentioned assumption, the matrix element of equation 1.19 breaks into two different matrix elements [3]:

$$R_{gr\rightarrow ex} \propto \left|\langle \varphi_{ex}(\mathbf{r},\overline{\mathbf{Q}'})|e\mathbf{r}|\varphi_{gr}(\mathbf{r},\overline{\mathbf{Q}})\rangle\right|^2 \left|\langle \theta^{n}_{gr}(\overline{\mathbf{Q}'})|\theta^{m}_{ex}(\overline{\mathbf{Q}})\rangle\right|^2 = |D|^2 \left|M^{nm}_{gr\rightarrow ex}\right|^2 \tag{1.20}$$

where the first term $|D|^2$ is the electronic part, that is proportional to the overall probability (*and so the intensity of the band*) of the transition; the nuclear part $\left|M^{nm}_{gr\rightarrow ex}\right|^2$, gives the transition probability between the $n-th$ vibrational state of the ground electronic state to the $m-th$ vibration state of the excited one.

Owing to the orthogonality of the wave function, if we consider even the spin multiplicity (not done in our discussion), it is important to know that the transition between the ground and excited electronic state is allowed only if the two states have the same spin state: if the ground state is a singlet state, the transition is allowed only toward another singlet state; on the contrary, if the excited state has a triplet spin multiplicity, the transition is forbidden.

Considering that during the optical transition different nuclear transitions are allowed, from the $n-th$ vibrational state of the ground electronic state to the $m-th$ vibration state of the excited one, the sum of all transition probabilities will be

$$\sum_{m}^{\infty} |D|^2 \left|M^{nm}_{gr\rightarrow ex}\right|^2 = |D|^2 \sum_{m}^{\infty} \left|M^{nm}_{gr\rightarrow ex}\right|^2 = |D|^2 \tag{1.21}$$

where $\sum_{m}^{\infty}\left|M^{nm}_{gr\rightarrow ex}\right|^2 = 1$ because the nuclear θ wave functions are orthonormal. So, it is evident that the nuclear contribution does not influence the intensity of the band, since it has unit

magnitude, but rather influences its shape. Accordingly, the probability of the optical transition depends on the electronic part.

Furthermore, the nuclear term is called the Franck-Condon integral, since it provides the overlap between the vibrational wave functions:

$$\langle \theta_{gr}^{n}(\overline{\mathbf{Q}'}) | \theta_{ex}^{m}(\overline{\mathbf{Q}}) \rangle = \int \theta_{ex}^{m\,*} \theta_{gr}^{n} d\mathbf{Q} \tag{1.22}$$

It differs from zero only when the overlap between the θ_{ex}^{m} wave function and the θ_{gr}^{n} differs from zero. When there is no coupling between electronic and vibrational modes, that basically means that there is no relaxation of the electron in the excited state after the excitation, the minima of the two potential wells in the excited and ground state coincide ($\Delta = 0$). Then $\theta_{ex} = \theta_{gr}$, the transition between vibrational states with different quantum numbers ($M_{gr\rightarrow ex}^{nm} = \delta^{nm}$) are forbidden because of the orthogonality of the eigenfunctions of an harmonic oscillator. In this way, the optical absorption line will be very sharp, because once that is defined the $n-$th vibration state of the ground electronic eigenfunction, according to the Boltzmann distribution, only the transition toward the excited state with $n-$th vibrational state will be allowed. On the contrary, when $\Delta \neq 0$, basically when there is (at least) linear coupling between the ground and the excited electronic states, also the transition characterized by $n \neq m$ will contribute to the optical absorption, resulting in the electron thermalization and relaxation in the excited state. This possibility provides different allowed transitions with slightly different energy absorptions, enlarging the characteristic band associated to the optical transition.

It is now important to introduce a parameter able to measure the magnitude of the electron-phonon coupling, useful to describe the defect-matrix interaction. At $T = 0$ K, only the $n = 0$ vibrational level could be occupied in the ground electronic state, and the nuclear part in the equation 1.20 could then be evaluated analytically by a Poisson's distribution:

$$\left| M_{gr\rightarrow ex}^{0m} \right|^2 = \exp(-S)\frac{S^m}{m!} \tag{1.23}$$

where S is the dimensionless Huang-Rhys factor, which gives the vibrational relaxation energy expressed in unit of vibrational quanta ($\hbar\omega_{vib}$). The Huang-Rhys factor is defined as follows:

$$S = \frac{E_r}{\hbar\omega_{vib}} \tag{1.24}$$

E_r represents the energy lost after the electron thermalization in the excited state. The transition between $\theta_{gr}^0 \rightarrow \theta_{ex}^0$ is called zero-phonon line, which reflects the purely electronic transition without any coupling with phonons. As already mentioned above, S measures the magnitude of the electron-phonon coupling (Figure 1.8) [3]:

- **Weak electron-phonon coupling ($0 < S < 1$):** The optical transition is dominated by the sharp zero-phonon line, with weak sidebands.
- **Medium electron-phonon coupling ($1 \lesssim S < 10$)**: Notwithstanding the zero-phonon line is still evident, the spectrum is dominated by the transition to vibrational levels with $m > 0$, resulting in asymmetric spectrum with a non-Gaussian shape.
- **Strong electron-phonon coupling ($S \gtrsim 10$**): The zero-phonon line contribution is now negligible and the bands appear with a broad Gaussian-shape envelope without any vibrational structure.

The inverse optical process of the absorption is represented by the luminescence, which consists in a radiative decay of the electron from the excited state to the ground state. In case there is no electron-phonon coupling, the luminescence is a sharp line peaking at the same energy than the absorption. Within the linear electron-phonon coupling, the vibrational eigenfunctions of the excited and ground states are the same and for symmetrical properties due to the harmonic approximation the following relation is valid:

$$M^{nm} = M^{mn} \tag{1.25}$$

The equation 1.25 gives rise to a mirror symmetry between the absorption and luminescence spectra, with the symmetry plane located at the zero-phonon line. This property is illustrated in Figure 1.9.

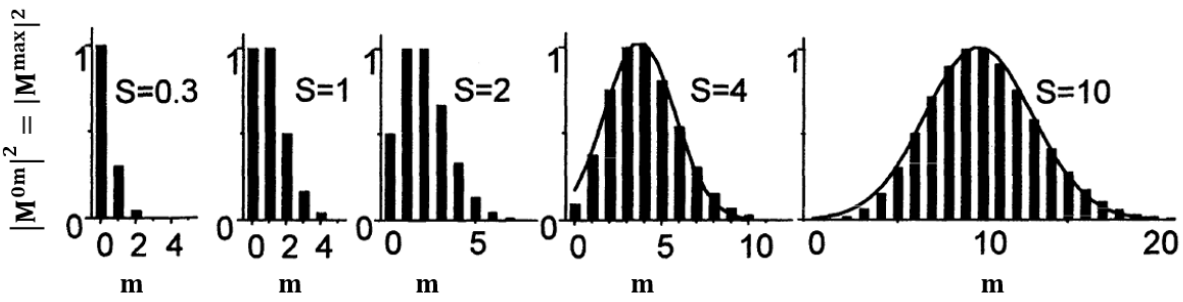

Figure 1.8. Poisson's distribution of equation 1.20, normalized for the transition maximum value, at the different electron-phonon coupling regimes. The transition is calculated from $0-$ th vibrational level in the ground state to $m-$ th vibrational level in the excited state for different values of Huang-Rhys factor S. The solid lines are Gaussian fits for the cases of $S = 4$ and $S = 10$, which demonstrate the remaining slight asymmetry of the band envelopes. Figure adapted from [3].

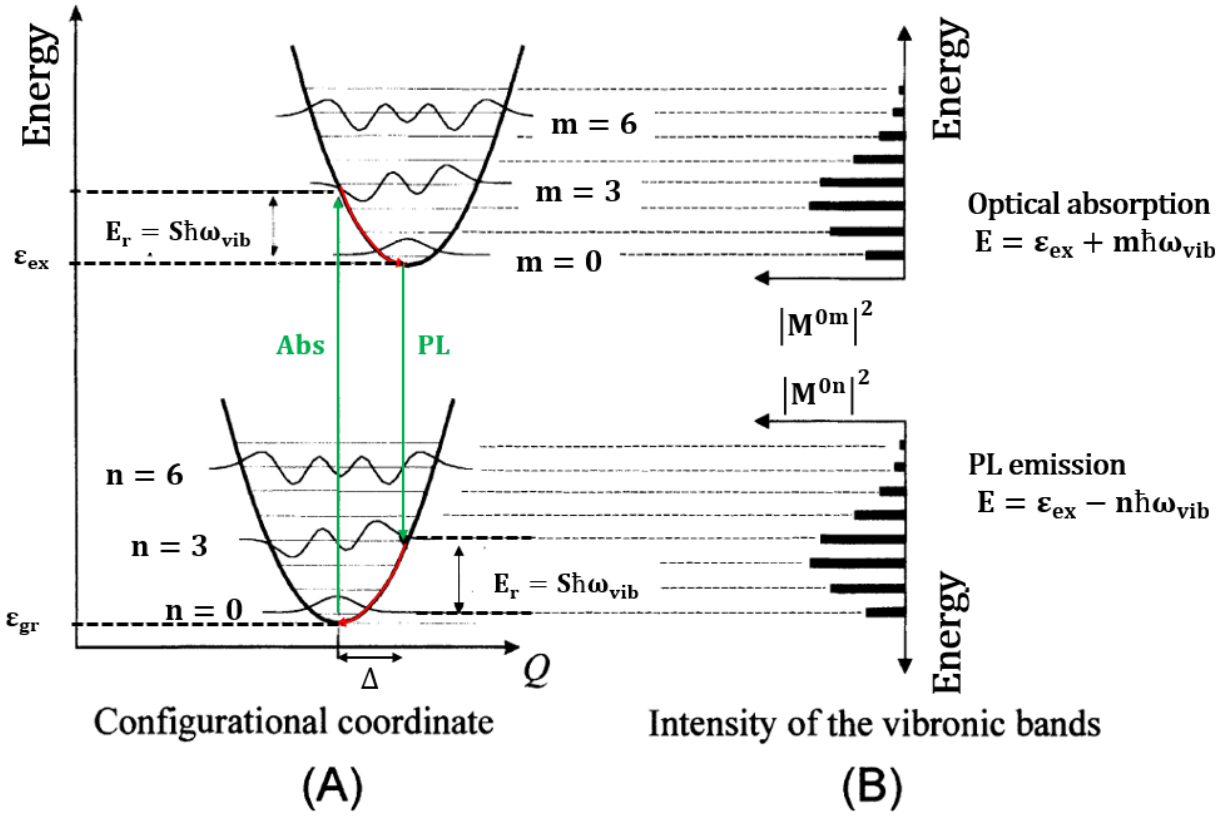

Figure 1.9. (A) Configuration coordinate diagram in linear electron-phonon coupling approximation, with vertical transition in agreement with the Franck-Condon principle. (B) Energy dependence of the Poisson's distribution that explains the mirror symmetry between the optical absorption and photoluminescence bands. Figure adapted from [3].

1. 2.3 Overview on intrinsic defects

The present paragraph is devoted to an overview about the most studied intrinsic defects, giving some spectroscopic properties and some details about their topological structures, illustrated in Figure 1.10. In particular, we will introduce a little bit more the STX and STH properties, while the properties of the NBOHCs will be reviewed later in the last chapter.

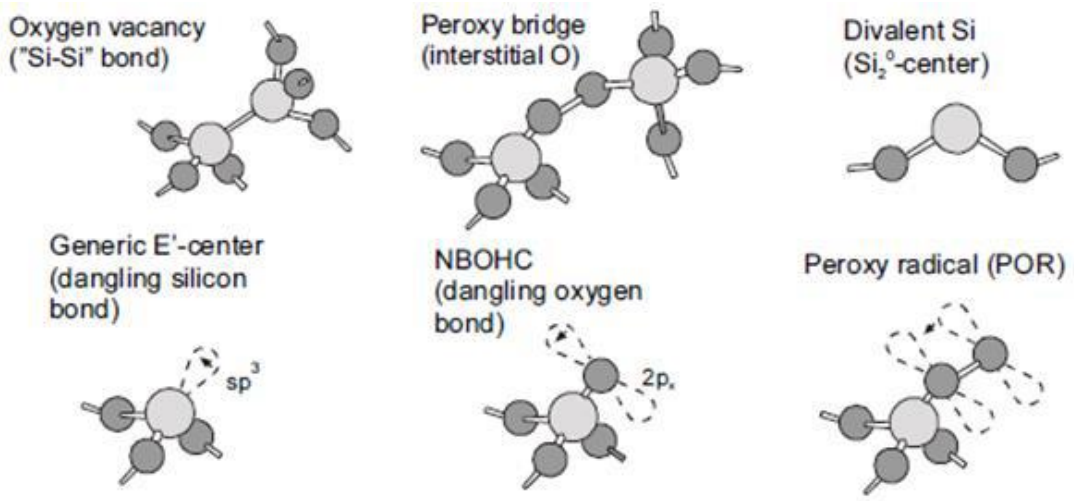

Figure 1.10. Topological microscopic structures of intrinsic point defects observed in amorphous silica. Taken from [35].

E´ center: $\equiv Si \cdot$

The E´ center is a paramagnetic defect and, based on the EPR measurements [36]–[38], its structure consists of a silicon dangling bond with an unpaired electron in the silicon sp^3 orbital (Figure 1.10) [1], [35]. This defect is characterized by an intense absorption band peaked at 5.8 eV with a Full Width at Half Maximum (FWHM) of 0.7 eV, but no-photoluminescence band is attributed to this defect [3], [4], [32], [35].

Non-Bridging Oxygen Hole Center (NBOHC): $\equiv Si - O \cdot$

The NBOHC is one of the most studied point defects, in addition to being paramagnetic [1], it is characterized by an absorption band at 2.0 eV (FWHM∼0.17 eV) and another spread absorption in the UV along 4.7 eV to 7.5 eV [4], [39]–[42]. It also possesses a PL band at 1.9 eV upon excitation of these absorption bands with a lifetime ∼15 μs [41], [43]–[45]. Thanks to these properties, its structure is well defined as an oxygen dangling bond with an unpaired electron on the oxygen 2p orbital [35], [46]–[49]. It is important to underline that this defect could be easily generated by the breaking of the Si-OH groups [41]:

$$\equiv \mathrm{Si} - \mathrm{OH} \xrightarrow{\hbar\omega} \equiv \mathrm{Si} - \mathrm{O} \cdot + \mathrm{H}^{+} \tag{1.26}$$

Moreover, NBOHC could be generated, together with the E´ center, by the breaking of a strained $\mathrm{Si} - \mathrm{O}$ bond [41]:

$$\equiv \mathrm{Si} - \mathrm{O} - \mathrm{Si} \equiv \xrightarrow{\hbar\omega} \equiv \mathrm{Si} - \mathrm{O} \cdot + \cdot \mathrm{Si} \equiv \tag{1.27}$$

Oxygen deficient center I (ODC I): $\equiv Si - Si \equiv$

The ODCs are diamagnetic defects. They are mostly observed in oxygen-deficient silica. ODC is characterized by an absorption band around 7.6 eV with a FWHM $\sim 0.5 - 0.6$ eV [4], [32]. Under 7.6 eV excitation, a PL at 4.4 eV is detected as a characteristic of the ODC (II) structure, highlighting a change in the excited state configuration. This defect could be depicted as a bonding between two adjacent silicon atoms [3], [32], [35], [50], [51].

Oxygen deficient center II (ODC II) or the divalent silicon: $= Si$:

Diamagnetic defect, often called divalent silicon, which presents a structure of a twofold coordinated silicon atom [3], [32], [35], [50]. It is characterized by different absorption bands at 3.15 eV, 5.05 eV and 6.9 eV and two photoluminescence bands at 2.7 eV and 4.4 eV, respectively by a triplet and a singlet states [3], [4], [32], [51]–[55].

Peroxy linkage (POL): $\equiv Si - O - O - Si$

Constituted by the two silicon atoms connected by two oxygen atoms bonded each other via a peroxy linkage (or peroxy bridge). POL is a diamagnetic center, and is typically observed in oxygen-rich silica [35], [56], [57]. Absorption bands peaking at 3.8 eV, 4.2 eV and $7.3 - 7.5$ eV have been attributed to this center by computational calculations [4], [56], [57].

Peroxy radical (POR): $\equiv Si - O - O \cdot$

POR is a paramagnetic center which generally dominates the a-SiO_2 EPR spectra in oxygen-rich silica [3], [4], [31]. The structure involves a dangling bond with an electron delocalized between the $O - O$ π orbital [35]. Absorption bands at 2.02 eV, 4.08 eV and 5.02 eV are attributed to this defect [3], [4], [58], [59]. Moreover, the POR concentration could be correlated to the population of NBOHC (anticorrelation) and E´ (correlation, by the POL dissociation) as shown by the following set of equations [60]:

$$\equiv \mathrm{Si} - \mathrm{O} - \mathrm{O} \xrightarrow{\hbar\omega} \equiv \mathrm{Si} - \mathrm{O} \cdot + \mathrm{O} \tag{1.28}$$

$$\equiv \mathrm{Si} - \mathrm{O} - \mathrm{O} - \mathrm{Si} \xrightarrow{\hbar\omega} \equiv \mathrm{Si} - \mathrm{O} - \mathrm{O} \cdot + \cdot \mathrm{Si} \equiv \tag{1.29}$$

Self-trapped excitons (STX)

Until now, in optical transition from the VB to the CB, we assume that the photon absorption generates the creation of a hole in the VB and a free electron in CB. Generally, the free electron and hole behave as independent particles in the insulator. However, because of the coulombian interaction (*the hole behaves like a positive charge*), it is possible that the electron in the CB and the hole in VB are bound, generating a neutral mobile system. Since the binding energy of the excitons is of the order of tens of meV, this defect is particularly unstable [26], [61].

In materials with a high dielectric constant, the electron is weakly bound with the hole and the electron-hole distance is of the order of several lattice constants, the type of created exciton is called Wannier-Mott [33]. On the contrary, in insulators where the dielectric constant is slightly higher than the unity, so with a strong coulombian interaction, the electron-hole distance is of the

order of the lattice constant: they form the Frenkel excitons [33], [62], [63]. The presence of the excitons involves the appearance of a localized level under the CB, influencing the optical properties of the lattice. In insulators with highly polarized matrix, the excitons tend to be self-trapped (STX), becoming a no more diffusive particle with charge and energy localized in a site of the intermolecular distance dimension.

After multiphoton ionization, STXs could be means of channeling of the electronic excitation, becoming an important feature of the relaxation process of the accumulated energy after intensive laser irradiation and the consequent lattice deformation.

For the SiO_2, the STX consists of a hole localized on an oxygen atom with the electron delocalized around the adjacent silicon atom [64]–[67]. The localization of the hole around the oxygen results in atom displacement and a consequent stretching and weakening of the $Si - O - Si$ bond. Because of the instability of the STX, their characterization was possible via the implementation of ultimate time-resolved techniques, revealing the excitons self-trapping in a time window of the order of $\sim 150\ fs$ after the free-carriers generation. Time-resolved absorption experiments attribute an absorption band at $5.2\ eV$ to the STX in amorphous SiO_2 [68], [69].

Moreover, it was observed that when the $Si - O - Si$ stretching is sufficiently strong because of the oxygen displacement, the bond breaks with the simultaneous creation of the NBOHC and E´ center, as stated by equation 1.27, accompanied by a characteristic photoluminescence at $2.5 - 2.8\ eV$ [70]–[72]. The above-mentioned process is illustrated in Figure 1.11.

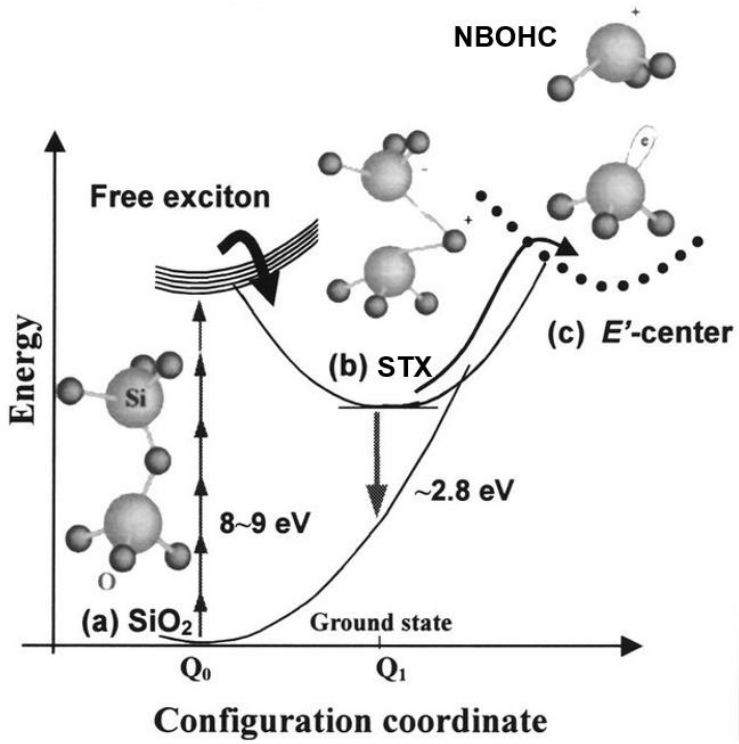

Figure 1.11. Configuration coordinate diagram from the STX generation to the formation of NBOHC and E´ center in amorphous SiO_2. (a) The multiphoton absorption formed the free excitons. Then the free excitons are self-trapped, inducing lattice distortion due to strong electron-phonon interactions, forming the STX. (b) Part of STXs lead to the $Si - O$ bond breaking and after (c) 2.8 eV PL channel with the E´ and NBOHC creation. Figure adapted from [72].

Self-trapped holes (STH)

An extremely important role is played by Self-Trapped Holes (STHs) defects [73], [74], since they represent one of the major absorbing defects in pure-silica fiber cores [4], [75]–[84]. STHs are paramagnetic defects and are metastable at room temperature. Two types of STHs have been identified by D.L. Griscom through EPR-spectra analysis [73]. The STH_1, constituted by a hole localized on a non-bonding p-orbital of a single bridging oxygen atom (Figure 12 (a)), and the STH_2 consisting in a hole delocalized over non-bonding p-orbitals of two neighboring bridging oxygen atoms of the same SiO_4 tetrahedron (Figure 12 (b)) [29], [74]. The former is characterized by an absorption band at 2.61 eV (FWHM~ 1.2 eV), while the latter is associated with a band peaking at 2.16 eV (FWHM$\sim 0.3 - 0.6$ eV). It is important to know that in optical fibers stretched variant of such defects were observed: the strained-assisted STH_1 and the strained-assisted STH_2, with absorption bands at 1.88 eV (FWHM$\sim 0.2 - 0.5$ eV) and 1.66 eV (FWHM$\sim 0.3 - 0.7$ eV).

Furthermore, a wide non-Gaussian absorption in the infrared domain, known as “low temperature infrared absorption” (LTIRA) is also attributed to STHs.

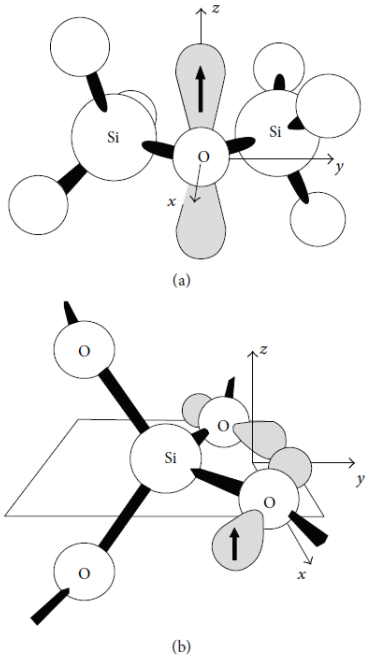

Figure 1.12. A model of self-trapped holes point defects: (a) STH_1 and (b) STH_2. Figure taken from [29].

1. 2.4 Overview on extrinsic defects

Extrinsic defects are related to the presence of impurities or dopants embedded in the silica network. The most common extrinsic defects involve hydrogen, chlorine, germanium, phosphorus, aluminum, cerium, nitrogen…. Clearly, the number of these defects is relatively huge. So, in the following we will provide only the main properties for some of the most studied extrinsic defects and basically the most important ones for this PhD work. In particular, the GLPC will be deepened in the last chapter.

OH group

The OH group is a defect related to the hydrogen-based variety of extrinsic defects in amorphous silica, which is at the basis of the silica glass classification. The main spectroscopic features attributed to the OH presence in the glass [85] are the absorption bands at 0.9 eV, 0.99 eV,

1.09 eV, 1.3 eV and 1.46 eV, manifestation of overtones and combination modes of the main absorption band peaked at 0.46 eV (2.7 μm). In particular, the band at 0.9 eV (1380 nm) was a limiting factor in previous long-distance telecommunication network and is now used in order to estimate the OH concentration in optical fibers. Furthermore, the presence of OH groups in the silica network increases its photosensitivity, allowing the control of the radiation glass response.

Chlorine impurities

The most known chlorine impurities are the molecular Cl_2 (diamagnetic) and Cl^0 defect (paramagnetic) [4], [65]. These defects are characterized by intense absorption bands at 3.7 eV (FWHM∼0.7 eV) and 3.26 eV (FWHM∼1.2 eV), respectively. The chlorine impurities arise from the glass synthesis process and generally, the visible spectral range of optical fibers manufactured through the Modified Chemical Vapor Deposition (MCVD) process is dominated by the tails of the above-mentioned absorption bands [86]. In particular, studying the temperature dependence of the Cl^0 defect, it is possible to argue that the hole diffusion, could be responsible for the generation of interstitial chlorine atoms (the most known model of the Cl^0 defect) through the distortion and the consequent rupture of a $\equiv Si - Cl$ bond. The hypothesis was enforced by D.L. Griscom, who proposed a more complex model of the Cl^0 center, not seen as a simple interstitial chlorine atom, but as a $[O_3 \equiv Si - Cl]^0$ unit that traps a free hole, becoming a $[O_3 \equiv Si - Cl]^+$ [65], [78]. This tendency cannot be appreciated at room temperature because of the faster diffusion dynamics of the free hole.

Germanium related defects

In general, the macroscopic effect of Ge-doping in silica network is to increase its refractive index and then germanium is widely incorporated in the fiber cores to guarantee the signal guidance [4], [79], [87], [88]. The optical properties of the most relevant Ge-defects will be listed in chapter 4.

The germanium belongs to the fourth group of the periodic table, such as the silicon atom, resulting in the silicon substitution with the same number of bonds with the surrounding oxygen atoms. For this reason, it is reasonable to expect some Ge-variety of defects analogous the silicon ones, such as the Ge-NBOHC and the GeE´ [4], [88]. The properties of some of these defects, such

as the Ge(1) and Ge(2) centers, have been deeply studied as they can be easily investigated in bulk or preform samples, especially via their paramagnetic signatures [1], [4], [88]. Another important defect is the germanium lone pair center (GLPC), analogous of the ODC(II) with the germanium substitution of the silicon atom, which is a diamagnetic defect characterized by an absorption band at 5.2 eV and two PL bands at 4.2 eV and 3.1 eV, with lifetimes of $1-2$ ns and 110 µs, respectively [1], [4], [89]–[93].

For the transient irradiation exposures case, as those associated with ignition experiments at laser megajoule, the contribution of a metastable defect absorbing around 3.28 eV appears as mandatory to reproduce the absorption spectra, called *transient defect* [4], [79], [87], [94], [95]. This center seems absent under steady-state γ-ray irradiation.

Other defects, only impacting at higher wavelengths (typically above 400 nm) have been less characterized even if they strongly affect the fiber optical properties in the visible-near-IR spectral domains [79], [87], [94]–[96]. The GeX properties remain mostly unknown despite its practical importance for visible, near-IR applications. Recently, an OA band around ~900 nm (1.38 eV) has been observed and associated to a Ge-related defect, named as GeY [95]. At larger wavelengths, the attenuation has been tentatively explained by the generation of Ge-STHs by analogy with the pure silica [97].

Phosphorus related defects

The phosphorus presence in the silica matrix increases its refractive index and decreases its melting temperature [1]. The phosphorous atom belongs to the periodic table fifth group and is embedded in the SiO_2 network bonding with four oxygen atoms: three bridging oxygens and one is displaced as a non-bridging oxygen linked by a double bond [98], [99]. It was shown, in P-doped bulk glasses or optical fibers, that the irradiation exposure produces the appearance of different strong absorption bands in the UV-visible and in the NIR domain [4], [30], [99]–[102]. Many defects are attributed to the phosphorous in doped silica, and for our purpose, we will highlight the most important for the present manuscript. The main optical properties will be listed in chapter 4.

There are two important classes of P-related defects: the phosphorus oxygen hole centers (POHC) and P1 center [4], [87], [101]. In literature, two POHC types are identified differing by their thermal stabilities and then named as stable and metastable POHCs. The first type is

constituted by an unpaired electron shared by two oxygen atoms linked to a P atom bonded to two bridging oxygens. The second type is constituted by an unpaired electron located on an O atom linked with a P, forming three linkages with three bridging oxygens. The P1 defect is a three-fold coordinated P atom which hosts an unpaired electron. At RT, these centers are not thermally or photo-bleached (with infrared probe signal) after irradiation.

1.3. Radiation-matter interaction

In this section, we will describe the interaction between amorphous silica and radiation. The first paragraph will provide relation between the electromagnetic field of the incoming light, in linear regime, with the silica based material. In the second and in the third paragraphs, we will present the structural transformation and defect creation under ionizing irradiation or intense femtosecond laser pulses.

1. 3.1 Silica optical properties

The classical theory of the electromagnetic wave propagation in a solid, and the solid response to the light, are described by the Maxwell equations [26], [103]–[106]. In a linear interaction regime, the constitutive relations are valid, defining the dipole moment per unit volume **P** and the current per unit of area **J** induced by the incoming electric field as:

$$\mathbf{P} = \alpha \mathbf{E} \tag{1.30}$$

$$\mathbf{J} = \sigma \mathbf{E} \tag{1.31}$$

where α and σ are the material polarizability and electric conductibility tensors, characteristics of the material. Moreover, the propagating wave in the glass could be described as function of the material permittivity, defined as

$$\varepsilon = \varepsilon_0 + \alpha \tag{1.32}$$

where ε_0 is the vacuum permittivity ($8.8 \cdot 10^{-12}$ F/m), that in general is a complex number (ε *now* $\tilde{\varepsilon}$*, indicating a complex number*). For our purpose, we are not considering the magnetic properties of the material.

It is possible to describe the material response through α and σ: indeed, both terms appear in the Maxwell's equations as expressions of two different induced currents from the incoming electric field. The polarization current, $\mathbf{P_c} = \alpha \frac{\partial \mathbf{E}}{\partial t}$, orthogonal to the electric field E does not absorb the light, and a dissipative current $\mathbf{J} = \sigma \mathbf{E}$. Considering that the propagation of the electromagnetic wave in the media has a time dependence proportional to $e^{-i\omega t}$, we obtain the dispersion law

$$\omega^2 = \frac{c^2 k^2}{\tilde{\varepsilon}} \tag{1.33}$$

where c is the speed of light ($3 \cdot 10^8$ m/s) and k is the wave-vector. Defining in this way the complex refractive index $\tilde{n} = n + iq$. Since $\tilde{n}^2 = \tilde{\varepsilon}$, we obtain

$$n^2 - q^2 = \frac{\varepsilon_1}{\varepsilon_0} \tag{1.34}$$

$$2nq = \frac{\varepsilon_2}{\varepsilon_0} \tag{1.35}$$

where ε_1 and ε_2 are the real and imaginary parts of the medium permittivity. Taking into account that the light wave propagation in the material is proportional to $e^{i(\mathbf{q}\cdot\mathbf{r}-\omega t)}$, as function of $\tilde{n}$, the electric field will be

$$\mathbf{E} \propto e^{-\frac{\omega q}{c}x} e^{-i\omega\left(\frac{n}{c}x - t\right)} \tag{1.36}$$

where $e^{-i\omega\left(\frac{n}{c}x - t\right)}$ describes an electromagnetic wave propagating without attenuation, while $e^{-\frac{\omega q}{c}x}$ represents the wave attenuation. Indeed, defining the absorption coefficient as

$$\eta = \frac{2\omega q}{c} \tag{1.37}$$

we obtain the Lamber-Beer law (will be deepened in chapter 2):

$$I \propto |\mathbf{E}|^2 \propto e^{-\frac{2\omega q}{c}x} = e^{-\eta x} \tag{1.38}$$

Moreover, it is important to underline that the real (ε_1) and imaginary (ε_2) parts of the material permittivity (and so the dispersive and dissipative properties of the material) are linked by the Kramers-Kronig relations:

$$\varepsilon_1(\omega) = 1 + \frac{2}{\pi} P \int \frac{\omega' \varepsilon_2(\omega')}{\omega'^2 - \omega^2} d\omega' \tag{1.39}$$

$$\varepsilon_2(\omega) = -\frac{2\omega}{\pi} P \int \frac{\varepsilon_1(\omega') - 1}{\omega'^2 - \omega^2} d\omega' \tag{1.40}$$

These expressions imply that the appearance of new absorption bands, for example due to the defect generation in the material, leads to a corresponding refractive index variation.

Furthermore, since $\varepsilon \propto n^2$ equation 1.32, the refractive index depends on the material polarizability α , which is a function of the oscillator number (*and so of the material's density* ρ). Considering the atomic dipole and how the local atomic field is influenced by the surrounding other dipoles, it possible to find a relation between the refractive index and the material density through the Lorentz-Lorenz (Clausius-Mosotti) relation [106], [107]:

$$\frac{n^2 - 1}{n^2 + 2} = \frac{\rho}{3M} \alpha_n \tag{1.41}$$

where M is the glass molar weight and α_n the molar polarizability. The importance of this relation is evident differentiating the equation, showing the refractive index change dependence on the silica densification:

$$dn = \frac{(n^2 - 1)(n^2 + 2)}{6n} (1 + \Omega) \frac{d\rho}{\rho} \tag{1.42}$$

in which we have defined the ratio between the relative polarizability change and the relative density change as $\Omega = (d\alpha/\alpha)/(d\rho/\rho)$.

In conclusion, we have found these possibilities to induce variation on the silica refractive index:

- through an induced densification, since $dn \propto d\rho/\rho$, therefore to the glass density increase corresponds a positive refractive index change;
- through the appearance of new absorption bands, which influence the dispersive component of the material permittivity, linked to the dispersive properties via the Kramers-Kronig relation.

This last case is taken into account considering that the optical properties are defined by the electronic states and their surroundings. In particular, in the next paragraphs, we will treat the silica interaction with ionizing radiation and femtosecond laser pulses, generating defects in the matrix and free carriers electrons in the conduction band (plasma generation) endow the material with metallic properties.

1. 3.2 Defect generation: ionizing irradiation

As already mentioned above, high energy radiation exposure of silica and/or silica-based materials, such as optical fiber or Bragg grating, alters the optical properties through different phenomena. The major effects are [4], [6]

- Radiation Induced Attenuation (RIA)
- Radiation Induced Emission (RIE)
- Radiation induced refractive index change (RIRIC).

The RIA and the RIE are basically linked to point defects generation, associating the material with new absorption and emission bands, strongly modifying its properties. The RIRIC can change the glass structure, leading to a pure or doped silica compaction and so refractive index changes, as already seen in equation 1.41. RIA and RIRIC are also linked via the Kramers-Kronig relation, since RIRIC increases with the amplitude of the induced absorption.

For our purpose, the ionizing radiation processes investigated in the manuscript are the pulsed X-rays (ASTERIX machine from CEA) and steady state X-rays irradiation (MOPERIX X-ray tube from LabHC). The defect generation, in this case, is due to a radiolysis process which

implies a change in the electron state, resulting in the promotion of the electron to the conduction band and leaving a hole in the valence band [29], [108]. After the electron-hole pairs generation, other processes take place up to the relaxation to a new stable electronic state or the generation of a stable defect. Indeed, the electron-hole pairs lead (Figure 1.13) to the free carrier generation, and therefore trapped carriers, and/or excitons generation and then to radiative recombination phenomena. Moreover by interacting with phonons, it is possible to cause the displacement of atoms from the original position and then to a bond distortion that may cause its rupture.

The radiation damage on silica could be estimated by the deposited energy in the material during the irradiation run. In order to quantify this energy we define the scattering differential cross section $\sigma_E(\theta, E)$, which represents the probability density that a projectile particle transfers energy from E to $E + dE$ to the target atom and is deflected from θ angle to the to $\theta + d\theta$. We can now define the average (with respect to all the incident directions and the energies of the incoming particles) energy transferred over a range dr of the glass as

$$\langle E \rangle = N dr \int_0^{\pi} \int_{E_{min}}^{E_{max}} E \sigma_E(\theta, E) d\theta dE \tag{1.43}$$

where N is the number of scattering centers per unit volume, E_{max} and E_{min} are the maximum and minimum energy transferred, respectively, and dr is small enough to account for a single collision. Therefore, the stopping power, i.e. the energy transferred to the target per unit of length (dx), is

$$-\frac{dE}{dx} = N \int_0^{\pi} \int_{E_{min}}^{E_{max}} E \sigma_E(\theta, E) d\theta dE \tag{1.44}$$

We can now define the absorbed dose (or only dose), as the deposited energy on a target with a thickness x:

$$D = \frac{\Phi \Delta t}{x} \int_0^x \left| \frac{dE}{dx} \right| dx \tag{1.45}$$

where $\Phi \Delta t$ is the fluence of incoming particles per unit of area. There are many units for the dose, the most used is the Gray ($1\ Gy = 1\ Joule/1\ Kg$), but the older rad unit is also largely used by the radiation effects community: $100\ rad = 1\ Gy$.

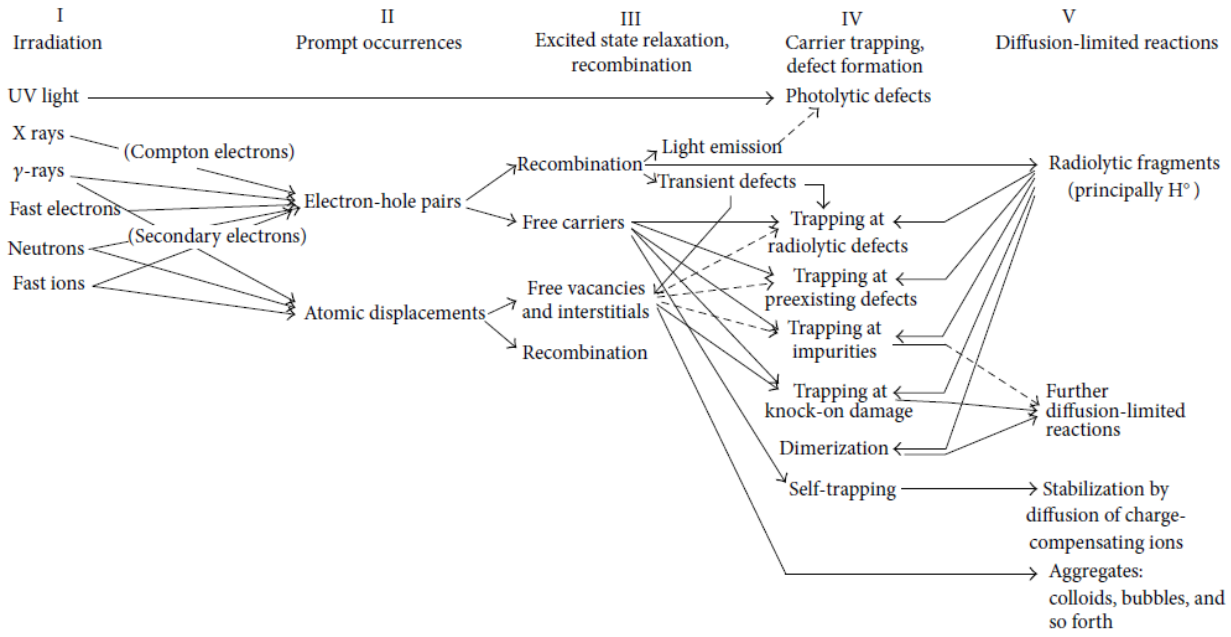

Figure 1.13. Diagram of the most relevant radiation damage processes in glasses. Figure taken from [29].

1. 3.3 Defect generation: non-linear photoionization

In silica, as well as in other insulators, the electronic system is strongly bound with the ions, resulting in a wide energy bandgap. In general, the photoionization process is referred to the energy deposition in the material determining an electron-hole pair creation by the laser field. Commercially available femtosecond lasers [109], [110], are generally characterized by lower frequencies, making the silica based materials transparent to these kinds of photons. The development of high intensity femtosecond pulsed lasers, thanks to the CPA technique [109], has given a strong boost to the production of efficient very high power density (~10 TW/cm^2). The use of these focalized lasers, allows reaching sufficiently high intensities inside the material to trigger the processes to a nonlinear optical absorption (photoionization), in a spectral range where the material is generally transparent [7], [9], [111]–[114]. Indeed, at high intensities the nonlinear phenomena are predominant, leading to the excitation of the electrons in the CB. For the "seeds" electrons in the CB (the first electrons promoted), depending on the laser frequency and intensity, there are two different regimes: the *multiphoton absorption* and/or the *tunneling photoionization*. Once that a relevant population of electrons is present in the CB, another process becomes

dominant, the so-called *avalanche photoionization* (or *inverse bremsstrahlung*). The electrons populating the CB constitute the plasma, which interacts itself with the light, modifying the propagation of the laser pulse within the material. Once the plasma relaxes, the deposited energy in the lattice results in the material network modification. In the following section we will provide an overview (Figure 1.14) on the above-mentioned phenomena.

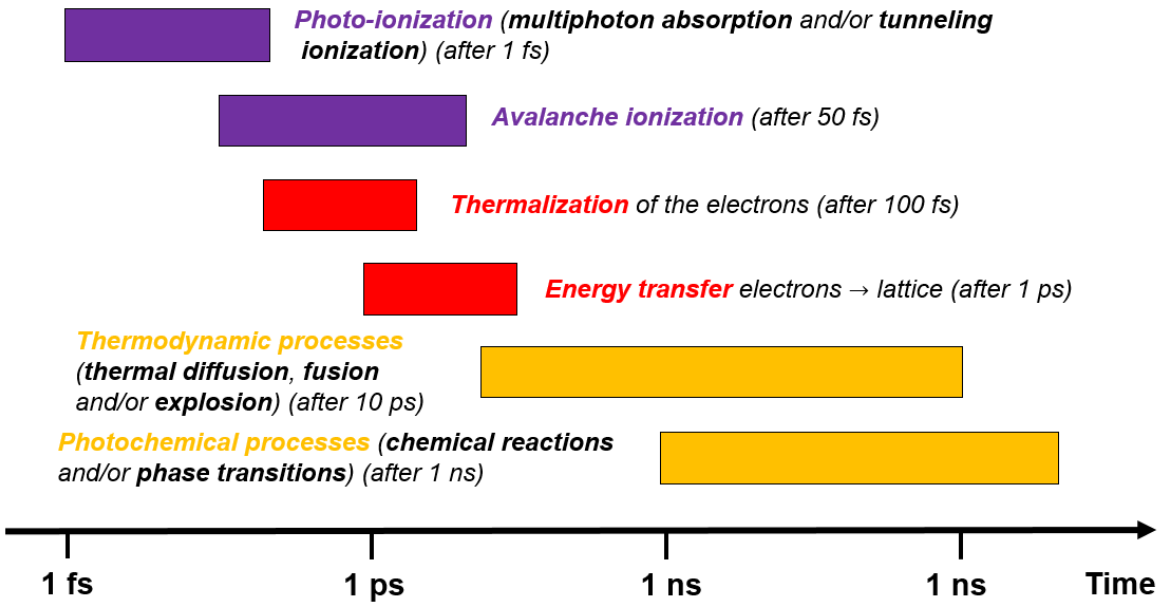

Figure 1.14. Timescale of the physical phenomena taking place during the laser-material interaction in wide bandgap materials.

Seeds electrons

At very high laser intensity, the electron transition from the VB to the CB could be realized by the simultaneous absorption of several photons by a single electron, resulting in a total absorbed energy that exceeds the energetic barrier. The process is illustrated in Figure 1.15 (a). This effect is called *multiphoton ionization* (MPI) and the probability of such optical phenomena is given by the relation [7], [115], [116]:

$$W_{MPI} \propto \sigma_N I^N \tag{1.46}$$

where N is the number of photons necessary for the absorption, I is the laser intensity and σ_N is the corresponding cross-section of N-photon absorption process. Notwithstanding the probability

is proportional to the N-th power of the intensity, the cross-section is strongly increased if the order is low. For this reason, the MPI is associated with high laser frequencies. In wide bandgap materials, MPI could also happen via intermediate states because of the inter-band electronic levels presence due to impurities and/or point defects [117] presence. In cases of laser-induced defects, the laser repetition rate is a crucial parameter, especially when intermediate states were generated in previous cycle interaction, leading to incubation effect. This is evident from the reduction of the ionization threshold for multiple-shots experiments in comparison with single-shot experiments, precisely because in multiple-shots regime there is a reduced cross-section thanks to the intermediate states [118].

The second nonlinear phenomenon which generates the seeds electrons in the CB (depicted in Figure 1.15 (b)) is the *tunneling ionization* (TI) [119], that is predominant when the incident laser electric field is sufficiently high to distort the potential wall that maintains the valence electron bound to its parent nucleus. The electron, through the lowered potential barriers, is then ejected by the tunneling effect from the valence to conduction band. The band-to-band transition probability through the TI is:

$$W_{TI} \propto e^{-\frac{4\sqrt{2m}E_{gap}^{3/2}}{3e\hbar E_{laser}}} \tag{1.47}$$

where m and e are the reduced mass ($5.8 \cdot 10^{-28}$ kg) and the electron charge, E_{gap} is the energy band gap and E_{laser} is the laser pulse electric field.

Based on the experimental conditions (*material and laser characteristics*), we can define a parameter which qualitatively describes the ionization regime [120]: the Keldysh parameter (or adiabatic parameter) is expressed as

$$\gamma = \frac{\omega}{e}\left[\frac{mcn\varepsilon_0 E_{gap}}{I}\right]^{\frac{1}{2}} \tag{1.48}$$

in which ω is the laser frequency, I its intensity at the focal point (here in power density units: $Jm^{-2}s^{-1}$), n and E_{gap} are the refractive index and the material band-gap, respectively. For $\gamma \gg 1$, i-e. when there is a high laser frequency a low laser electric field, the photoionization is dominated by a multiphoton process. On the contrary, when $\gamma \ll 1$, in conditions when laser electric field is high and the laser frequency is low, the tunneling ionization is the favorite process. Of course,

around $\gamma \sim 1$, in an intermediate regime, the photoionization is a mix between the multiphoton and the tunneling ionizations.

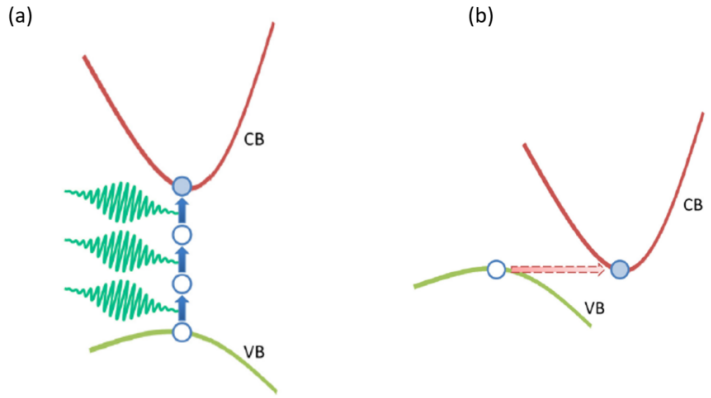

Figure 1.15. Schematic illustration of (a) multiphoton photoionization and (b) tunneling ionization. In green the laser photons. Figure adapted from [7].

Avalanche photoionization

The avalanche photoionization (API) requires an initial population of free electrons ('seeds' electrons) in the material CB [7]–[9], [121], [122]. These electrons are provided by the interaction with the ultrashort laser pulses by MPI and TI. Once the seeds electrons are promoted in the CB, they continuously absorb kinetic energy due to the inverse bremsstrahlung (free-electron absorption mechanism) [123], moving toward higher energy states in the CB. When the kinetic energy exceeds a particular critical value $E \gtrsim E_{cr} \sim E_{gap}$, the hot electron in the CB could ionize a bound electron in the VB producing two cold electrons in the CB (Figure 1.16). This process is called impact ionization. The probability of the avalanche photoionization is given by the formula

$$W_{API} = \sigma_{coll} I(t) n_e(t) \tag{1.49}$$

which results proportional to electron-electron collisional cross-section σ_{coll}, to the laser intensity $I(t)$ and to the initial density of seeds electrons $n_e(t)$ at the time t.

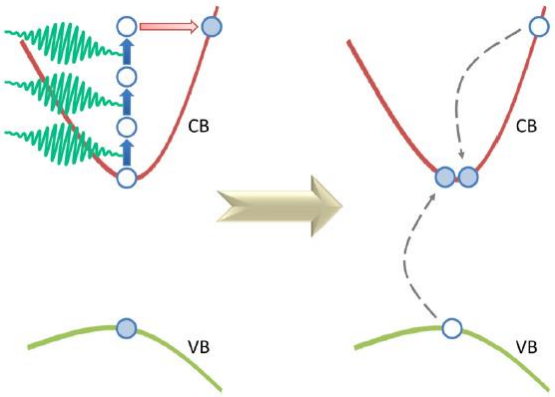

Figure 1.16. Schematic illustration of avalanche photoionization. The free electron in the CB linearly absorbs several laser photons through inverse bremsstrahlung, and then impacting with another electron in the VB, produces two cold electrons in the CB. Figure adapted from [7].

Non-linear propagation of the pulse

Upon strong laser field, different nonlinear effects arise in the focal region, changing the laser pulse propagation in the material also dependent on the generated free electrons density in the CB. Indeed, the laser field amplitude is an important parameter involved in the laser-matter interaction nonlinear properties , and in isotropic materials (*such as amorphous silica*), the nonlinear response to the external field could be written as [119], [124]:

$$\mathrm{P} \approx \varepsilon_0 \left(\chi^{(1)} + \frac{3}{4} \chi^{(3)} |\mathrm{E}|^2 \right) \mathbf{E} \tag{1.50}$$

where $\chi^{(1)}$ and $\chi^{(3)}$ are the linear and the nonlinear (third order) susceptibilities, respectively. It is important to underline that the second order of the permittivity is zero in isotropic media [124].

From relation 1.50, it is evident that the nonlinear contribution is correlated to the laser intensity ($\mathrm{I} \propto |\mathrm{E}|^2$), that becomes relevant when the laser intensity is strong. Equation 1.50 allows us to determine, in first approximation, the dependency of the medium refractive index by the laser pulse intensity.

$$\mathrm{n(I)} = \mathrm{n}_0 + \mathrm{n}_2 \mathrm{I} \tag{1.51}$$

where, $\mathrm{n(I)}$ is the material refractive index in the focal volume, n_0 is the material linear refractive index and $\mathrm{n}_2 = \frac{3\chi^{(3)}}{4\mathrm{n}_0 \varepsilon_0 \mathrm{c}}$ is the nonlinear one. For fused silica, $\mathrm{n}_2 = 2.48 \times 10^{-16} \mathrm{cm}^2/\mathrm{W}$.

The refractive index dependence on the pulse intensity spatial envelope is known as the nonlinear Kerr effect. Indeed, considering a laser beam having a Gaussian spatial profile, once its focalization inside the material, the Gaussian pulse induces a transverse refractive index variation larger at the center of the beam than at the focal region edge, acting as a positive lens. Moreover, taking into account the laser light intrinsic diffraction divergence and the plasma defocusing effect, the beam can be self-trapped when the self-induced lens effect balances the laser beam divergence, resulting in a beam propagating with a constant diameter (Figure 1.17). This condition is reached when the laser beam power assumes the following critical value [125]:

$$P_{cr} = \frac{\lambda^2}{4\pi n_0 n_2} \tag{1.52}$$

where λ is the laser wavelength. For fused silica we estimate the critical power at $P_{cr} \sim \frac{\lambda^2\,[nm]}{0.45}$ W, that could be reached easily with commercial femtosecond lasers. If the beam power is greater than critical value $P > P_{cr}$ then self-focusing can occur.

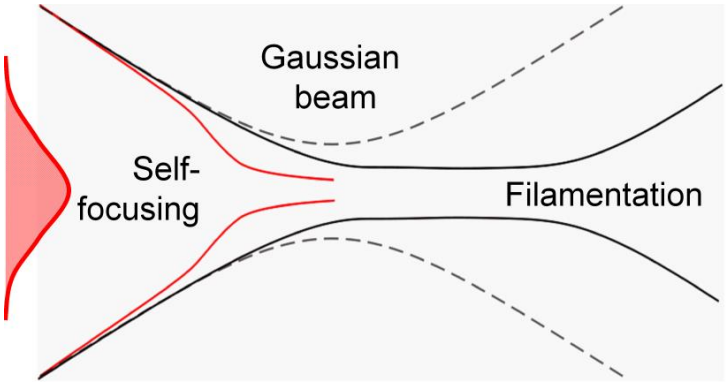

Figure 1.17. Schematic illustration of the focused Gaussian beam nonlinear propagation (*in linear conditions should be the dashed gray curve*). Two regimes can be obtained: the self-focusing regime (red curve) due to nonlinear Kerr effect and filamentation propagation regime (black curve) due to the balance between the Kerr effect and intrinsic diffraction divergence of the laser or the plasma defocusing.

Material modification

The laser pulse energy is primarily deposited in the electronic system exciting electrons in the CB; then the plasma transfers its energy to the lattice via phonons scattering [7], [8], [121], [126]. Due to the difference between the response timescales of the electron subsystem and the nuclei one , the femtosecond pulse's photocycle processes of absorption and energy redistribution could be time decoupled, since the main energy transfer takes place from the hot electrons to the ions after the pulse has stopped [127]–[131]. When the deposited energy is sufficiently high, structural changes could occur via different processes: heat deposition and consequent thermo-elastic relaxation processes causing phase transformation of the material and/or electronically induced microscopic structural transitions (*for example point defects generation*). The network silica structural reorganization within the focal region can be described as function of the changes of the mean angle and distances between Si and O atoms, ring statistic modification and point defect formation [114], [132]–[134]. Thus, the femtosecond laser induced network reorganization mechanisms are:

- temperature rapid increase and subsequent fast cooling;
- material densification by the pressure wave in response to the volume changes in the focal region;
- STXs generation succeeded by defect formation.

Viscoelastic relaxation and glass transition

When the temperature local increase exceeds the softening temperature, the induced isotropic refractive index changes has been attributed to melting and rapid solidification of the glass in the focal region [114], [135]–[137]. The schematic volume-temperature diagrams for a) common glasses and b) fused silica under two different cooling rates are illustrated in Figure 1.18. As it is evident, in common glasses a fast cooling determines lower densities as indicated, while in fused silica, due to an anomalous behavior between $1200 \div 1700$ K, the material density (*and consequently the refractive index*) is higher if the glass is quenched from a higher temperature. Therefore, if the material in the focal region is melted and just after quenched, an increase of the refractive index and the density is observed compared to the non-irradiated region.

During the cooling, the glass network modifies its configuration following the corresponding equilibrium at its temperature T. If the cooling is going very fast, the time to adjust network configuration defined by the glass viscosity at the glass temperature becomes longer than the time defined by the cooling rate. Since in these conditions the silica network is prevented to follow the cooling process, the structure freezing happens. To give an idea of the involved timescale, in general the time needed for a small deviation of the structure to follow the equilibrium form, is defined by viscoelastic relaxation time given by

$$\tau_r = \frac{\eta}{G} \tag{1.53}$$

where η is viscosity of the glass and G is bulk modulus. At temperatures close to the softening point at the range of $1500 \div 1700$ K, η should be $\sim 10^5 \div 10^6$ Pa $\cdot$ s, with G$\sim$30 GPa. In these conditions, the time needed by silica to reach its equilibrium can be estimated longer than 10 μs, while after few picoseconds the fast cooling takes place and around $\sim$1 μs the focal region is cold, preventing the possibility to reach the equilibrium condition.

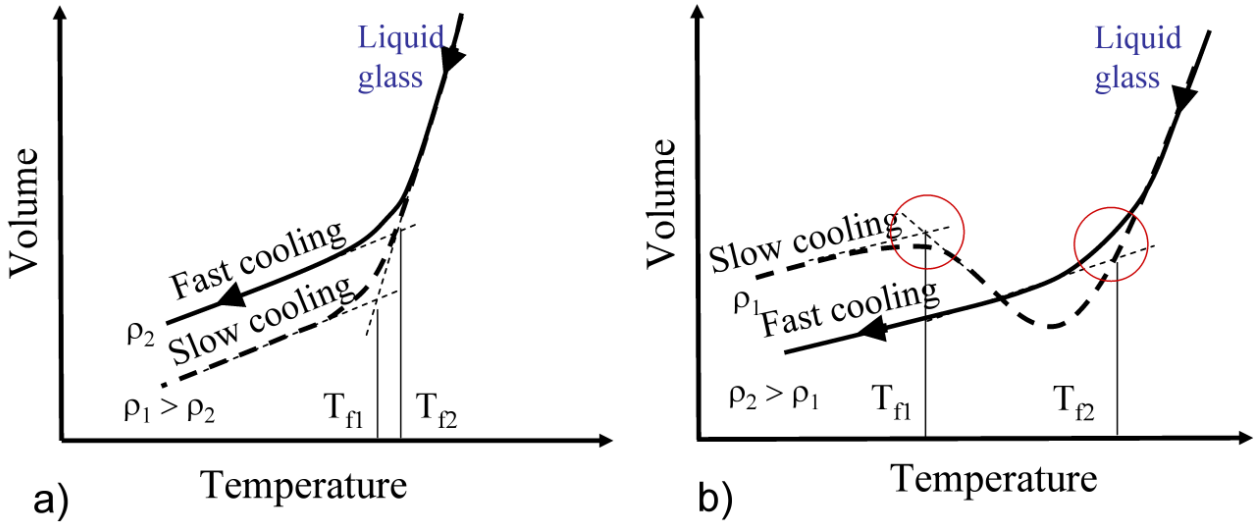

Figure 1.18. Schematic volume-temperature diagrams for a) common glasses and b) fused silica under two different cooling rates. T_{f1} and T_{f2} represent the temperatures at which structural relaxation is blocked for slow (cooling rate of seconds) and fast cooling (cooling rate of microseconds and shorter), respectively, defining the fictive temperature of glasses and the consequent densities ρ_i.

Pressure compaction

The laser-matter interaction above the ionization threshold drives the free carrier generation around the focal volume, with the absorption increase because of the inverse bremsstrahlung and nonlinear effects. This process leads to a fast energy transfer in a very small focal volume. After the fast temperature increase in the irradiated region, the heated material exhibits a thermal expansion. As a consequence, a shock wave is generated and spreads into the surrounding cold material [114], [135]–[137]. The shock wave propagation in the glass is accompanied by compression at the shock wave front and rarefaction behind it. Different regimes are observed depending on the focalization conditions, such as the rarefaction but also micro-explosions and voids formation when the energy densities in the focal region reach sufficiently high values to evaporate the silica.

Color center generation under femtosecond laser pulses

It has been suggested that femtosecond laser pulses focused inside the silica network lead to the generation of a sufficient number of color centers [7]–[9], [11], [13], [14], [72], [138], [139] to observe a variation of the glass refractive index through a Kramers–Kronig mechanism or defect-assisted densification. Indeed, when the generation and accumulation of stable defects take place, a network reorganization is observed. The most accepted model is linked to the STX's relaxation, which is considered at the origin of the stable defect pair generation such as E´ and NBOHCs (*process described in Figure 1.19*). It is important to underline that the network reorganization is often accompanied by the smaller ring formation, driving to a material densification. One of the present work purposes is to understand which defects are generated during and after the laser irradiation and the corresponding microscopic modifications in the silica network. Chapter 5 will be focused on this topic.

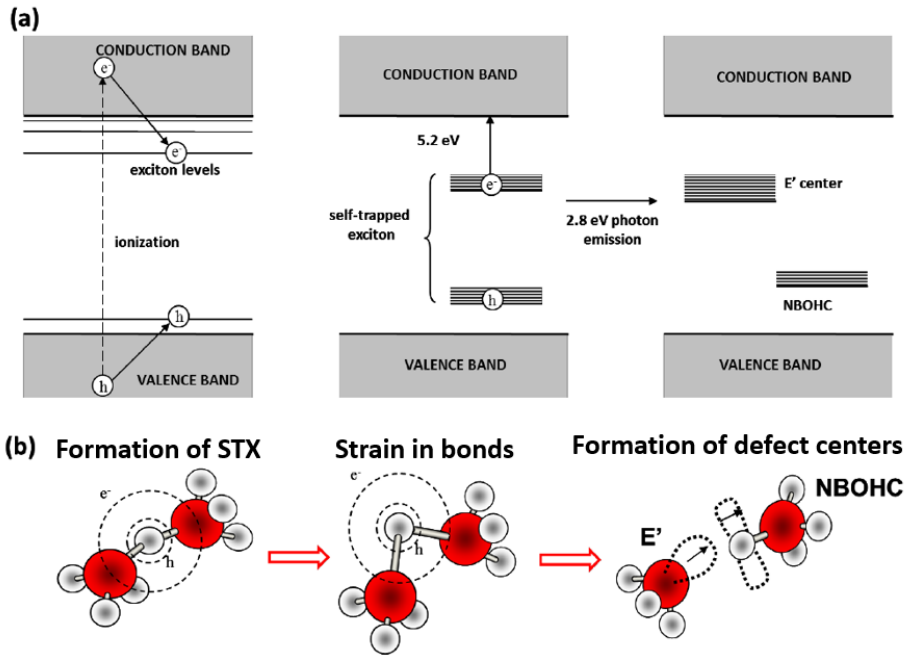

Figure 1.19. (a) Illustration of the energy level diagram of the exciton generation and successive self-trapping, with the consequent defects generation. In the figure are also highlighted the correspondent STX absorption/photoluminescence bands (b) Scenario of self-trapped exciton formation: the hole self-trapping strain the Si – O bonds leading to the generation of defect centers.

Chapter 2. Basic concepts

The present chapter introduces the theoretical concepts at the basis of the experimental techniques used, along this PhD thesis work, to characterize the radiation effect on silica samples (bulk or optical fiber) and/or to study the induced defect post irradiation dynamics. Indeed, to have a clear view on the sample's properties (both during and/or after the irradiation), several spectroscopic techniques are combined. In order to investigate the sample response to the irradiation, the experiments were done mainly using: steady state optical absorption (OA), Radiation Induced Attenuation (RIA), Transient Absorption (TA); online and steady state photoluminescence (PL); Raman spectroscopy. Moreover, to better characterize the morphology of some studied samples (chapter 5), Phase Contrast Microscopy (PCM) and the Rayleigh scattering were also used.

2.1. Optical absorption

As already mentioned in the previous chapter, the presence of point defects in the silica network introduces inter-bandgap electronic levels, which can be accounted by analogy to a molecular system. As a consequence, a photon with energy $E = h\nu$ that matches the electronic state energy difference could be absorbed thus inducing an optical transition. Therefore, it is easy to understand how the point defect generation under irradiation can influence the optical properties of transparent materials such as the amorphous SiO_2.

The absorption process gives rise to bell shaped bands. In fact, in the case of a point defect embedded in a solid, the interactions with the nuclear vibrations and the local structure inhomogeneities, especially in an amorphous network, lead the absorption bands to have usually a Gaussian shape.

Every defect is characterized by particular absorption bands [1], [3], [4], [20], [29], [35], footprint of the difference between their ground and excited states. For this reason, the optical absorption (OA) study is crucial to characterize the silica optical properties and to probe the defect presence in the silica network. Notwithstanding the OA importance, it is relevant to note that in most of the cases several absorption bands are observed and usually overlap, because of the simultaneous presence of a wide variety of point defects. This entails difficulties in the unambiguous identification of the absorbing point defects, and makes necessary the support of other complementary experimental techniques, such as PL, electron paramagnetic resonance (EPR), Raman, etc... to identify all the optically active centers.

2. 1.1 Lambert-Beer's Law

If we consider a light beam, with monochromatic component intensity $I_0(\lambda)$, propagating along the x direction (Figure 2.1); this beam crosses a sample with a certain absorber concentration (for example point defects, also called chromophores in the case of incoming visible light). Considering that

$$\lambda = \frac{2\pi\hbar c}{E} \tag{2.1}$$

where c is the light speed, $\hbar$ the Plank constant and E the photon energy. If E matches the energy difference between two electronic levels, it is absorbed, the light intensity crossing through the sample is reduced [140]. Then, at the sample exit along a thickness d, the measured intensity $I_T(\lambda, d)$ will represent the transmitted light measured by the detector, providing information about the spectral range for which the sample absorbs the light. These considerations are reassumed in the Lambert-Beer law, according to which, considering a homogeneous medium, the transmitted light is described by the following relation [140], [141]:

$$I_T(\lambda, d) = I_0(\lambda)e^{-\alpha(\lambda)d} \tag{2.2}$$

where $\alpha(\lambda)$ is the absorption coefficient magnitude, which characterizes the sample OA profile, expressed as an inverse of a length.

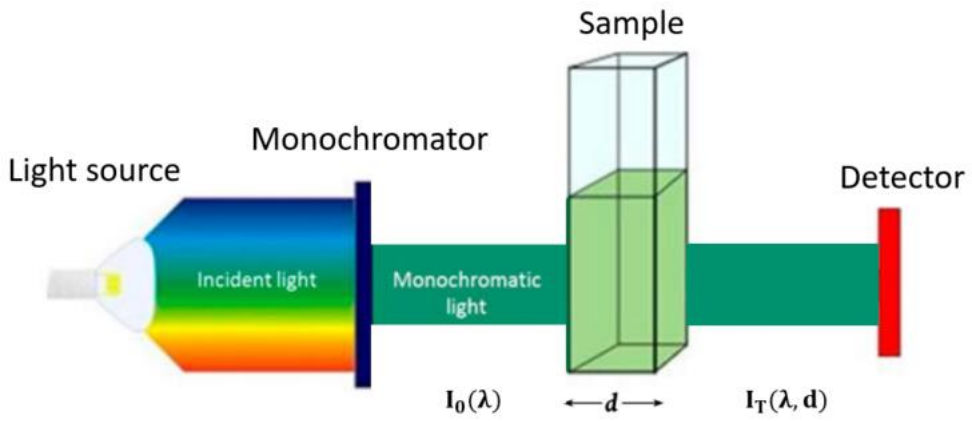

Figure 2.1. Representation of a light beam absorption at wavelength λ passing through a sample. Figure adapted from [141].

2. 1.2 Optical absorption measurements

In agreement with eq. (2.2), the absorption coefficient $\alpha(\lambda)$ can be measured by the natural logarithm:

$$\alpha(\lambda) = \frac{1}{d} \ln \frac{I_0(\lambda)}{I_T(\lambda, d)} \tag{2.3}$$

Generally, in OA experiments, the measured absorption is the optical density (OD), defined by [141]

$$OD(\lambda) = \log_{10} \frac{I_0(\lambda)}{I_T(\lambda, d)} \tag{2.4}$$

The relation between $\alpha(\lambda)$ and $OD(\lambda)$ is:

$$\alpha(\lambda) = \ln(10) \frac{OD(\lambda)}{d} \approx 2.303 \frac{OD(\lambda)}{d} \tag{2.5}$$

The absorption process could be related to two non-degenerate electronic levels belonging to the absorbing defect: φ_g with energy E_g and φ_u with energy E_u, where $E_g < E_u$. In molecular's like systems, as in the case of defects embedded in the silica matrix, we can consider an electric

dipole with dipolar momentum $\mathbf{D} = \sum_i e_i \mathbf{r_i}$, were e_i are the electronic charges and $\mathbf{r_i}$ their positions.

To describe the probability that the incident electromagnetic wave induces an electronic transition between the φ_g and φ_u defect electronic levels, the quantum mechanics theory states that this probability is proportional to the Einstein coefficients for absorption B_{gu} and stimulated emission [33], [34], [140], [142]:

$$B_{gu} = \frac{2\pi}{3n\hbar^2 c} |\mathbf{D}^{gu}|^2 \tag{2.6}$$

where n is the refractive index of the sample in which the defect is embedded and $\mathbf{D}^{gu}$ is the electric dipole matrix element between the φ_g and φ_u states, in agreement with the following relation

$$\mathbf{D}^{gu} = \int \varphi_u{}^* \mathbf{D} \varphi_g d\tau \tag{2.7}$$

with $\varphi_u{}^*$ the $\varphi_u$conjugate complex and $d\tau$ the volume element.

The absorption coefficient can be expressed as a function of the photon energy, $\alpha(E)$, using the relation expressed by equation 2.1. Supposing a silica sample containing one point defect specie with a concentration ρ, it is easy to see that the absorption coefficient $\alpha(E)$ is proportional to ρ [1]:

$$\alpha(E) = \sigma(E)\rho \tag{2.8}$$

where the coefficient $\sigma(E)$ defines the single photon absorption cross section.

The overall integrated absorption coefficient, in the energy space, is related to the Einstein absorption coefficient B_{gu}, then to the dipolar momentum $\mathbf{D}^{gu}$:

$$\int \alpha(E)\, dE = \frac{\rho B_{gu} \hbar \omega_{ug}}{c} = \frac{2\pi\omega_{ug}}{3n\hbar c^2} \rho |\mathbf{D}^{gu}|^2 \tag{2.9}$$

where ρ is the number of absorbers per unit volume, and $\omega_{ug} = (E_u - E_g)/\hbar$ is the Bohr frequency necessary to have the transition. The relation expressed in equation 2.9 is important because it allows us to estimate $|\mathbf{D}^{gu}|$ and then to provide information about φ_g and φ_u, by the

α(E) measurements. Furthermore, the color center absorption properties could be characterized by a dimensionless quantity called the transition oscillator strength , often used to compare absorption bands intensities [1], [3], [34], [140]. The oscillator strength is defined as

$$f = \frac{2m\omega_{ug}}{3\hbar e^2}|\mathbf{D}^{gu}|^2 \tag{2.10}$$

with m and e the electronic mass and charge, respectively. When f∼1, the measured band can be related with a strongly allowed via electric dipole transition between the involved states, while if $f \ll 1$, the band can be attributed to a forbidden transition, with a relatively low absorption band intensity. Moreover, knowing f and the maximum absorption coefficient value α_{max}, we can estimate the absorbing defect concentration through the Smakula formula [143]:

$$\rho f \approx 9.111 \cdot n\left(\frac{\epsilon_0}{\epsilon_{eff}}\right)^2 \alpha_{max}\Gamma\Delta \cdot 10^{15} eV^{-1}cm^{-2} \tag{2.11}$$

where Δ is the band full width at half maximum (FWHM), $\left(\frac{\epsilon_0}{\epsilon_{eff}}\right)$ is the ratio between the electric field amplitude of the incident light ϵ_0 and the effective electric field amplitude at the defect site ϵ_{eff} while Γ is the band shape factor, with $\Gamma = 1.0645$ for a Gaussian lineshape. For silica-based materials, $n\left(\frac{\epsilon_0}{\epsilon_{eff}}\right)^2 \sim 1$ in a spectral range comprising the NIR to UV domains, then equation 2.11 results

$$\rho f \approx 0.97 \cdot \alpha_{max}\Gamma\Delta \cdot 10^{16} eV^{-1}cm^{-2} \tag{2.12}$$

2. 1.3 Online Radiation Induced Attenuation

Up to now, we discussed only the optical absorption (in our case) related to the optical defects already present in the sample. Actually, it could also be very useful to study the properties of the defects that are induced during the irradiation, monitoring the sample's optical properties variation. As already mentioned in the previous chapter, silica-based materials are in principle transparent materials, but (meta)stable point defect could be induced by radiation [1], [2], [4], [29], [33]. In first approximation, this effect can be directly evaluated by the spectral difference study before and after the irradiation. Although many information are available with this kind of

procedure, many processes involved during the irradiation can be lost, especially the contribution of the metastable defects induced by the irradiation and quickly disappearing during post irradiation regime. To get around this phenomenon, the online or in situ Radiation Induced Attenuation (RIA) is often used, consisting, as depicted in Figure 2.2, in the evaluation of the transmitted light during the irradiation, as a function of the irradiation time (or dose), and normalized by the sample length [4]. The RIA technique is particularly suitable to study the radiation effects on optical fibers, allowing us to measure the fiber darkening kinetic during irradiation as well as the recovery kinetic often observed after the irradiation stop. This allows us to obtain very useful information on both stable and metastable defects and on their generation/bleaching processes. In this kind of experiments, the optical fiber under test (FUT) is usually connected, through radiation hardened fiber pigtails, to a white light source (with a low intensity to avoid photo-bleaching effects) and to a detector located in a radiation-free zone, while a part of the FUT is in an X-ray irradiator (in our case). Comparing the transmitted spectra before the irradiation, with intensity I_0, with the ones during the irradiation as a function of the time, with intensity $I(\lambda, t)$, normalized by the fiber length l, we obtain the measured RIA spectra.

$$RIA(\lambda, t) = -\frac{10}{l}\log_{10}\left(\frac{I(\lambda, t)}{I_0}\right) \tag{2.13}$$

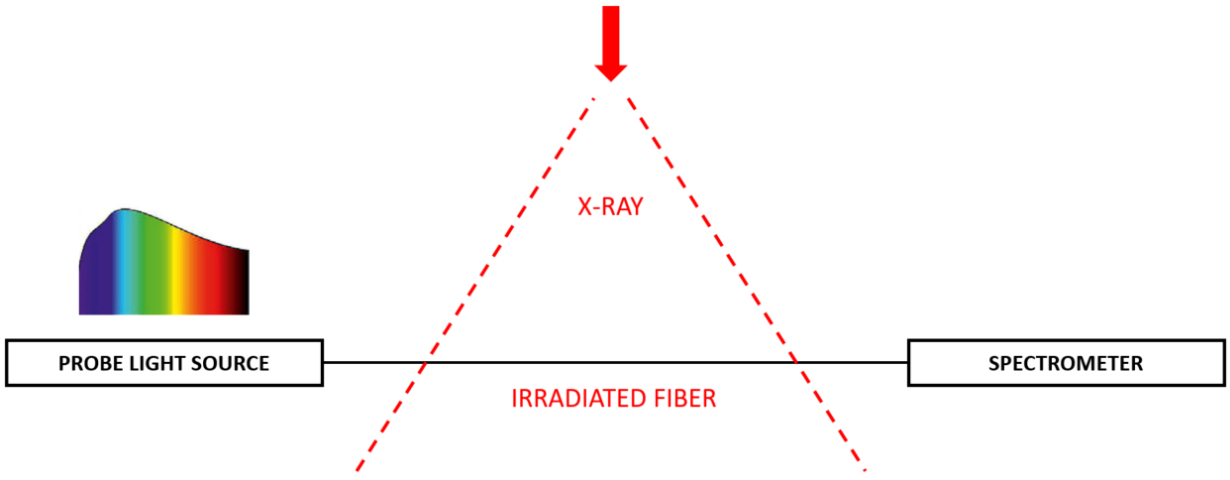

Figure 2.2. Basic scheme of the online RIA experimental setup under X-ray irradiation.

2.2. Photoluminescence

After the photon absorption , the excited point defect (or in general the excited molecular site) will go back to the ground state through relaxation process: this could happen via radiative or not radiative effects [1], [3], [34], [140], [144], [145]. Photoluminescence (PL) phenomena is a fingerprint of the photon emission detection. Since PL measurements are excitation and emission energy dependent, many information on the involved electronic levels could be obtained.

To describe the PL phenomena it appears useful to start with the Jablonski diagram [144], [145] depicted in Figure 2.3.

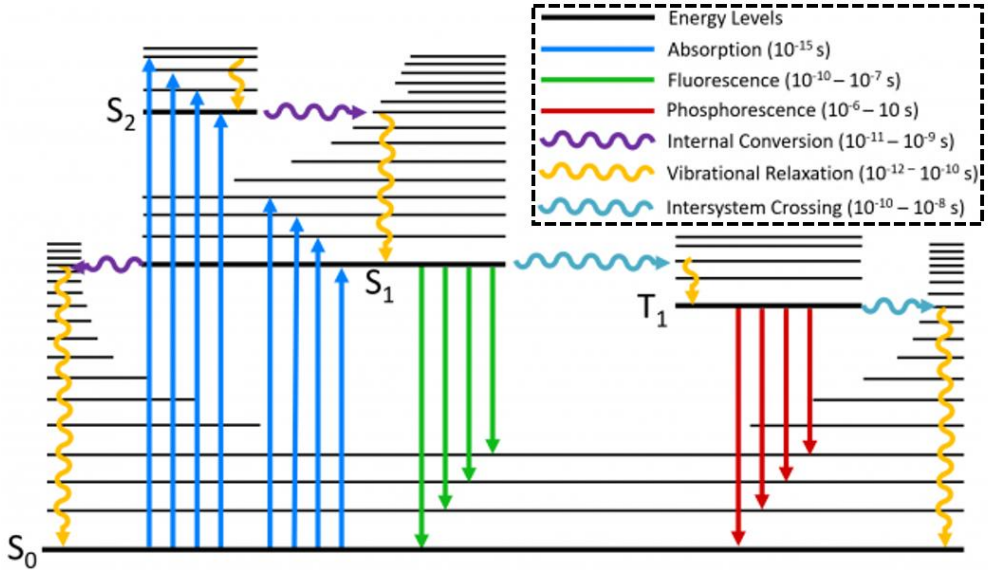

Figure 2.3. Jablonski diagram for the radiative and non-radiative transitions, with the relative timescale process: horizontal lines are the electronic levels, vertical arrows represent the optical transitions (blue the absorption, green the fluorescence and in red the phosphorescence) and the wavy arrows represent the non-radiative transitions (violet the internal conversion, yellow the vibrational relaxation and in light blue the intersystem crossing).

In Figure 2.3 the thicker horizontal lines represent the electronic states in the bandgap, belonging to a point defect embedded in an insulating matrix, while the thinner lines correspond to the possible vibrational levels (equivalent to the energy levels in harmonic approximation shown in Figure 1.6) associated to the electronic states, occupied according to the Boltzmann distribution. As stated by the selection rules, the dipolar transitions are favored when the total spin multiplicity

of the electronic system is conserved. Considering the S_0 ground state as an electronic level with a spin singlet multiplicity, for two electrons in the same orbit with opposite spin orientations ($S_{tot} = 0$), the most probable absorption transition will be toward higher energy electronic levels with the same spin, that in our case are the singlet excited states S_1 and S_2: these kinds of transitions are called spin-allowed transitions (timescale $\sim 10^{-15}$ s). Once the electron is promoted in one of these two states finding a particular vibrational state, following the Franck-Condon principle, it relaxes with respect to the Boltzmann statistics (vibrational relaxation) in a time scale of $10^{-12} \div 10^{-10}$ s. To come back to the ground state, the electron could follow different pathways: i) radiative process involving the emission of a photon from the excited state to the ground one. This spin-allowed process is called fluorescence, with a time scale of $10^{-10} \div 10^{-7}$s; ii) non-radiative process via internal conversion, which represents a vibrational relaxation between two states with the same spin multiplicity, then between $S_1 \rightarrow S_0$ or $S_2 \rightarrow S_0$, but also $S_2 \rightarrow S_1$ and then $S_1 \rightarrow S_0$.

When the absorption gives rise to a radiative emission we observe the Stokes shift, already mentioned in chapter 1. Indeed, the emission band is centered at lower energies compared to the absorption band peak (in linear regime conditions).

As depicted in Figure 2.3, non-radiative transitions between excited states with a different spin multiplicity are also possible, such as $S_1 \rightarrow T_1$, where T_1 represents a triplet spin multiplicity ($S_{tot} = 1$). The above-mentioned process is called intersystem crossing (ISC), which implies a non-radiative vibrational relaxation toward an electronic level with a different spin multiplicity. The ISC process strongly depends on temperature and is characterized by a time scale of $10^{-10} \div 10^{-8}$s. Once the electron relaxes to a triplet state, there are even in this case, two possible pathways to go down to the ground state: via non-radiative intersystem crossing process $T_1 \rightarrow S_0$, or through a photon emission. The radiative $T_1 \rightarrow S_0$ transition is a spin-forbidden transition, since there is a change of the spin multiplicity, and it is called phosphorescence. The phosphorescence is characterized by a relatively long emission lifetime ($10^{-6} \div 10$ s) with a large Stokes shift which takes into account both the vibrational relaxation and the internal conversion.

In general, we refer to photoluminescence process all the phenomena related to the emission of a photon after an absorption, therefore both the fluorescence and the phosphorescence. The PL intensity is proportional to

$$I_{PL}(E_{em}) = \eta(E_{em}) I_0(E_{exc}) \left(1 - e^{-\alpha(E_{exc})d}\right) \quad (2.14)$$

where E_{em} and E_{exc} are the emission and the excitation energies, respectively, $I_0(E_{exc})$ is the incident radiation intensity at energy E_{exc}, $\alpha(E_{exc})$ is the absorption coefficient at the energy E_{exc} and d is the sample thickness crossed by the incident beam. The dimensionless factor η is the quantum yield, it is given by the ratio between the emitted and the absorbed photons and is related to the competition between the radiative and non-radiative processes in agreement with the following expression:

$$\eta = \frac{k_r}{k_r + k_{nr}} \quad (2.15)$$

where k_r and k_{nr} are the radiative and non-radiative decay rates, respectively, with k_{nr} strongly temperature dependent ($k_{nr} \sim 0$ when $T = 0$).

From eq. (2.14), we can investigate the excitation spectrum by monitoring the emission intensity $I_{PL}(E_{em})$ at a fixed energy E_{em} and scanning E_{exc}. The measured spectrum, which is expected to reproduce the absorption spectrum line shape, is called excitation spectrum.

2.3. Pump-probe measurements

The pump-probe spectroscopy is very powerful to investigate ultrafast dynamics, studying the change in the absorption spectrum induced by an ultrashort pulse. Normally, the experimental setup is composed of a fs-ps laser beam, split into two parts: the larger part of the laser power is employed to photo-excite the sample (the pump), generating a non-equilibrium phase, resulting in a transition from the ground to the excited states in the sample exposed to light; the remaining beam part is used (at the fundamental wavelength, with its harmonic or broadened by non-linear processes) to probe the pump-induced changes in the sample OA spectrum. The transient absorption (TA) signal is defined as the difference between the OA spectrum with (pumped OA spectrum) and without the pump excitation (un-pumped OA spectrum). Performing this kind of measurements as a function of the pump-probe delay, we reconstruct the sample TA spectrum at each delay time, thus providing information on dynamic processes induced by the fs pulse.

In general, the TA spectrum is composed of three contributions from the different processes [146]–[149] listed in the following and represented in Figure 2.4.

- **Ground State Bleach (GSB):** since a fraction of absorbers has been promoted in the excited state after the pump pulse, they will not necessarily come back to the ground state when the probe pulse arrives, therefore the defect number in the ground state could be lowered compared to the un-pumped case. Hence, the ground-state absorption in the pumped configuration is less than that in the un-pumped one, because the still photo-excited defects cannot contribute to the absorption. Practically, this effect results in a negative signal in the spectral range of TA spectrum corresponding to the ground-state typical absorption bands.

- **Stimulated Emission (SE):** when the sample is characterized by a PL activity, it is possible to stimulate an emission to the ground state when the probe pulse spans the photo-excited sample. Indeed, a photon coming from the probe beam stimulates an emission of another photon from the excited to the ground state, both of them are coherent, have the same direction and can be detected. It is worth to notice that, according to the Einstein's coefficients of stimulated and spontaneous emission, the SE intensity is proportional to the emission frequency, while the spontaneous PL intensity is proportional to the cubic of the emission frequency. Stimulated emission results in a light intensity increase on the detector, corresponding to a negative signal in the TA spectrum.

- **Excited-state Absorption (ESA):** it gives the only positive signal in the TA spectrum, and consists of a new allowed optical transition of the photo-excited sample after the pump induced excitation, from an excited state to another at higher energies.

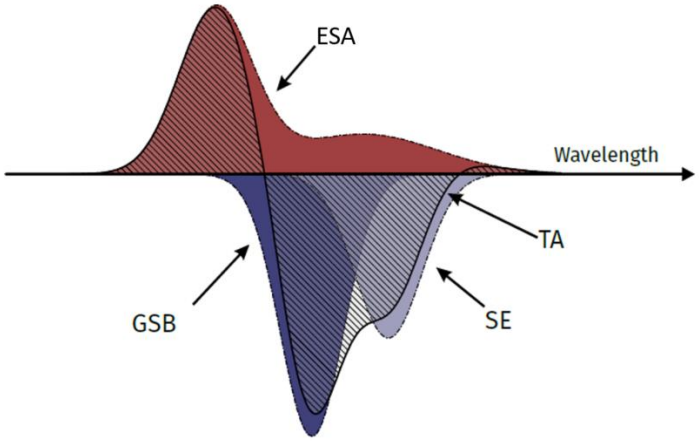

Figure 2.4. TA spectrum composed by the overlaps of GBS, SE and ESA contributions. Figure taken from [149].

In the following paragraphs we will provide an overview of some phenomena involved, in our pump-probe experimental setup, which need a short description from a physical point of view:

- fs-laser pulse generation;
- White light generation;
- Group velocity dispersion;
- Pump wavelength generation;
- Cross-Phase modulation.

An overview of the transient absorption signal from a formal point of view will be presented in section 2.3.5. Moreover, in order to extract further information, but also to clean the signal from noise, the singular value decomposition (SVD) analysis will be performed on the acquired data. This procedure will be described in the chapter 2.3.6.

2. 3.1 fs-laser pulse generation

The laser (Light Amplification by Stimulated Emission of Radiation) is a technological device which provides a collimated coherent monochromatic light beam, representing the key element of a wide research area, from both the fundamental and applied points of view [150], [151]. As depicted in Figure 2.5, a laser is composed of a cavity (resonator) made by two mirrors, one highly reflective, while the second one is a partially reflective mirror, in which the light travels back and forth. The active medium amplifies the signal with each pass. In absence of the active medium, the light would lose its energy every round trip in the resonator. The laser light is generated by the stimulated emission, induced by the travelling light in the active medium excited by a flashlamp (for example) as pump source: the emitted photons will be collinear and coherent with the round-trip light, generating then the laser signal. Of course, if the gain in the medium is lower than the losses in the partially reflective mirror, the laser cannot operate.

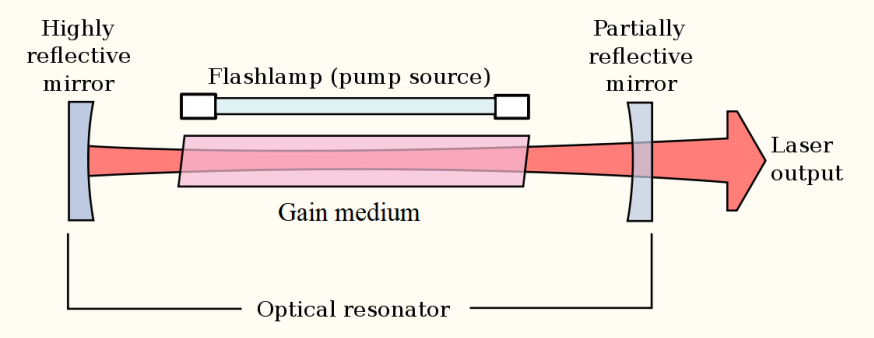

Figure 2.5. Laser cavity basic scheme.

The phenomenon which drives the laser emission generation is the population inversion in the active medium, that could be described as a (at least) three level system where the third level has a larger electronic population than the second one thanks to the pump source, thus causing the amplification of the travelling light through the stimulated emission. Since the active medium is within a cavity with two mirrors placed at a distance L, only some modes of the field could be excited during the amplification process because of the geometry of the cavity. The allowed modes have to satisfy the boundary condition with zero amplitude at the cavity extremes: for this reason,

the length L must be an integer multiple of the travelling light half wavelength: $L = n\frac{\lambda}{2} = n\frac{c}{2\nu} = n\frac{\pi c}{\omega}$. The final laser output spectral bandwidth will be the convolution between the allowed field modes and the window of resonant frequency with the active medium (Figure 2.6).

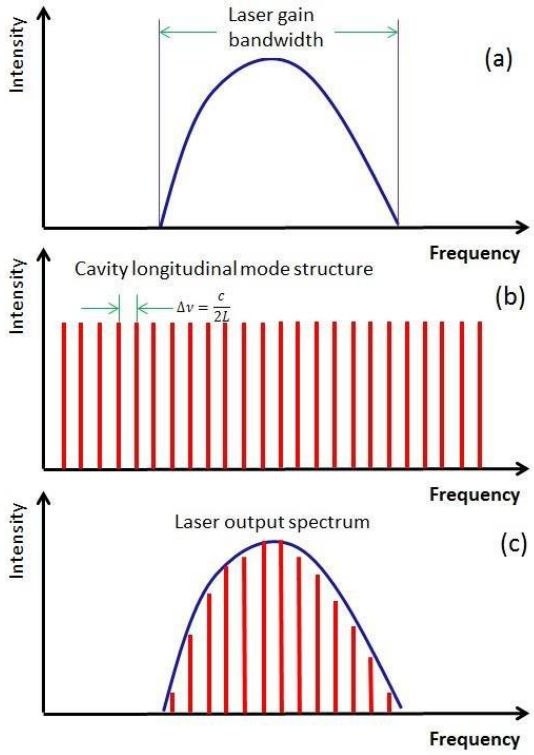

Figure 2.6. The mode structure in a laser. (a) The laser gain medium amplifies the light over certain range of frequencies. (b) All the longitudinal modes allowed in cavity. (c) Only the modes whose frequencies fall into the laser's gain bandwidth will be amplified.

Femtosecond laser emit optical pulses with a duration below the ps (10^{-12} s). The generation of ultrashort light pulses could be achieved employing the mode locking technique [150], [151], that leads to the generation of moderate energy pulses (often in the nanojoule region) and high pulse repetition rates. This method requires to force a well-defined and constant time relation between the modes into the laser cavity. Assuming, for sake of clarity, all the modes allowed in the cavity as a plane wave with each electric field mode defined as:

$$E_{sm}(t) = E_0 e^{i(\omega t+\varphi)} \qquad (2.16)$$

where ω is the angular frequency and φ the phase. The resulting electric field, composed of the $N = 2n + 1$ modes inside the cavity, could be written as

$$E(t) = \sum_{m=-n}^{n} E_0 e^{i[(\omega_0 + m\Delta\omega)t + m\Delta\varphi]} = E_0 e^{i\omega_0 t} \sum_{m=-n}^{n} e^{im(\Delta\omega t + \Delta\varphi)} \tag{2.17}$$

ω_0 is the central angular frequency and all the other frequencies are symmetrically distributed around it, Δω and Δφ are the differences between the angular frequencies and phases of two adjacent modes, respectively.

We can now introduce the condition to have a mode locked laser, which implies a well-defined relation between the allowed modes inside the cavity. Assuming that Δφ is mode and time independent (then a mode locked laser) and using the following relations

$$\sum_{m=-n}^{n} e^{im\alpha} = 2\sum_{m=0}^{n} \cos(m\alpha) - 1 \tag{2.18}$$

$$\sum_{m=0}^{n} \cos(m\alpha) = \frac{\cos\left(\frac{n\alpha}{2}\right) \sin\left[\frac{(n+1)\alpha}{2}\right]}{\sin\left(\frac{\alpha}{2}\right)} \tag{2.19}$$

The total electric field can be written as:

$$E(t) = E_0 e^{i\omega_0 t} \frac{\sin\frac{N(\Delta\omega t + \Delta\varphi)}{2}}{\sin\frac{\Delta\omega t + \Delta\varphi}{2}} \tag{2.20}$$

Equation 2. 20 represents a wave of frequency ω_0 with an amplitude modulated by a factor like $\frac{\sin(nx)}{\sin(x)}$. Therefore, the intensity will be proportional to $\left(\frac{\sin(nx)}{\sin(x)}\right)^2$, thus giving an ultrashort laser pulse, the inter-pulse time (illustrated in case of three allowed modes in Figure 2.7) being $T = \frac{2\pi}{\Delta\omega} = \frac{2L}{c}$ (round trip time). In the same way, it is possible to estimate the pulse duration as the time separation between two minima around a peak: $\tau = \frac{2L}{Nc}$. From this expression the ultrashort pulse duration is driven by a high mode number N.

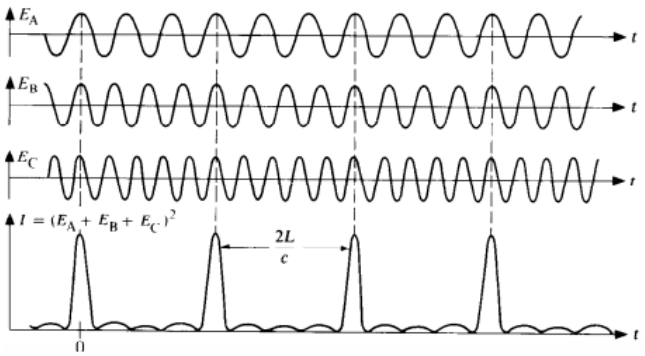

Figure 2.7. Illustration of the pulse intensity resulting from by the sum of three different modes.

As already mentioned above, this process leads to the generation of femtosecond pulses with a moderate energy per pulse (~nJ). One of the main problems in making these ultrashort lasers is due to the very high peak intensity that could damage the active medium. A solution to amplify the pulse intensity was proposed by G. Mourou and D. Strickland through the Chirped pulse amplification (CPA) technique [109], [150], [151]. The basic concept, as illustrated in Figure 2.8, needs that the generated mode-locked pulse (with a pulse width of ~ 10 fs and energy per pulse ~nJ) is spectrally dispersed and temporally stretched by a pair of gratings (or also prisms), causing the widening of the pulse up to $\sim 10^2$ ps thus lowering the peak intensity. In this way, there is no more risk to seriously damage the active medium, and the pulse is driven into a power amplifier (a new cavity with an active medium) where the pulse continuously gain energy. The higher energy pulse, after the amplifier, is guided into a second pair of gratings (or prism) in order to reverse the light dispersion and operating as compressor of the pulse temporal width, obtaining a laser pulse with a temporal width of $\sim 10 \div 10^2$ fs, with an energy per pulse $\geq 10^2$ μJ. Nowadays, almost all the commercially available femtosecond lasers are based on the CPA technique to obtain high intensity femtosecond pulses.

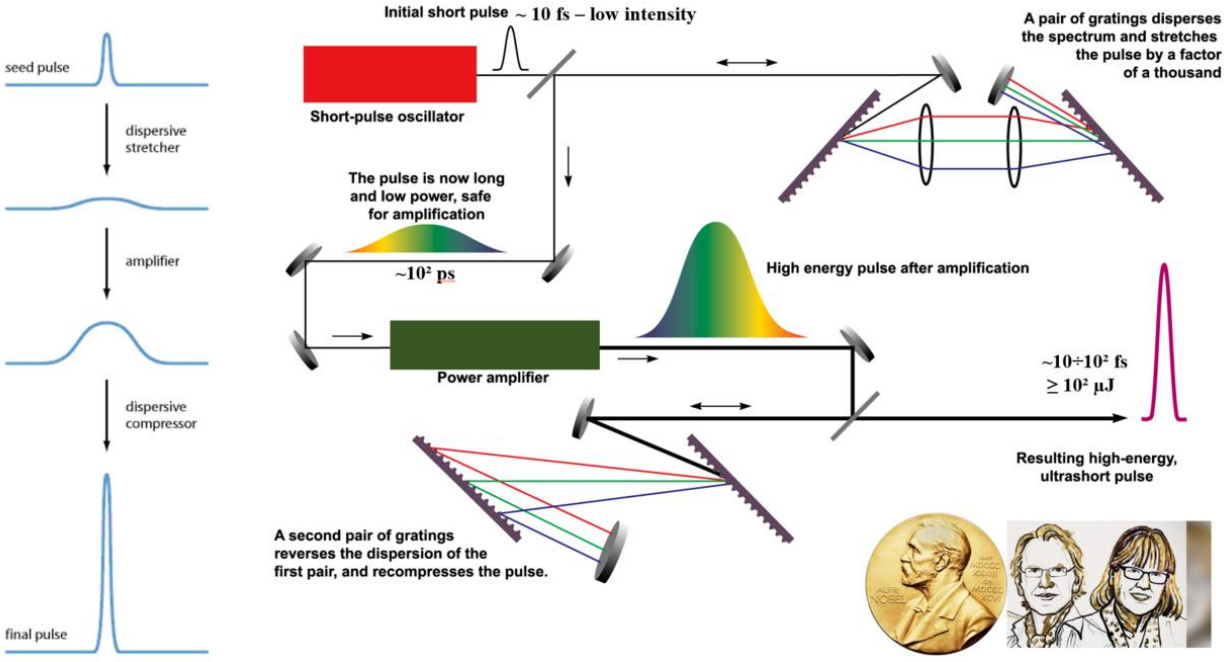

Figure 2.8. Illustration of the CPA basic mechanisms. In the bottom at right, the Nobel Prize winners G. Mourou and D. Strickland which proposed this technique to amplify the fs-laser pulses.

2. 3.2 White light generation

In our experimental setup, the probe is a white light (or supercontinuum light) generated by a component of the fundamental femtosecond pulses [150]–[152]. Moreover, in some cases also the pump is generated by "seeds" photons taken from a broad spectral light induced in the same way. In general, the white light is generated by a third non-linear phenomenon which is called Self-Phase Modulation (SPM) and amplified by the Self-Focusing (SF), a non-linear phenomenon which increases the generated white light efficiency.

Considering the material devoted to the white light generation as centrosymmetric (defined by the zero second order material susceptibility $\chi^{(2)} = 0$), the instantaneous polarization density $\frac{\mathbf{P}}{\varepsilon_0}$ in the irradiated volume by the femtosecond pulses could be written according to equation 1.50, while the nonlinear refractive index is described by equation 1.51. Delivering the spatial and time dependencies of the refractive index n we have

$$n(r,t) = n_0 + n_2 I(r,t) \tag{2.21}$$

where n_0 and n_2 are the linear and non-linear refractive index of the material, respectively. According to equation 2.21, the spatial and temporal refractive index modulation (in the irradiated material) are affected by the spatial and temporal beam envelop dependence following the correspondent intensity dependence. The spatial dependence will give rise to the SF, while the temporal one to the SPM. Assuming that the beam is described by $E(t,x) = E_0 e^{-i(\omega_0 t - kx)}$, the SPM will affect the pulse phase, because $k = \frac{\omega_0}{c} n(t)$. Then, the instantaneous phase depends on the time in the following way:

$$\varphi(t) = \omega_0 t - \frac{\omega_0}{c} n(t) x = \omega_0 t - \frac{\omega_0 n_0}{c} x - \frac{\omega_0}{c} x n_2 I(t) \tag{2.22}$$

Following equation 2.22 we define the instantaneous frequency $\omega(t)$ as

$$\omega(t) = \frac{\partial}{\partial t}\varphi(t) = \omega_0 - n_2 \frac{\omega_0 x}{c} \frac{\partial I(t)}{\partial t} \tag{2.23}$$

where the dependence of $\omega(t)$ on $\frac{\partial I(t)}{\partial t}$ implies the variation of the propagating light frequency controlled by the time envelope of the beam intensity. The consequence of this dependence is the introduction of new frequencies in the pulse spectrum, symmetrically placed around the fundamental ω_0 value (Figure 2.9).

The SF, already presented in the description of the pulse non-linear propagation in section 1.3.3, induces a dramatic increase of the local electric field intensity, enhancing the SPM and contributing to amplify the white light generation.

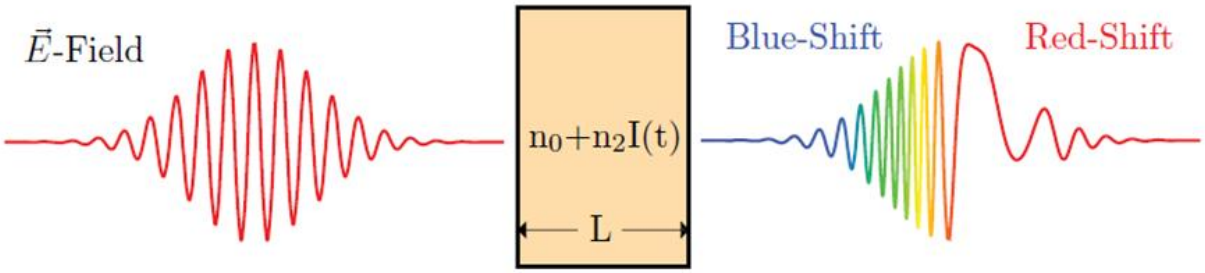

Figure 2.9. Illustration of the white light generation through the SPM phenomena in a centrosymmetric medium.

Group velocity dispersion

After the beam passes through the centrosymmetric medium, the pulse is temporally chirped, because of the Group Velocity Dispersion (GVD) defined as [147], [150], [151]:

$$\mathrm{GDV} = \left(\frac{\mathrm{d}^2\mathrm{k}}{\mathrm{d}\omega^2}\right)_{\omega_0} = \frac{\mathrm{d}}{\mathrm{d}\omega}\left(\frac{1}{\mathrm{v_g}}\right)_{\omega_0} \tag{2.24}$$

where $\mathrm{v_g}$ is the femtosecond pulse group velocity. The $\mathrm{v_g}$ can be written as

$$\mathrm{v_g} \approx \mathrm{v_\varphi}\left(1 - \frac{\omega}{\mathrm{n}(\omega)}\frac{\mathrm{dn}(\omega)}{\mathrm{d}(\omega)}\right) \tag{2.25}$$

where $\mathrm{v_\varphi}$ is the pulse phase velocity. In the propagating pulse within the material, all the spectral components acquire a different delay, as a function of the refractive index and on their frequency, resulting in a temporal broadening of the pulse spectral components. Depending on the GVD value, we have the slowing down of different spectral components:

- $\mathrm{GVD} > 0$ implies $\frac{\mathrm{dn}(\omega)}{\mathrm{d}(\omega)} > 0$, then the smaller wavelengths are slower than the higher ones;

- $\mathrm{GVD} < 0$ implies $\frac{\mathrm{dn}(\omega)}{\mathrm{d}(\omega)} < 0$, then the higher wavelengths are slower than the lower ones.

2. 3.3 Pump wavelength generation

In the pump-probe experimental setup used in the present work we have the possibility to choose the pump wavelength through two processes: the harmonic generation (second and third ones in our case) and the optical parametric amplifier (which gives us the possibility to tune continuously the pump wavelength). In the Chapter 3 we will describe in details the setup devoted to the wavelength selection, while in this paragraph we present the above mentioned phenomena.

Second harmonic generation

In general, the polarization density **P** of a medium, in the frequency space, could be written as follows [124], [150], [151]

$$\frac{\mathbf{P}(\omega)}{\varepsilon_0} = \chi^{(1)}(\omega)\mathbf{E}(\omega) + \chi^{(2)}(\omega)\mathbf{E}(\omega)\mathbf{E}(\omega) + \chi^{(3)}(\omega)\mathbf{E}(\omega)\mathbf{E}(\omega)\mathbf{E}(\omega) \ldots \tag{2.26}$$

As already mentioned, the first term is the linear approximation, while the others are devoted to the non-linear ones. We generate a second harmonic by doubling the fundamental laser frequency when two photons of frequency ω_1, crossing a non-centrosymmetrical medium (characterized by $\chi^{(2)} \neq 0$), are combined to produce a photon of frequency $\omega_2 = 2\omega_1$. This phenomenon is called Second Harmonic Generation (SHG). Assuming to be in not-depleted condition (then a negligible pump absorption), the process requires the energy and momentum conservation:

$$\omega_2 = \omega_1 + \omega'_1 \tag{2.27}$$

$$\mathbf{k_2} = \mathbf{k_1} + \mathbf{k'_1} \rightarrow \; n_2\omega_2 = n_1\omega_1 + n'_1\omega'_1 \tag{2.28}$$

where ω_2 is the double frequency while ω_1 and ω'_1 are the fundamental frequencies of the two photons. The resulting beam intensity is proportional to

$$I(2\omega_1) \propto \frac{{\omega_1}^2 {\chi_{eff}}^2 l^2}{n^3} I(\omega_1)^2 \left(\frac{\sin\left(\frac{\Delta k l}{2}\right)}{\frac{\Delta k l}{2}} \right)^2 \tag{2.29}$$

where l is the material length, $\Delta k = k_2 - 2k_1$ (phase mismatch condition) that implies the momentum conservation and χ_{eff} the effective susceptibility resulting from the combination of the tensor $\chi^{(2)}$components , depending on the material and its own orientation.

It is important to observe that to satisfy equation 2.28 the two beams $I(2\omega_1)$ and $I(\omega_1)$ have to propagate in the medium with the same velocity, then it is necessary that the refractive index at those frequencies are the same. The materials in which such condition is achievable are the birefringent materials, in which the refractive index depends on both the light polarization and the direction of propagation. In this case we define an ordinary (n_o) refractive index and an extraordinary (n_e) one, where the latter depends on the angle between the wavevectors **k** of the

beam and the crystal optical axis (Figure 2.10). For example, if the beat at ω_1 propagates along the ordinary refractive index orientation and the beam at $2\omega_1$ along the extraordinary one, it is possible to reach the mismatch condition by the control of the crystal orientation, obtaining $n_e(2\omega_1) = n_o(\omega_1)$.

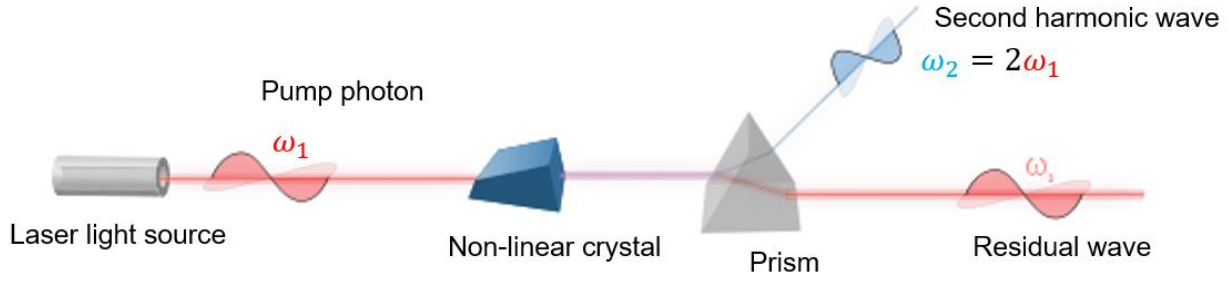

Figure 2.10. Illustration of the SHG: the fundamental beam passes through the non-linear non-centrosymmetrical crystal generating a beam with a double frequency. In the figure the two collinear beams are separated using a prism.

Third harmonic generation

The Third Harmonic generation (THG) is a non-linear process which involves the third order of the material susceptibility [124]. In our case THG is generated by the sum of the fundamental wavelength together with the already collinear SH generated beam. The energy and momentum conservation are imposed by the equations:

$$\omega_{3H} = \omega_f + \omega_{2H} \tag{2.30}$$

$$\mathbf{k_{3H}} = \mathbf{k_f} + \mathbf{k_{2H}} \rightarrow \; n_{3H}\omega_{3H} = n_f\omega_f + n_{2H}\omega_{2H} \tag{2.31}$$

where ω_{3H} is the THG photon with frequency $\omega_{3H} = 3\omega_f$, ω_f being the fundamental frequency, and ω_{2H} is the SHG frequency; $\mathbf{k_{3H}}$, $\mathbf{k_f}$, $\mathbf{k_{2H}}$ and n_{3H}, n_f, n_{2H} are the corresponding wavevectors and refractive index, respectively. Equation 2.31 represents the mismatch condition, which implies that the fundamental and the SHG share the same polarization, while the THG photon has an orthogonal one.

Optical Parametric Amplifier

The Optical Parametric Amplifier (OPA) is a technique used to generate a tunable laser light starting from the interaction of a non-linear crystal (β-BBO crystal in our case) of a strong laser pump (ω_p) and a weak spectral broadband light (generated as a supercontinuum light, already described in the previous paragraph) used as "seed" to stimulate the photon emission (also called signal) of a frequency $\omega_s < \omega_p$ [147], [153], [154]. To amplify the seeds photons, the pump is used to create another beam, called idler, with frequency ω_i. All the three involved photons have to satisfy the energy and momentum conservation laws (Figure 2.11):

$$\omega_p = \omega_s + \omega_i \tag{2.32}$$

$$\mathbf{k_p} = \mathbf{k_s} + \mathbf{k_i} \rightarrow n_p\omega_p = n_s\omega_s + n_i\omega_i \tag{2.33}$$

It could be interesting to note that changing the crystal orientation the mismatch condition allows to optimize different wavelengths, giving the possibility to tune the output laser wavelength.

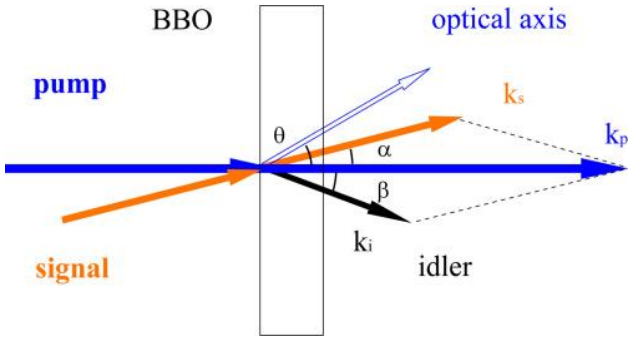

Figure 2.11. Illustration of the wavevectors of the pump, the signal and the idler photons used in an OPA. Figure taken from [153].

2. 3.4 Cross-phase modulation

The Cross-Phase Modulation (XPM) is a non-linear process due to the spatial overlap between the pump and the probe beams, caused by the time dependence pump modulation of the

medium refractive index, according to equation 2.21. During the overlap, the time modulation of the refractive index in the material is experienced by the broadband probe, giving rise to an artifact in the TA signal around the zero delay (pump-probe spatial overlap) [155].

Assuming a delay window within the time range in which are interacting the two beam frequencies , the probe frequencies are shuffled in a way that the part which is interacting with the maximum of the pump (in the overlap delay window) is pushed outwards, producing a weakening of the intensity in the probe pulse central part (that the detector measures as an absorption, then as a positive signal) and an amplification of the probe pulse wings (resulting in more light on the detector, then a negative signal). A simulation of the process is illustrated in Figure 2.12, to simplify the comprehension of the phenomenon, in which we considered the probe continuum light with a linear temporal chirp.

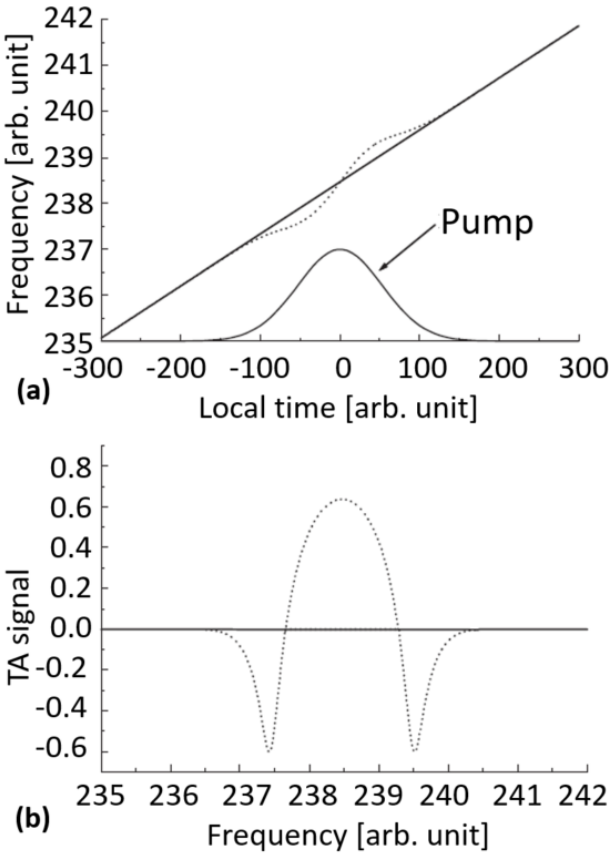

Figure 2.12. XPM signal simulation: the dotted curve represents the perturbed distribution of probe's frequencies due to the overlap with the pump; while the solid line is the unperturbed distribution of probe's frequencies (a); resulting modification of ΔOD signal's shape (b). Figure taken from [155].

2. 3.5 Transient absorption signal

The TA signal is defined as the difference between the absorption spectrum of the investigated sample excited by the pump pulse (pumped spectrum) and that without the pump (un-pumped spectrum), therefore the sample in the ground state [146], [148], [149], [156]. Considering the absorber density in the excited sample as $N_s = N_g + N_e$, then composed of the N_g absorbers in the ground state and N_e in the excited state, it is possible to express the Lambert-Beer law (equation 2.2) as a function of the cross section (following equation 2.8):

$$I_{unpumped} = I_0 e^{-\sigma_g(\omega) d N_s} \tag{2.34}$$

$$I_{pumped} = I_0 e^{-\sigma_g(\omega) d (N_s - N_e) - \sigma_e(\omega) d N_e} = I_{unpumped} e^{-\Delta\sigma(\omega) d N_e} \tag{2.35}$$

where $\sigma_{g(\omega)}$ and $\sigma_{e(\omega)}$ are the cross sections of the attenuation in the ground and in the excited states, respectively, $\Delta\sigma_{(\omega)} = \sigma_{g(\omega)} - \sigma_{e(\omega)}$ is the variation of the attenuation cross section and d is the sample thickness. Using the equations 2.35, it is possible to define the transient absorption signal as

$$\Delta OD = OD_{pumped} - OD_{unpumped} = \frac{\Delta\sigma(\omega) N_e d}{2.303} = -\frac{1}{2.303} \ln \frac{I_{pumped}}{I_{unpumped}} \tag{2.36}$$

Considering that the transient absorption signal ΔOD is very small in comparison to the unpumped beam, which means that $I_{pumped} - I_{unpumped} \ll I_{unpumped}$, we have

$$\Delta OD \sim -\frac{1}{2.303} \frac{I_{pumped} - I_{unpumped}}{I_{unpumped}} \tag{2.37}$$

2. 3.6 Singular value decomposition

Pump-probe measurements consist in the evaluation of the TA induced by the pump excitation in a broad spectral range, for each pump-probe delay explored by the experimental setup.

All the spectra are arranged into 2D structure, such a matrix, where each row corresponds to a measured spectrum at a fixed delay time, while every column corresponds to the absorbance variation at a particular wavelength. At each row of these matrix is associated a pump-probe delay. It is possible to describe the TA measurements as a function of the time as the sum of spectra contributions arising from k different components, weighted by their respective time-dependent concentrations [146], [148], [156], that in the matrix formalism results

$$\mathrm{TA} = \mathrm{C} \cdot \mathrm{S}^{\mathrm{T}} \tag{2.38}$$

where TA is the matrix including the pump-probe measured value, the columns of the C matrix ($m \times k$) represent the time-dependent profiles of the k components at the $m-$th delay, while the rows of the matrix S^T ($k \times n$) are the k transient spectra measured at the $n-$th spectroscopic variable. The TA matrix reconstruction is illustrated in Figure 2.13.

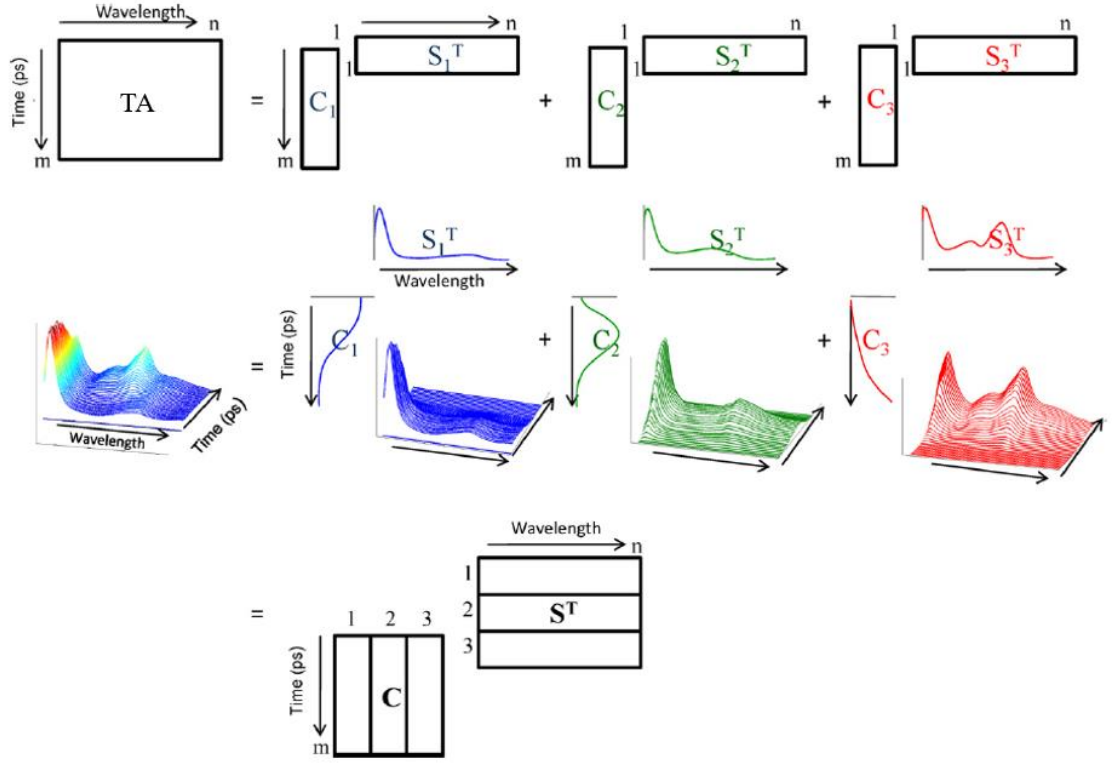

Figure 2.13. TA spectrum reconstruction with a model related to a three-component process monitored by time-resolved spectroscopy. Figure taken from [146].

The Singular Value Decomposition (SVD) is a mathematical tool to obtain the rank of the analyzed matrix, and then it allows us to decompose the TA matrix into a minimum number of relevant kinetics and spectra, removing at the same time the white noise component from the data. The original matrix $TA(\lambda, t)_{m\times n}$, as function of the wavelength λ and the delay t, is expressed as

$$TA(\lambda, t)_{m\times n} = U(\lambda)_{m\times m} \times D_{m\times n} \times V(t)^{T}_{n\times n} \quad (2.39)$$

where $U(\lambda)_{m\times m}$ and $V(t)_{n\times n}$ are the eigenspectra and eigentraces orthonormal matrices, respectively, while $D_{m\times n}$ is the diagonal matrix $m \times n$, m being the wavelength number and n the delay number, of which the elements are called eigenvalues or singular values arranged in descending order; the other elements of the $D_{m\times n}$ are zero. It is important to note that the single eigenspectrum or eigentrace has no physical meaning alone, but could be helpful to describe the dynamic of the $TA(\lambda, t)_{m\times n}$ matrix as function of the $U(\lambda)_{m\times m}$ and $V(t)_{n\times n}$ matrices. Once the $D_{m\times n}$ matrix is defined, the eigenvalues are used to discriminate between the components: a significant contribution is described by a large value of elements, while it is possible to consider as noise the elements associated to an eigenvalue small enough. Of course, the first components (the ones characterized by a large value, since the $D_{m\times n}$ has descending values elements) will be taken into account to reconstruct the original $TA(\lambda, t)_{m\times n}$ matrix, reducing in this way the number of spectra and kinetics vectors used to describe the matrix and removing an important noise component of the measured signal.

2.4. Rayleigh and Raman scattering

When an incident light beam strikes a spherical particle (with a frequency below the scattering particle resonant frequency), it will be scattered in all the directions.

When the scattering process is elastic, the scattered light has the same wavelength of the incident light, giving rise to the Rayleigh scattering (Figure 2.14) [157]. In this case, the scattered intensity is proportional to the incident beam and other variables such as the volume V of the spherical particle, the distance r to the observation point, the wavelength λ, and the refractive

indexes n_1 and n_2 of the particle and medium. We can derive an expression for the scattered beam intensity I_s for small diameter spheres $l \ll \lambda$ with refractive index of the medium n:

$$I_s = I_0 \frac{1 + \cos^2\theta}{2r^2} \left(\frac{2\pi}{\lambda}\right)^4 \left(\frac{n^2 - 1}{n^2 + 2}\right)^2 \left(\frac{l}{2}\right)^2 \tag{2.40}$$

where θ is the scattering angle. Averaging θ over all the directions, we demonstrate that the Rayleigh scattering cross section σ_s is proportional to the fourth power of the wavelength inverse:

$$\sigma_s = \frac{2\pi^5}{3} \frac{l^6}{\lambda^4} \left(\frac{n^2 - 1}{n^2 + 2}\right)^2 \tag{2.41}$$

The Raman spectroscopy [158] is based on the photon inelastic scattering due to the phonons exchange (associated with the nuclear vibration) after the photon excitation toward a virtual electronic state (not resonant Raman scattering). Therefore, this technique is very useful to investigate the studied system vibrational levels. As depicted in Figure 2.14, when the incoming light beam with a frequency ν_0 is far away from the resonance, the scattered electromagnetic wave consists in one very intense spectral component of frequency ν_0 (the Rayleigh scattering) and other less intense lines with higher and lower frequencies compared to ν_0. The value of $\Delta\nu = \nu_{vib}$ corresponds to the vibrational frequency of the studied system and is called the Raman shift. The Raman scattering intensity is much lower than the Rayleigh one.

The emitted photon with lower energy than the incident one is called the Stokes contribution ($\nu_0 - \nu_{vib}$), while the one with higher energy than the incoming photon is called anti-Stokes contribution ($\nu_0 + \nu_{vib}$). The relative contributions of the Stokes and anti-Stokes components are not the same in the involved transition, because they are controlled by the vibrational state populations, in agreement with the Boltzmann distribution temperature dependence. The Stokes contribution intensity is always higher than the anti-Stokes one, for this reason the instrumentations used to study the Raman spectra are (usually) configured to measure the Stoke component. Conventionally, the Raman shift is measured in wavenumber units (cm^{-1}), where $1\ eV = 8065.5\ cm^{-1}$.

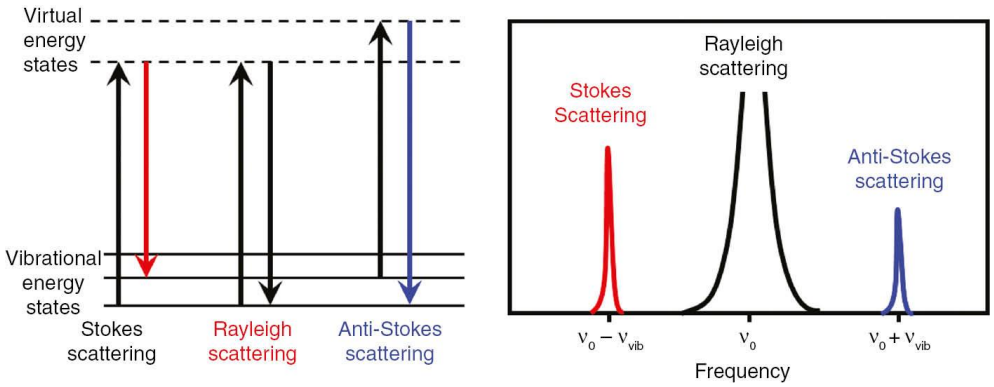

Figure 2.14. Basic principle of the Raman scattering. Figure taken from [159].

2.5. Phase contrast Microscopy

Phase Contrast Microscopy (PCM) is a micro-optical technique employed to reproduce high-contrast images of transparent samples [160]. In Figure 2.15 is depicted an illustration of the PCM basic concept. The principle to make phase variation observable is to separate the zero-th order of the illuminating light from the sample scattered light at the objective rear focal plane. The mechanism for generating relative phase retardation is a two-step process, with the scattered waves retarded in phase by a quarter wavelength (generally for transparent materials) at the sample, while the surround illuminating wave is advanced (or retarded) in phase by a plate positioned in, or very near, the objective rear focal plane. For this purpose, the zero-th order illuminating light is ring shaped and passed the condenser (a lens) before the sample. As the hollow light cone crosses the sample, it reaches the objective focal plane in the shape of a light ring. To speed up the direct undeviated zero-th order light, a plate is installed with a ring shaped phase shifter attached to it at the objective rear focal plane. In this way, the undeviated light pathway through the phase annulus travels a shorter distance in traversing the objective glass than the diffracted light. At the image plane, the diffracted and direct lights can interfere destructively because they are now half wavelength out of phase with each other, then the sample's details appear dark against a lighter background.

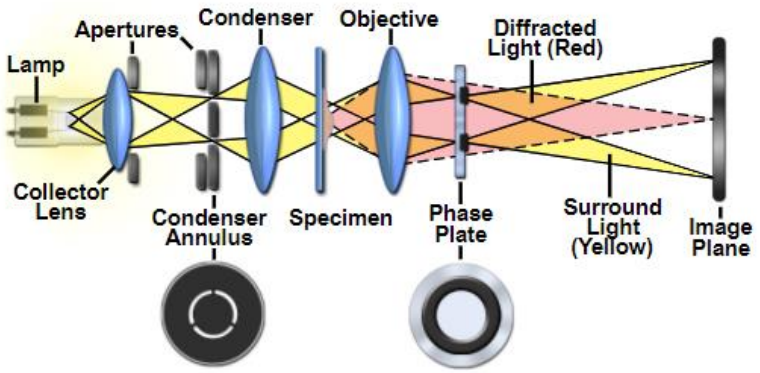

Figure 2.15. PCM basic concept. Figure taken from [161].

Chapter 3. Experimental setup

The present chapter describes the samples investigated in the PhD thesis framework, such as the canonical optical fibers and the bulk samples. It also describes the experimental setups employed for the characterization of such samples and measuring the evolutions of their properties during irradiation (laser or X-rays) exposure. Both the samples and their associated instrumentations will be presented following the order of the next chapters and then the different topics covered by this PhD research work. First, we detail the properties of the fiber samples devoted to the study of the RIA levels and kinetics under X-rays (chapter 4). Second, the bulk samples used for the waveguide's inscription are presented as the tools allowing to probe the modifications induced by high intensity femtosecond laser (chapter 5). Finally, the bulk glass samples selected for the pump-probe measurements (chapter 6) are introduced as well as the associated experimental setup.

3.1. Canonical optical fibers

We focus the present work on the origins of pulsed and steady state X-ray RIA on four different canonical samples [87], [162]–[164]: pure-silica-core (PSC), fluorine (F), germanium (Ge) and phosphorous (P) doped OFs. For the tests, the fiber length exposed to the radiation is adapted with respect to the expected RIA levels that depend on both the sample type and the investigated spectral range as well as the irradiation temperature. For both types of X-ray irradiation, we have investigated the sample behaviors at both room temperature (RT, around 20°C) and at liquid nitrogen temperature (LNT).

To understand the fiber intrinsic parameter influence on its radiation response, *ad hoc* OFs with known process parameters have been developed thanks to the LabH6 Joint Research Laboratory [165] between the UJM, the CNRS and the iXblue fiber manufacturer [166]. These samples, referred as canonical samples, present optical properties and performances similar to the

commercial OFs. Their use allows us to better highlight the relative influence of each process parameter (such as Ge, P or F doping element role) on the fiber radiation response. Among the wide range of existing fiber types, the ones designed with the F, Ge, P and Al-doped silica have been selected as these chemical elements are the most spread core-dopants for fiber-based telecom and sensing applications [4].

It is also possible to keep a pure silica core (PSC) by decreasing the fiber cladding refractive index through F-doping [167]. More usually we increase the OFs core refractive index by the Ge (or P, Al)-doping [4]. Germanosilicate OFs are also sensitive to the UV-light exposure [88], leading to applications such as the fiber Bragg gratings inscription . Differently, it is well-known that both P- and Al-dopants strongly increase the fiber radiation sensitivity [30], [168]. As a consequence, those fibers are not interesting choices for data transmission under irradiation, but could be exploited to design radiation detectors or even distributed fiber-based dosimeters. They are also incorporated in the cores of rare-earth-doped fibers used to build optical amplifiers and laser sources. Both P and Al decrease the fiber melting temperature.

In the following parts, a short description of the investigated canonical samples is provided, to a have a deeper analysis of these samples, one should refer to the PhD thesis work of D. Di Francesca [169].

Samples for X-ray pulsed irradiation experiments

Several multimode canonical optical fibers from iXblue manufacturer have been selected, varying their core compositions to highlight the core doping influence: PSC, F-, Ge-, Ge+F- and P-doped silica cores. The fluorine and germanium radial distributions (*measured along the diameter of a cleaved fiber*) within these samples are depicted in Figure 3.1. These doping profiles are measured by energy dispersive X-ray analysis (EDX), in the F- and Ge-doped samples [79]. The F content in the fluorine doped sample cores is ~ 0.25 wt. % and ~ 0.1 wt. % for the F-doped and Ge+F-codoped OFs, respectively. The germanium content in both Ge-doped fiber cores under test (FUT) is around 8.5 wt. %. The Ge amount and radial distribution in the Ge+F canonical sample were chosen to have the same refractive index profile as the Ge-doped OF. For all the samples, the SiOH groups' concentration is below 10 ppb. This threshold was estimated by the manufacturer, considering that no 1380 nm absorption peak was detectable in the attenuation

spectra measured by the cut-back method. The chlorine impurities concentration has been also measured by EDX to be around 0.2 wt. % in the whole sample set, while the concentrations of other impurities, if any, are below the 100 ppm limit of the EDX analysis.

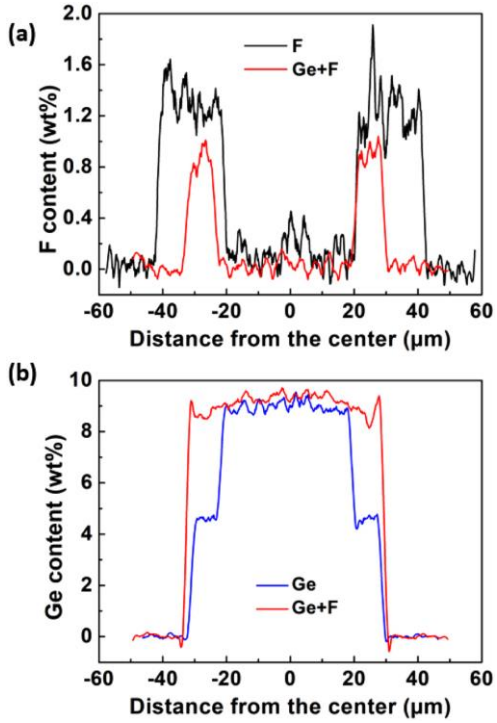

Figure 3.1. (a) Fluorine and (b) Germanium radial distributions in the F-doped and Ge-doped samples, respectively, as function of the distance from the center, measured by EDX analysis. Figure taken from [79].

In Figure 3.2, we report the P radial distribution as measured by electron microprobe analysis [101]. The P-dopant reaches its maximum content (7.5 wt. %) at the fiber core center, while it decreases by steps down to 0% in the cladding 30 μm away from the fiber center. Fiber characteristics are summarized in Table 3.1.

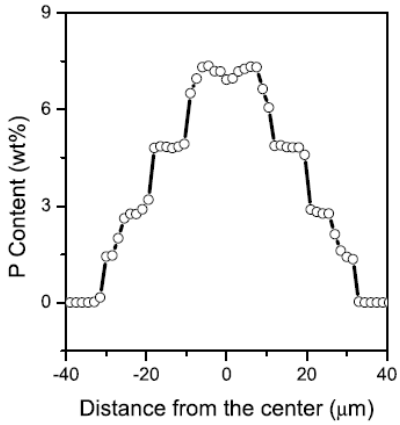

Figure 3.2. Phosphorous doping levels as a function of the distance from the fiber center. Figure taken from [101].

Table 3.1. Samples, dopant type and concentrations in the core, used sample lengths for irradiation tests, the Δn, core, cladding and coating dimension and the initial loss measured at 1310 nm.

Fiber	PSC	F-doped	Ge-doped	Ge+F-doped	P-doped
F content in the core [wt %]	none	0.25	none	0.1	none
Ge content in the core [wt %]	none	none	8.5	8.5	none
P content in the core [wt %]	none	none	none	none	7.6
UV/visible RT length (m)	10	10	1	10	0.5
Near-IR RT length (m)	50	50	10	50	5
UV/visible LNT length (m)	1	10	1	1	0.5
Near-IR LNT length (m)	1	50	10	50	5
Δn ($\times 10^{-3}$)	5.3	5	9	9	6
Core dimension (μm)	62.5	42.5	62.5	62.5	62.5
Cladding dimension (μm)	125	125	125	125	125
Coating dimension (μm)	250	250	250	250	250
Initial loss @ 1310 nm (dB/km)	10	6	2	2	5

Samples for steady state X-ray irradiation experiments

Under steady state X-ray irradiation we have characterized the following single mode canonical samples: PSC, Ge- and P-doped single mode optical fibers [87]. The main characteristics are listed in table 3.2.

Table 3.2. Samples, dopant nature and core concentrations, sample lengths used for irradiation tests, the Δn, core, cladding and coating dimension and the initial loss measured at 1310 nm.

Fiber	PSC	Ge-doped	P-doped
F content in the core [wt %]	none	none	none
Ge content in the core [wt %]	none	5	none
P content in the core [wt %]	none	none	10.5
UV/visible RT length (m)	10	10	0.5
Near-IR RT length (m)	40	30	5
UV/visible LNT length (m)	10	0.18	0.5
Near-IR LNT length (m)	40	0.5	4
Δn ($\times 10^{-3}$)	Not available	9	9
Core dimension (µm)	9	8.2	4
Cladding dimension (µm)	125	125	125
Coating dimension (µm)	245	245	244
Initial loss @ 1310 nm (dB/km)	0.5	0.34	1.04

3.2. Bulk samples

In the following section, we described the different silica glasses exposed to high intensity femtosecond pulses: Suprasil 300, Herasil 1 and Corning 7980. These silica glasses could be classified following the Brückner classification [170]:

- Type II: the so-called natural wet silica, is obtained by quartz melting through flame. It contains a higher OH number compared to the type I silica with concentrations between 150 and 400 ppm. It can also contain a few metallic impurities. Herasil 1 is such a type II silica and it is characterized by the presence of germanium impurities at concentrations on the order of ~1 ppm.
- Type III: is a synthetic silica made from the hydrolysis of silicon tetrachloride in gaseous form ($SiCl_4$). The material is characterized by high OH groups content, on the order 1000 ppm, with no detectable metallic impurities, but with chlorine traces (derived from the production process). The Corning 7980 is representative of this silica type.
- Type IV: also called synthetic dry silica, it is characterized by a very low OH content ($[OH] < 10$ ppm). Such type I glass can be obtained from $SiC1_4$ in a water vapour-free plasma flame. The glass contains negligible metallic impurity amounts, resulting in a glass of high purity. The Suprasil 300 belongs to this category.

From the above classification, the sample under test could be classified by their OH content, as summarized in table 3.3. Since it is possible to estimate the OH concentration through the absorption peak at 1380 nm associated with the OH overtone, we reported the absorption spectra of these glasses in Figures 3.3 – 3.5 with an insert highlighting the spectral region around 1380 nm.

Table 3.3. Various types of silica samples with the corresponding OH and Ge contents.

Sample	[OH]	[Ge]
Suprasil 300	< 10 ppm	none
Herasil 1	150 ÷ 400 ppm	~1 ppm
Corning 7980	~1000 ppm	none

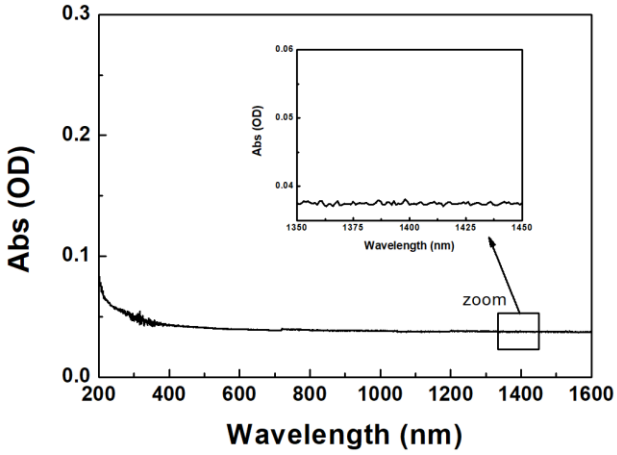

Figure 3.3. Absorption spectrum of the Suprasil 300 sample. The inset highlights the spectral region around 1380 nm: no OH overtone is observed in this sample.

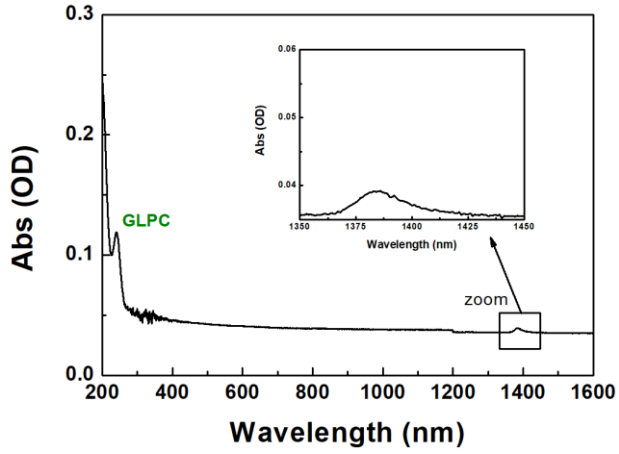

Figure 3.4. Absorption spectrum of the Herasil 1 sample. The inset highlights the spectral region around 1380 nm: a small band corresponding to the OH overtone. Around 245 nm, the GLPC absorption band can be clearly observed.

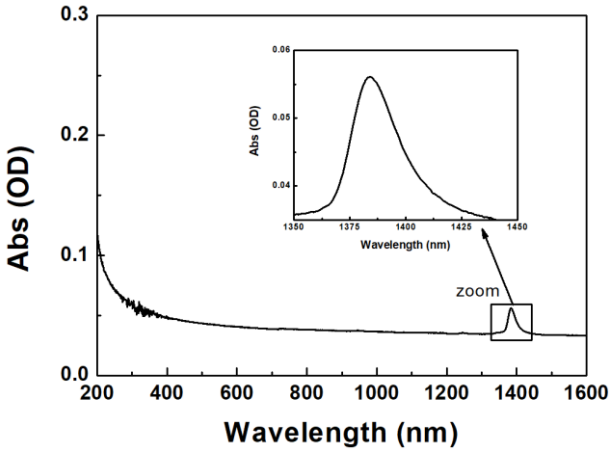

Figure 3.5. Absorption spectrum of the Corning 7980 sample. The inset highlights the spectral region around 1380 nm: a band is clearly observable corresponding to the OH overtone.

3.3. Samples for pump-probe experiments

3. 3.1 β-irradiated sample

The tested sample is a Suprasil 1 $5 \times 5 \times 0.5\ \mathrm{mm}^3$ sized that is basically a synthetic wet silica specimen, supplied by Heraeus [171]. It is produced by the hydrolysis of $SiCl_4$ in a H_2/O_2 flame, of high purity (metallic impurities below 1 ppm by weight) except for the presence of SiOH groups with a 1000 ppm concentration. NBOHCs are present that were induced by β-irradiation exposure at the huge dose of $5 \times 10^9\ \mathrm{Gy}(SiO_2)$, using a Van de Graff electron accelerator (2.5 MeV). It is possible to estimate the defect concentration around $\sim 3.2 \times 10^{18}\ \mathrm{cm}^{-3}$ with accuracy of $\sim 15\%$, on the basis of the 2.0 eV absorption band intensity and its oscillator strength $f = 1.91 \times 10^{-4}$, through Smakula's equation (equation 2.10 – 2.11) [172]. Its absorption spectrum is reported in Figure 3.6.

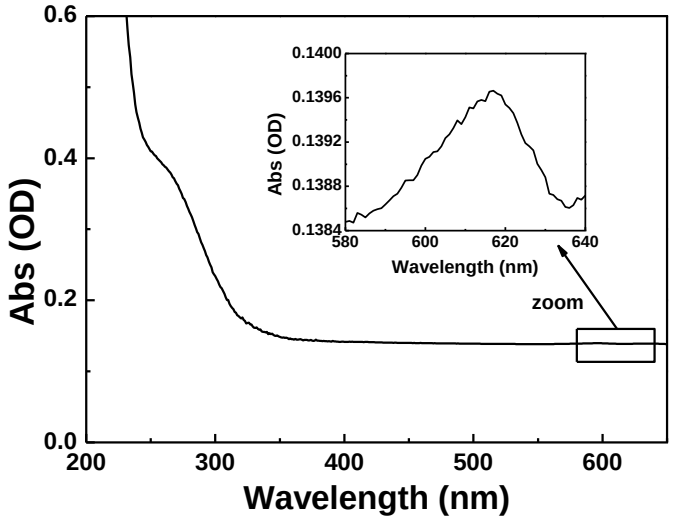

Figure 3.6. Absorption spectrum of the β-irradiated Suprasil 1 sample. The inset reports the zoom of the 620 nm absorption band of NBOHCs.

3. 3.2 Ge-doped preform

To investigate the GLPC photocycle a germanium doped preform was selected, it has a size of $4 \times 4 \times 0.67$ mm^3. In terms of composition, the core contains 6% of Ge and has a pure silica cladding. It is important to underline that a strong germanium presence in the silica network entails a strong decrease of the silica bandgap [89]. Indeed, it is possible estimate the bandgap around 193 nm (6.4 eV) from the absorption spectrum in Figure 3.7. Moreover, being the preform sample, there is a varying germanium content along the sample diameter, which implies that during the absorption measurement the beam passes through an inhomogeneous sample, resulting in a deformation of the band centered at 240 nm.

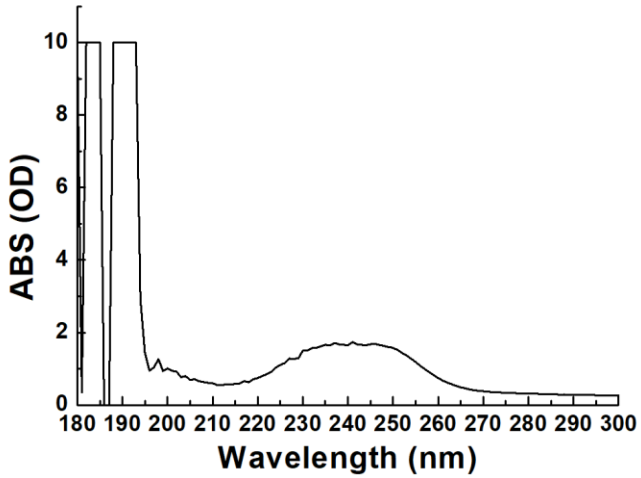

Figure 3.7. Absorption spectrum of the Ge-doped preform reaching, in the center, the 6% of germanium content.

3. 3.3 Ge-doped samples

To study the GLPC photocycle as a function of the Ge content and to overcome the problem linked to the bandgap lowering (that could involve transition to the bandgap) we have studied the GLPC photocycle in samples of size $3 \times 3 \times 1$ mm^3 and with a Ge content of either around ~1% and ~0.1%. Both samples exhibit an intense absorption bands around 245 nm. The corresponding absorption spectra are reported in Figure 3.8.

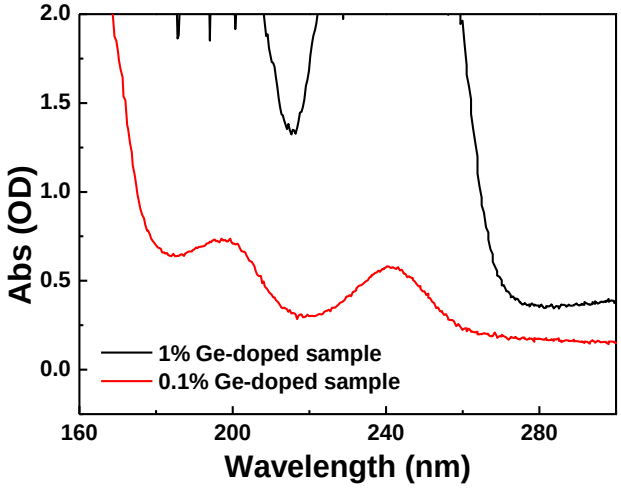

Figure 3.8. Absorption spectra of the Ge-doped samples with a Ge concentrations of ~1% (black curve) and 0.1% (red curve).

3.4. ASTERIX facility experimental setup

The ~1 MeV X-ray pulse generator ASTERIX facility from CEA DAM (pulse duration around tens of nanoseconds) [173], [174] allows simulating the dose and dose rate encountered with the ignition shots at the megajoule class laser facilities [175], [176]. These very extreme experimental conditions lead to a very high dose rate (>1 MGy/s) and moderate total accumulated dose (~ 10 Gy(SiO_2)) on the fiber.

The generator structure, depicted in Figure 3.9, is composed of a cylindrical section (8.5 m long, 2.85 m in diameter). The whole cylinder is filled with 130 m^3 of insulating oil. A large test room allows to accommodate samples. ASTERIX has a sixty-four stages 6.4 MV, 192 kJ Marx generator.

Figure 3.9. The ASTERIX pulsed X-ray generator, Centre d'Etudes de Gramat, France.

The basic scheme of the experimental setup is shown in Figure 3.10: the optical fibers are coiled within 8 cm of diameter and the source-sample distance is adjusted with respect to the expected total accumulated radiation dose and dose rate. The fiber under test (FUT) is connected with FC-PC connectors to rad hard fiber pigtails (even if the fiber pigtails are not in the beam-path) allowing the signal transmission between the instrumentation and the irradiation zones. FUT's input and end are respectively connected to a white light Deuterium–Halogen source (Ocean Optics DH-200-BAL) and to miniature spectrometers (Maya 2000 spectrometers for the

UV-Vis measurements and the NIR512 spectrometer for IR measurements, both from Ocean Optics), with a resolution time of tens of milliseconds. For LNT measurements [79], [80], [101], the fibers were located in a container filled with liquid nitrogen: the experiments started after full fiber thermalization. In order to guarantee the same dose and dose rate for the measurements in both UV/visible and near-IR ranges, these data acquisitions were performed simultaneously (during the same shot).

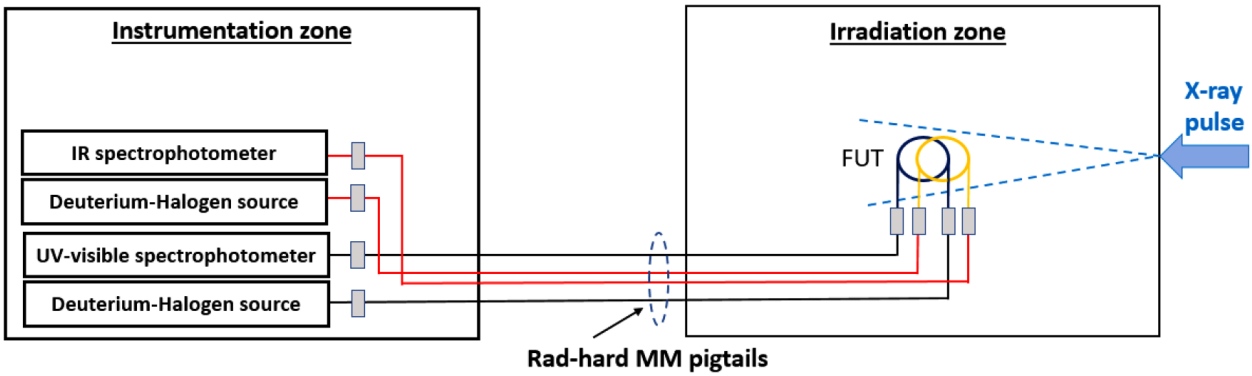

Figure 3.10. Experimental setup for online RIA measurements at ASTERIX pulsed X-ray facility. Figure taken from [79].

3.5. MOPERIX facility experimental setup

The Laboratoire Hubert Curien (LabHC) MOPERIX facility (160 kV X-ray tube with W-target) [177] has been used to irradiate with steady-state X-rays having an average energy of ~40 keV the canonical OFs samples. Even in this case, the dose rate is adjusted by changing the distance between the samples and the X-ray source, while the total accumulated dose is controlled by the exposure time. All the tested samples have been coiled in a spiral shape to avoid possible overlapping between the different coil layers and shielding effects. The beam is characterized by a homogeneity better than 5% for a radius of 7 cm at a dose rate of 100 mGy/s. Samples under test are connected to light sources (Ocean Optics DH-2000-BAL) and detectors (QE65000 spectrometer for the UV-Vis measurements and the NIR512 spectrometer for IR measurements,

both from Ocean Optics). The RIA spectra have been acquired with an integration time of ~1 s during the whole irradiation run. The experimental setup is presented in Figure 3.11.

More difficult was the evaluation of the total accumulated dose of the fiber at LNT [87]. For these kind of measurements, the FUT were folded inside an isolated container filled with liquid nitrogen. After the full thermalization of the fiber sample the experiment was started. At RT, the accumulated dose was of the order of 200 $Gy(SiO_2)$ at a fixed dose rate of 100 mGy/s. At LNT measurements, because the liquid nitrogen used to cool down the fiber evaporates, its X-ray shielding effect is influenced.

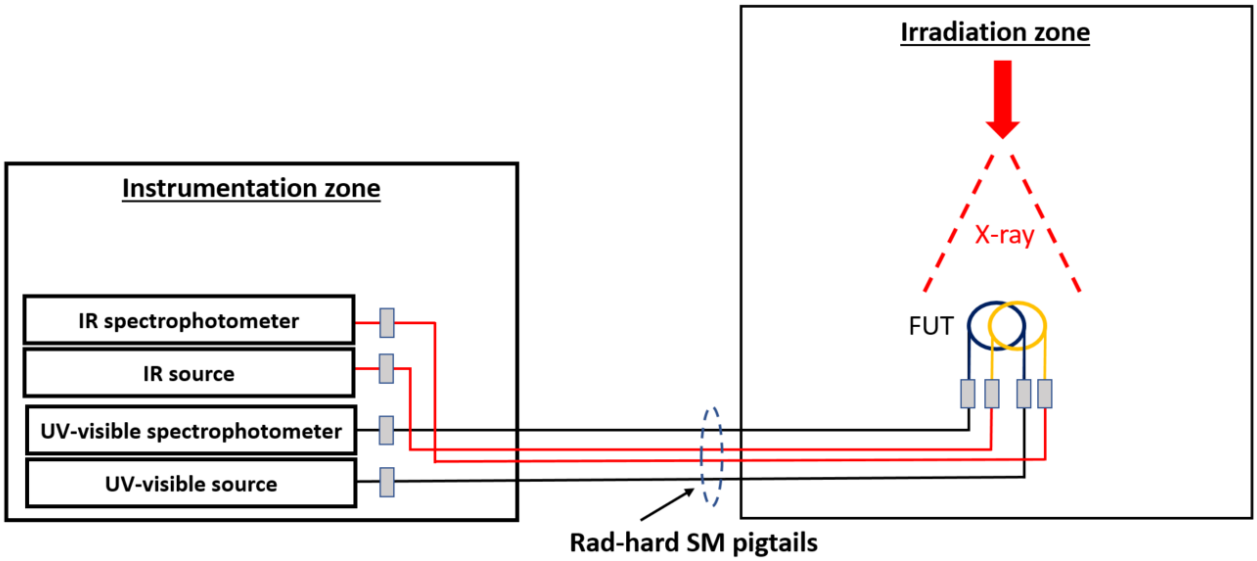

Figure 3.11. Online RIA experimental setup for the steady-state X-ray irradiation: canonical samples are coiled inside the region in which the X-ray beam is homogeneous (within the 5%), ensuring the same dose rate and dose deposition over the whole fiber length.

Then, notwithstanding the sample is maintained at a constant temperature during and after the irradiation, in liquid nitrogen, however the decreasing level of nitrogen above the sample causes a slight time dependence of the dose rate on the sample. To have an experimental and reasonable estimation of the dose and dose rate experienced by the samples under test at LNT, we have coupled each measurement with the one of the P-doped single-mode OFs in the infrared. Indeed, it is well known that P-doped fibers at RT represent one of the most promising photonic device employed in dosimetry [4], [100]–[102], [178]. This because the induced absorption in the near-IR, mostly driven by the P1 defect (see chapter 4 for further spectroscopic details about this

defect), is totally linear at $1550\ \mathrm{nm}$ with the dose (until $\sim 500\ \mathrm{Gy}$), dose rate independent and not affected by any recovery effect after irradiation.

Since it was recently established [101] that these properties are also valid at LNT, the P-doped OF is still an efficient dosimeter at LNT. Consequently, we have found an easy procedure to estimate the total accumulated dose by fibers immersed in liquid nitrogen. As already mentioned above, in absence of the liquid nitrogen shielding effect, the RIA level induced in a P-doped OF at LNT and at $1550\ \mathrm{nm}$ linearly increases with the accumulated dose, independently on the dose rate and with the same rate at both RT and LNT. Since nitrogen implodes from the container, the dose rate undergone by the sample increases with time. By coupling the measurements on the P-doped fiber with one of the fibers under test, we can have in real time an accumulated dose estimation on the fiber under test during the run [87]. Defining the

$$\mathrm{Dose\ (LNT)} = \frac{\mathrm{RIA_{P-doped}(LNT)@1550\ nm}}{\mathrm{C}} \tag{3.1}$$

as the accumulated dose on the different P-fibers, $\mathrm{C} = 0.0036\ \mathrm{dBm^{-1}Gy^{-1}}$ is the dose sensitivity of the P-doped OF at RT, and RIA (LNT) is the P-fiber RIA at $1550\ \mathrm{nm}$ recorded at LNT. At this point, it is possible to estimate the total dose experienced by both fibers (the P-doped and the FUT fibers), comparing the P-doped fiber spectra measured at LNT with their counterparts acquired at RT. The first derivative of equation 3.1 will give us the dose rate experienced by the fibers at LNT. The validity of the process is illustrated in Figure 3.12, via the comparison of the dose rates between the P-doped fibers measured at RT, with the ones measured at LNT following the above described process: LNT a (red curve), LNT b (blue curve), and LNT c (magenta curve) are associated with the irradiation runs of different investigated optical fibers at LNT. This comparison confirms that the dose calibration is repeatable from one run to another. In these conditions, the air equivalent dose rate of MOPERIX, for LNT measurements, was fixed at $530\ \mathrm{mGy/s}$ to ensure a dose rate of $\sim 100\ \mathrm{mGy/s}$ on the samples.

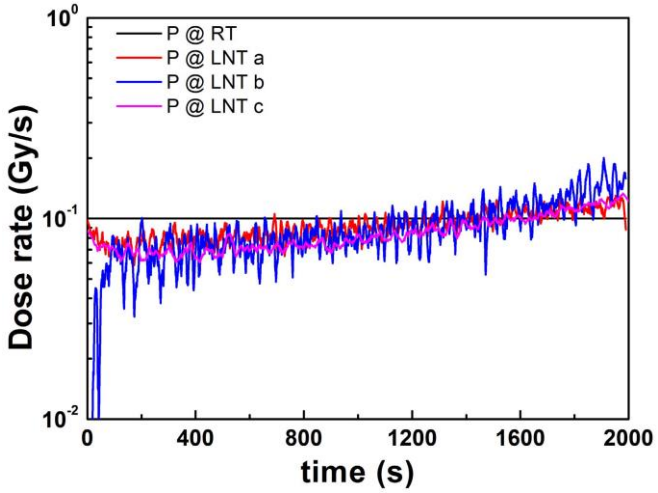

Figure 3.12. Comparison of the dose rates experienced by the P-fiber at RT and LNT. LNT a, LNT b, and LNT c are the RIA measurements with these P-fibers acquired during the runs devoted to the characterization of the other fibers in different runs at LNT, highlighting the repeatability of the adopted method. Figure taken from [87].

3.6. Spectrophotometer CARY 5000

The Cary 5000 (Agilent technology) is a UV-Vis and near-IR spectrophotometer with high performance in the 175-3300 nm spectral domain. It was employed to measure the absorption spectra of the investigated bulk samples **[179]**. Since it is a single beam spectrometer, it is necessary to register the reference transmitted spectra before the one of the sample exposed to the radiation. The instrument is equipped with a tungsten halogen source for the visible/near IR spectral range and a deuterium source for the UV. The UV-Vis detector is a high performance R928 photomultiplier tube, while the near-IR detector is an electrothermally controlled lead sulfide photocell. The absorption spectrum is acquired as function of the wavelengths (nm), then converted in energy (eV) via the relation:

$$\mathrm{E(eV)} = \frac{1240}{\lambda(\mathrm{nm})}. \tag{3.2}$$

In the all performed measurements, the following well-known relation was respected:

$$\frac{\mathrm{BW}}{\mathrm{SS}} > \mathrm{DTR}, \tag{3.3}$$

where BW is the bandwidth to select the wavelength on the sample, SS the scanning speed and DTR is the detector time response, to have the best signal-to-noise ratio without deforming the observed absorption bands.

3.7. PHAROS fs-laser

The laser used for the high intensity femtosecond pulses and pump-probe measurements in Saint-Etienne is the PHAROS (Light Conversion) femtosecond laser based on a Yb:KGW (Ytterbium-Doped Potassium Gadolinium Tungstate) with a fundamental centered at 1030 ± 10 nm [180]. The PHAROS offers a set of tunable parameters such as the pulse duration (190 fs – 20 ps), the repetition rate (single pulse to ~600 kHz) and pulse energy (up to 2 mJ). The whole system [181], shown in Figure 3.13, is composed of an oscillator which employs a Kerr lens based mode-locking and chirped mirrors for the GVD. The oscillator provides ~50 fs pulses driven into the stretcher: these are broadened in time up to 200 ps, and then guided into the regenerative amplifier (RA). After the RA, the pulse is recompressed in order to return as an ultrashort pulse becoming a 200 fs pulse at the selected energy and repetition rate. Furthermore, it is also possible to exploit the harmonic of the PHAROS's fundamental employing the HIRO harmonic generator (Light Conversion) which provides the second, the third and the fourth harmonic, allowing us to generate femtosecond pulses at 515 nm, 343 nm and 257 nm, respectively. The HIRO has also integrated a half wave plate to control the output power.

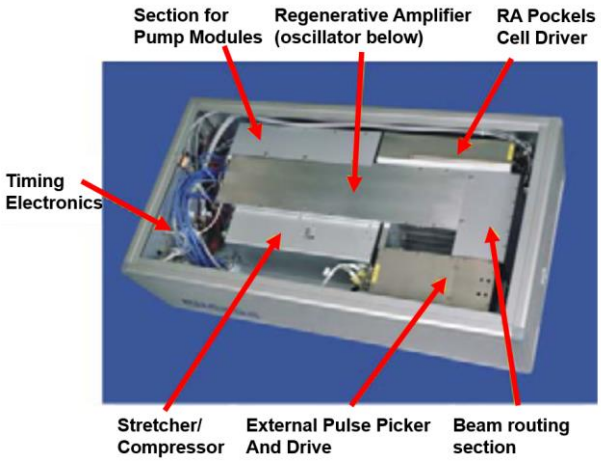

Figure 3.13. Scheme of the femtosecond CPA laser system PHAROS. Figure adapted from [181].

3.8. AEROTECH setup for waveguides inscription

The translation of a focused single laser spot into a transparent dielectric material has the ability, under certain experimental conditions, to induce both positive and negative refractive index changes, allowing various 3D photo-inscribed optical components [7]. For this reason, it is mandatory to study the interaction between the high intensity femtosecond laser and the silica material, which represents a transparent dielectric archetype. Depending on the laser interaction regime, it is possible to induce different types of modification by controlling the energetic dose, pulse duration, repetition rate and focusing conditions. While the pulse duration could be controlled by the PHAROS laser parameter setting, the deposited energy and the focusing condition depend on the setup characteristics: the dose (fluence) is controlled by the irradiation time per μm in the sample, associated to the sample scanning speed, while the latter is controlled by the objective performances in transversal geometry. In the following paragraphs we will describe the experimental setup used to inscribe waveguides in bulk silica volume.

3. 8.1 Experimental setup

As depicted in Figure 3.14, the two laser wavelengths, centered at 1030 nm and 343 nm, respectively, are generated by the PHAROS femtosecond laser (the fundamental) coupled with the HIRO harmonic generator (the third harmonic) with a pulse duration of ∼200 fs and a repetition rate of 100 kHz.

Laser pulses are focused ∼200 μm below the bulk surface by microscope objectives with a nominal NA of 0.42 (Mitutoyo M PLAN NIR) and 0.5 (Thorlabs UV coated lens), for the laser wavelengths at 1030 nm and 343 nm respectively. The sample is aligned perpendicular to the laser direction using a CMOS camera with a white light to visualize the sample surface, in reflective configuration (using a beam splitter (BS) and a mirror (M) to drive the light into the sample surface and the CMOS camera). A dichroic (DM) mirror is employed to avoid damage on the CMOS coming from the scattered laser light. A polarizer (P) coupled with a half-wave plate (HWP) drove the power control. By moving the sample, thanks to a XYZ computer-controlled stages (AEROTECH), it is possible to monitor the amount of pulses on each material local zone. The dynamic damage, represented basically by the effective number of interacting pulses, will depend (at fixed energy per pulse) on the sample translational speed and the dimension of the focal region, following the relation state by equation 3.4 [7]:

$$N_{eff} = RR\frac{L}{nv} \tag{3.4}$$

where RR is the laser repetition rate, n is the sample refractive index, v is the velocity of the translation stage movement and L is the interaction length.

It is possible to set the experimental setup with a sample parallel (longitudinal writing) or perpendicular (transverse writing) movement compared to the laser light propagation direction (optical axis). In the former case, the induced damage replicates the laser beam symmetry during the writing phase with respect to the optical axis, resulting in a circular damaged area but giving problems on the dimensions of the induced traces, since it is limited by the focal length of the objective. While in transverse writing there are no problem related to the traces' length, but the geometry of the induced damage is elliptical along the laser propagation direction, less favorable for the mode propagation along the inscribed waveguides, compared to a circular waveguide [7].

In the present work, the waveguide inscription was performed in transverse geometry and a slit was employed to guarantee a cylindrical profile of the induced material modifications [182], [183]. Indeed, thanks to the beam diffraction along its circular section, it is possible to enlarge it along such direction compensating the limitation of the transversal configuration. Figure 3.15 reports the damage zone as function of the slit width: the damage acquires a circular profile when the slit width decreases. By moving the sample, we have performed the inscription of a 9 mm long waveguide with 8 passes. In addition, to evaluate the impact of the laser wavelength choice on the inscription process, we analyzed the waveguides characteristics as a function of the scanning speed (100 µm/s, 300 µm/s and 600 µm/s), the incident wavelength as well as the energy per pulse (1.20 µJ/pulse and 1.30 µJ/pulse @ 1030 nm and 0.20 µJ/pulse and 0.35 µJ/pulse @ 343 nm).

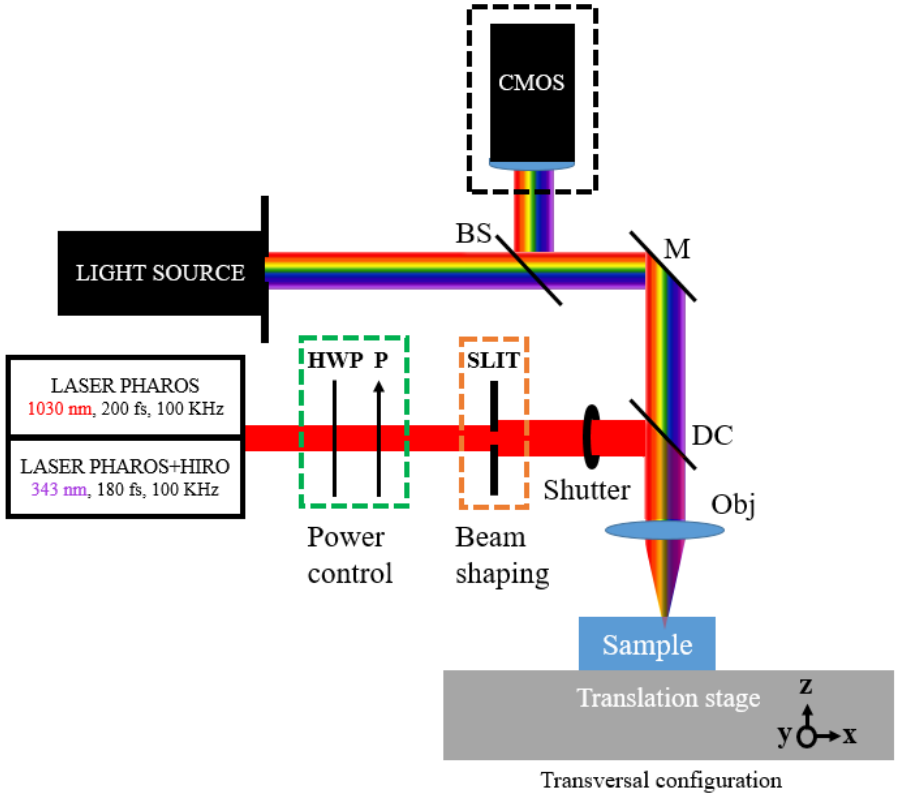

Figure 3.14. Experimental setup used to inscribe waveguides in bulk silica.

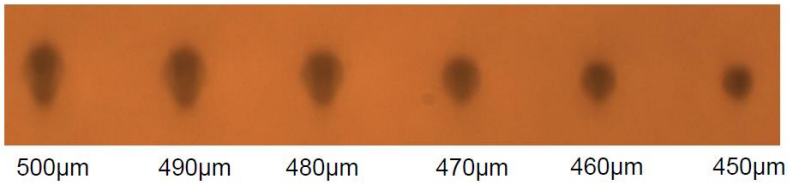

Figure 3.15. Slit shaping procedure to find the best slit width and to achieve a circular damage in the focalized region, figure obtained using phase contrast microscopy technique.

3. 8.2 Δn estimation

To evaluate the induced positive refractive index change, we have estimated the numerical aperture (NA) of the inscribed waveguides through the formula reported in equation 3.5

$$\mathrm{NA} = \frac{\mathrm{W}(\mathrm{d}_2) - \mathrm{W}(\mathrm{d}_1)}{\sqrt{[\mathrm{W}(\mathrm{d}_2) - \mathrm{W}(\mathrm{d}_1)]^2 + (\mathrm{d}_2 - \mathrm{d}_1)^2}}, \tag{3.5}$$

where $\mathrm{W}(\mathrm{d}_1)$ and $\mathrm{W}(\mathrm{d}_2)$ are the light mode sizes at the waveguide output at d_1 (near field) and d_2 (far field) distances respectively, with $\mathrm{d}_2 > \mathrm{d}_1$.

The experimental setup used for the refractive index change Δn evaluation via the NA determination is reported in Figure 3.16. The refractive index change is estimated by reversing equation 3.6:

$$\mathrm{NA} = \sqrt{2\mathrm{n}\Delta\mathrm{n}} \tag{3.6}$$

with n the amorphous silica refractive index and Δn the induced refractive index change.

The experimental setup (Figure 3.16) used to measure Δn is composed of a white light source (range from 350 nm to 2000 nm), generated by nonlinear processes within a fiber, injected into the waveguide. The output near and far field light modes are acquired using an objective (Mitutoyo M PLAN APO) focusing the light into a CMOS camera (Thorlabs DCC1645C) at the distances d_1 and d_2, respectively. The above described procedure allows us to obtain a Δn which is basically an average value over the visible range.

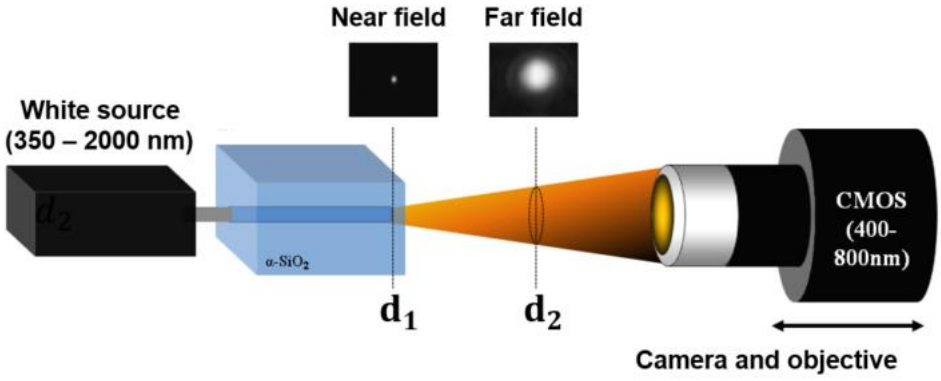

Figure 3.16. Experimental setup used to estimate the laser induced refractive index change Δn. Figure adapted from *[184]*.

3.9. ARAMIS micro-Raman

The local structural modifications and the defects induced by the femtosecond pulses irradiation in the studied materials were characterized with an ARAMIS micro-confocal spectrometer (Horiba Jobin-Yvon). The system is equipped with:

- Four CW laser excitations: a HeNe line at 633 nm (1.96 eV); an Ar+ at 488 nm (2.54 eV); a HeCd at both 442 nm (2.81 eV) and 325 nm (3.82 eV);
- Several gratings (150 l/mm, 600 l/mm, 1200 l/mm and 2400 l/mm);
- 3 computer-controlled micrometer translation stages;
- Several OD attenuators to adapt the laser probe power on the sample under test and avoid additional modifications;
- A microscope with several objectives ×10, ×40, ×50 and ×100 (for UV and visible spectral domains);
- A video camera for the sample's direct-imaging;
- CCD camera for the spectral detection;

- The overall system is well adapted to both Raman and luminescence analysis with a micron spatial resolution.

The integrated confocal micro-spectrometer ARAMIS was used in a backscattering configuration [185]. In Figure 3.17 is reported the ARAMIS integrated confocal system scheme. The objectives ($UV - 40\times, 10\times, 50\times$ and $100\times$) drive the focused light into the sample with a beam size depending on the objective choice. For our purpose, we employed the He-Cd laser (325 nm) acting as the probing laser for both the PL and Raman measurements. The choice of a confocal diaphragm was made in order to ensure a high signal but with the ability to preserve the observation of local changes in the bulk. Sample was mounted on an XYZ controlled stage (micrometric precision) and the beam focalized with a $40\times$ UV objective. The microRaman parameters were chosen to achieve a spatial resolution (in the XY plane) of $\sim$5 µm thanks to a confocal pinhole of 50 µm of diameter. All the Raman data have been acquired with 2400 lines/mm grating and a spectral resolution of $\sim 5\ cm^{-1}$.

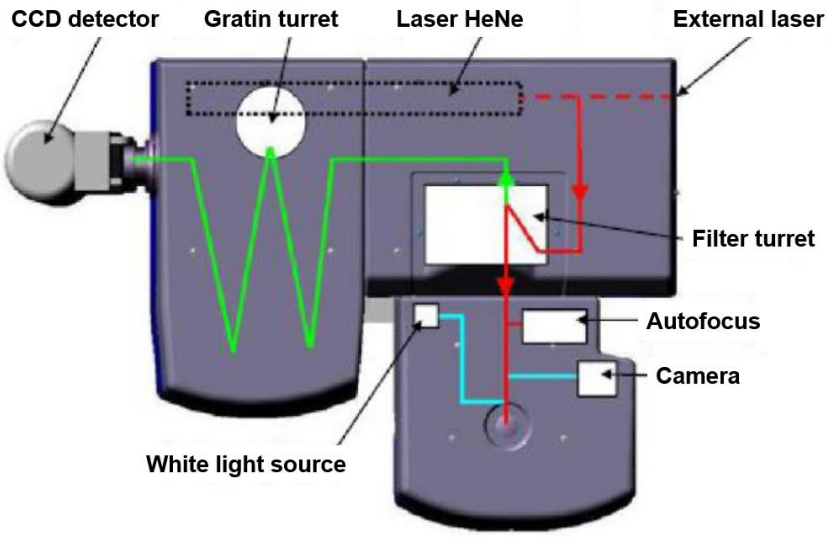

Figure 3.17. Schematic representation of the light optical path in the ARAMIS integrated confocal system.

It is important to keep in mind that for PL measurements, the relation between wavelengths and the intensities is not linear, but follows the relation described by equation 3.7:

$$I(E) \propto I(\lambda)\lambda^2. \qquad (3.7)$$

3.10. ZEISS AXIO microscopy

For the damage induced by the high intensity femtosecond laser, the refractive index contrast was estimated using a negative phase contrast microscopy in transmission configuration. Basically, an Axio cam MRC5 CCD camera (2574×1936 pixels, with pixel size of 4.4×4.4 μm^2) is mounted on as Axio imager M1m microscope manufactured by ZEISS for a phase contrast microscopy image acquisition [186]. It is important to note that a negative PCM provides refractive index contrast, between the damaged area and the pristine surrounding, with black colors if the irradiated area has a higher refractive index (then $\Delta n>0$) and in white the negative ones (then $\Delta n<0$).

3.11. OBR 4600

The waveguide attenuations at 1550 nm were evaluated by using an optical backscatter reflectometer (OBR 4600) from Luna technologies [187], which records the backscattered Rayleigh signal along the waveguide length by sweeping the laser wavelength in a small range of ~40 nm centered at 1550 nm. This equipment achieves spatial resolution of ~40 μm along the probe beam propagation.

3.12. PL online setup

In order to deeply study the phenomena occurring during and after the fs laser exposure, especially those related to the induced defects, we have developed a homemade experimental setup dedicated to the online characterization of the photoluminescence signatures of optically active defects under fs laser irradiation. Figure 3.18 illustrates the experimental setup. The sample alignment is associated to a LED light source (collinear to the laser path) from Thorlabs, coupled to a CMOS camera (Thorlabs DCC1645C) in back reflection configuration, giving the possibility

to zoom on the sample surface. A sample holder with various orientation degrees of freedom allows us to set the sample perpendicular to the beam light.

The irradiation is performed using the laser PHAROS fundamental signal at 1030 nm (pulse time width ~200 fs) and its third harmonic centered at 343 nm (pulse time width ~200 fs), both at 1 kHz repetition rate, in transversal geometry. The power is controlled by using a half wave plate (HWP) coupled with a polarizer. Focusing of the beam on the sample is ensured by an objective (Obj) with a nominal numerical aperture NA = 0.42 (Mitutoyo M PLAN NIR) and NA = 0.5 (Thorlabs UV coated lens) for the IR and UV laser beams, respectively. During the irradiation, the induced PL is acquired, perpendicularly to the laser path, by a high performance Hamamatsu spectrometer, in the spectral range between 320 nm and 1070 nm. The chosen integration time is ~100 ms: every measured spectrum is an average on 100 pulses, with a total accumulated pulses of $\sim 10^4$ per fixed power. The exposure time was monitored by a controlled beam-blocker which is programmed to stay open for 10 s. The acquired spectra are not corrected for the system response. The static damage (since the sample is not moving during the irradiation) indeed is controlled by the number of pulses acting on the material. In order to do not overlap the signal linked to the induced defects' PL and the strong plasma-related emission, the detector is focused slightly out of the objective focal region (which dominates the plasma contribution [188]–[190]) but in an upper position along the laser's direction. The right position is driven by the optimization of the 650 nm signal. After the irradiation at a fixed energy, the sample was moved thanks to a motorized translation stage (THORLABS MTS25-Z8), to measure the PL for the next laser power. The distance between two adjacent irradiated regions is ~50 μm.

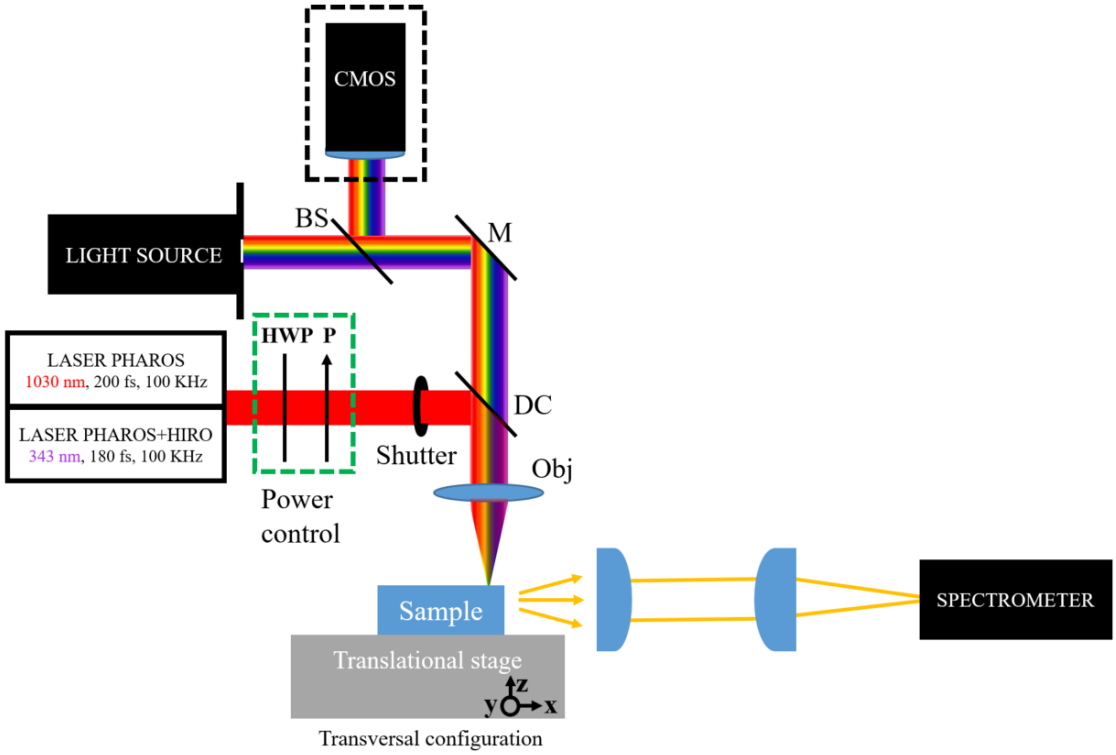

Figure 3.18. Experimental setup devoted to the acquisition of the on-line PL induced by the fs irradiation.

3.13. Pump-probe setup in Saint-Etienne

The Laboratoire Hubert Curien is equipped with a versatile pump-probe experimental setup to investigate the ultrafast dynamics of molecular systems, such as chromophores, chemical reactions and point defects. The global setup is reported in Figure 3.19.

The whole system is composed of the laser source, the PHAROS, delivering ~6 W femtosecond pulses, divided into 10 % and 90 % of the power by a beam splitter (BS in Figure 3.19). The first beam (10 % of power) is directly driven into the HARPIA [149] ultrafast spectroscopy system to generate the white light, while the latter (90 %) is used to generate the laser pump inside the OPA (composed of the ORPEHUS system and the two LYRA harmonic generators) [154]. After the pump-probe measurement, the super continuum transmitted light after the sample is guided into the detector and acquired [191]. In the following steps we will detail the OPA and HARPIA systems.

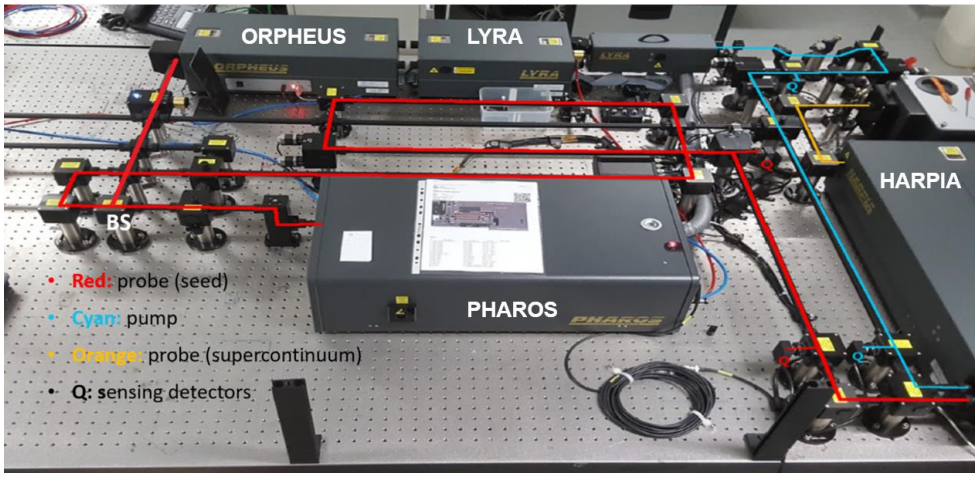

Figure 3.19. Experimental setup for ultrafast pump-probe measurements in Saint-Etienne: the red line is the fundamental signal used as seed to generate the pump through the OPA (ORPHEUS+LYRA) and the white light inside the HARPIA ultrafast spectroscopic system, in cyan the pump after the OPA driven inside the HARPIA and in orange the super continuum light that already passed from the sample toward the detector.

3. 13.1 OPA

Coupling the laser Pharos with an OPA (Light Conversion, composed of three sub-units), generate a tunable pump laser in the [210 nm – 20 μm] spectral range [154]. As already explained in chapter 2, the non-linear process requires the interaction of two beams in a β-BBO crystal (anisotropic crystal): a pumping beam (ω_p) and a broadband seed generating an output pump beam at ω_s (under the condition $\omega_s < \omega_p$).

The pump amplifies the seed intensity generating a new beam at ω_i, the idler, when the following conditions are respected [124]:

- $\omega_p = \omega_s + \omega_i$ energy conservation ($\Delta E = 0$)
- $n_p\omega_p = n_s\omega_s + n_i\omega_i$ phase matching condition ($\Delta k = 0$)

Considering that the seed is a broadband pulse, changing the orientation of the nonlinear crystal allows amplifying different wavelengths which fulfill the phase matching condition.

The first sub-unit is the ORPHEUS optical parameter amplifier, delivering a tunable laser in the [630 nm ÷ 2600 nm] wavelength range (comprising both the signal and idler). The LYRA system produces lower wavelengths through the SHG process (starting from the one generated by the ORPHEUS) and higher ones through the different frequencies generation (DFG, never used in the present work), enlarging the possible tunable range from 315 nm to 20 μm. A second LYRA system can be used to extend the wavelength generation in deeper UV domain, through the SHG employed from the first LYRA system. Therefore, the entire equipment can provide pump laser in the [210 nm ÷ 20 μm] spectral range. The PHAROS+OPA architecture is reported in Figure 3.20.

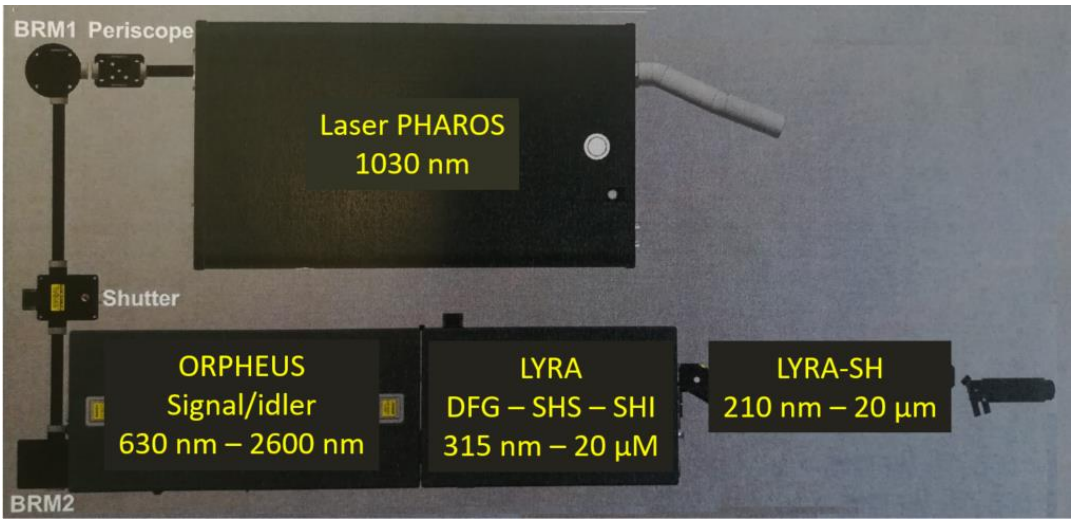

Figure 3.20. PHAROS+OPA complex: the fundamental is generated by the PHAROS. After the ORPHEUS the system generates signal/idler photons from 630 nm÷2600 nm. The LYRA extends the wavelength range through the SH of the signal (SHS), the SH of the idler (SHI) and the DFG, leading to a tunable laser from 315 nm to 20 μm. The last component enlarges the spectral domain via the SHG to 210 nm÷20 μm.

OPA: ORPHEUS

The ORPHEUS system is a two-stage optical parametric amplifier employed to generate a white light continuum. The fully computer-controlled system is equipped with translation and rotation stages providing fast automated wavelength tuning. The basic configuration consists of several sub-units [154]:

- White light continuum generator
- Second harmonic of the pump beam generator
- First amplification stage (non-collinear two pass pre-amplifier)
- Second amplification stage (collinear power amplifier).

These sub-units are arranged as shown in Figure 3.21.

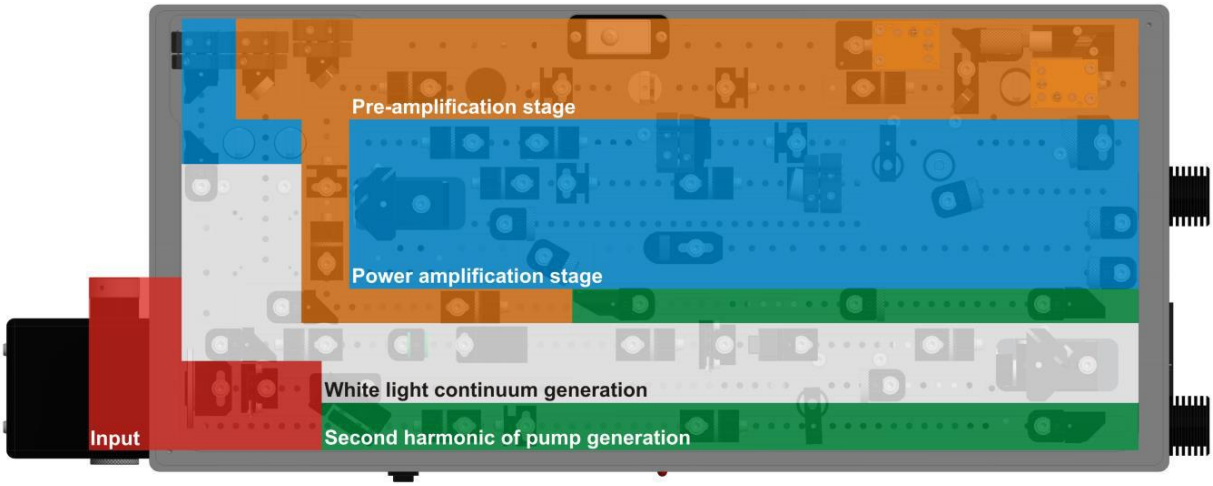

Figure 3.21. Different sub-units inside the ORPHEUS. Figure taken from [154].

In the following we will describe the laser pump generation in the ORPHEUS system, referring to the detailed scheme reported in Figure 3.22. Once the 1030 nm fundamental laser pump, provided by the PHAROS, is driven into the ORPHEUS (pink line Figure 3.22), a polarizer P1 reflects most of the pump beam energy for SHG path and transmits ~ μJ for white light continuum generation. The beam transmitted through the polarizer (smaller fraction) is used for the seed white light generation (white line), while the reflected beam will be used for the amplification stages (green line). After the P1 polarizer, to generate the seed white light, the beam is focused into the white light continuum generation substrate by the lens L1. In the meanwhile, the major part of pump beam is used for the SHG, and will be used as pump beam in the generation of the signal/idler light. The lens L4 focuses both the WLG and the SH beams into the Crystal 1, where amplification occurs. The wavelength of the amplified pulse is selected by tuning the Crystal 1 angle, reaching

the phase-matching condition with a particular wavelength of the seed white light. After Crystal 1 both pulses travel above the first pass beams and this time they travel through the C1 compensator crystal. The amplified beam travels above the M4 mirror and onward to the power amplification stage. The amplified beam (seed) after the first amplification stage travels through two delay plates DP2 and DP3, used to fine-tune the temporal overlap of seed and pump pulses at the Crystal 2. Dichroic mirror DM2 transmits the seed and reflects the pump beam. After amplification at the nonlinear Crystal 2 (The pump beam reflected by polarizer P2), parametric radiation is separated from the pump beam by mirror DM3 and is emitted from the ORPHEUS output port A.

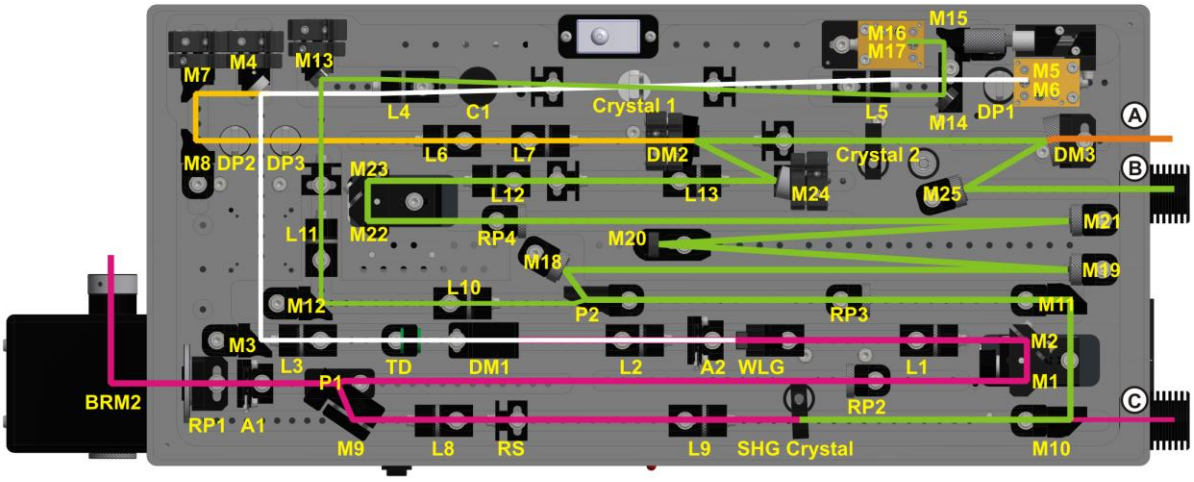

Figure 3.22. Detailed scheme of the ORPHEUS optical parametric amplifier unit. The symbols are: iris aperture (A), compensator (C), amplification crystal (Crystal), dichroic mirror (DM), delay plate (DP), lens (L), mirror (M), polarizer (P), half-wave plate (RP), reflection shield (RS), second harmonic generation crystal (SHG Crystal), temporal dispersion medium (TD), white light generation substrate (WLG). Figure taken from [154].

OPA: LYRA harmonic generator

LYRA is designed to SHG of signal/idler, fourth harmonic generator (FHG) of signal/idler and higher wavelength beams by using the residual pump beam (residual of the beam utilized for the SHG in the ORPHEUS, with the C output). The scheme of the LYRA is reported in Figure 3.23. The two processes used to generate the pump wavelength in the present work are basically:

- SHG: signal/idler doubling process at the ORPHEUS output (Crystal stage 1)
- FHG: signal/idler doubling process at the output of the LYRA-SH (Crystal stage 3), after the SHG in the crystal stage 2.

It is important to know that with this system it is possible to generate even higher wavelength by the DFG: using the optical parametric amplification process, pumping with the residual 1030 nm and the ORPHEUS idler as seed. LYRA crystal stage 1 is used to generate wavelengths between 2 μm and 5 μm and LYRA crystal stage 2 is devoted to the 5 μm ÷ 20 μm spectral domain.

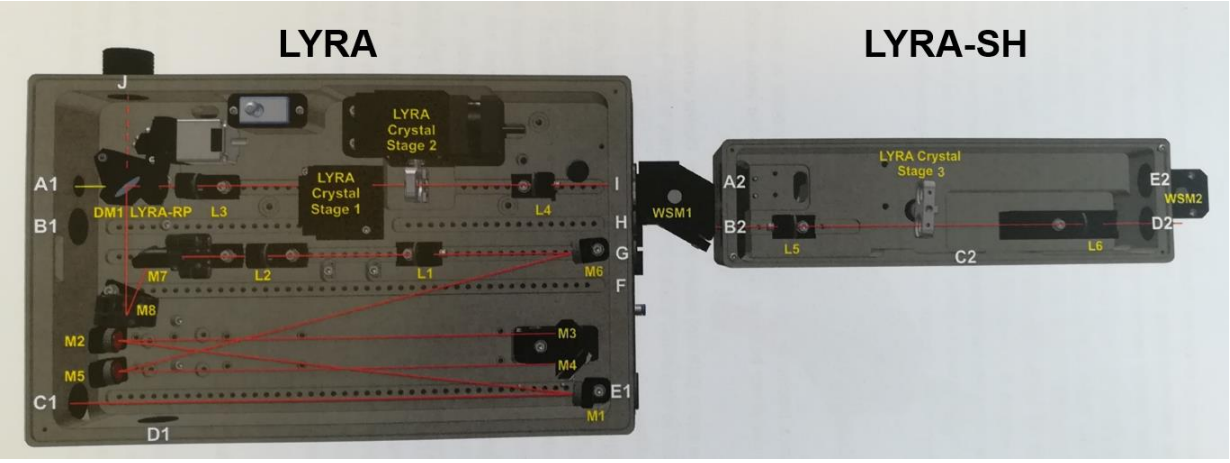

Figure 3.23. Detailed scheme of the LYRA units. The symbols are: dichroic mirror (DM), lens (L), mirror (M), half-wave plate (LYRA-RP), non-linear Crystal stage (LYRA Crystal stage) and wavelength separating mirror (WSM). Figure taken from [154].

OPA: wavelengths separator

Due to the collinear nature of amplification, signal and idler beams both exit at the same position and direction. The beams can be separated by using wavelength separators (WS). Each WS consists of two dielectric mirrors with high reflectivity coatings for a specific wavelength region which separate wavelengths on the base of their polarizations (Figure 3.24). The output polarization is reported in table 3.4.

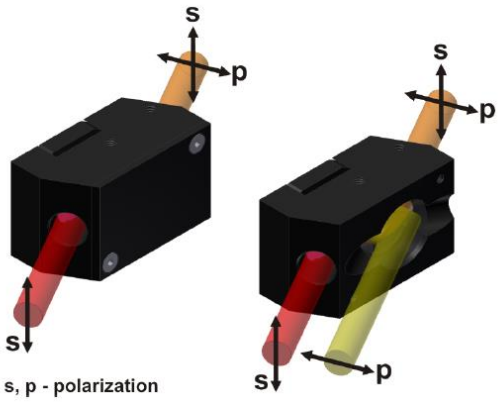

Figure 3.24. Wavelengths separator which separates the beams on the base of their polarizations. Figure taken from [154].

Table 3.4. Output polarization in correspondence of the reflected special range.

Range of reflected wavelengths	Interaction	Polarization
$620 - 1030$ nm	SIG	H
$1030 - 3041$ nm	IDL	H
$310 - 515$ nm	SH-SIG	H
$515 - 630$ nm	SH-IDL	H
$420 - 515$ nm	SH2-SIG	H
$520 - 630$ nm	SH2-IDL	V
$210 - 257.5$ nm	SH-SH2-SIG	H
$257.5 - 315$ nm	SH-SH2-IDL	H
$2200 - 5000$ nm	DFG-IDL	V
$4000 - 20000$ nm	DFG2-IDL	H

3. 13.2 HARPIA system

Inside the ultrafast laser absorption spectrometer HARPIA (Light Conversion) **[149]** we have two guided beams: the pump beam, which arrives just after the OPA, and the 10% of the power at the PHAROS output, used to generate the white light and then the probe beam (Figure 3.25).

Once the pump wavelength is chosen, the signal is then chopped at 75 Hz and a beam splitter is used to drive a small fraction of the pump beam on a photodiode to discriminate the pumped and un-pumped absorption spectra. In the pump path, a Berek's compensator controls the relative polarization between pump and probe signals. This component was never used in our measurements, maintaining the laser output polarization.

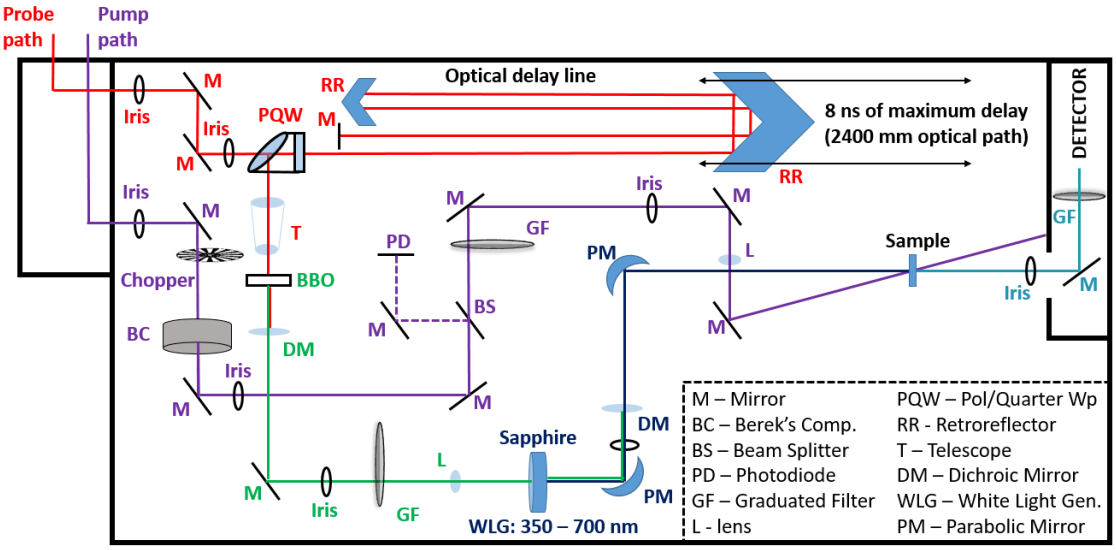

Figure 3.25. Detailed scheme of the HARPIA ultrafast absorption spectrometer.

A filter is placed along the pump path to monitor the power control and a lens (focal length of 200 mm) focuses the beam on the sample before being stopped by a beam blocker. The whole pump path is the violet line in Figure 3.25.

The remaining 10% output power from the PHAROS is guided directly into the HARPIA system (red line in Figure 3.25). The optical delay line is installed in the probe path, before the white light generation, allowing us to control the time delay between the two beams up to a maximum of ~8 ns.

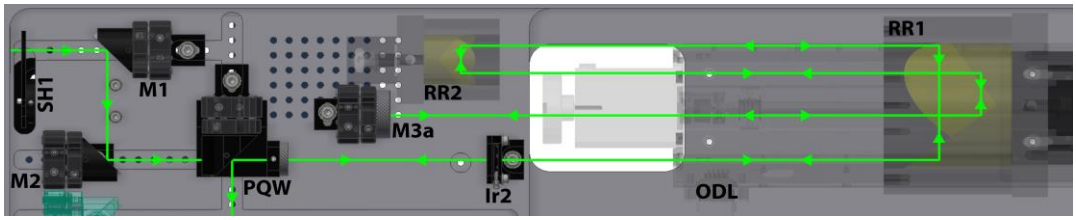

Figure 3.26. Detailed scheme of the optical delay stage in the HARPIA ultrafast absorption spectrometer. Figure taken from [149].

Indeed, the beam is reflected toward a thin film polarizer/quarter-wave plate unit, which leaves the p-polarized beam to pass. A quarter-wave plate turns the outward beam polarization to circular. This circularly polarized beam then enters the optical delay stage (ODL, Figure 3.26). After completing passage between the retroreflectors (RR) RR1 and RR2, the beam hits mirror M3a that sends the beam backwards along its original path. After making an additional passage between the two retroreflectors, the beam passes once more through the quarter-wave plate, which now turns the circularly-polarized beam into an s-polarized one. The total optical path in this configuration is 2400 mm (8 ns). After the ODL, the beam intensity is increased with a telescope, before to generate the white light, decreasing the beam dimensions. Indeed, depending on the needed investigation range we can generate a white light starting from the fundamental of the PHAROS (1030 nm) producing a white light from 550 nm to 900 nm (then a visible near-IR spectral range); or if necessary (as in our case) to investigate the UV/visible spectral range, to use the fundamental SH to produce a 515 nm femtosecond beam with a β-BBO (Beta Barium Borate) Crystal. The probe beam is generated by focusing 515 nm (green line in Figure 3.25) femtosecond pulses on a 3 mm thick Sapphire crystal, which delivers a white light between 350 nm and 650 nm, subsequently focused onto the sample by a parabolic mirror (blue line in Figure 3.25). With a graduated filter and an iris, we control the laser intensity through a stable filament in the Sapphire crystal. The white light signals at the two possible spectral ranges are reported in Figure 3.27.

Generally, the pump and the probe are both focused on the sample with beam spot diameters around 100 μm and 70 μm, respectively.

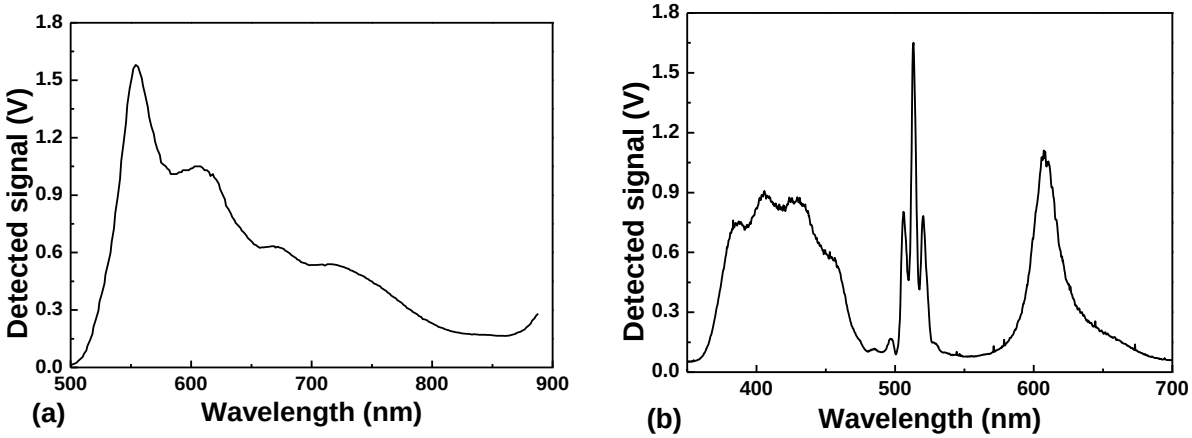

Figure 3.27. Generated white light in the a) visible/near-IR and b) UV/visible spectral range.

The transmitted probe light is collected using the imaging spectrograph (Kymera 193i, OXFORD instruments) [191], where it will be decomposed in its spectral components with a grating. This spectrograph is equipped with a NMOS linear image sensor (HAMAMATSU S8380-256Q), whose spectral resolution is ~1.7 nm, acquiring 32 pulses/spectrum (0.5 ms of integration time). Every spectrum is the average of 2500 spectra and 5 scans were performed in the whole investigated window under these experimental conditions. The imaging spectrograph is reported in Figure 3.28.

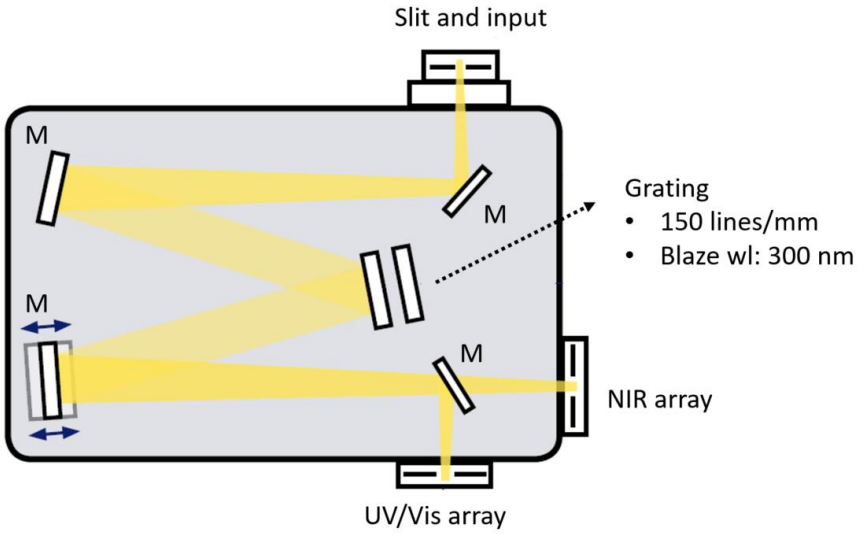

Figure 3.28. Detailed scheme of the imaging spectrograph Kymera 193i. Figure taken from [191].

3.14. Pump-probe setup in Palermo

Part of this Ph.D. was devoted to learn, practice and start the NBOHC's photocycle investigation at the University of Palermo in the laboratory of the ATeN Center (Advanced Technology Network Center). In the following, I will describe such transient absorption setup, which is different and complementary to the one installed in Saint-Etienne. Indeed, even if we cannot tune continuously the pump wavelength, this setup is characterized by a faster resolution time, allowing us to probe dynamics under 200 fs (time resolution of the Saint-Etienne's system) and by a single pulse revealing detector.

3. 14.1 Spectra physics Solstice-Ace

The employed laser is a 5 kHz Ti:sapphire femtosecond amplifier (Spectra Physics Solstice-Ace) [192]. The whole system is composed of a Mai Tai seed laser [193], a pulse stretcher, a regenerative amplifier, a pulse compressor and a Empower pump laser (15 W) which pumps the amplifier. First, the Mai Tai laser provides 35 fs pulses at a repetition rate of 80 MHz. The

generated pulses are driven into the stretcher, being broadened in time from 35 fs to 500 ps, and then directed into the Ti:sapphire rod of the amplifier. After the pulse amplification through multiple passages of the seed pulse through a Ti:Sapphire rod, where the Ti:sapphire rod is pumped at 5 kHz, the pulse is recompressed in order to have in return an ultrashort pulse. In this laser, the CPA produces a train of amplified pulses decreasing down the repetition rate from 80 MHz to 5 kHz. The output signal after the compressor is nominally a 50 fs pulse peaking at 800 nm (FWHM = 30 nm). The beam power is 3.5 W, therefore the energy per pulse is 700 μJ/pulse.

3. 14.2 Transient absorption setup

The whole experimental setup is reported in Figure 3.29: The 800 nm beam (red line in Figure 3.29) with a temporal pulse width of ~50 fs (~350 μJ/pulse) at 5 kHz is divided by a BS into two beams of 80 % and 20 % powers, respectively. The 80 % power is used as pump beam: after the BS its intensity is increased by a telescope and chopped at a frequency of 500 Hz. Therefore, it is guided into the delay stage (maximum delay~200 ps). Since we are interested to pump the sample in the UV domain, it is necessary to generate the third harmonic of the fundamental (800 nm), having in this way a 266 nm femtosecond pulses pumping laser. In order to do that, we have first generated the second harmonic by the use of a β-BBO, obtaining at the crystal output a horizontal polarized signal at 800 nm and a vertical polarized beam at 400 nm (cyan line in Figure 3.29). To generate the third harmonic we have summed the 800 nm and 400 nm pulses: using a retardation plate we compensate the delay between the two pulses into a second β-BBO, and since both pulses need to have the same polarization we have employed a half-wave plate to turn the 800 nm signal to a vertical polarization. In this way, both the vertical polarized 800 nm and 400 nm femtosecond pulses will arrive at the same time onto the second β-BBO generating in this way a horizontally polarized 266 nm beam (violet line in Figure 3.29). The residual 800 nm and 400 nm will be filtered after the β-BBO in order to pump the sample only with the 266 nm beam. The 266 nm beam with an energy/pulse ~100 nJ is focused in the sample through a parabolic mirror, reaching a diametric dimension of ~140 μm. Then the pump is blocked by a beam blocker.

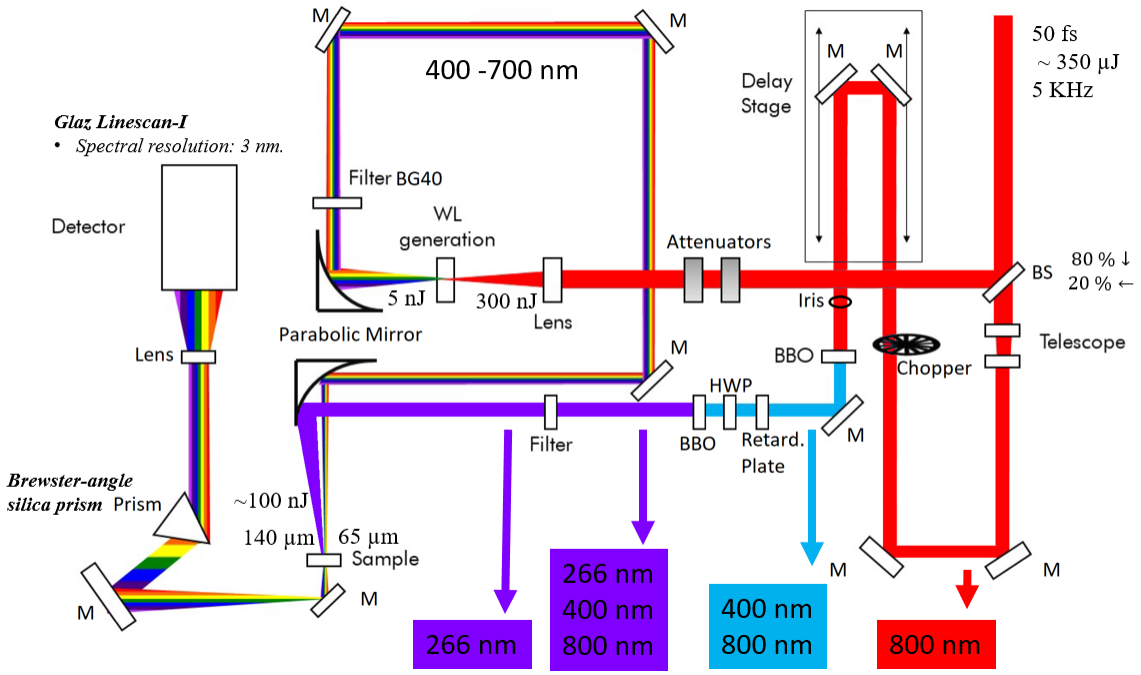

Figure 3.29. Pump-probe setup in Palermo. The symbols represent: beam splitter (BS), mirror (M), β-BBO crystal (BBO), half-wave plate (HWP), and retarder plate (Retard. Plate).

The remaining 20% is directly used to generate the white light, usually fixed at a value which creates a single stable filament in the medium (D_2O), focusing the 800 nm pulses with a 150 mm focal length lens and stabilized by the use of two graduated filters. The generated white light is reported in Figure 3.30.

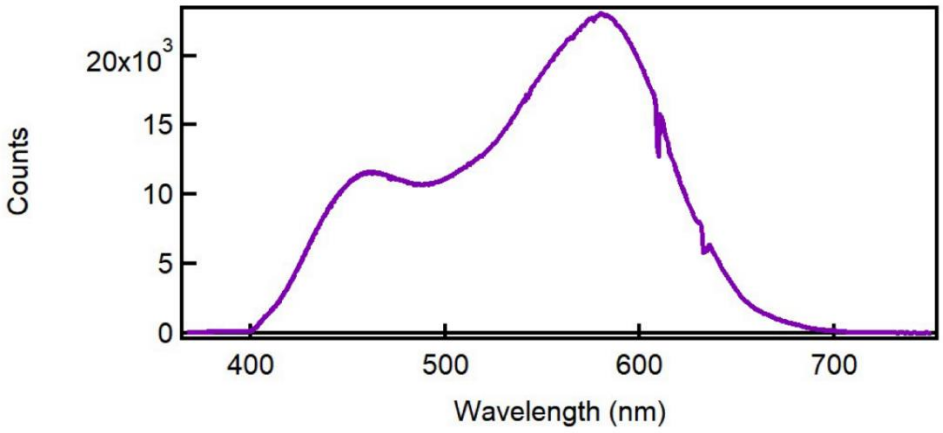

Figure 3.30. White light generated in the pump-probe setup installed in Palermo.

The white light beam, after passing through a filter which removes the fundamental, is collimated by a 50 mm parabolic mirror to form a 4 mm diameter circular spot. The probe is then focused on the sample by the same parabolic mirror used to focus the pump, having a ~65 μm spot on the sample. Then the transmitted light is driven into the detector (Glaz Linescan-I CMOS linear array sensor), after being decomposed in its spectral components by a Brewster-angle prism.

Chapter 4. Origin of steady state and pulsed X-ray radiation-induced attenuation in canonical optical fibers

Notwithstanding more than 50 years of research on silica-based optical fibers (OFs) [194], thanks to the continuous development of new types of optical fiber classes and their integration as part of new devices or sensors [5], [102], [195]–[198], the research community is still improving this technology for different scientific and industrial fields [4], [5], [178]. The increasing interest, through all these years, is ascribable to their revolutionary importance in various domains, such as the high-speed data communication, fiber lasers, diagnostics, dosimetry and point or distributed sensing devices. Furthermore, two OFs stronger advantages for integration in radiation-rich environments are their good tolerance to ionizing and non-ionizing radiations, compared to alternative microelectronic technologies and also their immunity to most of the electromagnetic perturbations encountered in harsh environments [163], [175], [176], [178], [199]. Accordingly, optical fibers are integrated as part of diagnostics, control-command applications in the huge facilities devoted to the fusion by inertial confinement study such as the Laser Mégajoule in France and the National Ignition Facility in USA [4], [173], [175], [176]. For this research, the OFs' have to survive to ignition shot series , each one being associated with a burst of X-rays, γ-rays and 14 MeV neutrons. For ITER devoted to the fusion by magnetic confinement study [200], the fibers are used as sensors, diagnostics and have to resist to steady state γ-ray irradiation at high MGy doses.

It is known that the fiber exposure to radiation degrades its transmission properties, increasing the signal absorption along the waveguide [4]. This effect is called radiation-induced attenuation (RIA). Moreover, in certain cases, the irradiation can generate an unwanted/parasitic light emission (RIE) which can interfere with the OF response or lead to a reduction in the signal to noise ratio. Both effects can lead as a worst case to the loss of the transmitted signal. These macroscopic phenomena are caused by the point defect generation under irradiation, resulting in the appearance of absorbing energy states within the silica bandgap (normally transparent) [1]–[4], [20], [29], [35]. Therefore, the study of the fundamental basic mechanisms at the fiber

degradation origin under irradiation is necessary to properly evaluate the vulnerability of fiber-based applications in complex environments, to design radiation hardened fibers or fibers for dosimetry. Indeed there are still many lacunas and open questions related to the involved physical phenomena.

This chapter will be devoted to the mechanisms that govern the point defect generation as well as their post-irradiation recovery. The guiding line is to better understand the fiber response from both fundamental and applicative point of views. This approach allows us estimating the fiber vulnerability and, when needed, to imagine ways to improve its radiation tolerance to fulfill the application requirements. As already mentioned in the previous chapters, to deepen our understanding on the fiber radiation response, it is crucial to have a complete knowledge of all the fiber intrinsic parameters known to influence its radiation response such as its core and cladding compositions, the potential treatments applied on either the preform and/or the fiber. For this reason, in our experiments we used only the so-called "canonical" and well defined fiber specific samples produced by iXblue [162], [163], [169], [199].

In this chapter, we report and discuss the results obtained under X-ray pulsed irradiation, characterizing the canonical OF RIA evolutions on the basis of already known defects absorbing in the investigated spectral range. In order to go deeper in the understanding of their transient behavior, room temperature (RT) measurements will be compared to analogous experiments performed at liquid nitrogen temperature (LNT), taking advantage from its slowing down effect on the defect recombination kinetics. Furthermore, the results obtained after pulsed X-ray irradiation will be compared with those acquired on the same OFs under steady state X-rays. All these experiments were performed on the most spread classes of OFs: PSC, F-doped, Ge-doped and P-doped, which can be considered as radiation hardened, radiation tolerant and radiation sensitive optical fibers [79], [87], [101].

4.1. RIA measurements

In the following section we reported all the RIA results obtained during the pulsed X-ray irradiation of the canonical fibers at the CEA Gramat with the ASTERIX machine [173], [174].

First we will discuss about the irradiation temperature effect on the induced losses under X-rays and will successively study the OFs' radiation response at room temperature (RT) and at liquid nitrogen temperature (LNT). For every sample, we will analyze the point defects at the origin of the RIA through the spectral deconvolution using the Gaussian curves associated with the defect structures. The transient RIA spectra after pulsed X-rays will be also compared to the ones under steady state continuous X-ray irradiation (using the X-ray machines from LabHC) [177] and the difference will be discussed.

4.2. Temperature effects

It is well known that the OFs' temperature strongly influences the fiber radiation response as temperature changes the defect generation and bleaching rates [4], [75], [79], [80], [87], [94], [101], [201]. At low temperature, the RIA signal is generally more intense as the defects are more stable, allowing to better distinguish the absorption bands of the metastable defects than at room temperature.

The advantage to study the RIA spectra at low temperature lies on the possibility to slowing down the defects' decay kinetics, allowing us to highlight the contribution of the metastable defects. This opportunity supplies a powerful access key to the defects' dynamics overcoming the complexity of time-resolved measurements, even with time resolution of the order of tens of ms. Indeed, as is it depicted in Figure 4.1, the 1550 nm RIA response of the PSC and Ge-doped OFs, generally considered as radiation tolerant OFs [4], at the earlier times after an X-ray pulse, present an attenuation higher than the P-doped OF, one of the most sensitive optical fiber. While, for longer timescale (tens of ms), where the most available detectors work, the RIA shows the picture of the fibers' response coherent with the normal tolerance classification established for steady state γ-ray irradiations [4].

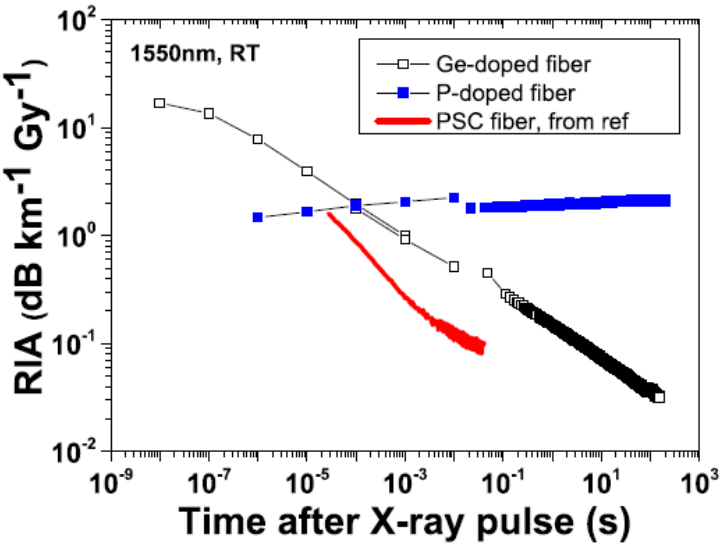

Figure 4.1. RIA kinetics decays just after the X-ray pulse in the Ge- and P-doped SM optical fibers (RT). The transient response of a radiation-hardened pure silica core (PSC) under pulsed X-rays, reported by [202] is added for comparison. In all cases, the RIA has been normalized by the deposited dose per pulse. Figure taken from [101].

The advantage of studying the RIA at low temperature is evident from the comparison, shown in Figure 4.2, between the 650 nm RIA kinetics observed in the various classes of optical fibers at both RT and LNT under X-ray pulse irradiation.

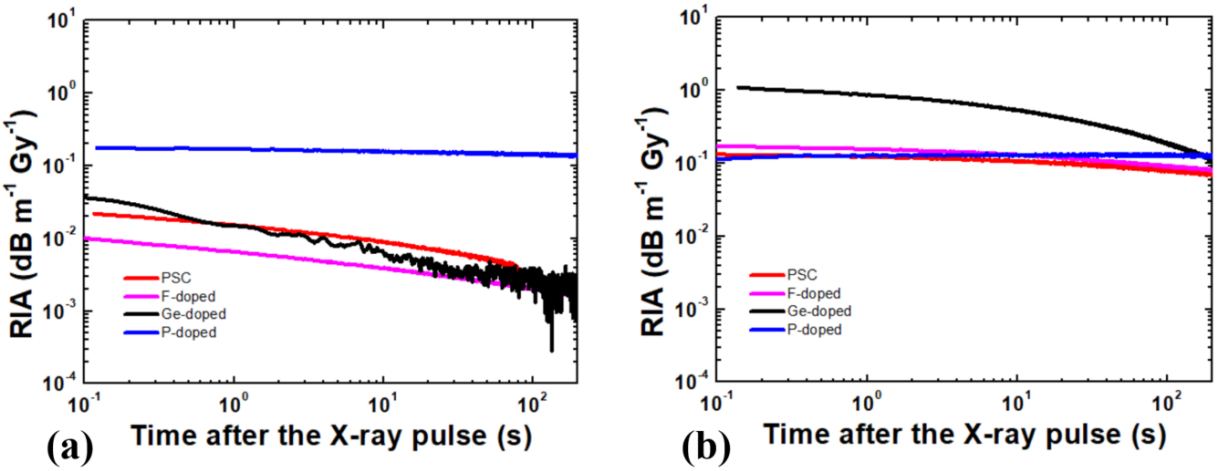

Figure 4.2. Post pulse recovery kinetics for the four different types of optical fibers at RT (a) and LNT (b), at 650 nm: PSC in red, F-doped in magenta, Ge-doped in black and P-doped in blue. In all cases, the RIA has been normalized by the deposited dose per pulse.

Figure 4.2 (a) shows RIA levels and evolutions in this time range agree with the known radiation tolerance classification [4]: the P-doped OF represents, over the studied samples, the most radiation sensitive one, having an almost constant RIA during the first hundreds of seconds after exposure. On the contrary, the "radiation tolerant" OFs, such as the PSC, F- and Ge-doped, exhibit a fast recovery, reaching quickly (post pulse irradiation) RIA levels two orders of magnitude lower than the one measured in the P-doped sample. LNT measurements, in Figure 4.2 (b), exhibit for the earlier times (~80 ms) a framework comparable to the dynamics observed for fast times in Figure 4.1 (~μs). In fact, the RIA of the P-doped samples remains almost the same than at RT, the RIA levels of the other "radiation tolerant samples" is higher by one or two orders of magnitude compared to RT results. Coherently, much slower RIA decay rates are observed at LNT for these fibers.

This procedure, allows us not only to have more information about the defect dynamics, but also gives us the possibility to detect more easily the metastable defects that are bleached in a time scale faster than the resolution time of our spectrometers of a few milliseconds at RT.

4.3. Pure silica core optical fiber

4.3.1 RIA spectra

Figures 4.3 (a) and 4.3 (b) report the RIA spectra measured one second after the X-ray pulse, between 380 nm and 1500 nm for the PSC optical fiber, at RT and LNT, respectively. At RT (Figure 4.3 (a)), the fiber radiation response is mainly explained by the UV tail(s) of absorption band(s) centered at energy values higher than 3 eV, out of our investigated spectral range. From literature, we assumed that the involved defects are probably those associated with the Chlorine impurities (absorbing at 380 nm and 330 nm) and a small contribution from both SiE´ and NBOHC centers (absorbing respectively at ~215 nm and ~260 nm). It is worth to know that the main contributor in the UV part of the measured spectra, is due to the chlorine variety of defects, as already observed, in other irradiation conditions, on the same samples [203], [204], where above 3 eV, it was observed that the SiE´ and NBOHC contributions to the RIA are negligible.

At LNT (Figure 4.3 (b)) the intensity and the shape of the RIA spectra strongly differ from RT results. Notwithstanding the almost similar total accumulated dose, the detected RIA is larger below 3 eV, while the RT-RIA is higher above this energy value. By comparing the spectra at the two different temperatures, the presence of new absorption bands at low energies, between 500 nm and 600 nm, is evident. These new profiles can be explained by the major contribution of new absorption bands, as already observed under pulsed and steady state X- and γ-rays [75], [80], [87], [205]. At least for the PSC, these bands were interpreted as the STHs manifestation at low temperature. Moreover, as mentioned in the previous section, the radiation induced loss recovery is slower at LNT than at RT.

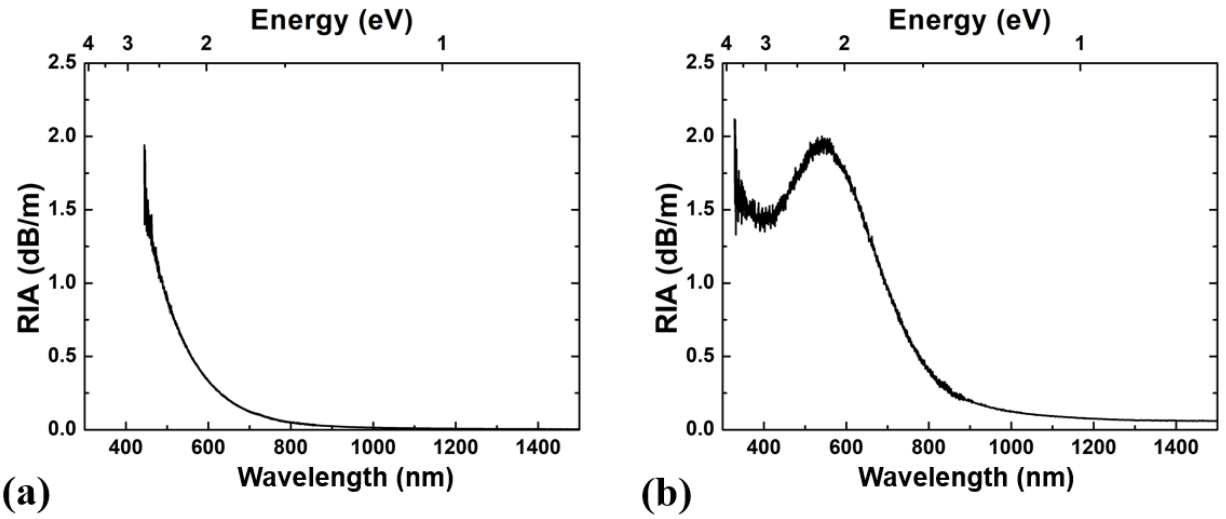

Figure 4.3. RIA spectra measured 1 s after the X-ray pulse for the PSC at (a) RT and (b) LNT, at a total accumulated dose of ~10 Gy(SiO_2).

Figure 4.4 shows the RIA spectra evolution, for different times after pulse, at both RT and LNT. As it is possible to note, the spectra at LNT are associated with much more complex dynamics than the ones acquired at RT, highlighting a competition between different recovery processes. Indeed, at RT the spectral shape seems to be the same as function of the time, while at LNT the fiber exhibits a very fast kinetics in the near-IR (around ~0.8 eV) and a slower one in the UV (around ~3.3 eV).

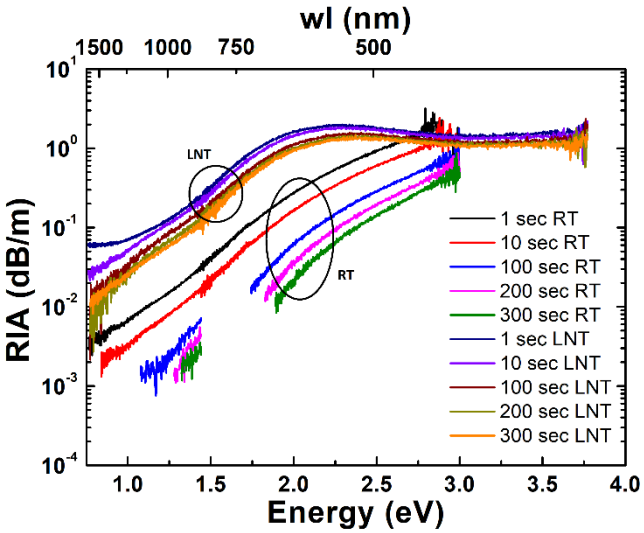

Figure 4.4. RIA spectra recorded for the PSC optical fiber at LNT (starting from the upper navy curve: 1, 10, 50, 100, 200, and 300 s) and RT (starting from the black curve: 1, 10, 50, 100, and 200 s) at different times after the X-ray pulse with a total accumulated dose of ~10 Gy(SiO_2).

4.3.2 Spectra decomposition

To better characterize the induced defects generated under pulsed X-ray irradiation, we reproduced the RIA spectra as sum of a Gaussian function set representing the contribution of the absorption bands associated to point defects already discussed in the literature. The Gaussian function is defined by:

$$G(x) = \frac{A}{\sqrt{2\pi\sigma^2}} e^{-\frac{(x-x_c)^2}{2\sigma^2}} \quad (4.1)$$

where A is the band area, x_c is the center of the optical absorption (OA) band and σ (the standard deviation) is defined in relation to its Full Width at Half Maximum (FWHM) as: $FWHM = 2\sqrt{2\ln(2)}\sigma$.

The fitting routine consists in using a set of Gaussian bands with fixed parameters, such as the Gaussian center and its FWHM, taken from ref. [4]. The Gaussian area is the free parameter and is proportional to both the defect concentration and its oscillator strength. The least squares algorithm is the convergence method used in the present work. The obtained results are reported

in Table 4.1. Point defects for which the detection of the optical absorption band, by our fitting routine, is under the detection limit, are not reported. This choice is justified by their negligible contribution to the total RIA compared to the other defects: they may be present in the irradiated optical fibers but do not contribute significantly to the measured RIA.

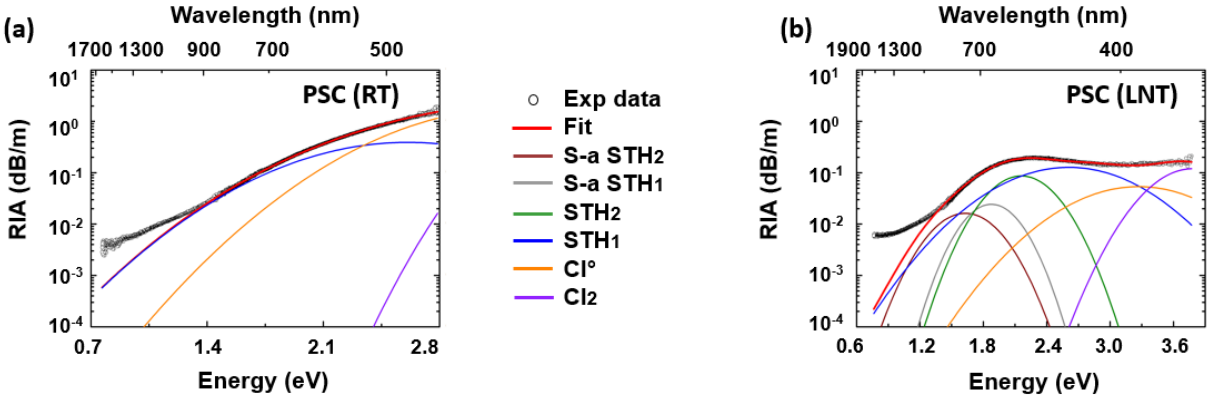

Figure 4.5. Decomposition of the RIA spectra measured 1 s after the X-ray pulse for the PSC ((a) RT and (b) LNT), with a total accumulated dose of ~10 $Gy(SiO_2)$: open circles are the experimental data, red lines are the global fitting functions, the brown and grey lines are the strain-assisted STH_2 and strain-assisted STH_1 contributions, in green and blue the inherent STH_2 and inherent STH_1 and in orange and purple the Cl^0 and the Cl_2 contributions. Figure adapted from [79].

At RT (Figure 4.5 (a)), the spectrum at high energies is quite well reproduced with a limited set of Gaussian bands attributed to specific defects associated with chlorine impurities (Cl^0 and Cl_2 and their absorption bands at 3.26 eV and 3.78 eV, respectively) and the inherent STH_1 (absorption band at 2.6 eV). Notwithstanding the good match between experimental data and the fit function in the visible, a lack of knowledge regarding the RIA contribution in the NIR is obvious, resulting in an RIA underestimation, probably due to the contribution of additional defects having still to be identified.

A different panorama is depicted in Figures 5 (b) for LNT measurements: new spectral features appear between ~1.5 eV and ~2.0 eV, attributed in this analysis to the STHs' related absorption bands, such as the strained-assisted STH_2 peaked at 1.63 eV, the strained-assisted STH_1 peaked at 1.88 eV and the inherent STH_2, peaked at 2.16 eV. It is well known that these absorption bands are strongly unstable at RT, justifying the difference observed between the RIA spectra

acquired at RT and LNT. STHs are typically observed at low temperature in analogous experimental conditions [4], [75], [80].

Table 4.1. Parameters of the Gaussian absorption bands associated with a variety of pure silica related defects. This set, taken from ref. [4], serves to reproduce the acquired RIA spectra.

Defect	**OA peak (eV)**	**FWHM (eV)**	**PSC RT (dB eV/m)**	**PSC LNT (dB eV/m)**
S-a STH_2	1.63	0.6		0.10
S-a STH_1	1.88	0.5		0.13
STH_2	2.16	0.6		0.50
STH_1	2.61	1.2	0.50	1.60
Cl^0	3.26	1.2	2.40	0.70
Cl_2	3.78	0.7	2.90	0.90

Furthermore, the inherent STH_1 amount increased by a factor of ~ 3 at LNT compared to RT, as listed in table 4.1. These results, consistent with those observed in [80], show a decrease of the Cl^0 band contribution at LNT, thereby supporting the hypothesis from Griscom et al. [65] of the inter-dependence between STHs and Cl^0 defects. As in the RT case, it is not possible to reproduce the RIA profile in the whole spectral range. Indeed, as depicted in Figures 4.5 (b), below ~ 1.5 eV the fitting curve does not cross the experimental data. The missing contribution, especially at LNT, could be linked to the strongly non-Gaussian infrared contribution of strain-assisted STHs: the so-called Low-Temperature-Infrared-Absorption (LTIRA) [4], [75], [202]. In fact, the difference between the fitting function and the experimental data is higher at LNT for which the contribution of the strain-assisted STHs' bands is stronger.

Therefore, the above-mentioned fitting routine allows the experimental data reproduction, up to 1.5 eV, at both temperatures within a 10% error, as highlighted in Figure 4.6, where the normalized residuals between the experimental data and the global fitting function is reported. The discrepancy in the NIR spectral range lies between 40% and 80% at RT and even 100% at LNT for the longer wavelengths. In this spectral domain, data could not be fitted by only one Gaussian curve [202]. Recent works [202], [206] attributes this discrepancy to new absorption bands linked

to the STH and peaking around 1 eV (not used in our decomposition procedure). Clearly, further studies are still needed to clarify this contribution.

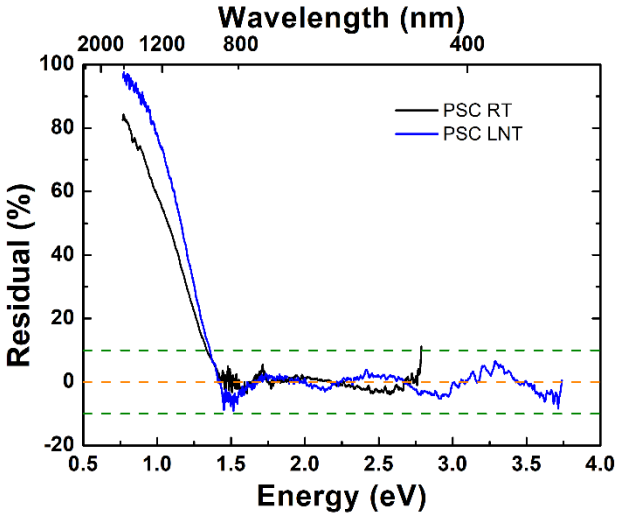

Figure 4.6. Normalized residuals between the experimental RIA data and the global fitting function: in black for the PSC OF at RT and in blue for the PSC OF at LNT. The green and the orange dashed lines are guide lines for the $\pm 10\%$ and the 0%, respectively. Figure taken from [79].

As done for the single spectra acquired 1 s after the X-ray pulse, applying the same fitting routine to all the recorded spectra at any given time, it becomes possible to study the kinetics related to every involved defect instead of the global RIA kinetics. For times longer than $200-300$ s, the RIA value is closer to our detection limit, making the fitting routine less robust, and then these longer times were not considered in our analysis. For the first 200 s after the shot, it was possible to achieve decomposition for the same spectral range (depending on each fiber type) keeping the same fitting quality than the one illustrated for the spectra acquired at 1 s after the pulse. We are then able to plot the intensity time evolution of each optical absorption band, highlighting the behaviors of the different point defects. In Figure 4.7 we reported the normalized decay kinetics of the various point defects used to reconstruct the RIA spectra in the PSC OF at RT and LNT. Furthermore, the extrapolated defects kinetics are reproduced with the fractal formalism proposed by Griscom et al. [207] by the following equation:

$$N\left[(kt)^{\beta}\right] = N(0)e^{-(kt)^{\beta}} \tag{4.2}$$

where $N[(kt)^{\beta}]$, is the defect concentration at a given time t, k is the decay-rate parameter and β is linked to diffusion-controlled reactions and its value ranges between 0 and 1. The best fit curves are depicted in Figure 4.7 for the defects involved in the fitting procedure.

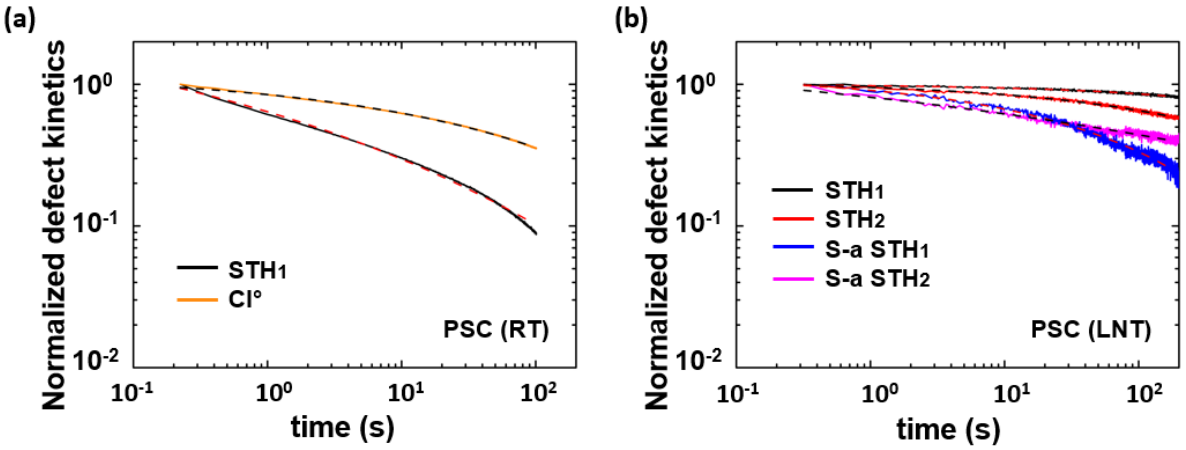

Figure 4.7. Normalized decay kinetics of the defects as extracted from the fitting routine for the PSC at RT (a) and at LNT (b). The lines in color are: in black the STH_1, in red the STH_2, in blue the strained-assisted STH_1, in magenta the strained-assisted STH_2 and in orange the Cl^0. The dashed lines are the fits relative to the overlapped defects kinetics. Figure adapted from [79].

For a few defects listed in Table 4.2, the measured RIA decay kinetics are too noisy in our results to be well analyzed in this PhD manuscript.

The good quality of each defect kinetic fit at both temperatures, highlights how the fractal model describes well the experimental data, at least within the investigated temporal window. The additional STH-related absorption band contributions (STH_2, strained assisted STH_1 and STH_2) at LNT explain the difference in the RIA spectra between the two temperatures. The slower kinetics reflect the slowing down effect of the temperature on the defects observed at both temperatures; while the difference in the shape is due probably to defects that at RT are too unstable and bleached in a time scale faster than the current experimental measurement setup. Their contribution to RIA at RT consequently appears negligible at our resolution time. The best fitting values of the defects kinetics are listed in table 4.2.

The $N(0)$ values are proportional to the defect concentrations and their oscillator strengths after the X-ray pulse. It is important to note that the $N(0)$ value in Table 4.2 (and also in the next tables) is the one obtained before applying the normalization routine. In particular, this parameter

can quantify the temperature slowing down effect in the defect kinetics. Indeed, comparing the centers observed at both temperatures defects present k values higher than 10^2 s^{-1} at RT, while at LNT these values are lower than 1 s^{-1}.

Table 4.2. Best N(0), k and β fit values obtained before the normalization routine, used to reproduce the kinetics in Figure 4.7.

Parameter	STH_1	STH_2	s-a STH_1	s-a STH_2	Cl^0
N(0) (dB/m) at RT	3				3.3
N(0) (dB/m) at LNT	1.05	0.29	0.08	0.18	
k (s^{-1}) at RT	155				0.02
k (s^{-1}) at LNT	0.0001	0.001	0.018	1.5	
β at RT	0.14				0.27
β at LNT	0.42	0.34	0.36	0.1	

4.4. F-doped optical fibers

4.4.1 RIA measurements

Figures 4.8 (a) and 4.8 (b) report the experimental RIA spectra measured one second after the X-ray pulse, between 400 nm and 1400 nm for the F-doped optical fiber, at RT and LNT, respectively. Analogously to the PSC response, at RT the F-doped RIA (Figure 4.8 (a)) is mainly due to the tail(s) of absorption band(s) centered at higher energy values, in the UV range.

Indeed, the involved defects correspond to the same variety characterizing the PSC OF's response, presenting also the chlorine impurities and the STH_1 absorption band.

Even at LNT (Figure 4.8 (b)) the spectra RIA shapes are comparable to the PSC measurements, with a slower decrease of the RIA levels, highlighting the appearance of the same absorption bands linked to the STH related contribution. Even the relation of the spectra at the two different temperatures is comparable with the one observed in the PSC manifesting a slower

recovery kinetics at LNT than at RT. Figure 4.9 compares the RIA spectra at both temperatures at different times after the X-ray pulse, exhibiting an analogous evolution to the one observed in PSC OF.

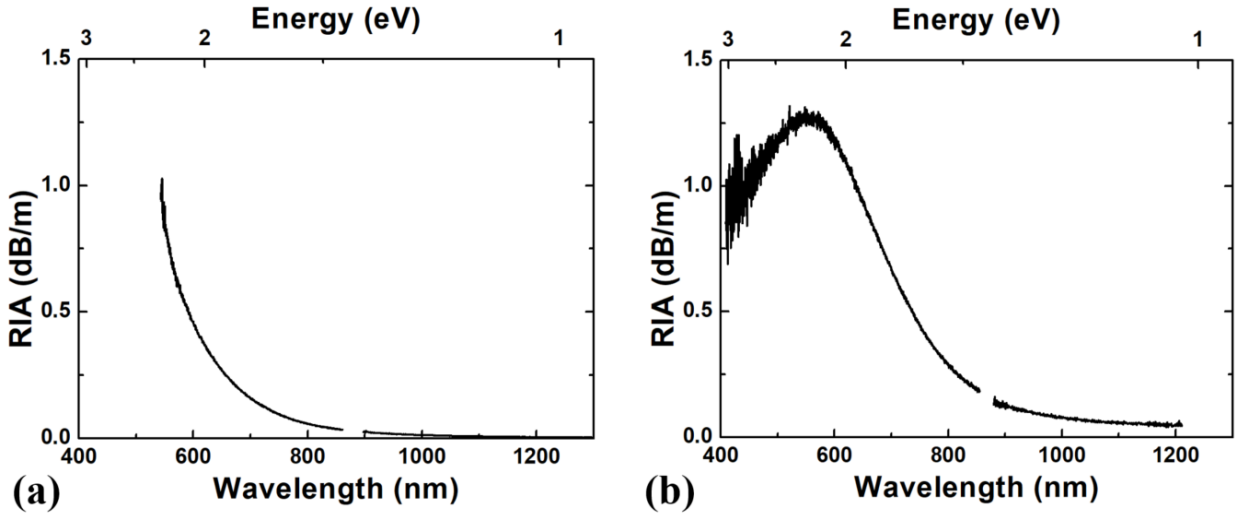

Figure 4.8. RIA spectra measured 1 s after the X-ray pulse for the F-doped ((a) RT and (b) LNT), with a total accumulated dose of ~10 Gy(SiO_2).

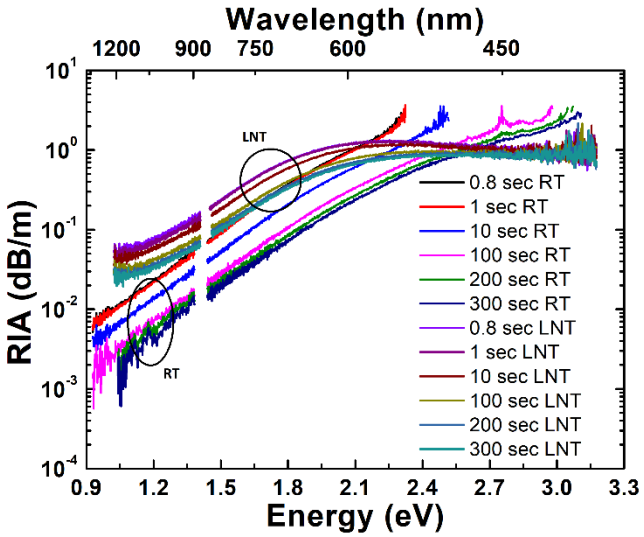

Figure 4.9. RIA spectra recorded for the F-doped optical fiber at LNT (starting from the upper purple curve: 0.8, 1, 10, 100, 200 and 300 s) and RT (starting from the black curve: 0.8, 1, 10, 100, and 200 s) at different times after the X-ray pulse, with a total accumulated dose of ~10 Gy(SiO_2).

4.4.2 Spectra decomposition

As already mentioned above for the Gaussian decomposition procedure, we used the same previous set of the defects for the F-doped sample and the result is depicted in Figure 4.10. A higher relative contribution of Cl-related defects is observed compared to the PSC OF, justifying its slightly higher RIA level in the UV at RT. Nevertheless, a lack of knowledge regarding the RIA contribution in the NIR is still present, resulting in a comparable underestimation of the RIA in this spectral range also for the F-doped fibers. The best fitting values are reported in table 4.3.

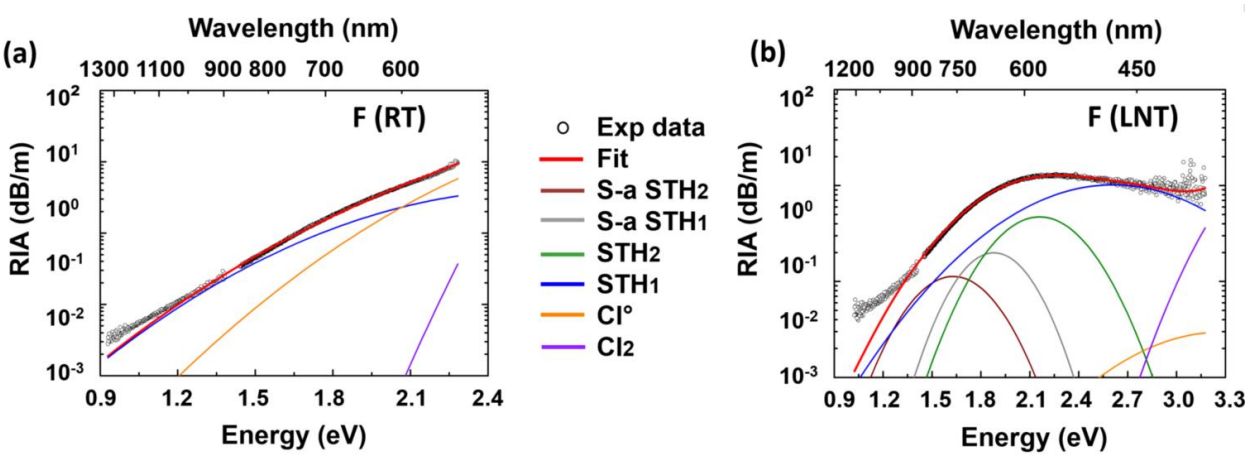

Figure 4.10. Decomposition of the RIA spectra measured 1 s after the X-ray pulse for the F-doped at (a) RT and (b) LNT, with a total accumulated dose of ~10 $Gy(SiO_2)$: open circles are the experimental data, red lines are the global fitting functions, the brown and grey lines are the strain-assisted STH_2 and strain-assisted STH_1 contributions, in green and blue the inherent STH_2 and inherent STH_1 and in orange and purple the Cl^0 and the Cl_2 Chlorine defect contributions. Figure adapted from [79].

As general remarks, our results show that fluorine co-doping seems to decrease the RIA related to the strain-assisted STHs absorption bands compared to the PSC OFs. Anyway, the fitting routine reproduces well the experimental data up to 1.5 eV, at both temperatures within a 10% error, as reported in Figure 4.11.

Table 4.3. Parameters of the Gaussian absorption bands associated with a variety of pure silica related defects. This set, from ref. [4], serves to reproduce the acquired RIA spectra.

Defect	OA peak (eV)	FWHM (eV)	RT (dB eV/m)	LNT (dB eV/m)
S-a STH_2	1.63	0.6		0.07
S-a STH_1	1.88	0.5		0.10
STH_2	2.16	0.6		0.30
STH_1	2.61	1.2	0.50	1.30
Cl^0	3.26	1.2	5.00	0.04
Cl_2	3.78	0.7	6.00	2.10

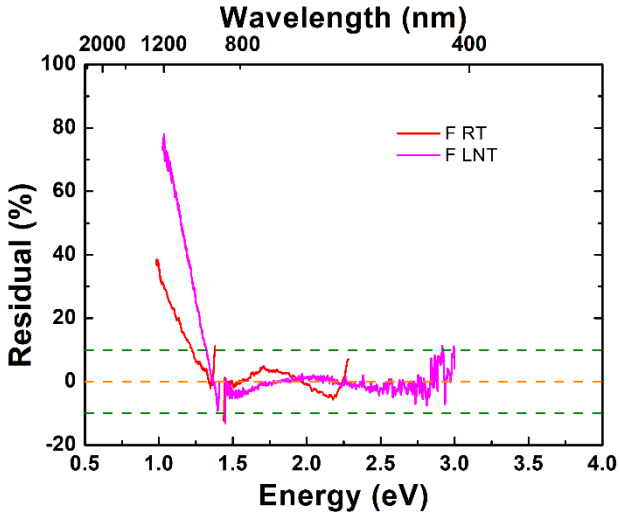

Figure 4.11. Normalized residuals between the experimental RIA data and the global fitting function: in red for the F-doped OF at RT and in magenta for the F-doped OF at LNT. The green and the orange dashed lines are guide lines for the $\pm 10\%$ and the 0%, respectively. Figure taken from [79].

Replicating the fitting procedure for all the spectra as function of the time, we obtain the defect kinetics. By employing the fractal formalism, we reproduce the defect decay kinetics.

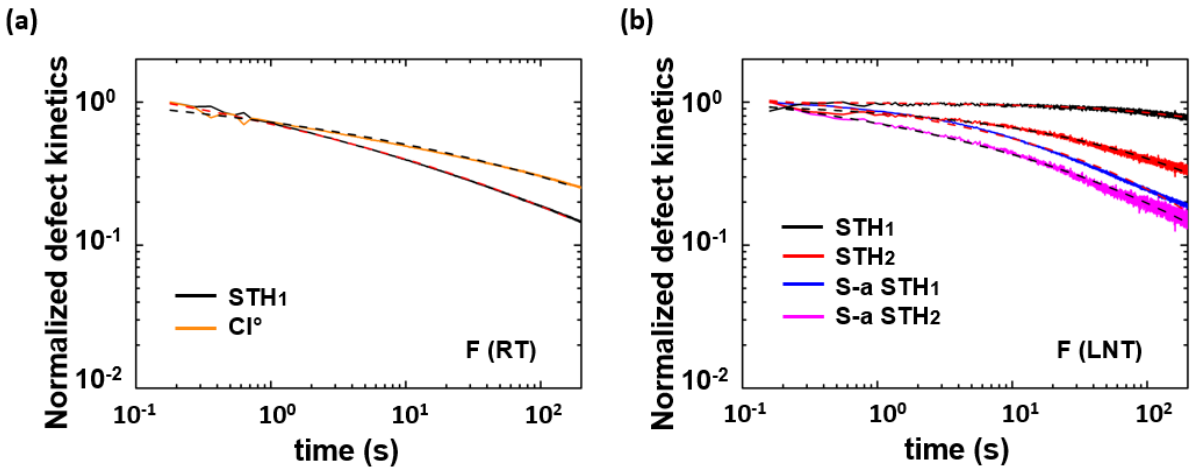

Figure 4.12. Normalized decay kinetics of the defects as extracted from the fitting routine for the F-doped at RT (a) and at LNT (b). The lines in color are: in black the STH_1, in red the STH_2, in blue the strained-assisted STH_1, in magenta the strained-assisted STH_2 and in orange the Cl^0. The dashed lines are the fits relative to the overlapped defects kinetics. Figure adapted from [79].

The theoretical decay fits the kinetics quite well. Notwithstanding the similarities between the PSC and the F-doped OFs, the STH related absorption bands behave in different ways: albeit a slower kinetics of the STH_1 at RT, the STH bands decay faster at LNT in the F-doped, showing how the presence of the fluorine works mostly at the earlier times after the pulse. The best fit parameters are reported in table 4.4.

Table 4.4. N(0), k and β fit values obtained before the normalization routine, used to reproduce the kinetics in Figure 4.12.

Parameter	STH_1	STH_2	s-a STH_1	s-a STH_2	Cl^0
N(0) (dB/m) at RT	6				19
N(0) (dB/m) at LNT	1.26	0.4	0.18	0.13	
k (s^{-1}) at RT	64				0.24
k (s^{-1}) at LNT	0.0004	0.008	0.065	0.5	
β at RT	0.13				0.16
β at LNT	0.55	0.32	0.28	0.2	

4.5. Ge-doped optical fibers

4.5.1 RIA measurements

In Figure 4.13 (a) is reported the Ge-doped fibers response measured one second after the X-ray pulse, between 400 nm and 1400 nm. The spectrum at RT is dominated by the contributions of GeX and Ge(1) centers with absorption signatures around 475 nm and 280 nm respectively. Despite the different origins of the RIA, since in this case the darkening is mainly due to the Ge-related point defects, the induced loss levels between the PSC, the F- and the Ge-doped fiber are comparable, still of the order of ~dB/m. At LNT (Figure 4.13 (b)) the RIA levels are higher and the spectral shape is strongly modified: the RIA as a function of the wavelength is more defined, highlighting new spectral features, probably composed of additional bands around 500-600 nm. These new profiles can be explained by the major contribution of new absorption bands, as already observed in other irradiation conditions [87]. Accordingly with the results obtained for the PSC, these bands were interpreted as the manifestation of STHs at low temperature. The absence of STHs in the RT spectra can be explained by their strong instability in these experimental conditions leading them to disappear within a millisecond time scale.

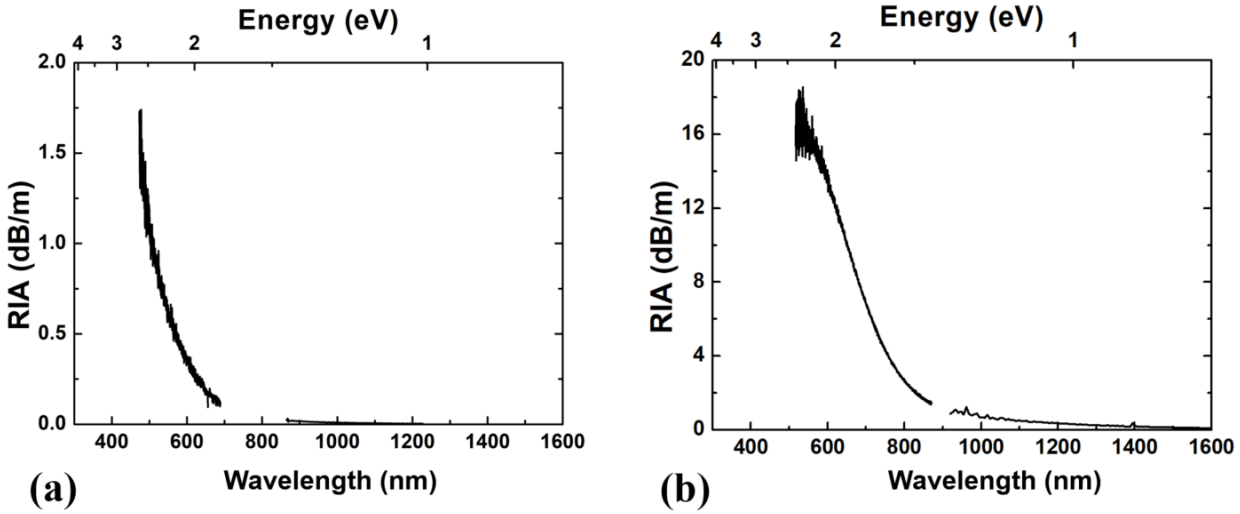

Figure 4.13. RIA spectra measured 1 s after the X-ray pulse for the Ge-doped at (a) RT and (b) LNT, at a total accumulated dose of ~10 Gy(SiO_2).

At LNT, the RIA observed for the Ge-doped OF is at least one order of magnitude higher compared to RT measurements, presenting the Ge-doped fiber as the less radiation tolerant fiber type at LNT among the investigated samples. All these observations are confirmed even for longer times after pulse, as highlighted in Figure 4.14 showing the time evolution of the RIA spectra after the pulse at RT and LNT, respectively.

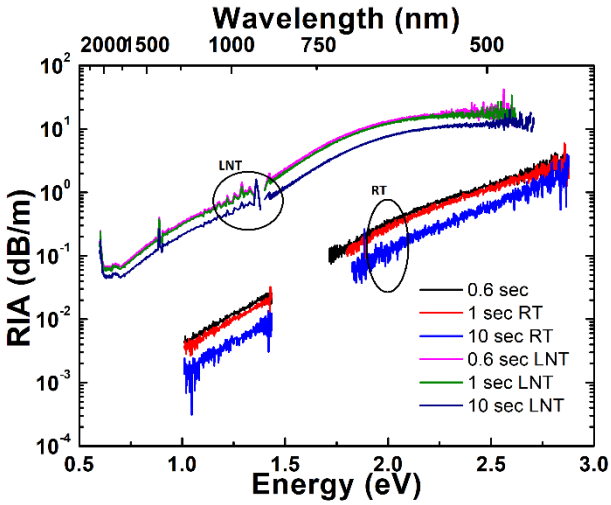

Figure 4.14. RIA spectra recorded for the Ge-doped optical fiber at LNT (starting from the upper magenta curve: 0.6, 1 and 10 s) and RT (starting from the black: 0.6, 1 and 10 s) at different times after the X-ray pulse, at a total accumulated dose of ~10 Gy(SiO_2).

4.5.2 Spectra decomposition

The same protocol for the fitting procedure was employed to analyze the Ge-doped optical fibers, as depicted in Figure 4.15. In this case, the defect set comprises both the Si and Ge-related centers having their main characteristics listed in the Table 4.5. At RT (Figures 4.15 (a)), the experimental data are quite well reproduced using the GeY [95] OA band at 1.38 eV and by the defect tails coming from the absorption bands located in the UV: GeX at 2.6 eV, the so-called "transient defect" (TD) at 3.26 eV, already observed after X-ray pulses [4], [208] and of Ge(1) defect absorbing at 4.4 eV.

Even at LNT (Figure 4.15 (b)) the discrepancy between the experimental data and the fit remains within the experimental data dispersion (~10% on the experimental value), meaning that

the selected set of defects reproduces well the RIA spectra. The best fit values are reported in table 4.5.

As already observed previously, low irradiation temperature increases the RIA of Ge-doped OF highlighting a strong temperature dependence of the defects. Furthermore, the large differences in the spectral shape are explained by the appearance of new absorptions bands, especially around ~1.5 eV and ~2.0 eV, which are not reported as Ge-defects. From the literature [87], the strain-assisted STHs appear to be good candidates to fill this discrepancy, having reported absorption bands in this spectral domain.

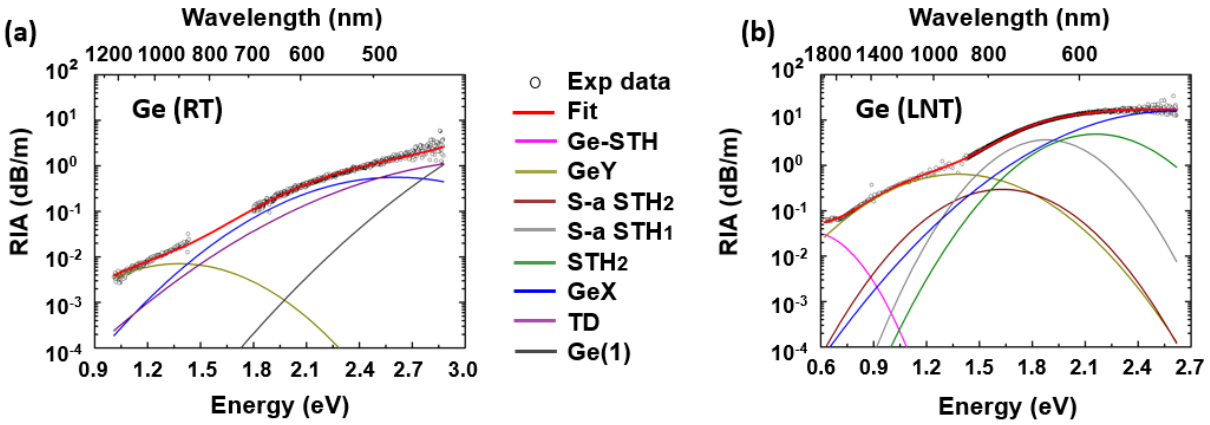

Figure 4.15. Decomposition of the RIA spectra measured 1 s after the X-ray pulse for the Ge-doped OF ((a) RT and (b) LNT), with a total accumulated dose of ~10 Gy(SiO_2): open circles are the experimental data, the red line is the global fitting function, the pink is the Ge-STH contribution, the yellow is the GeY band, the brown and grey the strained-assisted STH_2 and strain-assisted STH_1 contribution, respectively, in green the inherent STH_2 absorption band, in blue the GeX contribution, in magenta the transient defect and in dark grey the Ge(1) absorption band. Figure adapted from [79].

Indeed, these absorption bands were employed in our fitting routine, leading the theoretical function to reproduce quite well the experimental data at LNT. However, as expected, the Transient Defects present a much lower relative contribution to the total RIA at LNT, while the Ge(1) contribution decreases by a factor of 4; both defects start to be below our sensitivity threshold. The involved STHs' absorption bands are the Ge-STH ones which peaked at 0.54 eV, those of strain-assisted STH_2 and strain-assisted STH_1 peaked respectively at 1.63 eV and 1.88 eV and the inherent STH_2 at 2.16 eV. The inherent STH_1 absorption band is not needed to reproduce

our experimental data. This could be explained by the OA band overlap with the GeX one, in any case both defects should present similar temperature dependence.

At the present analysis stage, it is difficult to discuss the exact temperature dependence of Ge-related defects. For example, our results regarding GeX differ from those of ref [95], where the authors observed an opposite trend, with an increase in GeX concentration with the temperature. However, it should be reminded that the irradiation temperature effect on a single defect behavior is strongly dependent on irradiation conditions (dose, dose rate, and temperature) and could then have either a negative or positive impact on the RIA depending on the exact test conditions (this is more discussed in Ref. [201] for the Ge(1) case). More systematic experiments are then needed to clarify the defect dependencies as a function of irradiation temperature.

Table 4.5. Parameters of the Gaussian absorption bands associated with a variety of Ge- and Si-related defects. This set, from ref. [4], was used to reproduce the acquired RIA spectra.

Defect	OA peak (eV)	FWHM (eV)	RT (dB eV/m)	LNT (dB eV/m)
Ge-STH	0.54	0.35		0.014
GeY	1.38	0.71	0.006	0.48
S-a STH_2	1.63	0.60		0.20
S-a STH_1	1.88	0.50		1.90
STH_2	2.16	0.60		3.00
GeX	2.60	0.97	0.60	16
TD	3.26	1.30	1.9	
Ge(1)	4.40	1.20	180	

The quality of the fit is acceptable in the whole spectra, highlighting that the presence of germanium in the OF core prevents the unknown Si-related defects formation involved in the PSC and F-doped fiber responses. This is obvious from the normalized residuals between the experimental data and the global fitting function, as reported in Figure 4.16, in which the fit procedure quality is within $\pm 10\%$ for the whole spectral range.

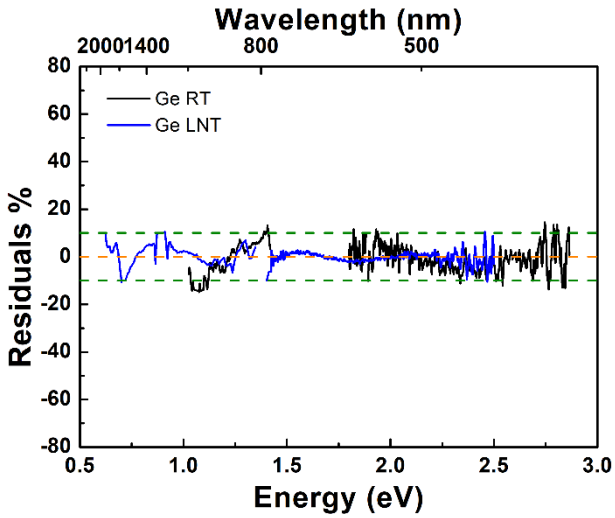

Figure 4.16. Normalized residuals between the experimental RIA data and the global fitting function: in black for the Ge-doped OF at RT and in blue for the Ge-doped OF at LNT. The green and the orange dashed lines are guide lines for the ±10% and the 0%, respectively. Figure taken from [79].

In order to shed light into the fluorine co-doping effect in OFs' response, we have studied even the RIA spectra in Ge+F-doped optical fibers. The obtained results are comparable, in terms of variety of detected defects, with the Ge-doped sample (the spectra decomposition could be found in [79]). The main difference, as already observed comparing the RIA in the PSC and F-doped OF, is a systematic higher tolerance to the radiation, confirming that the fluorine decreases the RIA related to the strain-assisted STHs absorption bands in both types of optical fibers. As already done for the PSC and F-doped OF, the defect decay kinetics responsible for the RIA in Ge- and Ge+F-doped fibers at both temperatures were extracted. The obtained results are reported in Figure 4.17 with the corresponding fit obtained using equation 4.2. By the comparison, at LNT the Si-STH-related absorption bands have the highest recovery rate, while the Ge-STH seems more stable. The STH-defect instability shows their contribution to be negligible in the RIA spectra of the Ge- and Ge + F-doped optical fibers at RT. To better compare the different kinetic behaviors, the best fitting values are listed in tables 4.6 and 4.7. In particular the analysis of the defects kinetics, depicted in Figure 4.17 in which are represented both the Ge-doped and Ge+F-doped fibers, highlights a new and important evidence: our results provide a clear linear correlation between the GeX and GeY centers kinetics.

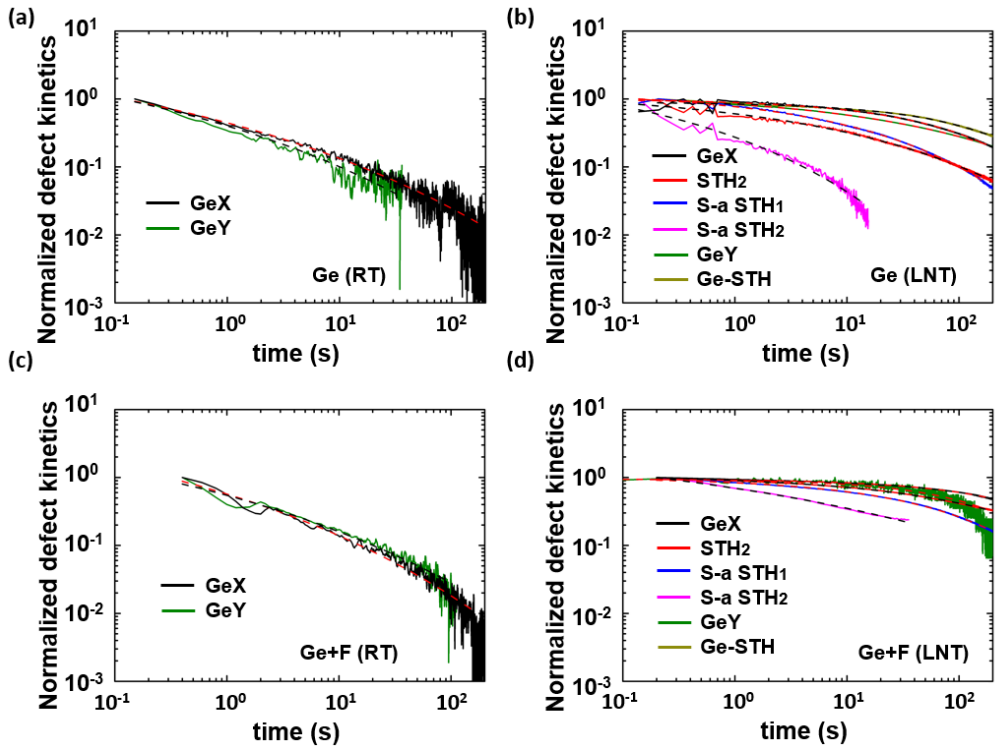

Figure 4.17. Normalized decay kinetics of the defects as extracted from the fitting routine for the Ge- and Ge+F-doped samples, at RT (a) and (c) and at LNT (b) and (d), with a total accumulated dose of ~10 Gy(SiO_2). The line in color are: in black the GeX, in red the STH_2, in blue the strained-assisted STH_1, in magenta the strained-assisted STH_2; in green the GeY and in dark yellow the Ge-STH. The dashed lines are the fits relative to the overlapped defects kinetics. Figure taken from [79].

As already mentioned above, the very important feature shown by Figure 4.17 involves the similarity between the GeX and GeY kinetics in both germanosilicate fibers and at both temperatures, as highlighted by the close values for the parameters given in tables 4.6 and 4.7. Even if temperature strongly affects the recovery rates, the two defects follow the same kinetics. To better highlight this relationship between these two defects, not yet identified in terms of structure, we investigate the GeY absorption band area dependence on the GeX area, as depicted in Figure 4.18.

Table 4.6. N(0), k and β fit values obtained before the normalization routine, used to reproduce the kinetics in Figure 4.17, describing the Ge-doped response.

Parameter	GeX	STH_2	s-a STH_1	s-a STH_2	GeY	Ge-STH
N(0) (dB/m) at RT	14				0.3	
N(0) (dB/m) at LNT	10	8.2	3	0.83	0.6	0.02
k (s^{-1}) at RT	1540				2500	
k (s^{-1}) at LNT	0.014	0.42	0.16	34	0.038	0.007
β at RT	0.15				0.15	
β at LNT	0.49	0.25	0.34	0.25	0.29	0.54

Table 4.7. N(0), k and β fit values obtained before the normalization routine, used to reproduce the kinetics in Figure 17, describing the Ge+F-doped response.

Parameter	GeX	STH_2	s-a STH_1	s-a STH_2	GeY
N(0) (dB/m) at RT	7.6				0.1
N(0) (dB/m) at LNT	9.8	3.4	1.4	1.2	0.3
k (s^{-1}) at RT	1500				2000
k (s^{-1}) at LNT	0.0024	0.009	0.19	40	0.006
β at RT	0.16				0.15
β at LNT	0.55	0.35	0.45	0.15	0.6

These results show a good linear dependency between the GeY and GeX kinetics for all the tested conditions and fibers. Even if dedicated experiments are needed to determine the nature of this relationship, two hypotheses could be suggested to explain this linear tendency: the first one is that the two defects could be generated from the same precursor site and could also recombine together; the second one is that the two absorption bands could indeed be related to the same defect structure. It could be interesting to compare this behavior with the observations done in ref. **[95]** under γ-ray steady state irradiation, in which an anti-correlation has been clearly shown between the intensities of the GeX and GeY absorption bands as a function of the temperature of irradiation.

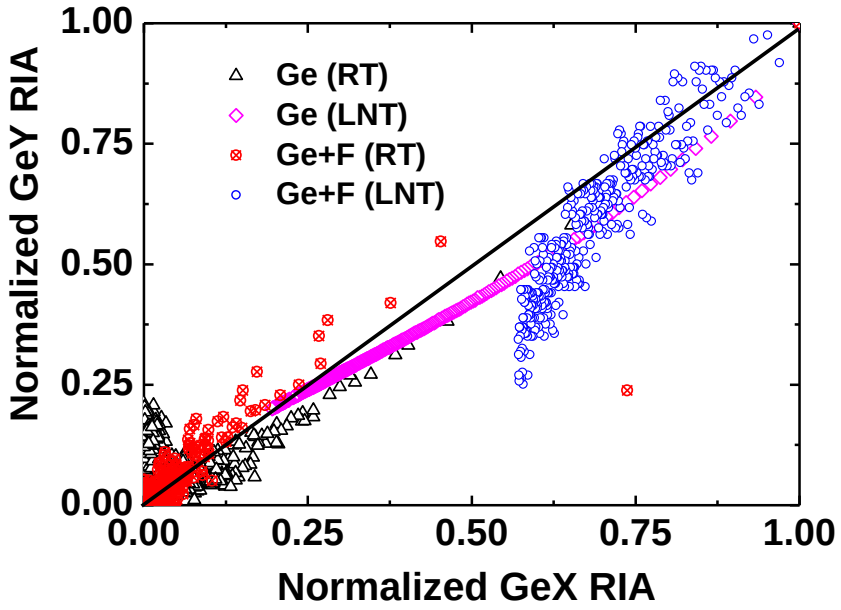

Figure 4.18. Dependence of the normalized GeY area versus the normalized GeX area. The black continuous line has a slope of 1. Figure taken from [79].

This apparent contradiction could be understood considering different thermal bleaching efficiencies for the two defects generated simultaneously from the same precursor site. The first hypothesis seems then more probable than the second that could not explain the results in ref. [95]. According to this framework, under pulsed ionizing irradiation, the same precursor site generates both GeY and GeX defects, and these defects mostly recover by direct recombination, justifying the linear correlation of the recovery kinetics at fixed temperature. Under steady state irradiation and varying the temperature of irradiation, it is evident that an additional process related to thermal bleaching should be considered in ref. [95]. The GeY bleaching is more efficient than the GeX one (almost flat as a function of the temperature in the tested range), justifying that an anti-correlation between GeX and GeY can be observed as a function of the irradiation temperature.

From our data set, finally, it appears possible to study in more depth the STHs' impact on the Ge-doped fiber radiation responses at LNT. To this purpose, Figure 4.19 compares the kinetics of the normalized STHs' kinetics areas of all the tested canonical samples. Furthermore, since the GeX absorption band overlaps strongly with the STH_1 one, seems to assume the same behavior during the fitting routine. Therefore, it is interesting to investigate the possible relationship

between these two defects, to understand if the GeX represents a variety of the inherent STH_1 structure, in a matrix disturbed by germanium presence. The GeX decay kinetics are thus compared to the ones of the inherent STH_1 in Figure 4.19.

Assuming the hypothesis that the GeX could represent a variety of the inherent STH_1 structure when surrounded by germanium atoms, Figure 4.19 highlights the strong STHs instability in the Ge-doped fiber in all the presented cases. In presence of Ge, the STH defects are bleached faster than in the PSC optical fiber. This could be assigned to germanium presence in the silica matrix, which distorts the structure making the STH sites in the lattice more unstable. The same tendency was observed when comparing the inherent STH_1 and the GeX, even if further studies, including theoretical calculations, appear necessary to underline this possible correspondence.

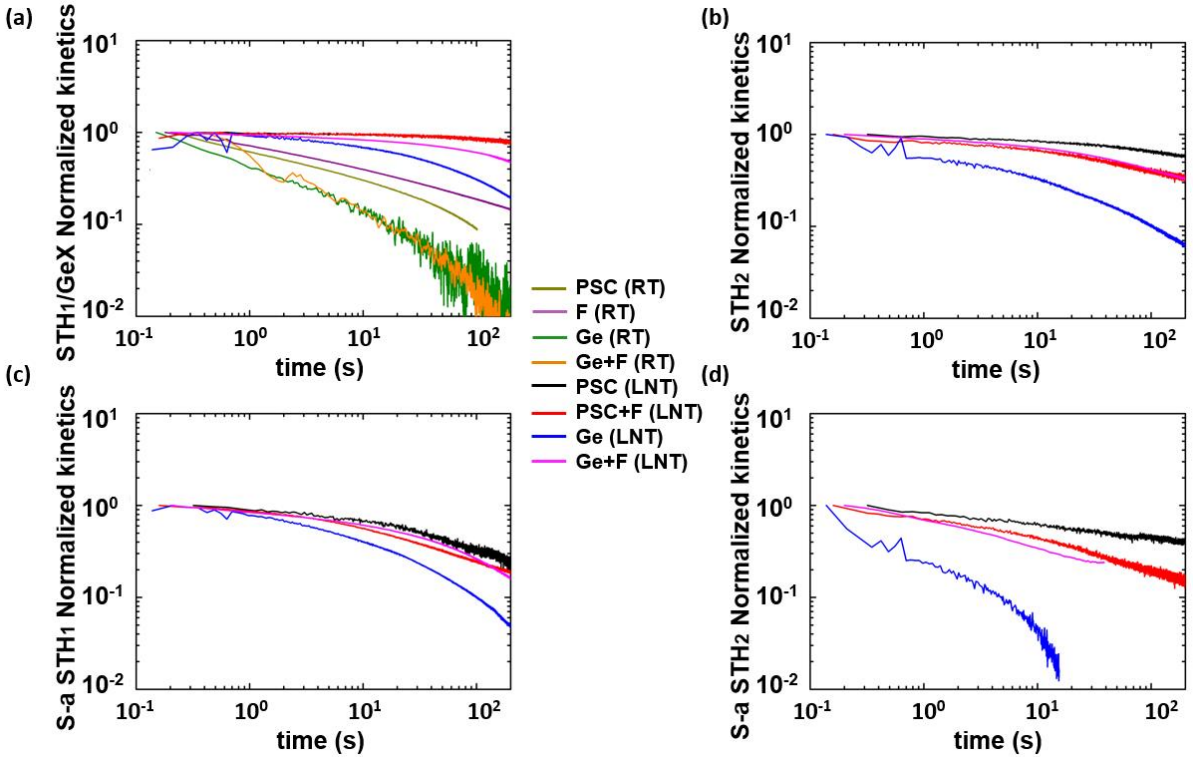

Figure 4.19. Normalized STH-related absorption bands area obtained by the fitting routine for all the samples. Inherent STH_1 for the PSC and F-doped and GeX for Ge- and Ge+F-doped fibers (a), Inherent STH_2 (b), strained-assisted STH_1(c) and strained assisted STH_2 (d). Figure taken from [79].

4.6. P-doped optical fibers

4.6.1 RIA measurements

Regarding the P-doped OFs results, illustrated in Figure 4.20 at RT and LNT, one second after the X-ray pulse, the fiber response is investigated between 500 nm and 1300 nm. The shape of the RIA spectra is quite similar at the two temperatures, suggesting close defects generation. The candidate to explain the attenuation in the NIR is the P1 center, having an absorption band peaked at ~1500 nm. Moving towards the visible range, our results provide evidence for differences in the RIA spectra, in the domain where the stable and meta-stable phosphorous-oxygen hole centers (respectively s-POHC and m-POHC) contribute, with absorption bands in the [500 – 600 nm] spectral range.

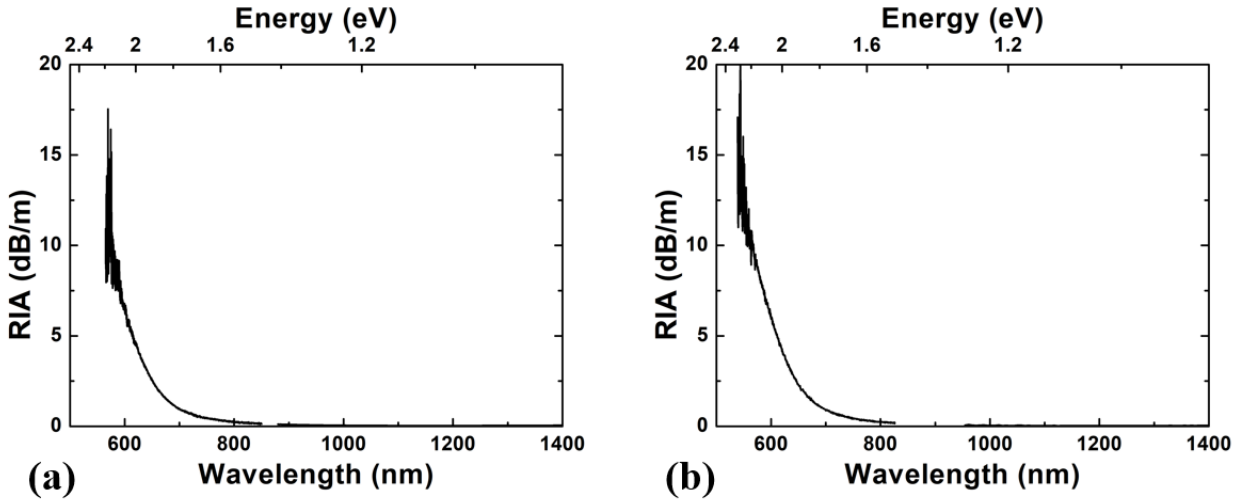

Figure 4.20. RIA spectra measured 1 s after the X-ray pulse for the P-doped optical fibers ((a) RT and (b) LNT), with a total accumulated dose of ~10 Gy(SiO_2).

Since the fiber responses of the P-doped are almost identical at the two temperatures, it is possible to assume that the same generation efficiency is observed for these various defects in these cases. The RIA kinetics post-pulse are almost the same, as highlighted by Figure 4.21. It is important to note that between 1.2 eV and 1.8 eV, even if it is difficult to observe because of the overlap between the spectra at the two temperatures, at RT the RIA experienced a little recovery

(black curve is the RIA at RT 0.6 s after the X-ray pulse, the green one is 200 s after the pulse). As already argued in [87], this could be related to the strained-assisted STHs absorption bands. No recovery was detected in the LNT spectra probably due to the slowdown of the defects bleaching kinetics at low temperature.

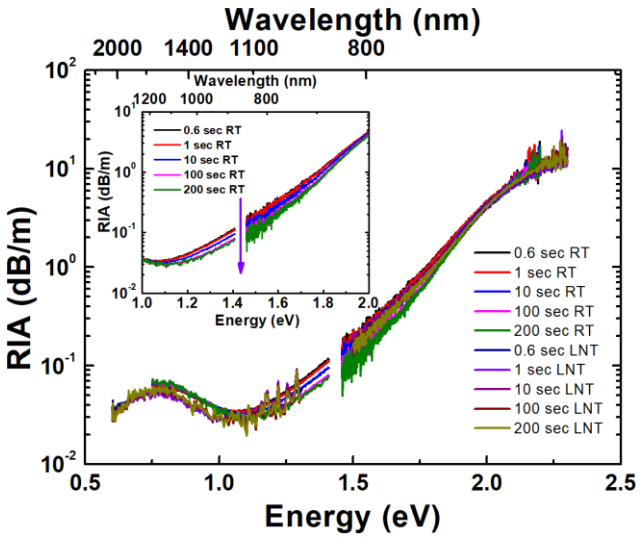

Figure 4.21. RIA spectra recorded for the P-doped optical fiber at RT (starting from the upper black curve: 0.6, 1, 10, 100 and 200 s) and LNT (starting from the navy curve: 0.6, 1, 10, 100 and 200 s) at different times after the X-ray pulse, with a total accumulated dose of ~10 Gy(SiO_2). In the insert is reported the zoom around 1 eV and 2 eV to highlight the recovery of the RIA at RT.

4.6.2 Spectra decomposition

To better understand the nature of point defects contributing to the transient response of P-doped fibers, the RIA spectrum has been reproduced in Figure 4.22 using the set of known P-related defects with the absorption bands' main characteristics listed in table 4.8. The IR- RIA is explained by the P1 defects at 0.79 eV but the global fitting function also reveals that at least another defect is needed to fully reproduce the experimental data. Further studies will be necessary to identify the defect(s) associated to this optical contribution. In the UV/Vis domain, the RIA is reconstructed using the s-POHC related band at 2.2 eV and 2.5 eV. Even if our investigated spectral range is not so far in the UV, there is even the contribution of the m-POHC (peaked at 3.1 eV), negligible in our RT measurements, but still detectable at LNT.

As already observed, defect recovery is seen around 1 and 2 eV, at least at RT. Following what it was argued in [87], we introduce the strain-assisted STHs' related band to fill this lacuna, especially considering the transient nature of those defects. On the contrary, but as expected, at low temperature the RIA of P-doped OF is much more stable in this spectral range, highlighting that at low temperature the STH's stability is strongly enhanced.

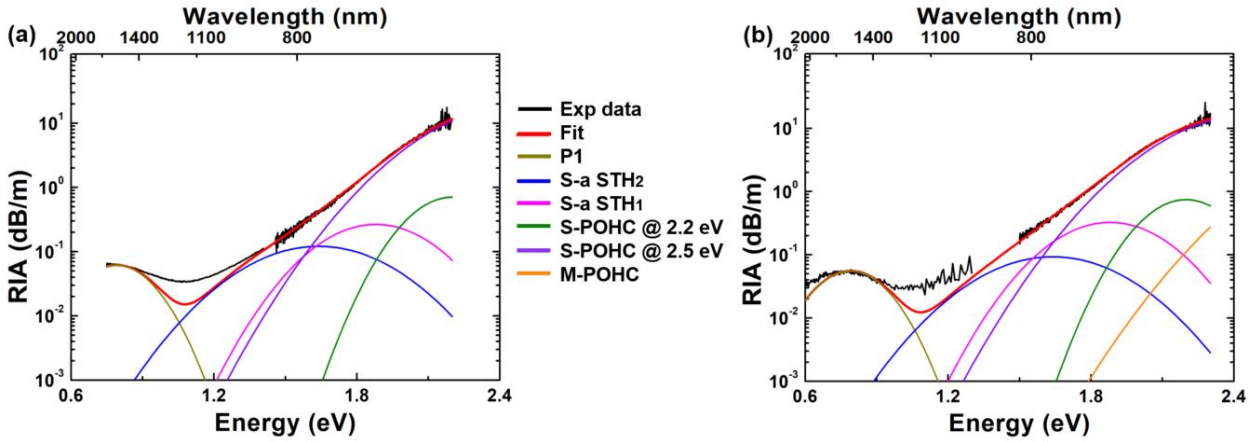

Figure 4.22. Decomposition of the RIA spectra measured 1 s after the X-ray pulse for the P-doped OF ((a) RT and (b) LNT), with a total accumulated dose of ~10 Gy(SiO_2): black line is the experimental data, the red line is the global fitting function, the dark yellow is the P1 contribution, the blue and magenta the strained-assisted STH_2 and strain-assisted STH_1 contribution, respectively, in green the s-POHC at 2.2 eV absorption band, in purple the s-POHC at 2.5 eV contribution and in orange the m-POHC absorption band.

However, as expected by the fits, the area value of the all involved defects is consistent within the uncertainty of the measurement (~10%), reflecting that the transient response of P-doped fiber is almost temperature independent. The main difference concerns the slight bleaching kinetics observed at RT in the visible domain. To reproduce the experimental data, it was not necessary to add the contribution of the inherent STH's related absorption bands, probably because it is negligible in this fiber compared to the influences of s-POHC at 2.5 eV and/or the m-POHC.

Table 4.8. Parameters of the Gaussian absorption bands associated with a variety of P- and Si-related defects. This set, from ref. [4], was used to reproduce the acquired RIA spectra.

Defect	OA peak (eV)	FWHM (eV)	RT (dB eV/m)	LNT (dB eV/m)
P1	0.54	0.35	0.02	0.018
S-a STH_2	1.63	0.60	0.08	0.06
S-a STH_1	1.88	0.50	0.13	0.16
s-POHC @ 2.2 eV	2.2	0.35	0.3	0.3
s-POHC @ 2.5 eV	2.5	0.63	14	12
m-POHC	3.1	0.73		6

The fit quality remains acceptable except around 1 eV as reported in Figure 4.23. This analysis highlights the existence of an (several) unknown defect(s) absorbing in this spectral range. Outside this spectral range, the discrepancy between the experimental data and the theoretical fitting function seems to be within $\pm 10\%$. The strong displacement observed under 0.7 eV is assumed to be due to the higher noise level affecting the LNT measurement.

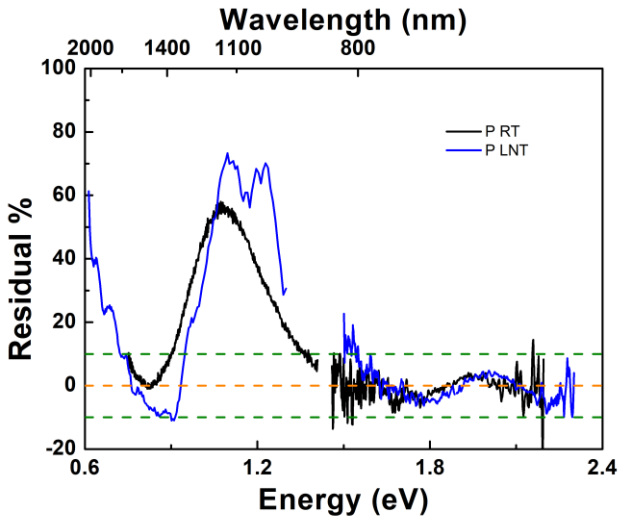

Figure 4.23. Normalized residuals between the experimental RIA data and the global fitting function: in black for the P-doped OF at RT and in blue for the P-doped OF at LNT. The green and the orange dashed lines are guide lines for the $\pm 10\%$ and the 0%, respectively.

As expected, no relevant recovery (a part a slight one in the [$500 - 600$ nm] spectral domain) is observed in the investigated time window at the two temperatures (Figure 4.24). For this reason it is impossible to apply the fractal model, since the corresponding k values will be divergent. By the way, even if it is less pronounced, the strain assisted absorption bands at RT present a slight recovery. In this framework, it is reasonable to argue that the presence of phosphorous atoms in the silica network makes the STHs more stable, presenting observable strain-assisted STHs absorption bands at RT. Further experiments will be performed in order to investigate this aspect.

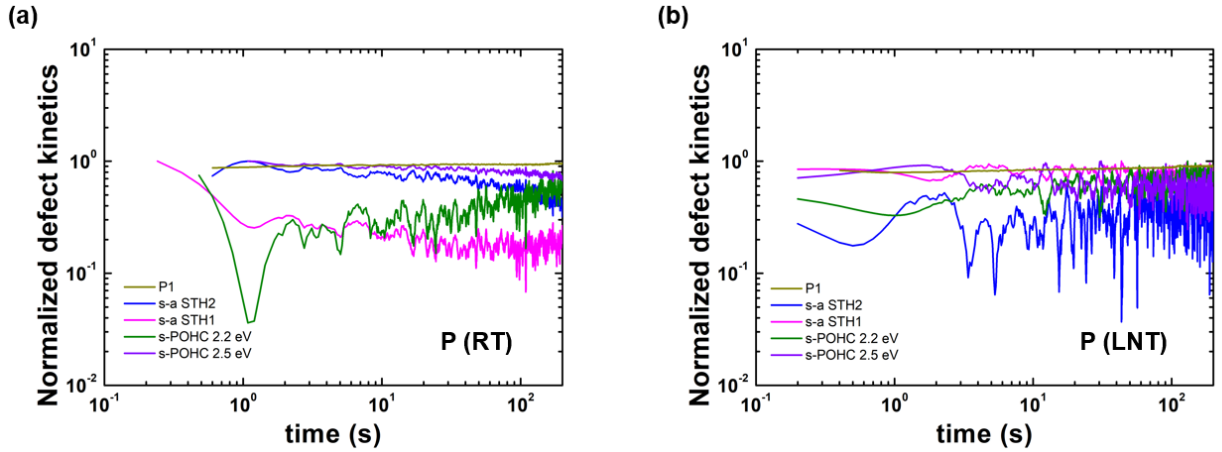

Figure 4.24. Normalized decay kinetics of the defects as extracted from the fitting routine for the P-doped at RT (a) and at LNT (b). The line in color are: in dark yellow the P1, in blue the strain-assisted STH_2, in magenta the strain-assisted STH_1, in green the s-POHC at 2.2 eV and in violet the s-POHC at 2.5 eV.

4.7. Pulsed and steady state X-ray irradiations

In the present section, we characterize the response, under steady state X-rays, of canonical samples representative of the most common fiber types differing by their core-dopants: pure silica, Ge and P. Their radiation induced attenuation (RIA) spectra were measured online at both room temperature (RT) and liquid nitrogen temperature (LNT), in the energy range [~0.6-~3.0] eV (~2100 nm - ~410 nm), highlighting the RIA growth kinetics during the fiber exposure up to an accumulated dose of ~200 Gy(SiO_2) at a constant dose rate of 100 mGy/s at RT. At LNT, the deposited doses varied between 100 and 180 Gy, with a time dependent dose rate caused by the liquid nitrogen **[87]**. In order to understand the origin of the excess losses and the difference between the RIA spectral shapes observed at the two temperatures, a spectral decomposition of the optical losses has been performed using a set of Gaussian absorption bands related to the already-known point defects.

Figure 4.25 compares the RIA growth kinetics at 1550 nm for both RT and LNT temperatures: for the PSC, Ge- and P-doped canonical samples. This figure highlights the sensitivity of the tested fibers at $\lambda = 1550$ nm.

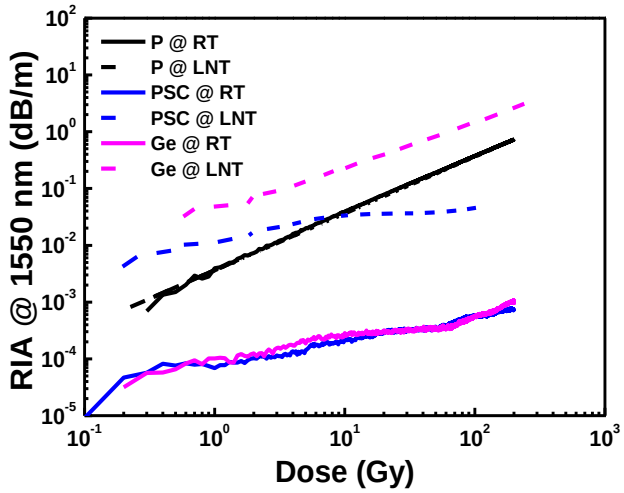

Figure 4.25. RIA growth kinetics of the canonical samples at 1550 nm during X-ray continuous irradiation up to ~200 Gy(SiO_2): continuous lines are the data acquired at RT, the dashed ones those measured at LNT. Figure adapted from [87].

At RT, the relationship between the RIA induced in the different fibers agrees with the one discussed in ref. [4]: the P-doped OF is the most radiation sensitive sample, with a measured RIA of $0.7\ \mathrm{dB/m}$ after a $\sim 200\ \mathrm{Gy}$ of total accumulated dose. Compared to the PSC (the most radiation hardened optical fiber) and the Ge-doped samples, they manifest a sharp and faster growth kinetics as a function of the dose.

Comparing the LNT and RT measurements, as already explained [101], the P-doped fiber shows the same kinetics at both temperatures. Differently, the PSC at lower temperature exhibits a higher RIA in the infrared as already observed under analogous irradiation conditions. This behavior was already observed in transient RIA measurements at shorter times ($< 100\ \mu\mathrm{s}$), because of the weaker effect of the low temperature on the defect decay kinetics. Even more evident in the case of the Ge-doped OF, presenting a very high RIA at LNT ($\sim$3 orders of magnitude higher than the value observed at RT), being the most radiation sensitive up to doses of $\sim 200\ \mathrm{Gy}$.

A more representative view of the induced point defects, could be given by the spectral investigation of the induced RIA at the two different temperatures. Figure 4.26 compares all the RIA spectra acquired after a total accumulated dose of $\sim 100\ \mathrm{Gy}$, providing evidence for a systematic increase of the OF sensibility at LNT in the whole investigated spectral range. Indeed, the most radiation-tolerant fibers, as the PSC and Ge-doped OFs, that have at RT a measured RIA of the order of $\sim 10^{-3}\ \mathrm{dB/m}$ in the near-IR up to 10^{-1} (PSC) and 100 (Ge-doped) $\mathrm{dB/m}$ in the visible, present RIA levels at LNT of the order of $10^{-1} \div 10^{0}\ \mathrm{dB/m}$ (PSC) and $10^{0} \div 10^{2}$ (Ge-doped) $\mathrm{dB/m}$. In particular, as highlighted by both Fig. 4.25 and Fig. 4.26, the Ge-doped sample shows an impressive increase of the induced RIA, becoming the most radiation sensitive fiber type at LNT. The same tendency, although less pronounced, is observed for the P-doped sample (at least in the UV/visible part of the spectrum).

All results show some clear differences between the RIA spectra acquired at the two temperatures, suggesting that either new absorbing induced point defects appear at LNT, or that there is a difference in their relative contributions to the RIA. A deeper study of the RIA spectra could help us to clarify the origin of the difference in the measured RIA.

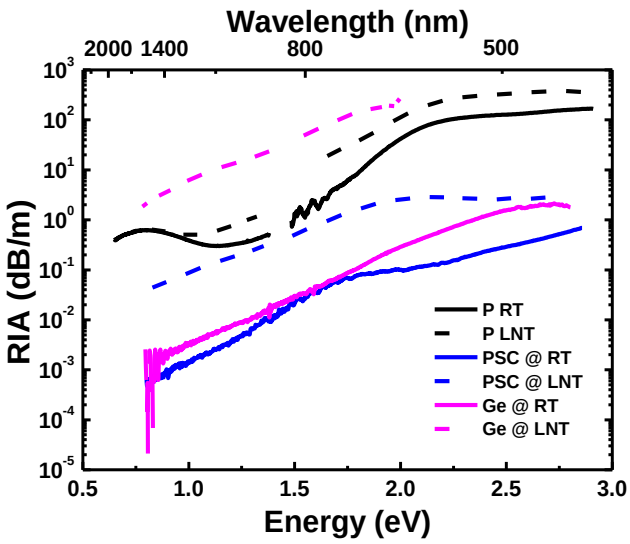

Figure 4.26. Comparison between RIA spectra of the canonical samples at a total accumulated dose of ~100 Gy(SiO_2): continuous lines are the data acquired at RT, the dashed ones those measured at LNT. Figure adapted from [87].

Figure 4.27 shows the achieved fit of the experimental data obtained for the PSC OF at RT and LNT. The parameters are listed in table 4.9. It is important to underline that when the value is not reported, it means that the contribution from the corresponding defect, if present, is under the detection limit of our analysis.

As observed under pulsed X-ray irradiation, the spectra analysis reveals that the difference in the RIA spectra at LNT and RT could be related to the changes regarding the STHs absorption bands. Indeed we observe an increase of ~1 order of magnitude in the STH_1 absorption bands and ~2 orders of magnitude for the feature characteristic of the strain-assisted STH_2. Moreover, the change in the shape around ~2 eV is due to the appearance of the STH_2 absorption band that is negligible at RT. An important contribution due to the Cl-related defects is also present, Cl_2 and Cl^0, these impurities being dependent on the manufacturing processes. Unfortunately, notwithstanding the presence of absorption in the near-IR (the tail of the 1.6 eV absorption band), the set of defects used to fit the data is not efficient enough to explain the losses in the IR (under ~1.2 eV), that could be due to the non-Gaussian absorption band related to the strain-assisted STHs.

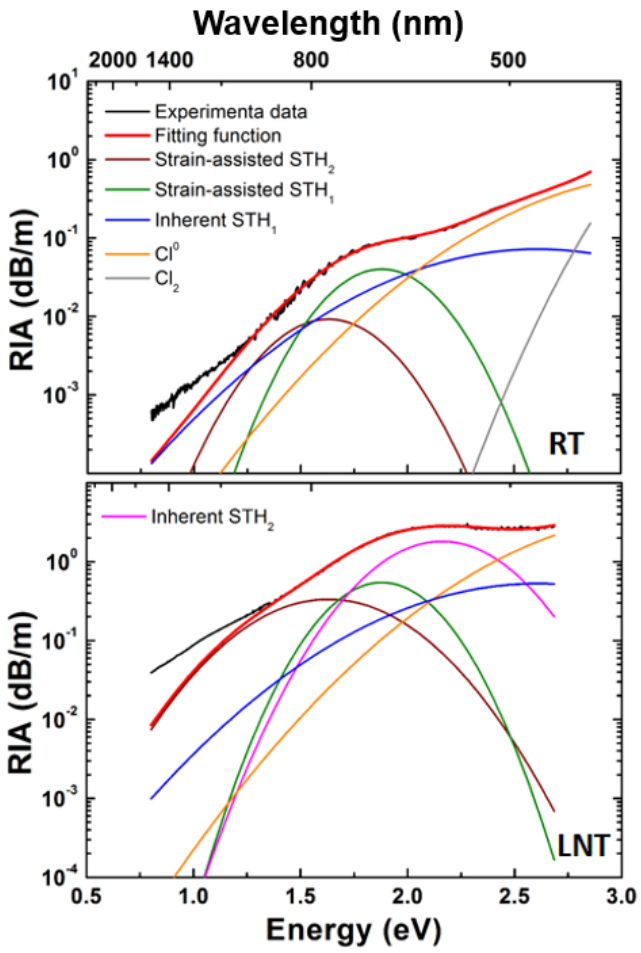

Defect	OA peak (eV)	FWHM (eV)	RT (dB eV/m)	LNT (dB eV/m)
S-a STH_2	1.63	0.6	0.005	0.25
S-a STH_1	1.88	0.5	0.02	0.3
Inherent STH_2	2.16	0.6		1
Inherent STH_1	2.61	1.2	0.09	0.7
Cl^0	3.26	1.2	0.8	5
Cl_2	3.78	0.7	13	

Table 4.9. Parameters of the Gaussian absorption bands associated with a variety of PSC related defects. This set was used to reproduce the RIA spectra generated by an X-ray continuous irradiation at the two temperatures. Parameters are taken from ref. [4].

Figure 4.27. Decomposition of the RIA spectra, in the PSC OF at RT (upper panel) and LNT (bottom panel), after an accumulated dose of ~100 Gy: black lines are the experimental data, the red line is the global fitting function, the brown line is the strain-assisted STH_2, the olive line is the strain-assisted STH_1, the magenta line is the inherent STH_2, the blue line is the inherent STH_1, the orange and the grey lines are the Cl^0 and the Cl_2 contributions, respectively.

Figure 4.28 compares the Ge-doped OF spectra acquired at the two different temperatures, at an accumulated dose of ~100 Gy. The RIA at LNT is ~3 orders of magnitude higher than the one measured at RT in the whole studied range, highlighting a strong temperature dependence on the radiation sensitivity. As argued previously for pulsed X-ray irradiation, the STHs absorption bands play an important role at LNT even in the case of Ge-doped optical fibers, between ~1.5 eV and ~2 eV. Indeed, the shape differences between these two spectra could be explained by the presence of strain-assisted STH absorption bands.

The fitting depicted in Figure 4.28 is based on the defects presented in table 4.10. By the way, to explain the strong increase of the RIA at LNT, the contribution of the STH related absorption bands is not sufficient. Indeed, we noted a high increase of the concentrations of Ge-related point defects, which implies an amplitude growth of ∼3 orders of magnitude.

Regarding the P-doped OFs response, illustrated in Figure 4.29, the shapes of the RIA spectra are almost similar in the near-IR (up to ∼1 eV) at the two temperatures. Moving towards the visible range, our results provide evidence for differences in the RIA spectra, differently from what we have observed under X-ray pulsed irradiation. Based on these observations, the attenuation induced at LNT in the P-doped fibers seems explained by a difference in the relative contributions of the absorption bands of the various P-related defects. As shown by table 4.11, at LNT the generation of the s-POHCs and m-POHCs seems enhanced by at least a factor ∼2, whereas the concentration of P1 defects seems unaffected in this temperature range. The discrepancy between the RIA spectra in Figure 4.29, can be attributed to the increase of the STH strain-assisted absorption bands, more stable at lower temperatures. Indeed, even if the P-doped fiber RIA is characterized by highly stable defects, it is also known that this class of fibers has a slight recovery in the visible, as already observed under pulsed X-ray RIA, suggesting the existence of less stable defects. P-related defects induced by the irradiation can explain the RIA in the near-IR and in the UV/visible. A lack of knowledge exists regarding the RIA origin between ∼1 eV and ∼1.5 eV, stimulating new and deeper studies to improve our knowledge.

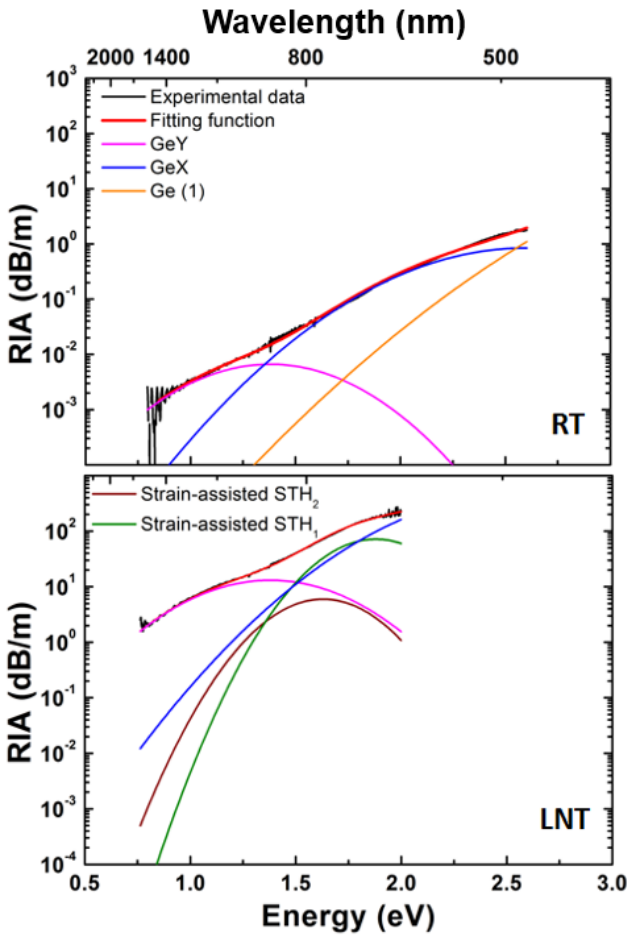

Defect	OA peak (eV)	FWHM (eV)	RT (dB eV/m)	LNT (dB eV/m)
GeY	1.38	0.71	0.005	9.8
S-a STH_2	1.63	0.6		3.0
S-a STH_1	1.88	0.5		36.0
GeX	2.61	0.9	0.85	520
Ge(1)	4.4	1.0	220	

Table 4.10. Parameters of the Gaussian absorption bands associated with a variety of Ge related defects. This set was used to reproduce the RIA spectra generated by an X-ray continuous irradiation at the two temperatures. Parameters are taken from ref. [4].

Figure 4.28. Decomposition of the RIA spectra, in the Ge-doped OF at RT (upper panel) and LNT (bottom panel), after an accumulated dose of ~100 Gy: black lines are the experimental data, the red line is the global fitting function, the magenta line is the GeY, the blue line is the GeX, the orange line is the Ge (1) and the brown and olive lines are the strain-assisted STH_2 and the strain-assisted STH_1 contributions, respectively.

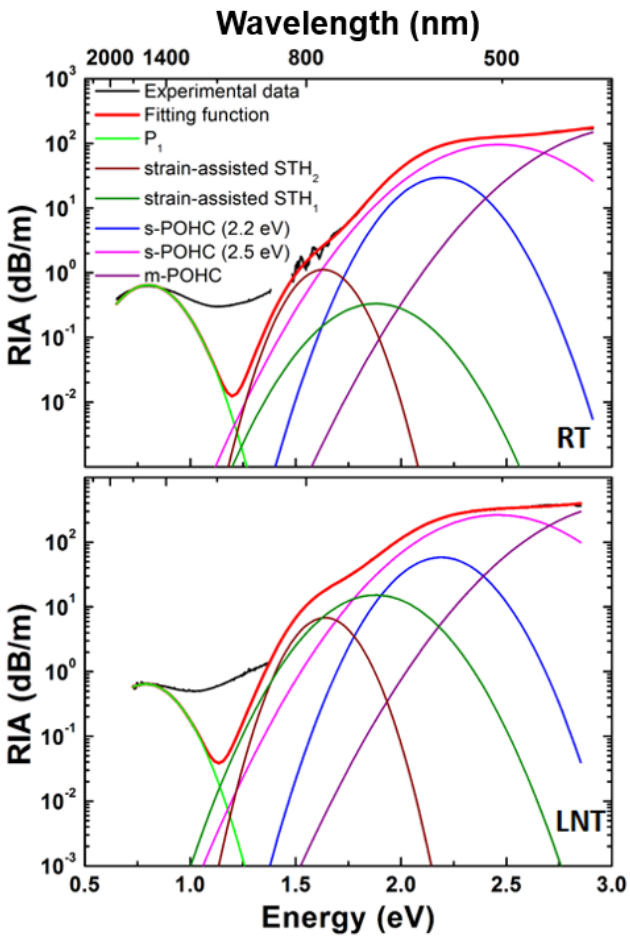

Defect	OA peak (eV)	FWHM (eV)	RT (dB eV/m)	LNT (dB eV/m)
P_1	0.79	0.29	0.2	0.2
S-a STH_2	1.63	0.6	0.34	2.1
S-a STH_1	1.88	0.5	0.17	7.5
s-POHC	2.2	0.35	13	25
s-POHC	2.5	0.63	70	185
m-POHC	3.1	0.73	140	320

Table 4.11. Parameters of the Gaussian absorption bands associated with a variety of P related defects. This set was used to reproduce the RIA spectra generated by an X-ray continuous irradiation at the two temperatures. Parameters are taken from ref. [4].

Figure 4.29. Decomposition of the RIA spectra, in the P-doped OF at RT (upper panel) and LNT (bottom panel), after an accumulated dose of ~180 Gy: black lines are the experimental data, the red line is the global fitting function, the green line corresponds to the P1 contribution, the brown and olive lines are the ones of strain-assisted STH2 and the strain-assisted STH1, respectively. Blue line corresponds to the contribution of s-POHC at 2.2 eV, the magenta line is the one of s-POHC at 2.5 eV and the purple line is that of the m-POHC.

4.8. Conclusion

In the present work, we have investigated the basic mechanisms governing the responses of canonical PSC, F-, Ge- and P-doped optical fibers when exposed to an X-ray irradiation, both pulsed and continuous. To better highlight the role of metastable defects in their transient response, we performed RIA measurements at both RT and LNT. The experiments were done online, investigating the RIA in a spectral range from the near-IR to the visible range, following the RIA spectra evolution during and after the X-ray irradiation. To identify the RIA origins in the tested ranges, we performed a Gaussian decomposition of the measured RIA spectra using point defect sets already known to be related to the dopants present in the fibers. The observed differences between the RIA spectra at RT and LNT are explained by the stronger contribution of STHs' related absorption bands at LNT. Regarding the near-IR spectral range, the RIA origins for the PSC and F-doped OFs remain still unresolved, and additional studies are required to identify the defect(s) contributing to this absorption spectral domain. However, for the two Ge-doped fibers, the used defect set is able to reproduce the RIA in the whole investigated spectral range, from the UV to the NIR. Moreover, it was clearly established a linear correlation between the kinetics of the GeY and GeX absorption bands. The nature of this correspondence need to be clarified in the future. Also the P-doped fibers exhibits unknown contribution to the RIA at ~1 eV, suggesting further experiment to reveal the defect responsible. By the way, the major results of the present investigation is to provide a detailed description of the RIA origin in canonical optical fibers at RT and LNT, highlighting the crucial role of the STHs variety of defects affecting the transmission properties of the most widespread doped optical fibers.

Chapter 5. Non-linear optical effects induced in silica by fs-laser.

Upon femtosecond laser exposure, the macroscopic consequence on wide-band gap material is a permanent refractive index change (RIC), leading the material to gain new optical properties [7]–[9], [111], [122], [126]. Indeed, the controlled translation of a single laser spot into the material bulk, depending on the experimental conditions, has the ability to induce both positive and negative RIC in the exposed region. The development of highly precise protocol for the control of the laser induced damage on transparent material has pushed forward all the technologies of integrated optics. In fact there are already applications in telecommunications, optical sensing and optical signal processing domains [7], [8], [209].

From the fundamental point of view, it is important to note that investigating the interaction between ultrashort laser pulses and transparent material new phenomena were observed: for example different types of permanent material modification and/or self-formation of organized volume nano-sheet arrays, leading to the formation of regions with birefringence phenomena [12], [14], [72], [132], [134]–[136], [210]–[212]. In order to characterize the mechanisms responsible for the structural modification, various spectroscopic studies were proposed in literature such as photoluminescence (PL) and Raman spectroscopies [13], [14], [133], [213], [214]. Indeed active PL sites were observed in the laser exposed region in fused silica, considered as a fingerprint of the type of induced modification in the glass structure. Then, further information about material network modifications could be provided by Raman spectroscopy, allowing us to obtain information about the atomic reorganization.

Actually, several fundamental questions remain unresolved, leading to an incomplete understanding of the modified silica structure. For example, the amorphous silica glass equally may experience a combination of structural relaxation, leading to either a positive or negative RIC, but also to defect formation [7]–[9], [111], [122], [126]. In this framework, the number of studies concerning defects generation under femtosecond laser exposure do not yet give a complete and satisfactory picture.

The present chapter will be devoted to the clarification of the defect generation in silica-based materials under femtosecond laser pulses, through combination of both post-mortem and online characterizations. First, we will focus on the induced defects under femtosecond laser exposure at the same experimental condition which are characterized by a positive refractive index change [10], [213], [215]–[217], studying the damage (which is represented by an inscribed waveguide) as a function of the laser power, deposited energy and laser wavelength. The investigation of the laser-material interaction will be performed with PL and Raman spectroscopies, but also through PCM and via the estimation of the induced refractive index change. Moreover, to provide an idea about the refractive index change contribution due to the densification (Lorentz-Lorenz relation) and on the induced defect (Kramers-Kronig relations) the sample was submitted to two selective thermal treatments. On the other hand, another study will be presented, related to the online PL induced by the laser exposure, to understand the defect generation mechanism under ultrashort laser pulses. The investigation is performed as a function of the laser deposited energy and the sample chemical composition varying the OH content. Samples under test are polished slab-shaped ($10 \times 10 \times 4\ \mathrm{mm}^3$) glasses with different OH contents: Suprasil 300 ($\mathrm{OH} < 1\mathrm{ppm}$), Herasil 1 ($150 - 400$ ppm, $\mathrm{Ge} \sim 1$ ppm) and Corning 7980 ($\mathrm{OH} > 500$ ppm), already described in chapter 3 together with the experimental setup and the irradiation conditions. Moreover, the damage is also characterized by PCM and steady state photoluminescence. Online PL measurements are done at two different excitation laser wavelengths (343 nm and 1030 nm) investigating the impact on the induced defect properties of the laser wavelength choice and/or the sample chemical composition.

5.1. Waveguides inscription as a function of the laser wavelength

The ultrafast laser manufacturing industry exploited the many advantages from the high peak intensity of the femtosecond laser pulses to induce permanent and controlled structural modifications in wide band bag materials, such as silica glasses [7]–[9], [111], [122], [126]. The induced damage leads to a refractive index variation along laser's path, with a high spatial

resolution (~μm) [7]. Such precision level is crucial for the inscription of optical waveguides or more complex 3D photonic structures [218]–[220]. Nowadays, the employment of these devices is limited by their optical losses and it is necessary to optimize the process parameters to reduce the propagation losses as much as possible.

As it is well known, the light guiding properties are strongly related to the control of the induced refractive index change. To this purpose, it is mandatory to investigate the effect of the different laser parameters during the exposure. In general, in silica glasses exposed to fs laser pulses it is possible to produce two interaction regimes: Type I, at relatively low pulse energies, and Type II at higher pulse energy. The former interaction type is characterized by an isotropic positive refractive index change along the laser path; while the latter by a negative refractive index variation [10], [221].

The effects of the laser scanning speed, pulse width, pulse shape, repetition rate, beam profile, laser polarization and focusing conditions were already widely investigated in the past years [114], [121], [213], [222], [223], whereas the impact of the laser wavelength on the waveguide properties is still unclear. However, the laser wavelength plays a key role in the femtosecond laser pulse exposure, especially in the control of the induced refractive index change [213], [224].

The purpose of the present study is the investigation of the laser wavelength influence on the waveguide direct inscription inside bulk silica, with particular interest on the induced defects generated by the high intensity femtosecond pulses. The inscription will be performed on a polished Herasil 1 slab ($10 \times 10 \times 4$ mm^3), natural glass.

The waveguides are inscribed with both UV and near-IR fs pulses as function of the scanning speed and the energy per pulse. The waveguides will be characterized in terms of induced modifications in the silica network and defects' creation. All the waveguides inscription conditions are already reported in Chapter 3. The Raman technique will be devoted to the structural modification characterization of the photo-inscribed traces, highlighting in this way the different effects on the network reorganization due to the wavelength choice. Raman scattering provides also information on the induced densification [22], [23]. The induced defects are investigated via photoluminescence (PL) spectroscopy, while the refractive index variation by the phase contrast microscopy technique. Furthermore, in order to characterize the guiding properties of such

waveguides, we have studied the optical properties of the manufactured waveguides, estimating experimentally the refractive index difference between the waveguides and the pristine glass. Finally, in order to gain more information on the nature of the induced refractive index change, the samples were submitted to two selective thermal treatments [39], [225], in order to anneal the photo-induced defects, in particular the NBOHCs. The goal of this thermal treatment is to provide us an evaluation of the defects contribution to the total induced refractive index variation.

5. 1.1 Type I and Type II responses

As already mentioned above, it is possible to induce, and then control, the optical properties of a modified glass depending on the experimental laser exposure regime [7]. In particular, amorphous silica shows different induced optical properties upon ultrafast laser pulses as a function of the irradiation conditions.

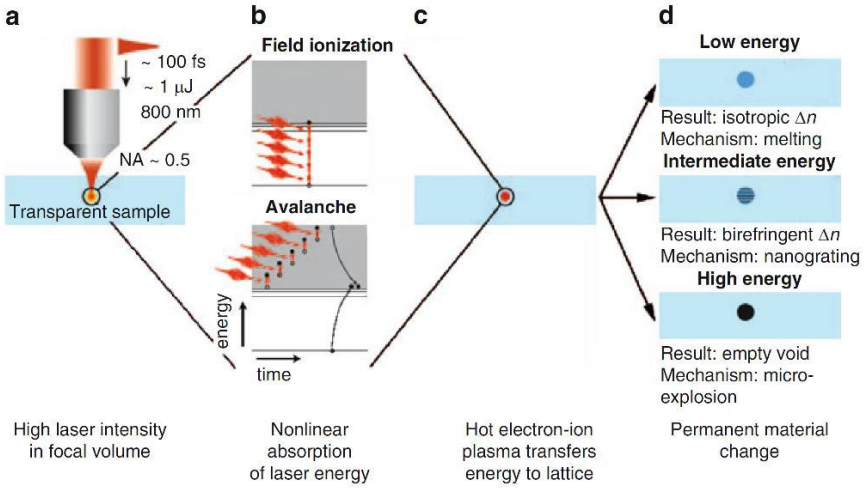

Figure 5.1. Illustration of the interaction of the focused femtosecond laser pulses and bulk silica. Adapted from [7].

Indeed, once the plasma, generated by the non-linear absorption of the incoming light, transfers its energy to the lattice, it is possible to produce different types of permanent modifications (Figure 5.1):

- **Low energy/pulse:** in the irradiated volume, a densification is observed resulting in an isotropic positive refractive index change compared to the pristine glass;

- **Intermediate energy/pulse:** the irradiated region is characterized by birefringent phenomena, due to the formation of nanogratings;
- **High energy/pulse:** formation of empty voids in the irradiated volume caused by microexplosion.

In general, in silica glasses it is possible, depending on the experimental conditions, to divide the interaction type basically in two regimes related to the type of induced RIC: Type I and Type II [7]–[9], [111], [122], [126].

Type I: this regime corresponds to moderate energy/pulse experimental conditions [7]. It is characterized by an isotropic refractive index change and then the possibility to guide the light, accompanied by a densification. Moreover, along the laser path it is possible to observe the PL band peaking at 1.9 eV and attributed to the NBOHC [3], [214]. The most accepted mechanism of the NBOHC's generation refers to the process described in Figure 1.11: after the multiphoton ionization, the relaxation process leads to the formation of STXs, which result in the E´center and NBOHC by the $Si-O$ breaking bond [72]. Figure 5.2 (a) reports a PCM image of Type I inscription, in which negative colors represent region with a higher refractive index compared the white ones; while Figure 5.2 (b) reports the NBOHC PL spectra , obtained with an excitation wavelength of $\lambda_{exc} = 325$ nm (E_{exc}=3.82 eV). The control on the positive modulation of the induced refractive index change makes Type I interaction regime of a great technological importance: fabrication of waveguides (even at three-dimensions), couplers, sensors and data storage [7], [209].

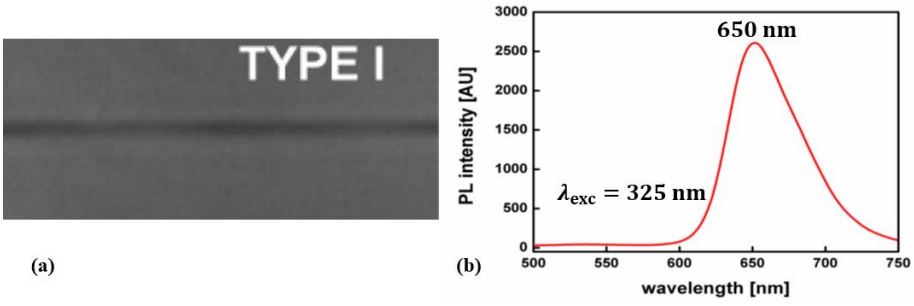

Figure 5.2. (a) Type I interaction regime in silica: black colors correspond to higher refractive index change compared to the white ones. (b) PL spectra taken in the irradiated region in Figure 5.2 (a): the 650 nm peaked band is excited with a 325 nm CW laser and is characteristic of the NBOHC PL.

Differently, the Type II interaction regime is driven by thermo-mechanical expansion, mostly caused by the high temperature reached in the focal region, resulting in negative refractive index change [7], [135], [137]. Indeed, this kind of traces provide no light guiding properties. Moreover, anisotropic phenomena are observed in the exposed region, caused by the self-organization of the material which lead to the formation of nanogratings [7], [211], [212]. In silica, the Type II inscription is associated with a decrease of the density along the laser path and with PL band peaked at 2.28 eV (545 nm) with a FWHM~0.44 eV, whose origin remains unclear [14], [226]. Figure 5.3 (a) and (b) report the PCM images of a Type II inscription and the 545 nm peaked PL band excited with a laser centered at 325 nm, respectively. The possibility to control the induced birefringence and the associated anisotropic scattered light of the ordered self-organized nanostructures leads to the design and the fabrication of polarization sensitive devices [7], [209], [227], [228].

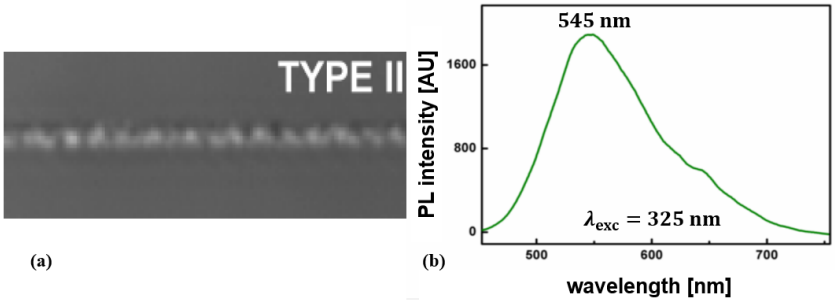

Figure 5.3. (a) Type II interaction regime in silica: black colors correspond to higher refractive index change compared to the white ones. (b) PL spectra taken in the irradiated region in Figure 5.3 (a): the 545 nm peaked band is excited with a 325 nm CW laser.

5. 1.2 Optical properties and phase contrast microscopy

To probe the light guidance properties of the waveguides, we have studied the induced refractive index contrast with a PCM microscopy (ZEISS AXIO microscopy). The induced damage, according to the PCM measurements in which black colors correspond to positive refractive index changes and white to negative ones, is coherent with the Type I interaction regime, having isotropic smooth positive refractive index changes. Type I enables the light guiding into the inscribed traces. Figure 5.4 reports the PCM image of the inscribed waveguides, with the

refractive index profile in grey level and the output mode of the corresponding waveguide. No waveguide is observed using the 1030 nm femtosecond pulses at 1.20 μJ/pulse at any scanning speed. From Figure 5.4 and at fixed energy per pulse, the higher refractive index contrast is measured for the lower scanning speed, because of the higher deposited energy per μm. Indeed, at 1030 nm with a scanning speed of 100 μm/s and 1.30 μJ/pulse, there are stronger modifications for the inscribed waveguides, being probably at the Type I/Type II threshold, manifesting some periodical structures along the trace, losing in this way its isotropic characteristic. Also, the waveguides inscribed using the laser pulses at 343 nm are already type II at a scanning speed of 100 μm/s and 0.35μJ/pulse. Moreover, comparing the sample trace modifications produced at different laser wavelengths, the higher refractive index contrast is observed in the waveguides inscribed with the UV wavelengths.

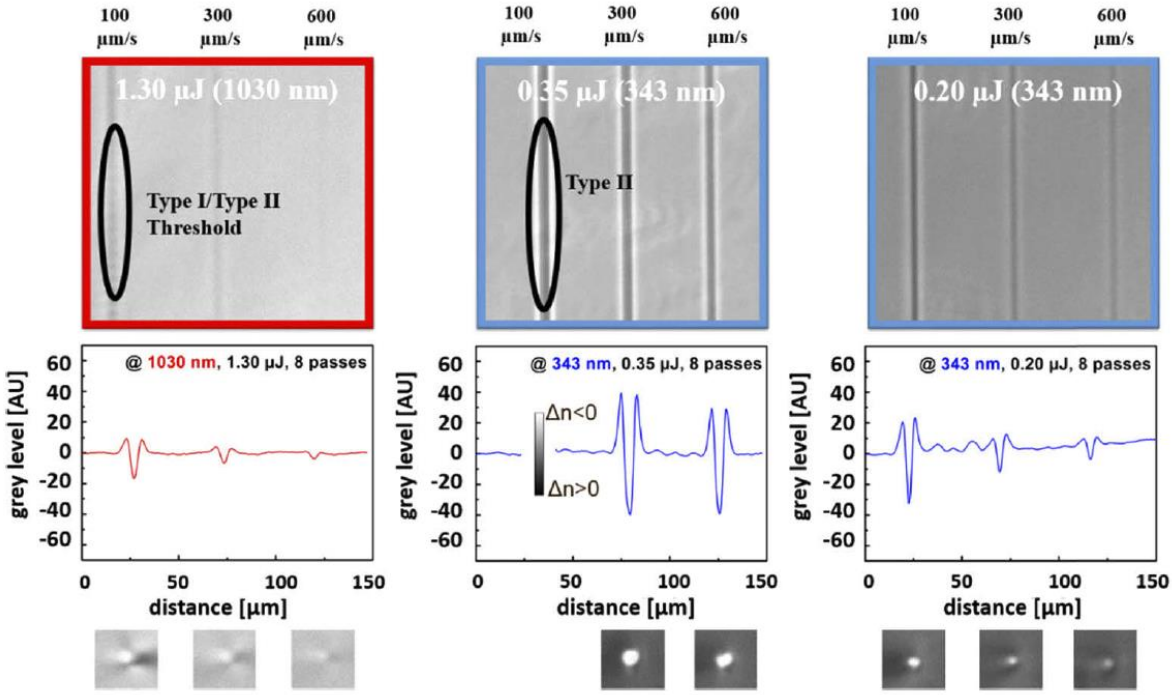

Figure 5.4. Top panel: PCM images as a function of scanning speed of the waveguides inscribed with the following experimental conditions: left at 1.30 μJ/pulse @ 1030 nm, in the center at 0.35 μJ/pulse and at right at 0.20 μJ/pulse both @ 343 nm. Medium panel: refractive index contrasts in grey levels. Bottom panel: output mode of the waveguides cross sections. Figure adapted from [139].

Coherently with the above arguments, the mode cross section is acquired in correspondence of the output of the waveguides. Figure 5.5 reports the near-field normalized large-band guided mode of the traces shown in Figure 5.4. From the normalization, it is easier to appreciate the mode confinement in the waveguides inscribed using the laser in the UV domain, resulting in better guiding properties under different experimental conditions, compared to the waveguides' transmitted mode inscribed at 1030 nm, whose confinement strongly depends on the writing parameters. Therefore, to evaluate the waveguides losses around 1550 nm (third telecommunication window), which is crucial in case of fiber-waveguides coupling, we have used the optical backscatter reflectometer (OBR 4600) from Luna technologies. The OBR measurements give transmission losses of the injected light in the [0.9 – 1.2 dB/cm] range for near-IR waveguides, in agreement with the results in literature [229], and between 0.4 dB/cm and 0.6 dB/cm for the UV waveguides.

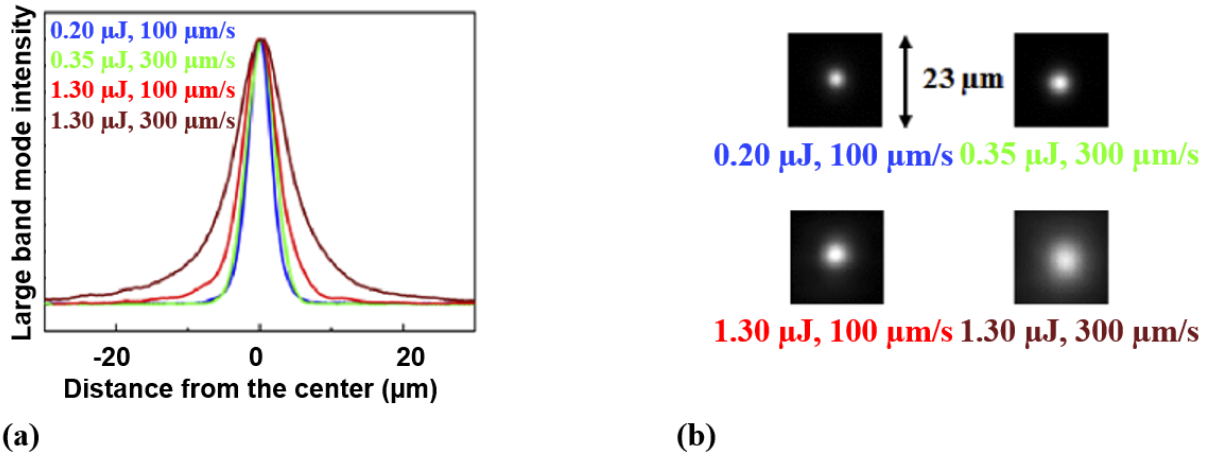

Figure 5.5. Normalized large band mode (a), with the corresponding measured spot at the waveguide outputs (b), of the inscribed waveguides: 0.20 µJ/pulse, 100 µm/s @ 343 nm in blue, 0.35 µJ/pulse, 300 µm/s @ 343 nm in green, 1.30 µJ/pulse, 100 µm/s @ 1030 nm in red and 1.30 µJ/pulse, 300 µm/s @ 343 nm in dark red line. Figure adapted from [139].

5. 1.3 Steady state PL and Raman spectroscopy

As mentioned above, after the energy deposition of femtosecond laser pulses, the hot electrons plasma relaxation transfers their energy to the ions, resulting in different structural

modification types. According to the PCM measurements, the present experimental conditions have induced smooth positive isotropic refractive index changes by defect-assisted permanent structural modifications. In the following, the inscribed waveguides will be investigated via PL and Raman measurements (using the integrated confocal micro-spectrometer ARAMIS). Figure 5.6 (a) reports the PL spectra excited at 325 nm of both the pristine sample and the waveguide inscribed at 0.20 μJ/pulse, 100 μm/s @ 343 nm. The comparison reveals the presence of the PL band of NBOHCs peaked at 650 nm in the sample exposed to femtosecond laser pulses.

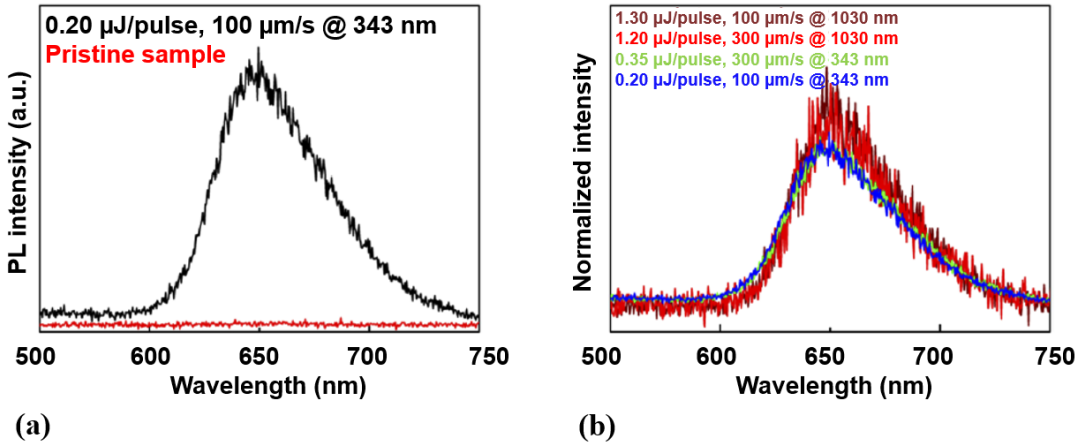

Figure 5.6. (a) Comparison between the PL spectra of the waveguide inscribed using 0.20 μJ/pulse, 100 μm/s @ 343 nm and the pristine sample (red line). (b) The normalized PL spectra of different waveguides: dark red line at 1.30 μJ/pulse, 100 μm/s @ 1030 nm, red line at 1.20 μJ/pulse, 100 μm/s @ 1030 nm, green line at 0.35 μJ/pulse, 300 μm/s @ 343 nm and the blue line at 0.20 μJ/pulse, 100 μm/s @ 343 nm. Figure adapted from [139].

Figure 5.6 (b), highlights the waveguide normalized (with respect to the total area) PL responses at different exposure conditions (irradiation wavelength, scanning speed and energy deposition). It is easy to see how, neglecting the different signal-noise ratios, the same spectral feature is present in all the inscribed waveguides, confirming that the NBOHC generation is a characteristic of Type I interaction regime, resulting as a mark of smooth positive refractive index change under femtosecond laser pulses deposition [14], [214], [226]. The most widely accepted picture of the NBOHC's generation dynamic is related to the free carrier trapping, as a channel of plasma relaxation, of the Self-Trapped Excitons. The deformation caused by the STX leads to breakage of the $Si-O$ bonds. The broken bond results in the formation of the E´ and NBOHC

paramagnetic centers [3], [65], [72]. The generation of these defects is also commonly observed in irradiated silica-based materials and is a fingerprint of the Type I regime of interaction, together with the densification along the laser path.

Indeed, in order to probe the matrix relaxation, and then the material densification after the interaction with the laser, Raman measurements were added to our investigation on the inscribed waveguides. Figure 5.7 reports the Raman spectrum of the pristine Herasil 1 sample.

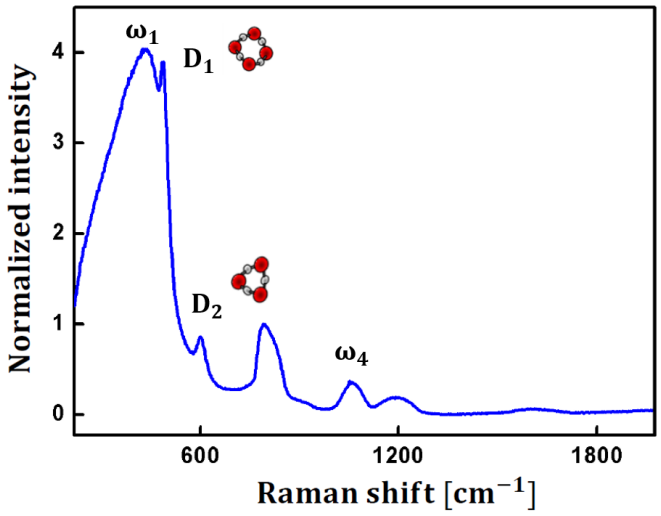

Figure 5.7. Raman spectrum of the pristine silica Herasil 1 sample.

The densification of the glass influences the following spectral features [22], [23]:

- the main ω_1 band at $440\ \mathrm{cm}^{-1}$, linked to the oxygen vibration along the $\mathrm{Si}-\mathrm{O}-\mathrm{Si}$ angle bisector of the high-membered rings. A shift of the main band is attributed to network modifications.
- The D_1 and D_2 bands, related to the breathing vibration of the 4-membered and 3-membered rings at $490\ \mathrm{cm}^{-1}$ and $605\ \mathrm{cm}^{-1}$, respectively. It is reasonable that the femtosecond laser exposition increases the number of small rings since densification is observed. For this reason an increase of these bands is expected in the densified silica.

- Also the ω_4 LO-TO (Longitudinal and transversal optical) doublet centered at 1130 cm^{-1} is a characteristic of structural modification. It highlights the $Si-O-Si$ bond asymmetrical stretching.

It is important to stress that the mark of the occurred densification could be associated by variation of the whole spectra and not to those involving only one of the above mentioned components. Figure 5.8 compares the Raman spectra before and after the femtosecond irradiation and different experimental conditions.

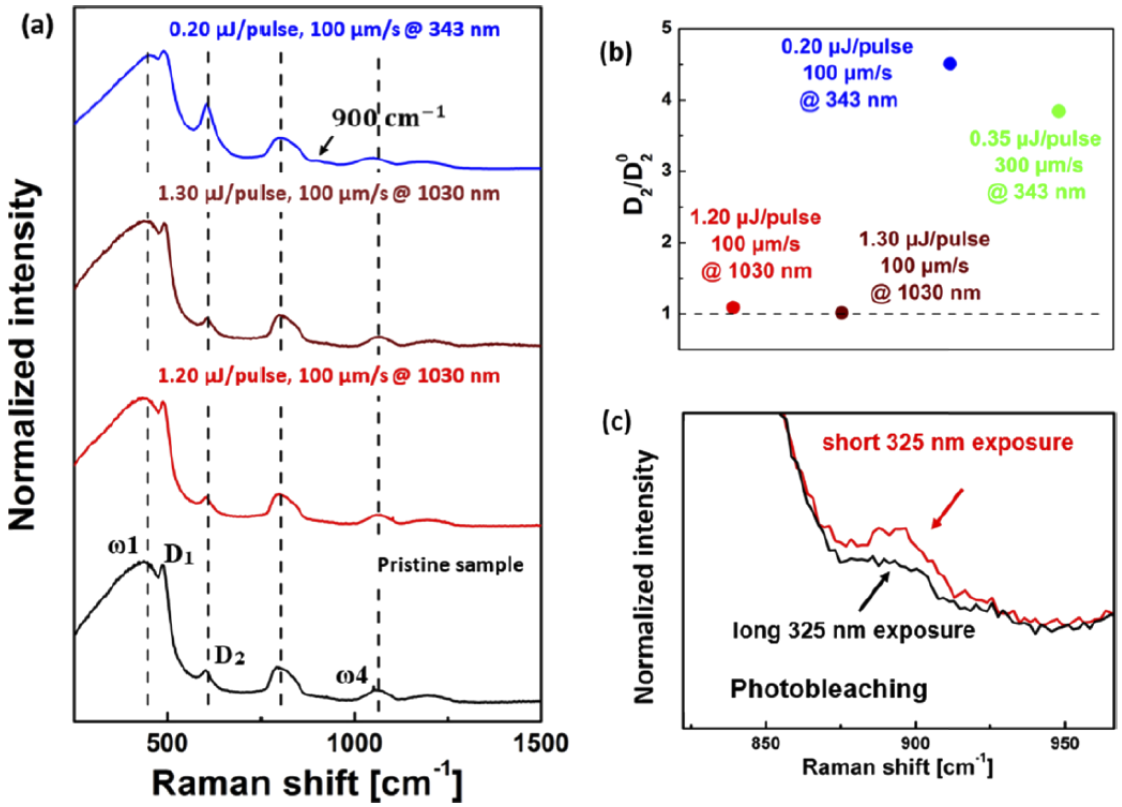

Figure 5.8. (a) Comparison of the Raman spectra measured pristine (black line) and in the irradiated at the following conditions: dark red line at 1.30 µJ/pulse, 100 µm/s @ 1030 nm, red line at 1.20 µJ/pulse, 100 µm/s @ 1030 nm and the blue line at 0.20 µJ/pulse, 100 µm/s @ 343 nm. (b) Ratio between the areas of the D_2 band of the inscribed waveguides and of the pristine sample (D_2^0). (c) Photo-bleaching investigation of the NBOHC 325 nm resonant band at 896 cm^{-1}: comparison between long (black line) and short (red line) laser exposure. Figure taken from [139].

By the comparison, reported in Figure 5.8 (a), of the pristine Raman spectra and the waveguides samples, inscribed using the laser in the UV domain, strong modifications are highlighted in the whole spectral features characteristic of the densification. For instance, a clear blue shift of the main band, from $440\ \mathrm{cm}^{-1}$ to $453\ \mathrm{cm}^{-1}$, marks of the decreasing $\mathrm{Si}-\mathrm{O}-\mathrm{Si}$ angle in the high-membered rings [230]. The LO-TO doublet exhibits a redshift, from $1130\ \mathrm{cm}^{-1}$ to $1110\ \mathrm{cm}^{-1}$ (the minimum in the center of the doublet). The different dependence on the $\mathrm{Si}-\mathrm{O}-\mathrm{Si}$ angle explains the opposite shift observed in ω_1 and ω_4. By the way, the most evident feature of the network compaction is the increase of the 3-membered ring concentration observable with the increase of the D_2 band area [231], [232], while it is not possible to evaluate the possible increase of the 4-membered rings, because of the main band overlap on the D_1 band, making any estimation of its variation very difficult. Differently, no densification and/or other structural modification signature is revealed by comparing the waveguides inscribed at $1030\ \mathrm{nm}$ and the pristine glass.

All the above-mentioned variations are clearer in Figure 5.8 (b) illustrating the ratio between the areas of the D_2 band of the inscribed waveguides and D_2 the pristine sample (D_2^0). The D_2 band amplitude increase can reasonably be associated to the material densification since the other signatures are also present. The magnitude of $D_2/{D_2}^0$ ratio for near-IR waveguides is ~ 1, while it results to be higher for the waveguides inscribed at $343\ \mathrm{nm}$ ($4-5$ times). Moreover, the laser-induced band at $896\ \mathrm{cm}^{-1}$ was also observed, in the Raman spectra acquired for the waveguide written with at $343\ \mathrm{nm}$ laser and pulse energy of $0.2\ \mu\mathrm{J}$ in Figure 5.8 (a): this spectral characteristic was observed in other samples under different classes of irradiations [214], [233]. According to ref. [234], this feature is assigned to the resonant Raman band of NBOHC at $325\ \mathrm{nm}$. In agreement with this hypothesis, the band is absent in Raman measurements with an excitation laser centered at $442\ \mathrm{nm}$, being not in resonance with this probing wavelength, but it could be also photo-bleached under long $325\ \mathrm{nm}$ exposure time as reported in Figure 5.8 (c). For the waveguides inscribed using the near-IR laser, despite the presence of NBOHC PL band, the signature of the laser-induced band at $896\ \mathrm{cm}^{-1}$ was not clearly observed.

Figure 5.8 compares the Raman responses of waveguides made with the two laser wavelengths and reveals that notwithstanding the lower energy per pulse adopted using the

343 nm laser wavelength, larger induced modifications are observed in terms of defects creation and densification.

5. 1.4 Refractive index change

To provide a qualitative evaluation of the guiding properties of the waveguides inscribed using the UV and infrared lasers, we compare in Fig. 5.9 the experimentally estimated refractive index change (Δn) as a function of the scanning speed, obtained by the procedure described in the paragraph 3.8.2. The corresponding Δn values are listed in table 5.1.

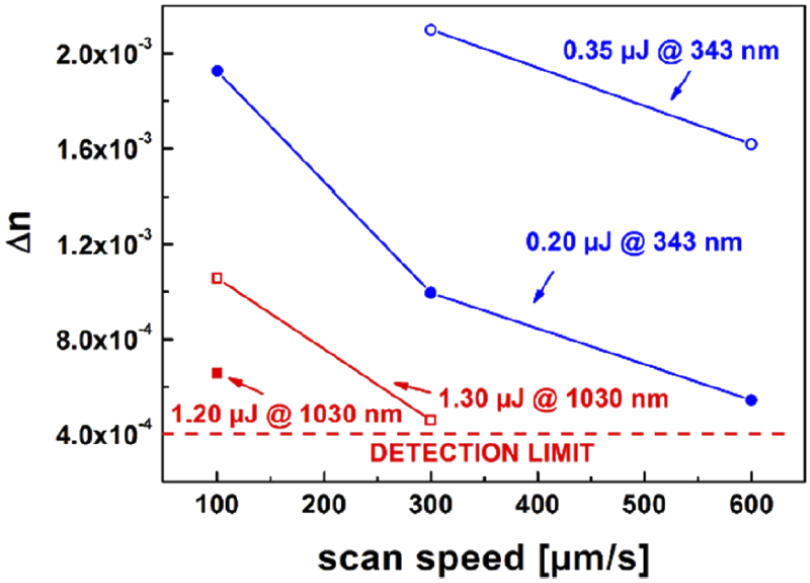

Figure 5.9. Measured Δn as a function of the scanning speed for the inscribed waveguides: empty blue circles at 0.35 μJ/pulse @343 nm, full blue circles at 0.20 μJ/pulse @ 343 nm, empty red squares at 1.30 μJ/pulse @ 1030 nm and full red squares at 1.20 μJ/pulse @ 1030 nm. Values with Δn lower than $4 \cdot 10^{-4}$ are below our detection limit. Figure taken from [139].

Table 5.1. Refractive index changes of the inscribed waveguides.

Scanning speed (μm/s)	1030 nm		343 nm	
	1.20 μJ/pulse	1.30 μJ/pulse	0.20 μJ/pulse	0.35 μJ/pulse
100	$6.6 \cdot 10^{-4}$	$1.1 \cdot 10^{-3}$	$1.9 \cdot 10^{-3}$	Type II
300	Detection limit	$4.6 \cdot 10^{-4}$	$1.0 \cdot 10^{-3}$	$2.1 \cdot 10^{-3}$
600	Detection limit	Detection limit	$5.4 \cdot 10^{-4}$	$1.6 \cdot 10^{-3}$

The measured Δn should be interpreted as an average refractive index change over the whole VIS-NIR spectral range and along the cross section of the inscribed waveguides. Figure 5.9 shows the higher Δn induced by the 343 nm laser irradiation, even at lower fluence, highlighting the better efficiency of the inscription process in the UV domain.

It is important to observe that in the present work we are comparing the efficiency of the induced refractive index contrast during the inscription and not the maximum obtained value. Indeed, using different experimental conditions, it is possible to obtain comparable or higher Δn, eg. by using 800 nm femtosecond laser pulses [214]. The explanation of the better efficiency could be linked to the different energies of the photon absorption: the multiphoton ionization, representing the main process involving the plasma generation, requires ~3 photons at 343 nm while it requires ~8 at 1030 nm, making the non-linear absorption more efficient in the UV domain [235].

5. 1.5 Thermal treatment

In chapter 1, we have described two main mechanisms which could lead the material to exhibit a positive refractive index variation: by densification (explained by the Lorentz-Lorenz relation) and through the presence of new absorption bands (Kramers-Kronig relations). In order to evaluate the contributions to the total refractive index change, due to the densification and/or to the defect generation, a thermal treatment was performed to anneal the induced defects. Indeed, the comparison of the refractive index contrast of the waveguides before and after the thermal treatment (so with the most of the defects annealed) allows estimating the induced point defects contribution to the total refractive index contrast. The first thermal treatment (TT 1) consists of

sample annealing at 500 °C (20 min). 500°C is a temperature for which the NBOHC defects should be bleached [39]. The second treatment, up to 750 °C (20 min), ensures the annealing of almost all the induced defects [225]. After a cooling down to RT, we have compared the refractive index contrast, in gray levels, of the waveguides before and after the treatments. The results are reported in Figure 5.10.

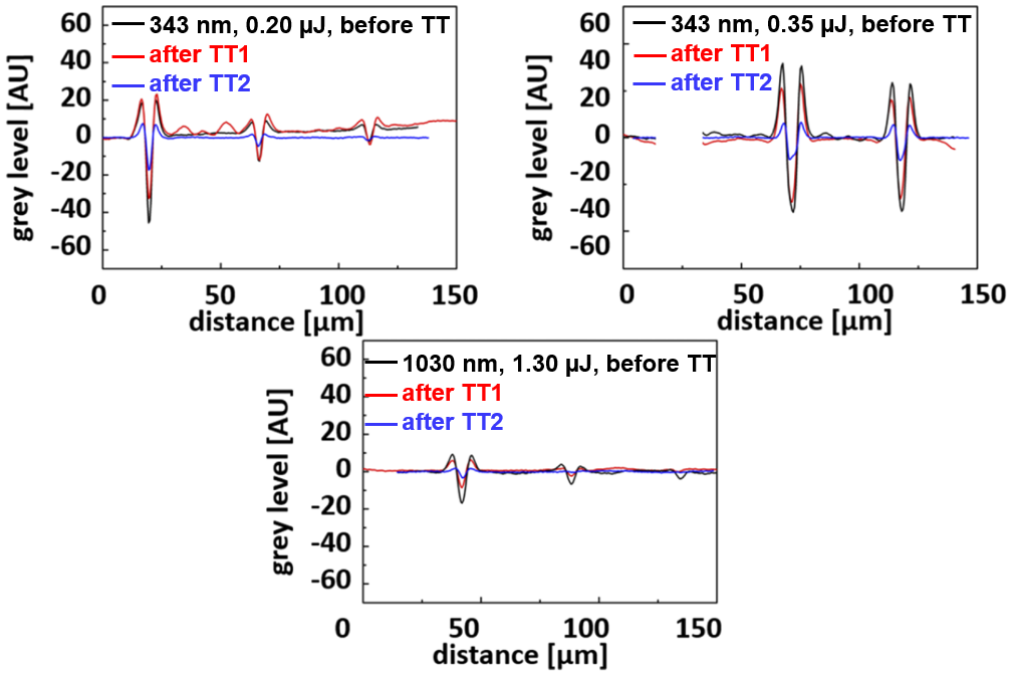

Figure 5.10. Refractive index contrasts in grey level of the inscribed waveguides before (black line) and after the thermal treatments (TT1 in red and TT2 in blue). For each graph, the waveguide at left is inscribed at 100 µm/s, in the center at 300 µm/s and at right at 600 µm/s.

In the TT 1 case (reported as the red line in Figure 5.10), the ratio between the Δn before and after the thermal treatment is around 1 for waveguides inscribed at 343 nm. It is possible to conclude that with a similar treatment the losses are reduced, because of the bleaching of the absorbing defects, without huge change in the induced positive Δn. On the contrary, the ratio between the Δn before and after the thermal treatment is of the order of 2 in the case of the waveguides inscribed at 1030 nm, highlighting a larger contribution of the defects. These waveguides are sensitive to the temperature increase. Indeed, under the second TT 2 (blue line in Figure 5.10), these waveguides are almost erased. It is clear that the contribution of other defects

than the NBOHCs is stronger compared to these ones, which are the only defects detectable with our PL or Raman measurements. TT 1 suggests that the Δn is mostly driven by the densification for the waveguides inscribed with the 343 nm laser, while TT 2 provide evidence for the defect role contribution to the total refractive index change. In conclusion, Figure 5.10 highlights the need for further studies with additional experimental techniques to discriminate between the different defects responsible of the annealed contribution observed at TT 2.

5.2. Online photoluminescence

5. 2.1 Online PL pumping at 343 nm

Synthetic dry silica

To study the induced photoluminescence under femtosecond laser pulses in a Suprasil 300 sample (Synthetic dry silica sample), the detector acquisition begins just before the beam blocker opening, starting the sample irradiation. Figure 5.11 reports the PL spectra resulting from $\sim 10^4$ pulses at a pulse peak power ~ 0.40 MW, while the inset shows the zoom in the spectral region between 2.0 eV and 3.1 eV. Two spectral features are clearly resolved in the figure: an asymmetric band peaked at ~ 1.9 eV and a Gaussian shaped band centered at ~ 2.65 eV with a FWHM~ 0.4 eV. The former could be easily associated with the PL characteristic of NBOHC, being nearly peaked at the same energy position and manifesting a specular asymmetry of the absorption band at ~ 2.0 eV [1], [3], [4], [29], [35], [88]. The origin of the other band is unclear. In fact, there are at least two luminescent defects with spectral characteristics consistent with a band around 2.7 eV: the STX (whose PL signature is in the $2.5 \div 2.8$ eV spectral range) signature is observed in both amorphous silica and crystalline quartz [64], [66], [69]–[72], and the ODC (II) has a PL band peaked at 2.7 eV [1], [3], [4], [32], [35], [51], [52], [236]. Moreover, a contribution coming from the plasma scattered light is observed [7], [13], [188], [189].

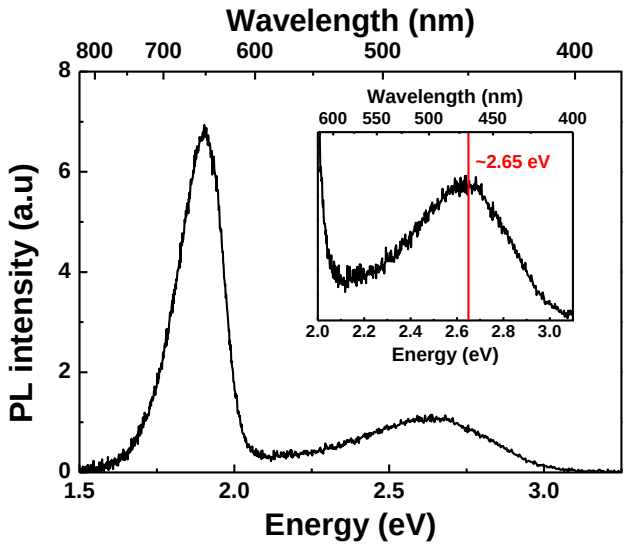

Figure 5.11. Suprasil 300 PL spectrum acquired with 343 nm femtosecond laser: after $\sim 10^4$ pulses and a pulse peak power ~0.40MW. The inset shows the zoom of the spectral region between 2.0 eV and 3.1 eV.

In order to study the dependence of the 1.9 eV and 2.65 eV peaked bands, as a function of the number of the pulses (equivalent, in the present experiment, to the irradiation dose), we report in Figure 5.12 the evolution of the spectra after different numbers of laser pulses (N_{pulses}). The inset reveals the evolution of the normalized PL intensity (I_{PL}) recorded at 1.9 eV and 2.65 eV, when increasing the laser pulses. From Figure 5.12 it is possible to understand that the two bands share the same precursor site, since their generation under multi-pulse regime is quite similar. Indeed they scale equally as a function of the number of the pulses, as demonstrated by their kinetics. In particular, it is possible to distinguish two different generation regimes: i) transient regime with I_{PL} proportional to N_{pulses}, up to ~800 pulses; ii) sublinear dependence, after ~800 pulses, suggesting an intrinsic generation process, that is described by equation 5.1 [41]:

$$I_{PL} \propto (N_{pulses})^{m} \qquad (5.1)$$

where the parameter m is between $0 < m < 1$. The best fit value is found to be $m = 0.33$. The same trend is observed in the measurements at different laser powers.

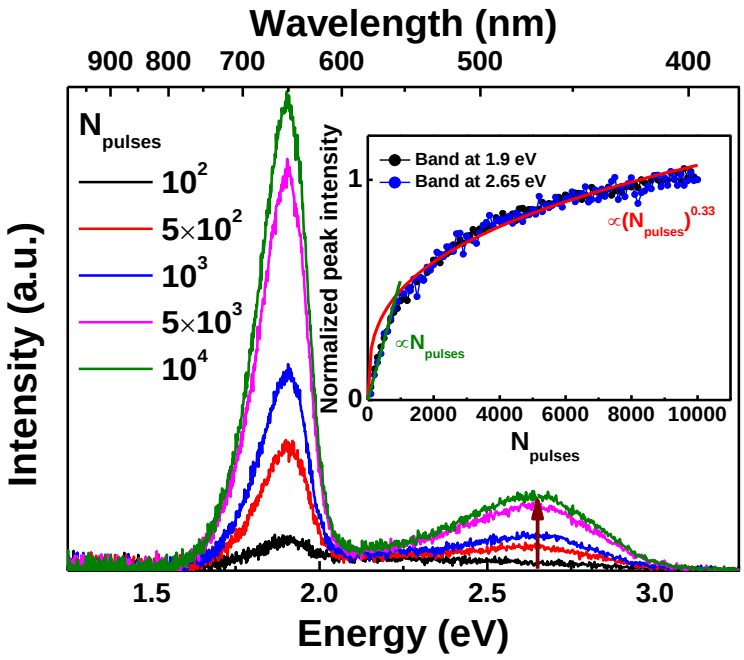

Figure 5.12. PL spectra at different accumulated numbers of laser pulses (excitation at 343 nm femtosecond laser): 10^2 pulses is the black, 5×10^2 in red, 10^3 in blue, 5×10^3 in magenta and in green after 10^4 pulses in Suprasil 300. In the insert the normalized peak intensity kinetics measured at ~0.40MW, normalized to the PL value at 10^4 pulses, at 1.9 eV and 2.65 eV, in black and blue respectively. The red line represents the best fit according to equation 5.1.

According with the observed spectra, it is possible to argue that the NBOHCs' generation is a consequence of $Si - O - Si$ breaking bond. As already discussed in the first chapter, when the $Si - O - Si$ bond is stretched enough, its breaking under laser irradiation is likely with the creation of the NBOHC and E´ center. Therefore it is also reasonable to argue the corresponding generation of E´ center in couple with the NBOHC's generation. Unluckily the E´ center is not a PL active color center, then it is not possible to confirm this hypothesis through our measurements.

Since the incoming photons are not resonant with any absorption band in the pristine sample, no linear processes are expected under an excitation at 343 nm (3.62 eV). The observed photoluminescence could be a consequence of the electron relaxation after a band-to-band transition, suggesting a multiphoton process regime. Then, it is possible to support the above discussed hypothesis studying the PL intensity as a function of the pulse peak power. Indeed, as already stated by equation 1.46, in multiphoton absorption regime $I_{PL} \propto I_l^n$, where I_l is the incoming laser intensity and n is the number of photons necessary to realize the investigated

transition. Figure 5.13 reports the evolution of the integrated PL area (over [1.5 eV – 3.3 eV] spectral range) as a function of the pulse peak power. Two distinct regimes are involved: i) a linear response for acquisitions up to 500 pulses and ii) a sub-linear response for acquisitions after 10^4 pulses with n∼3. Moreover, the rescaled responses exhibit the same behavior for two different pulse numbers of 500 and 10^4 respectively. In addition, the inset reports the normalized spectra after 10^4 pulses, acquired at the higher and lower investigated laser powers: the induced PL maintains the same shape, regardless the laser power. The obtained n value is totally coherent with a band-to-band transition involving three 3.62 eV photons, supporting a pure multiphoton absorption regime. In particular, the absorption of ∼3 photons corresponds to an absorption ∼10.8 eV, which is near the first excitonic absorption peak at 10.4 eV [1], [237], [238], suggesting the generation and a subsequent exciton self-trapping, which leads to the deformation of the $Si-O-Si$ bond and its breaking, with the emission of photons at 2.65 eV coupled with the NBOHC and E´ generations.

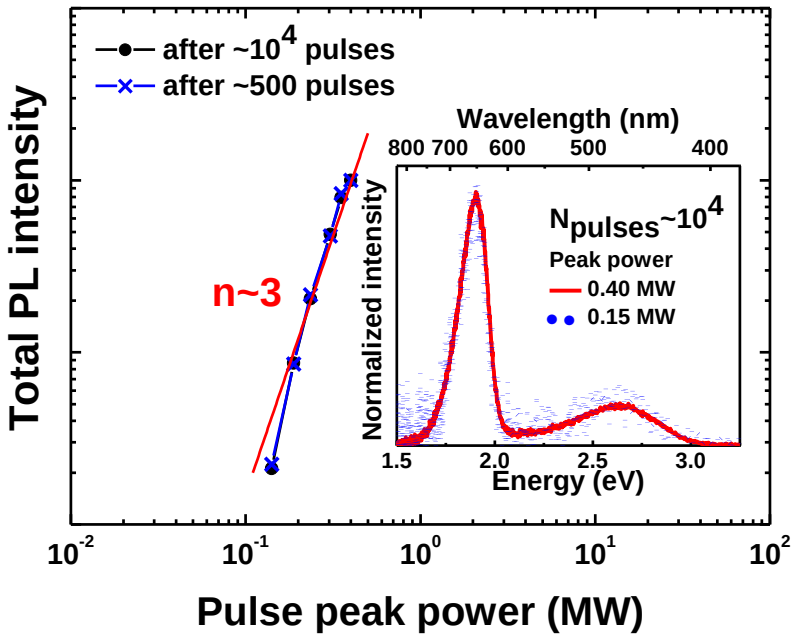

Figure 5.13. Total PL intensity as a function of the pulse peak power in Suprasil 300: after 10^4 pulses in black and after 500 pulses in blue. In red the best fit according to equation 1.46. The inset represents the normalized PL spectra at the higher and lower investigated laser powers.

Synthetic wet silica

An analogous investigation was performed on the Corning 7980 sample (Synthetic wet silica sample), which differs from the Suprasil 300 basically for the higher OH content (> 500 ppm). The online PL spectra, acquired under an excitation at 343 nm with the fs laser (at ~ 0.40 MW) and different pulse numbers, are reported in Figure 5.14 (a), while Figure 5.14 (b) presents the relative kinetics of the peaks intensities at 1.9 eV and 2.65 eV . The observed spectral features are analogous to the ones observed in the Suprasil 300: the NBOHC PL band, centered at 1.9 eV, and the 2.65 eV peaked band, already attributed to the STX.

In the normalized PL evolution as a function of the laser pulses number Figure 5.14 (b), the 2.65 eV kinetic could be described by an intrinsic process from the beginning of the irradiation, finding $n = 0.33$ according to equation 5.1, while the 1.9 eV PL reaches a maximum value around 500 pulses and slowly decreases down to the value measured after 10^4 pulses. Analogous trends are observed at lower laser powers.

The possible explanation of this different behavior could be attributed to the high OH content of the glass (negligible in the Suprasil 300), which introduces an extrinsic process described by equation 5.2 [41]:

$$\equiv \mathrm{Si} - \mathrm{OH} \xrightarrow{\hbar\omega} \equiv \mathrm{Si} - \mathrm{O} \cdot + \mathrm{H}. \tag{5.2}$$

leading to the NBOHC generation by the OH breaking bond. The free hydrogen could diffuse and passivate other NBOHC, but also E´ centers or recombine with another hydrogen atom forming a H_2 molecule. Furthermore, from the kinetics of Figure 5.14 (b), the NBOHC concentration reaches its maximum within the first 500 pulses, observing then a decrease of the PL band as a function of the pulse number . It is possible to argue that the fast growth is due to the OH conversion in NBOHC, and once these precursor sites are exhausted, even if the intrinsic process start to be relevant, the number of bleached NBOHC is dominant. The nature of the observed bleaching could be linked to unstable defects induced at RT or because they are bleached directly by the incoming laser pulses.

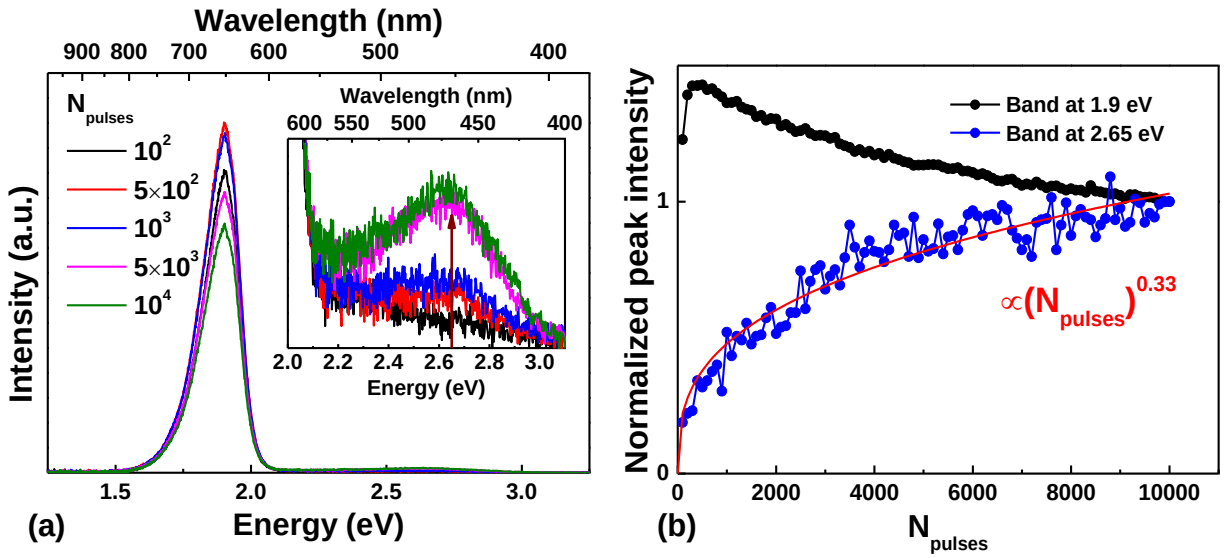

Figure 5.14. (a) Corning 7980 sample PL spectra at different accumulated number of pulses: 10^2 pulses case corresponds to the black line, 5×10^2 in red, 10^3 in blue, 5×10^3 in magenta and in green after 10^4 pulses, with a pulse power of ~0.40 MW. The irradiation is performed with 343 nm femtosecond laser. The inset zooms the spectral region between 2.0 eV and 3.2 eV. (b) Kinetics of the peak intensity measured at ~0.40MW, normalized to the PL value at 10^4 pulses, for at the 1.9 eV (black) and 2.65 eV (blue) bands respectively. The red line represents the best fit curve according to equation 5.1.

Therefore, for the Corning 7980 online PL, at fixed laser's fluence, we observed two different pathways for the NBOHC's generation: an extrinsic dominant process, described by equation 5.2, and an intrinsic one consequent to the STX relaxation (equation 1.46).

It is interesting now to study the dependence of the total PL intensity as a function of the laser pulse intensity. In particular, Figure 5.15 shows the PL intensities, measured at 1.9 eV and 2.65 eV as a function of the laser pulse peak power, after 10^4 pulses (Figure 5.15 (a)), then at the end of the irradiation, and after 500 pulses (Figure 5.15(b)), associated to the maximum PL intensity at 1.9 eV in Figure 5.13 (within the extrinsic process generation). The separated study of the dynamics at different total accumulated doses is mandatory because different kinetics are involved as a function of the accumulated laser pulses. In the figure, the two data sets are scaled for a direct and easy trend comparison.

In both cases the total PL intensity as well as the 1.9 eV evolution exhibit the same behavior as a function of the peak power pulse, since the total PL intensity is mostly driven by the area measured under the 1.9 eV peaked band. In Figure 5.15 (a) all the three contributions follow the same power law as already reported for the Suprasil 300, suggesting newly a multiphoton process requiring ~3 photons for a band-to-band transition. On the contrary, Figure 5.15 (b) shows a slightly different behavior: after 500 pulses, the intrinsic process, represented by the normalized PL at 2.65 eV (in which it was found the same value of n~3), is not the dominant one.

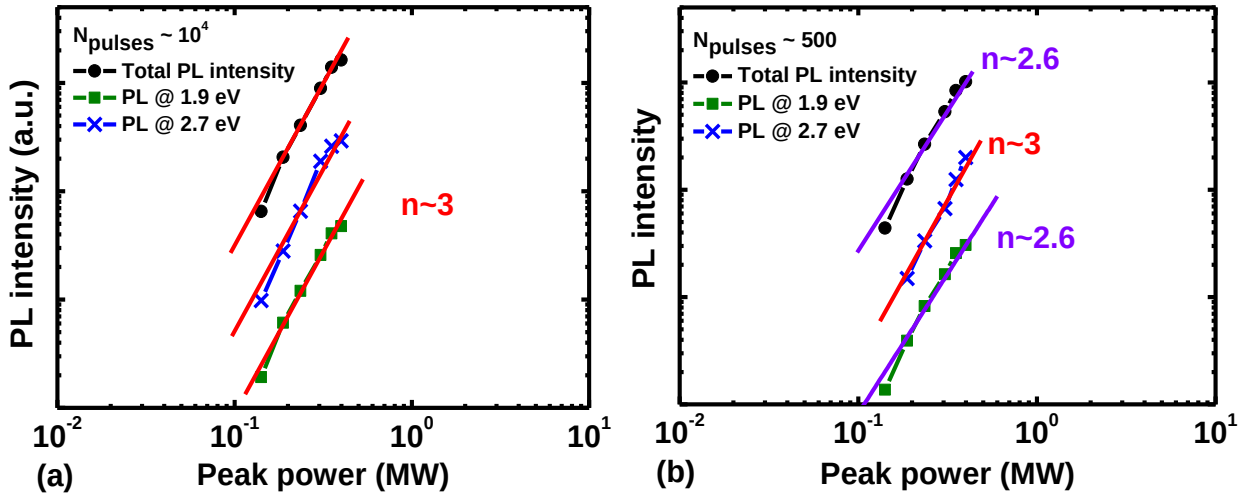

Figure 5.15. Total PL intensity (in black), PL value at 1.9 eV (in green) and the PL at 2.65 eV (in blue) as function of the pulse peak power after 10^4 and 500 pulses measured in the Corning 7980, respectively (a) and (b). The red and violet lines represent the best fit curves according to equation 1.46.

Indeed, the 1.9 eV PL band shows a different kinetic, described by equation 1.46 with n~2.6. Albeit in the present case the PL dependence by the laser peak power pulse suggests a multiphoton absorption, it is probable that this is the energy required to break up the OH bond, which drives the extrinsic process [41], [239].

Natural wet silica

Herasil 1 material has a OH content ranging between 150 and 400 ppm and is also characterized by the presence of germanium impurities. In Figure 5.16 (a), we observe the already

identified PL bands, linked to the NBOHC and STX centers. However a new component overlapping with the STX band appears, and its intensity decreases when increasing the number of the laser pulses. Indeed, this spectral feature, peaked at ~3.1 eV, could be associated to the GLPC's excitation [1], [4], [88], [92]. Therefore, such PL component is mainly driven by the laser induced photo-bleaching of preexisting GLPC. Indeed in Figure 5.16 (b), such Ge related defect reveals a PL intensity decrease of ~40% after ~10^4 pulses, analogous to the induced bleaching observed in different irradiation conditions [240]. The 2.65 eV peaked band remains almost constant as a function of the accumulated dose: this effect could be linked to a compensation between the intrinsic growth, already observed in the other glasses, with the GLPC bleaching. The PL kinetic observed at 1.9 eV reaches its maximum value after ~500 pulses and then the signal decreases. At this OH concentration, the extrinsic process described in equation 5.2 is dominant.

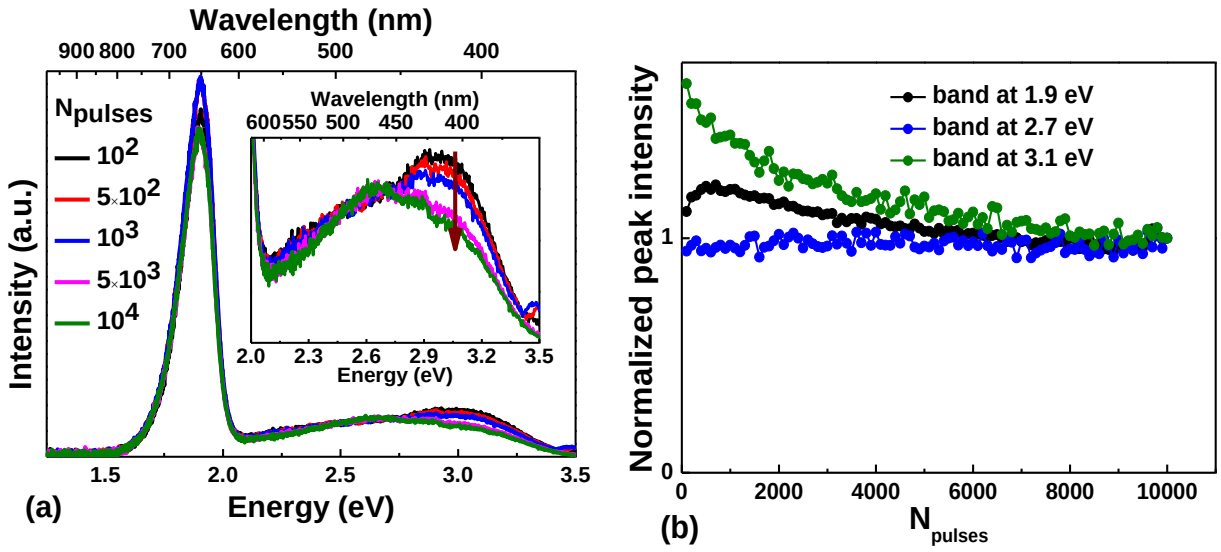

Figure 5.16. (a) Herasil 1 PL spectra at different accumulated number of pulses: 10^2 pulses case is the black, 5×10^2 in red, 10^3 in blue, 5×10^3in magenta and in green after 10^4 pulses, with a pulse power of ~0.40 MW, irradiation with 343 nm femtosecond laser. The inset zooms the spectral region between 2.0 eV and 3.5 eV. (b) Peak intensity kinetics measured at ~0.40MW, normalized to the PL value at 10^4 pulses, kinetics at 1.9 eV, 2.65 eV and 3.1 eV, in black, blue and green circles, respectively.

Because of the strong overlap between the STX and the GLPC PL bands, it not easy to follow the single band evolution. To overcome this problem, a best fitting procedure, described by equation 4.1, was performed. Indeed, considering Gaussian-shaped bands (or a sum of Gaussian

bands, as in the case of the NBOHCs), it is possible to fit the spectra, as reported in Figure 5.17 (a) for the spectrum acquired after 10^4 pulses exposed at $\sim$0.40 MW of pulse peak power. It is important to underline the following approximations:

- The plasma contribution was evaluated using a Gaussian band peaked at $\sim$2.5 eV with FWHM$\sim$1.15 eV.

- The NBOHC contribution, that is asymmetric, is accounted for by three different Gaussian bands, which singularly have no physical meaning.

- The STX band parameters are singled out by the data related to the Suprasil 300 and Corning 7980, where the PL is well resolved.

- The GLPC parameters are taken from literature, although some discrepancies could be related to the fact that the spectrum remains uncorrected for the experimental responses of monochromator and detector.

The best-fit parameters are reported in table 5.2.

By applying the same fitting routine to all the spectra acquired at different doses it is possible to estimate the single band kinetics as a function of the number of laser pulses. Figure 5.17 (b) reports the obtained kinetics: the NBOHC (composed by the sum of the three Gaussians associated to the NBOHC) maintains its behavior, while the STX assumes an intrinsic-like behavior and the GLPC shows a slightly higher bleaching, that is consistent with previous literature studies. The difference in the STX kinetics reported in Figure 5.18 could be linked to the low value of the STX area at low doses, as already observed in Figures 5.12 and 5.14 in the other samples, increasing the error in the fitting routine at the beginning of the irradiation (less than $\sim$2000 pulses).

Table 5.2. Best fit parameters of the Gaussian bands used for the PL spectra acquired in the Herasil 1 sample after 10^4 pulses, pulse peak power being ~0.40 MW.

Defect	OA peak (eV)	FWHM (eV)	Area (a.u.)
NBOHC$_1$	1.92	0.10	$7.6 \cdot 10^7$
NBOHC$_2$	1.86	0.16	$1.3 \cdot 10^8$
NBOHC$_3$	1.72	0.13	$1.3 \cdot 10^7$
Plasma	2.50	1.15	$1.1 \cdot 10^8$
STX	2.65	0.42	$2.5 \cdot 10^7$
GLPC	3.04	0.42	$2.9 \cdot 10^7$

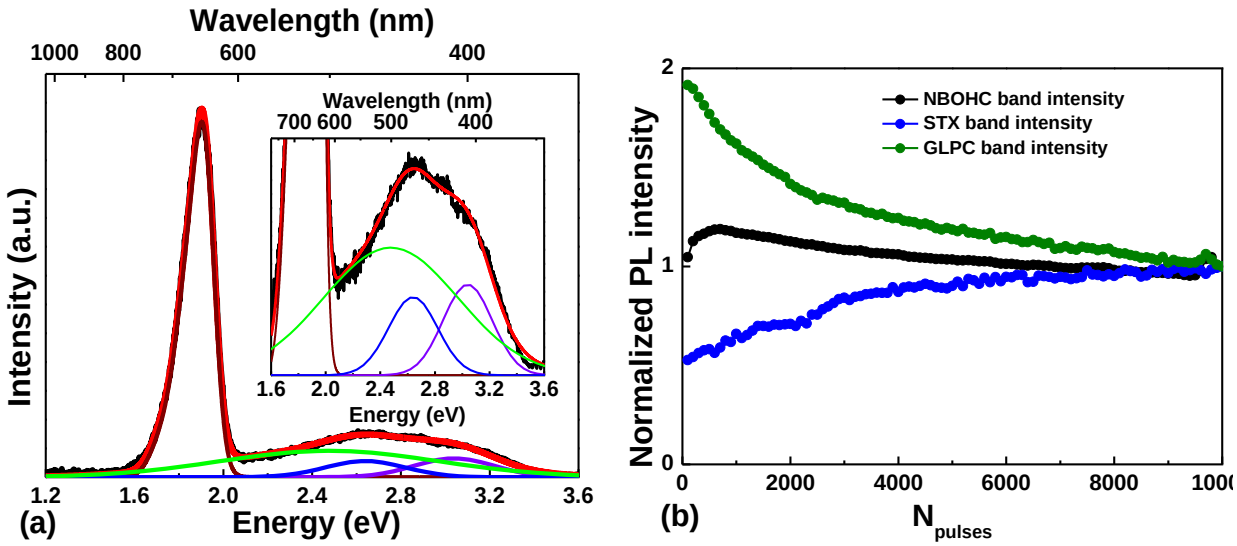

Figure 5.17. (a) Fitting routine performed on the PL spectra acquired after 10^4 laser pulses (pulse peak power of ~0.40 MW) in the Herasil 1: in black the experimental data, the global fitting function in red, in brown the NBOHC contribution, in green the plasma contribution, in blue the one of the STX and the GLPC in violet. The inset zooms the spectral region between 1.6 eV and 3.6 eV. (b) Kinetics of the area obtained by the fitting routine, normalized to the PL value at 10^4 pulses, of NBOHC, STX and GLPC, in black, blue and green respectively.

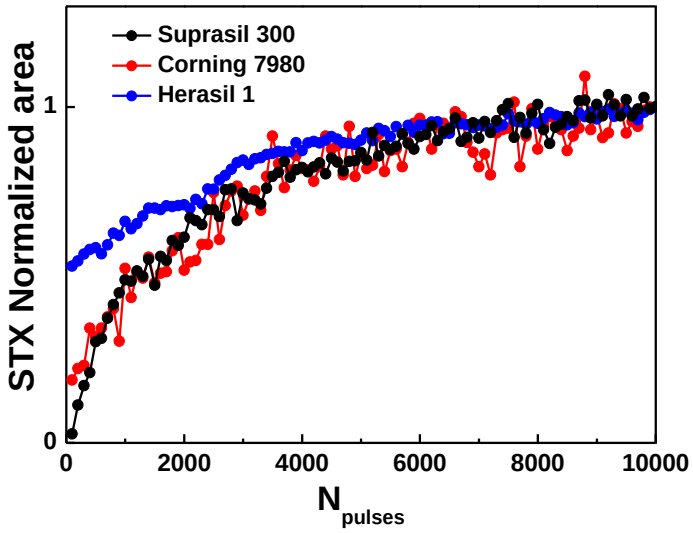

Figure 5.18. Normalized STX area as a function of the number of laser pulses, pulse peak power being ~0.40 MW, acquired in three different samples: in black the Suprasil 300, in red the Corning 7980 and in blue the Herasil 1.

Since the Herasil sample is characterized by 3 components with different behaviors, in Figure 5.19 we have studied the dependences of the total PL intensity and the intensities of the NBOHC, STX and GLPC related bands. This comparison is reported for the spectra after $\sim 10^4$ pulses (a), which corresponds to the last acquired PL responses, and after ~500 pulses (b), which corresponds to the 1.9 eV maximum and within the GLPC photo-bleaching regime. All the data sets are scaled in order to make the comparison easier. In both cases, the 3.1 eV PL manifests a slope lower than other components: indeed, notwithstanding a multiphoton absorption regime, the best-fit n parameter is not adapted to have a band-to-band transition. With the obtained value of n~2.1, the absorbed energy is ~ 7.5 eV, which corresponds to a real GLPC's excited singlet S_2 electronic level (more details about the GLPC's [42] will be included in chapter 6) [1], [4], [88], [92] . These results suggest that the 3.1 eV PL is a consequence of the relaxation toward the GLPC's triplet level after an absorption at ~7.5 eV. Both in Figure 5.19 (a) and (b) the values at lower energies are slightly lower than the best-fit curve: this is due to strong overlap between the 3.1 eV and 2.65 eV PL bands. The mutual influence could be appreciated in Figure 5.19 (b), for which the first values of the STX and GLPC bands are almost the same, especially considering that after ~500 pulses the value of the STX band is still low (Figure 5.17).

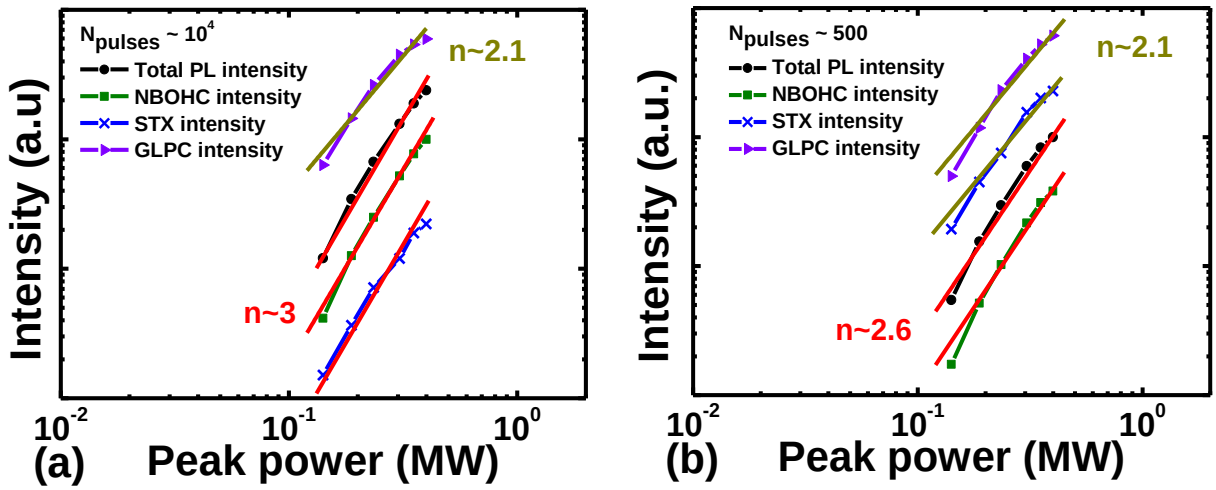

Figure 5.19. Herasil 1total PL intensity (black squares), NBOHC intensity (green), STX intensity (blue) and the GLPC intensity (violet) as a function of the pulse peak power after 10^4 and 500 pulses, respectively (a) and (b). The red and dark green lines represent the best fit curves according to equation 1.46.

Even for the Herasil 1, the total PL intensity is mostly driven by the 1.9 eV PL, having in the most cases approximatively the same value and followed by the STX band at high total accumulated dose (Figure 5.19 (a)). It is also evident that the extrinsic process is dominant at low doses, with n~2.6, while at the end of the irradiation, the generation of the NBOHC is due basically to the STX relaxation, coupled with the 3-photon absorption.

Sample comparison

The observed spectral features bring very close similarities with that observed in the all investigated samples: the NBOHC PL band peaked at 1.9 eV and the STX PL band at 2.65 eV (without considering the GLPC in the Herasil sample). From the spectroscopic point of view, the bigger difference is the relative ratio between these two bands and their evolutions. Indeed, notwithstanding the STX PL band follows an intrinsic-like generation process and then the final intensity depends on the total accumulated dose, the NBOHC related band has an amplitude which depends on the sample's OH content, and its kinetic is dominated by an extrinsic process. In particular the non-monotonically evolution of the NBOHC band, when the OH content becomes relevant, highlights a transition from an extrinsic generation process to an intrinsic one. Indeed,

by comparing Figures 5.13, 5.15 (a) and 5.19 (a) we could conclude that after ~10^4 pulses, the NBOHC generation is mostly an intrinsic process, being the only one observed in the Suprasil 300. Moreover, the observed super-linear dependence suggests that the NBOHC generation is basically due to the STX relaxation, coupled with the 3-photons absorption, which is in accordance with the first exciton absorption peak.

A different behavior between the samples is observed at low total accumulated doses: if the total PL intensity is still a third order multiphoton absorption process in the Suprasil 300, for the Herasil 1 and the Corning 7980, at low doses the multiphoton absorption order is n~2.6, which is near to the OH broken bond energy, strongly supporting the presence of the extrinsic process.

Despite the exciton self-trapping is a basic property of the material and not, in general, directly related to the presence of radiation-induced point defects, in all the investigated samples it was observed an increase of the STX luminescence with the number of accumulated pulses. To explain this phenomenon, we suggest that the increase of the 2.65 eV band considering the new levels between the conduction and the valence band, making more probable the defects' level-assisted 3-photons transition.

Post mortem characterization

The post mortem characterization of the induced damage was performed using the PCM microscopy (ZEISS AXIO microscopy) and the integrated confocal micro-spectrometer ARAMIS for the Raman and steady state photoluminescence. In Figure 5.20 is depicted the PCM image, as a function of the laser power, of the Suprasil 300 sample under a UV excitation fs laser excitation at 343 nm. The elongated damage along the laser direction and its length depends on the pulse peak power. Considering that in such PCM figure black colors correspond to a positive Δn, smooth isotropic positive refractive index change is observed at low pulse energies, while at higher ones a complex panorama appears. Both clearer and darker colors, with respect to the background, are present in the laser traces, suggesting a transition from the Type I to Type II interaction regimes.

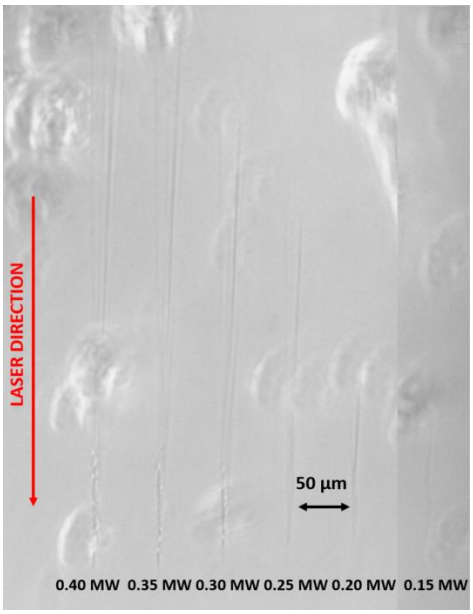

Figure 5.20. PCM image of the induced damage under 343 nm femtosecond pulses at different pulse peak powers for the Suprasil 300 sample. The red arrow indicates the direction of the laser propagation.

An analogous discussion is valid for the Corning 7980 (Figure 5.21) and Herasil 1 (Figure 5.22). It is important to note that the post mortem analysis did not reveal any difference between the three samples, supporting the necessity to perform online measurements to understand the radiation matter interactions. Indeed, Figure 5.23 is representative of the steady state PL and Raman post mortem characterization of all samples (Figure 5.23 reports the results recorded on the Corning 7980 sample): both the characteristic spectra of Type I/II interaction regimes are observed in the PL spectra, exciting at 325 nm, at different power pulses (Figure 5.23 (a)), indicating ~0.30 MW as the Type I/II threshold. Notwithstanding the smooth positive refractive index change observed at lower power, no densification is observed by Raman spectra of the damaged area (Figure 5.23 (b)). This could be due basically to a very smooth densification, under the experimental sensitivity, or that the positive refractive index change depends, through the Kramers-Kronig relation, on the induced absorption defects.

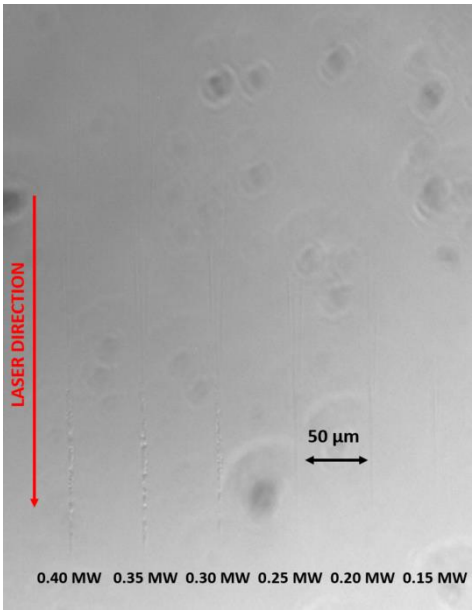

Figure 5.21. PCM image of the induced damage under343 nm femtosecond pulses at different pulse peak powers for the Corning 7980. The red arrow indicates the laser direction propagation.

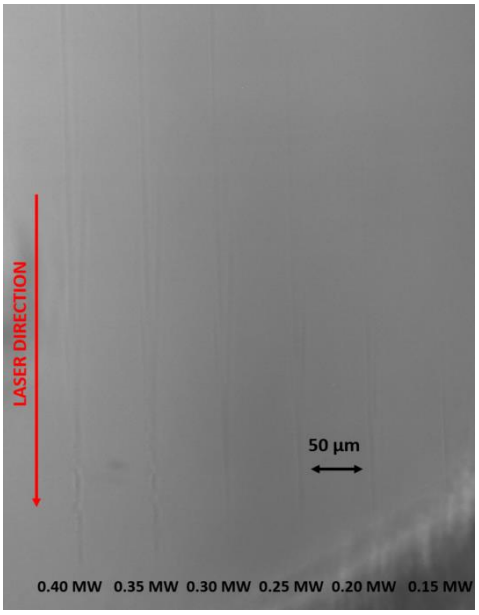

Figure 5.22. PCM image of the induced damage under 343 nm femtosecond pulses at different pulse peak powers for the Herasil 1. The red arrow indicates the laser direction propagation.

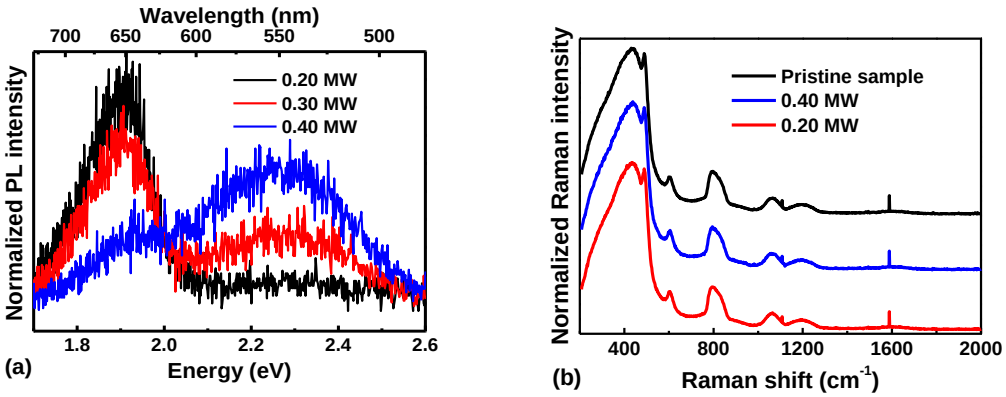

Figure 5.23. (a) Post mortem PL spectra, scaled for the area, of the laser induced traces at different powers, measured in the Suprasil 300 sample: 0.20 MW in black, 0.30 MW in red and in blue 0.40 MW. (b) Comparison between the Raman spectra, measured in the Suprasil 300 sample, acquired in the pristine sample (black line), 0.40 MW (blue line) and at 0.20 MW (red line).

5. 2.2 Online PL at 1030 nm

Synthetic dry silica

In the first section of this chapter, we highlighted the difference in the induced damages in silica glass attributable to the laser wavelength choice. In the same way, we describe the same experiment of paragraph 5.2.1 irradiating this time at 1030 nm (1.20 eV), then in the near-IR domain. Figure 5.24 reports the PL spectrum measured after $\sim 10^4$ pulses with a 1030 nm laser wavelength, the pulse peak power being ~300 MW. The spectra reveal different features: a very strong sharp peak at ~1.2 eV, which is the scattered fundamental light, the NBOHC band at 1.9 eV, an intense band peaked at ~2.7 eV and a signal at 3. 6 eV that could be associated with the scattered third harmonic generated by the non-linear interaction between the silica glass and the intense light at 1030 nm. Moreover it should be taken into account a background coming from the strong plasma emission. Compared to the PL generated by the 343 nm laser exposure, the main difference is an opposite ratio between the 1.9 eV and the 2.7 eV band amplitudes.

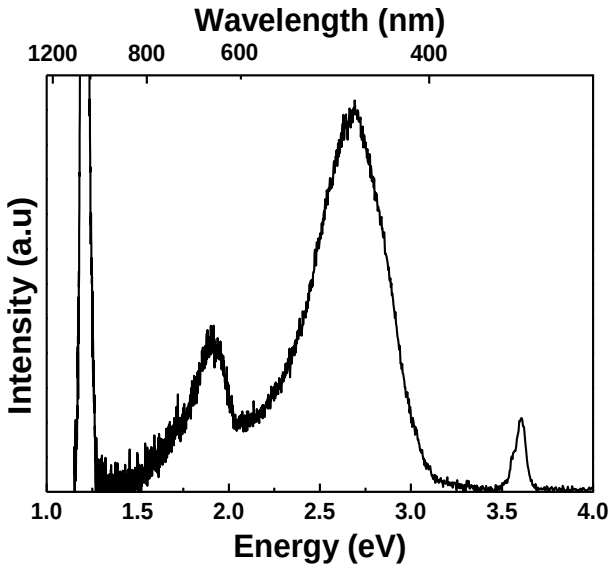

Figure 5.24. Suprasil 300 PL spectrum acquired after $\sim 10^4$pulses, with ~300 MW of peak power/pulse, irradiating with 1030 nm femtosecond laser.

Studying the PL as a function of the pulse number (Figure 5.25 (a) and (b)) we highlight a monotonic growth of the bands with the corresponding dose, while the plasma background seems to remain constant with the number of the pulses. Both the 1.9 eV and 2.7 eV bands are observed together since the beginning of laser irradiation and their intensities increase on increasing the number of laser pulses. The comparative study of these kinetics shows: the 1.9 eV NBOHC band reaches a saturation around ~4000 pulses; while the 2.7 eV band does not provide evidence for a saturation, this trend could be interpreted as an intrinsic process, in agreement with the previous observations under UV irradiation.

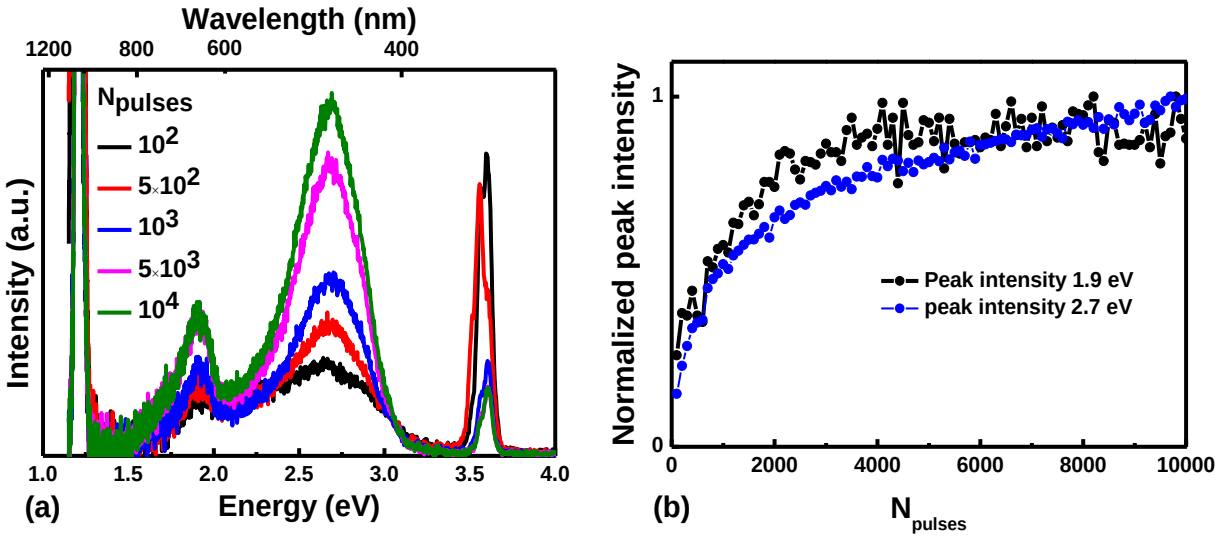

Figure 5.25. (a) Suprasil 300 PL spectra at different accumulated number of pulses: 10^2 pulses case is the black, 5×10^2 in red, 10^3 in blue, 5×10^3in magenta and in green after 10^4 pulses, with a pulse power of ~300 MW, irradiating with 1030 nm femtosecond laser sample. (b) Peak intensity kinetics measured at ~300 MW, normalized to the PL value recorded at 10^4 pulses: at 1.9 eV (black) and 2.7 eV (blue).

For a deeper analysis, we have also studied the dependence of the spectra as a function of the laser peak power, according to the investigation on the linear or non-linear photon absorption processes. Indeed, in Figure 5.26 we compare the PL spectra, scaled for the peak power, acquired at ~300 MW and ~100 MW. Differently from what we have observed with the UV irradiation, in which the spectra shape was independent of the laser peak power, under irradiation at 1030 nm the on-line PL spectra clearly depends on the laser peak power. Indeed, at low pulse power there

is no trace of the 1.9 eV band, while the main 2.7 eV observed band is slightly red-shifted compared to that one measured at high pulse power. It is important to underline that the asymmetry of the 2.7 eV band observed at low power could be due to the plasma scattering, which is characterized by a wide unstructured band along the whole investigated spectral range.

Figure 5.26 suggests that the PL around 2.7 eV observed with 300 MW peak power, could be composed of two different bands: the first is associated with the spectrum observed at low pulse power, the second is induced by the irradiation with higher pulse power, together with the 1.9 eV emission.

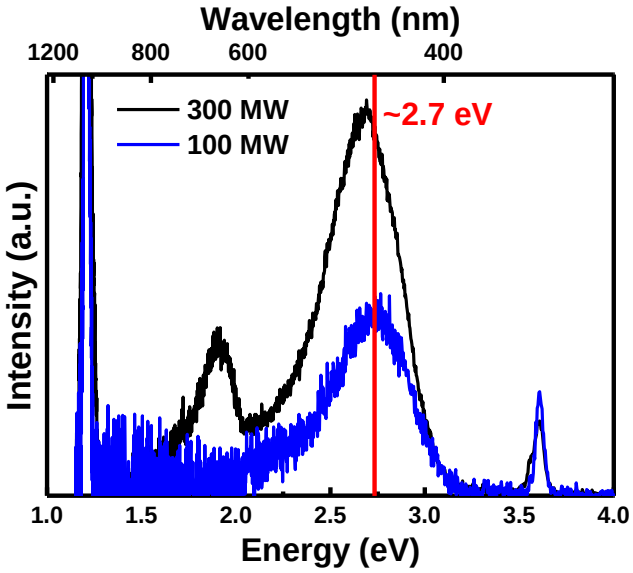

Figure 5.26. Comparison between the PL spectra, scaled for the laser peak pulse power, acquired at ~300 MW (in black) and ~100 MW (in blue) after $\sim 10^4$ pulses, in the Suprasil 300 sample.

Considering the spectrum acquired at low pulse power as composed only of one component peaked at ~2.7 eV and with a FWHM~0.45 eV, it is possible to obtain the parameter linked to the second component of the main band measured at high pulse power by a subtraction between the black and the blue curves in Figure 5.26. The difference spectrum, reported in Figure 5.27 (a), is characterized by a band peaked at 2.65 eV and a FWHM~0.4 eV, and of course, by the 1.9 eV band. In Figure 5.27 (b) we also report the comparison between this difference spectrum and the normalized spectrum, to the PL value at 2.65 eV, acquired using the 343 nm laser at ~40 MW: it is interesting to highlight the excellent agreement between the two bands at 2.65 eV, that

suggesting they are emitted by same PL active defect. In this way, it is possible to consider that after a particular threshold peak power, STX generation can also be involved. Moreover, these results strongly support the model related to the NBOHC's generation as a consequence of the STX relaxation, indeed the NBOHC band is observed only together with the STX photoluminescence.

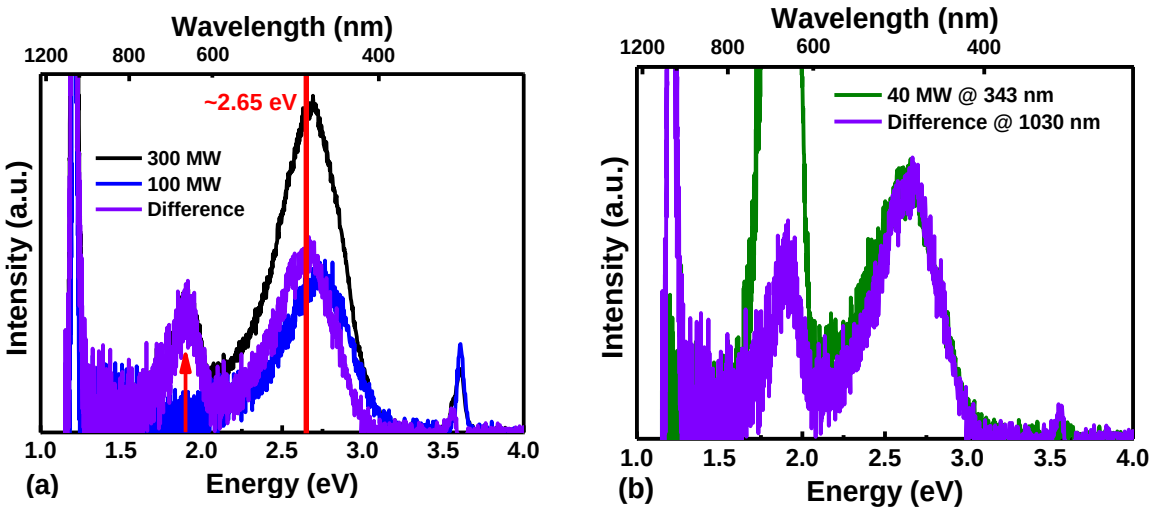

Figure 5.27. (a) Difference (in violet) between the PL spectra, scaled for the laser pulse peak power, acquired at ~300 MW (in black) and ~100 MW (in blue) after ~10^4 pulses, in the Suprasil 300 sample, irradiating at 1030 nm. (b) Comparison between the difference spectra (in violet) obtained in panel (a) and the normalized spectra acquired after ~10^4 pulses at 40 MW irradiating with the 343 nm femtosecond laser pulses (in green) in the Suprasil 300 sample.

The two PL components hypothesis is even supported by the PL spectra recorded at different laser intensities, that are corrected with respect to the peak power and are reported in Figure 5.28 (a). The red line is an eyes guide to appreciate the redshift of the main band on increasing the laser pulse power. Furthermore in correspondence of the redshift, we observe the growth of the 1.9 eV band. This behavior agrees with a transition between a regime in which the spectra are dominated by the 2.7 eV band to another regime in which the spectra is characterized by the 1.9 eV, 2.65 eV and 2.7 eV bands. On the basis of the already known PL active defects, the luminescence centered at 2.7 eV could be associated with the ODC (II).

Moreover, studying the evolution of the PL at 2.7 eV (Figure 5.28 (b)), the kinetic at very low power reaches a saturation value after ~1000 pulses, while at higher power the kinetic do not show a saturation tendency, in agreement with the previous equation 5.1. Through Figures 5.28 (a) and (b) we can detect the power threshold between the saturation and the intrinsic regime around ~ 180 MW. According to this framework, at laser power exceeding 180 MW, the process described by equation 1.46 starts to be relevant.

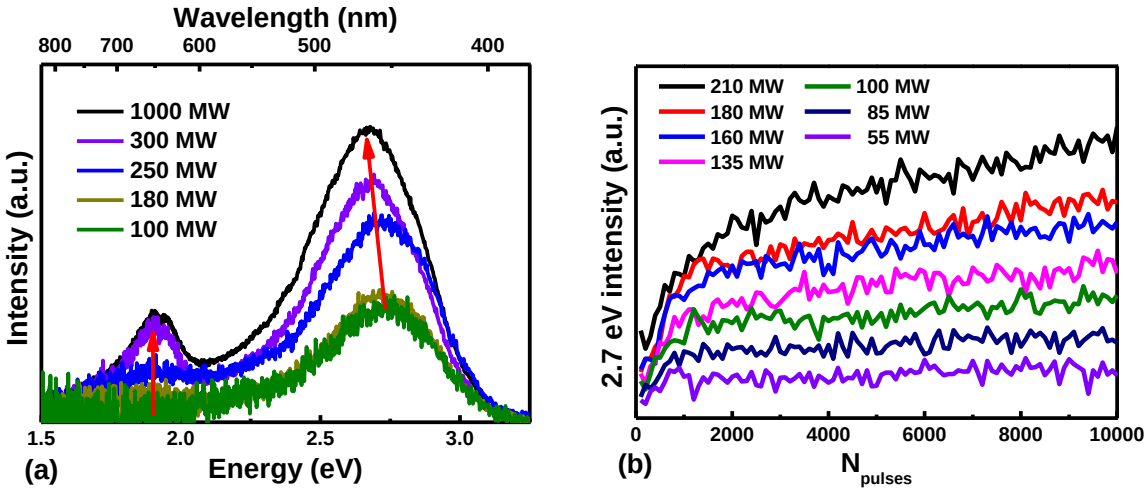

Figure 5.28. (a) PL spectra, scaled respect to the laser pulse peak power, after ~10^4 pulses at different peak pulse powers, in the Suprasil 300 sample. The red arrows are the eyes guide to appreciate the redshift of the main band, as a function of the laser pulse peak power and the growth of the 1.9 eV band. (b) Comparison of the kinetics, as a function of the number of the pulses, of the 2.7 eV PL at different pulse peak powers.

In order to evaluate the non-linear order of the absorption process, it is useful to study the PL dependence on the laser pulse peak power, not only at the maximum total accumulated dose (~10^4 pulses), but also at the beginning of the irradiation (~10^2 pulses). Figure 5.29 reports the PL at 2.7 eV and 1.9 eV (which is distinguishable from the noise after ~180 MW) with the relative fit according to equation 1.46, at different total accumulated doses. For each dose, we distinguish the low power regime (generation of the ODC (II)) and high power regime (generation of NBOHC, STX and ODC (II)), obtaining different n values. It is important to note that the PL value at 2.7 eV, up to the power threshold of ~180 MW, has the same dependence of n~1.1 on the pulse peak

power. Moreover, the 1.9 eV band has exactly the same dependence as the 2.7 eV band intensity supporting the occurrence of the STX/NBOHC photoluminescence.

In particular, the best-fit n value results to be $1 < n < 2$, thus describing a super-linear regime, due to a band-to-band transition or a defect excitation. We could hypothesize that our experiment is performed in such conditions that within the first spectra (after hundreds of pulses) the matrix is so strongly modified that it is no more comparable to the pristine sample. For example, the generation of a very high defect concentration within the first laser pulses could decrease the order of absorption to promote electrons in the conduction band, because of the presence of electronic levels related to the previously induced defects. To support the above mentioned hypothesis, Figure 5.29 shows the order of the fit decreasing with the dose, from $n \sim 1.9$ after $\sim 10^2$ pulses (then a matrix near to the pristine one) to $n \sim 1.3$ after $\sim 10^4$ pulses (end of the irradiation, with the matrix strongly differing from the pristine one). This behavior could explain the increase of the STX PL as a function of the number of pulses: a lower absorption order required for the band-to-band transition increases the careers ignition in the bands, simplifying their self-trapping and leading to an easier STX generation. Another detail to justify the low n value could be attributed to the γ factor: less than the unity in the present experimental conditions. As already explained in chapter 1, when $\gamma < 1$, the dominant non-linear absorption process in the glass is the tunneling photoionization.

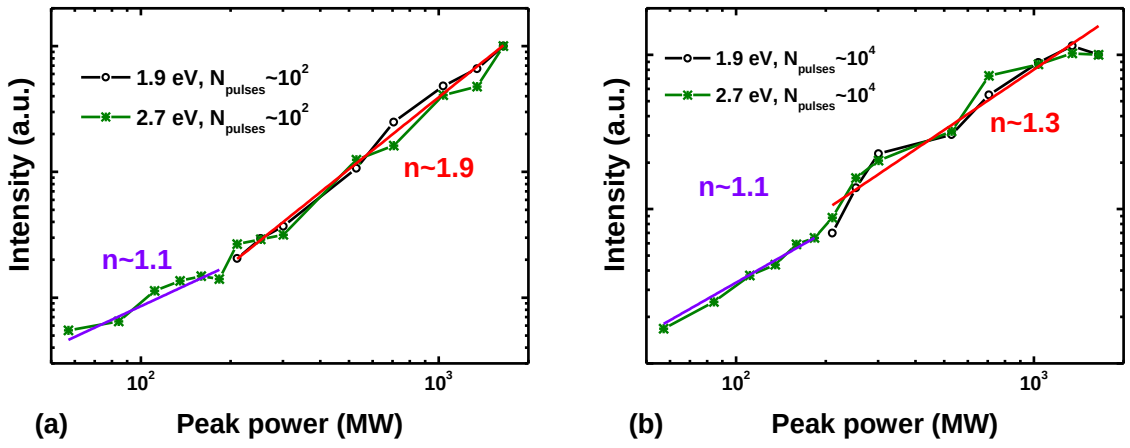

Figure 5.29. PL at 2.7 eV (green) and at 1.9 eV (black) as a function of the laser pulse peak power at different accumulated doses, in the Suprasil 300 sample: after 10^2 pulses (a) and after 10^4 pulses (b). The colored lines are the best fit for: low power regime, with $n \sim 1.1$, in violet and high-power regime in red.

From the above discussion it is possible to point out that irradiating with femtosecond laser pulses at 1030 nm, two different interaction regimes are observed:

- Low pulse peak power: ODC (II) generation with the PL band centered at 2.7 eV reaching a saturation value around $\sim 10^3$ pulses, with a slight super-linear dependence on the laser power and independent of the accumulated dose.
- High pulse peak power: beyond the ODC (II) PL band, we observed the growth of both NBOHCs and STXs photoluminescence bands. The evolution as a function of the dose is driven by the STX absorption band at 2.65 eV resulting in an intrinsic process according to equation 5.1. Even in this case, we observed a super-linear dependence of the PL on the laser pulse peak power, with a dose dependent n value.

Synthetic wet silica

The online PL, acquired on the synthetic wet silica corning 7980 sample at ~ 300 MW, is reported in Figure 5.30 (a), the kinetics recorded at 1.9 eV and 2.7 eV are reported in Figure 5.30 (b). These results evidence the same features already observed in the synthetic dry silica Suprasil 300: the NBOHC's band, more intense than in the previous case, according to the sample chemical composition and then to equation 5.2, and the composed band of the STX and ODC (II) contributions. In fact, we still observe the scattered contribution coming from the fundamental, the generated third harmonic and from the plasma.

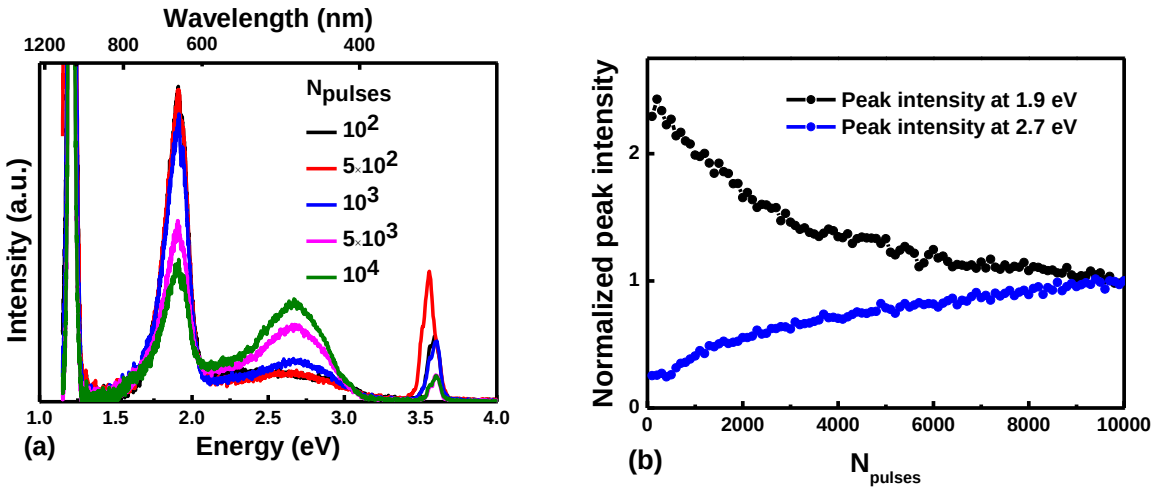

Figure 5.30. Corning 7980 responses under 1030 nm fs laser. (a) PL spectra recorded after different accumulated numbers of pulses: 10^2 pulses (black), 5×10^2 (red), 10^3 (blue), 5×10^3 (magenta) and 10^4 pulses (green) with a laser power of ~300 MW. (b) Peak intensity kinetics measured at ~300 MW, normalized to the PL value at 10^4 pulses, at 1.9 eV (black) and 2.7 eV (blue), respectively.

The evolution of the 1.9 eV band as a function of the pulse number is analogous to that observed in the same sample Corning 7980 after UV exposure with the third harmonic: it reaches the maximum value at ~500 pulses, after that it decreases down till the end of irradiation; the 2.7 eV band follows an intrinsic-like generation process dependence.

Figure 5.31 shows the redshift observed around 2.6-2.7 eV, highlighting the presence of the two regimes at high and low powers. It is interesting to note how the relative amplitude between this band and that related to NBOHC, peaked at 1.9 eV, depends on the pulse peak power. Moreover, it is possible to observe the appearance of the NBOHC band even in the low power regime, explained by the OH dissociation, according to equation 5.2.

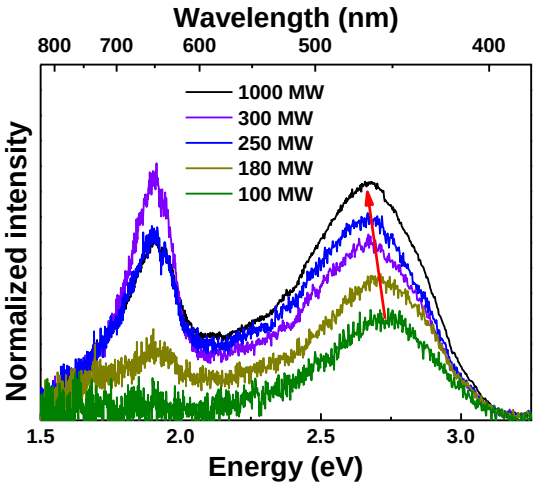

Figure 5.31. Corning 7980 PL spectra, scaled respect to the laser pulse peak power, after $\sim 10^4$ pulses at different peak pulse powers. The red arrow is eyes guide to appreciate the redshift of the main band.

Studying the PL intensities at 1.9 eV and 2.7 eV as a function of the pulse peak power, as reported in Figure 5.32, after $\sim 10^2$ (Figure 5.32 (a)) and $\sim 10^4$ pulses (Figure 5.32 (b)) we observe a super-linear dependence. The 2.7 eV photoluminescence agrees with equation 1.46 with n∼1.8 which reveals a multiphoton absorption not enough to promote the electron from valence to conduction band. At high power, a saturation tendency is highlighted, reaching the maximum value around $\sim 10^3$ MW. More interesting is the dynamic observed for the 1.9 eV band with: the first interaction regime that, in both cases, is proportional to the fifth intensity power, probably suggesting the multiphoton absorption nearly to the band-to-band transition.

This process could be linked to the extrinsic NBOHC's generation described by equation 5.2. After a pulse peak power of ~ 250 MW, the dynamic is similar to the 2.7 eV PL band, suggesting the transition to the regime of NBOHC generation due to the STX relaxation. Even in the present case, the experimental conditions are such that already within the first pulses the matrix is so strongly modified that it is no more comparable to the pristine sample.

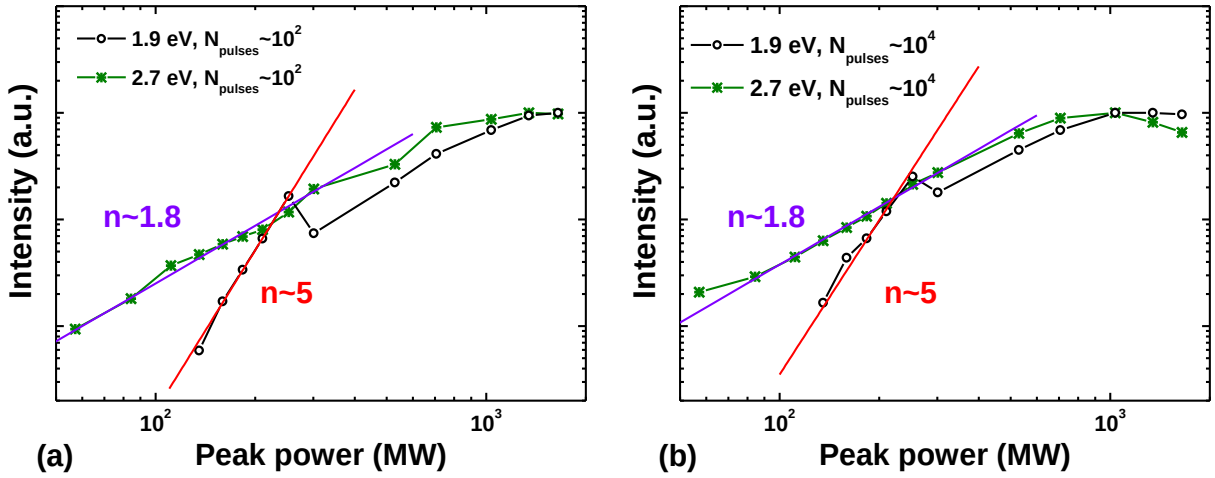

Figure 5.32. PL intensity at 2.7 eV (green color) and at 1.9 eV (black color) as a function of the laser pulse peak power at different total accumulated doses, in the Corning 7980 sample: after 10^2 pulses (a) and after 10^4 pulses (b). The colored solid lines are the best fits for: the 2.7 eV PL, with n~1.8 (in violet) and the low power regime of the 1.9 eV PL, with n~5 (in red).

Natural wet silica

Analogously, the induced PL in the Herasil 1 under ~300 MW pulse peak power after ~10^4 pulses, shows the 2.7 eV peaked band (composed of the STX and ODC (II) contributions) and the NBOHC related defect (Figure 5.33 (a)). The evolution of such bands, reported in Figure 5.33 (b), as a function of the number of pulses, highlights two different generation processes: an intrinsic one for the 2.7 eV band, and an extrinsic one at 1.9 eV. Figure 5.33 (a) gives a clear evidence for the scattering coming from the fundamental, the third harmonic and the plasma, while, differently than for the UV laser exposure at 343 nm, GLPC luminescence around 3.1 eV is not observed under IR (1030 nm) laser exposure.

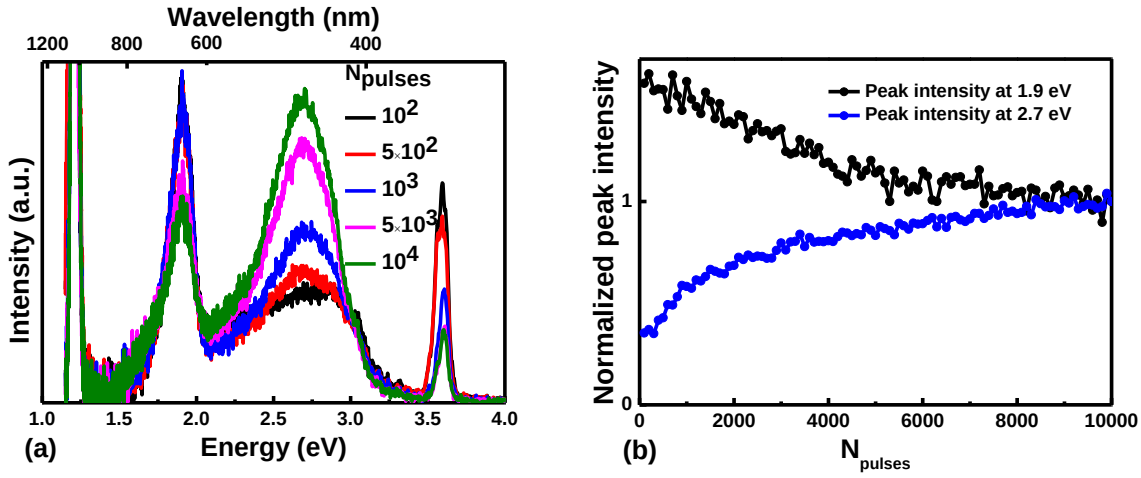

Figure 5.33. Herasil 1 responses at a pulse power of ~300 MW with 1030 nm femtosecond laser. (a) PL spectra at different accumulated numbers of pulses: 10^2 pulses case is the black, 5×10^2 in red, 10^3 in blue, 5×10^3 in magenta and in green after 10^4 pulses. (b) Peak intensity kinetics, normalized to the PL value at 10^4 pulses, for 1.9 eV (black) and 2.7 eV (blue) respectively.

Figure 5.34 reports the PL spectra at different pulse peak powers, and confirms the transition between the low/high power regimes with the appearance of the NBOHC/STX PL bands. This allows concluding that this transition is a general property of the amorphous silica, independently from its exact chemical composition. Indeed, even for the Herasil 1, at low power the PL spectra is dominated by the ODC (II) band, while, increasing the pulse peak power, the redshift appears accompanied by the growth of the NBOHC related PL band.

According to the Corning 7980 results, the PL intensities as a function of the laser power show (Figure 5.35) an average super-linear trend, at both doses (after 10^2 and 10^4 pulses), up to a saturation value. At low laser power, the growth of the NBOHC band follows a power law with exponent n ~ 4, thus suggesting a strong multiphoton absorption. Even in this case, it is reasonable to argue that such dynamic is mostly driven by the OH breaking, which starts before the intrinsic process, leading to a fast increase of the PL band at 1.9 eV. After a power threshold, ~250-300 MW, the dominant process to generate the NBOHC is the intrinsic one, according to equation 5.1.

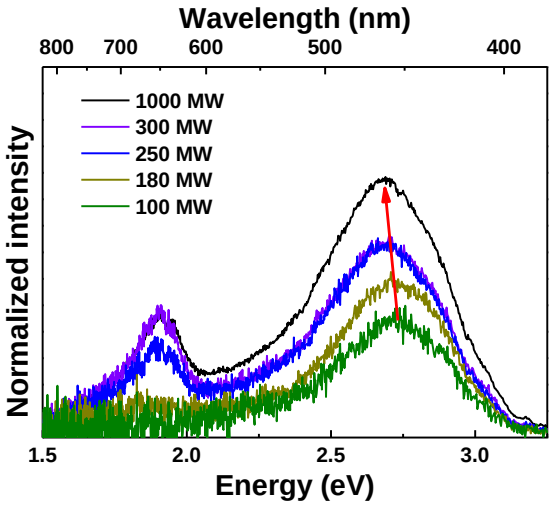

Figure 5.34. Herasil 1 PL spectra, scaled respect to the laser pulse peak power, after ~10^4 pulses at different peak pulse powers. The red arrow is an eyes guide to appreciate the redshift of the main band.

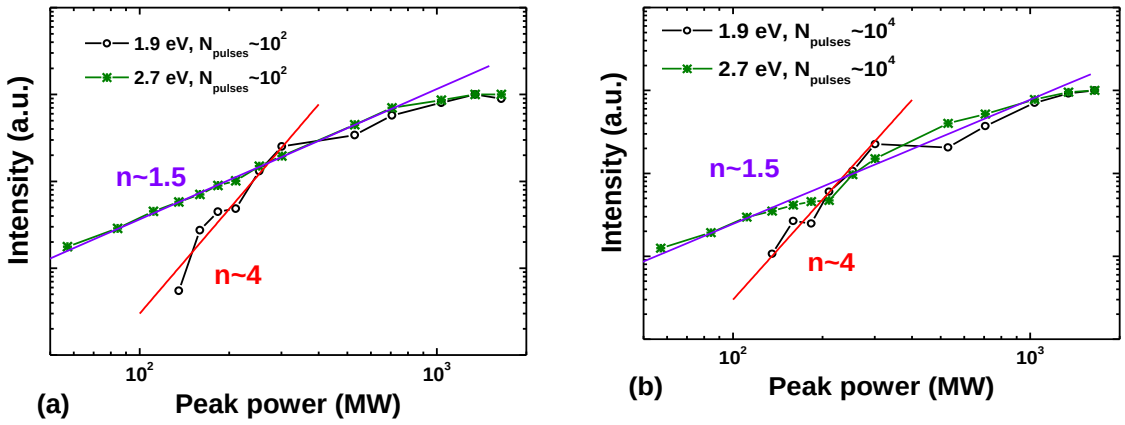

Figure 5.35. PL intensity at 2.7 eV (green color) and at 1.9 eV (black color) as a function of the laser pulse peak power at different total accumulated doses, in the Herasil 1 sample: after 10^2 pulses (a) and after 10^4 pulses (b). The colored solid lines are the best fits for: the 2.7 eV PL, with n~1.5, in violet and the low power regime of the 1.9 eV PL, with n~4, in red.

Sample comparison

Even upon 1030 nm femtosecond pulses excitation, the spectral features in the investigated samples are very close to each other. With the infrared exposure we highlighted two

interaction regimes : i) at low pulse peak power, in which the spectra manifest the ODC(II) generation by their characteristic PL band centered at 2.7 eV; ii) high pulse peak power regime of interaction with both the NBOHC and STX PL bands, peaked at 1.9 eV and the STX PL band at 2.65 eV, respectively. The transition's signature between the interaction regimes is highlighted through a blue shift observed in the main band peak. Notwithstanding the sample irradiated with the 1030 nm femtosecond laser provides a more complex panorama compared with the one observed with the UV exposition, it is important to note that by the subtracting the low power spectra to the ones acquired at high power, the resulting difference spectra agree, qualitatively, with the UV induced PL spectra. Albeit at low power the observed dynamics are sample independent as a function of the dose, in the high-power regime the NBOHC related band has an amplitude which depends on the sample OH content, and its kinetic is dominated by an extrinsic process. Indeed, the NBOHC behavior presents the same trend observed with the 343 nm exposure, following an intrinsic process with the Suprasil 300 and an extrinsic one when the OH content becomes relevant. The single band behavior of the 2.7 eV band is more difficult to estimate because of the spectral overlap between the ODC(II) and the STX PL signatures.

The OH content plays an important role also in PL intensity dependence on the laser pulse peak power, as highlighted by the comparison of Figures 5.29, 5.32 and 5.35, manifesting in all the investigated cases a super-linear dependence.

Post mortem characterization

Post mortem characterization (PMC) of the induced damage on silica samples using the fundamental wavelength, centered at 1030 nm, was performed by Raman and steady state PL investigations of the traces. Figures 5.36-5.38 report the corresponding PCM images, as a function of the laser power, over the three studied samples.

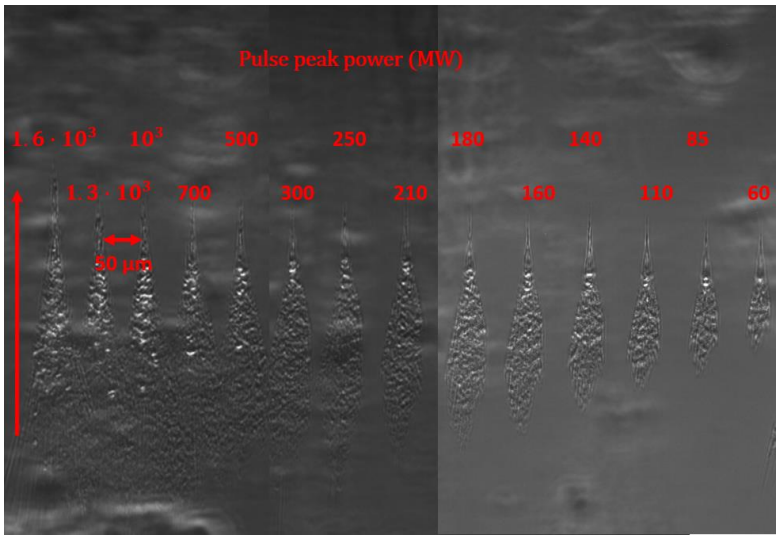

Figure 5.36. PCM image of the induced damage under 1030 nm femtosecond pulses at different pulse peak powers for the Suprasil 300. The red arrow indicates the laser direction propagation.

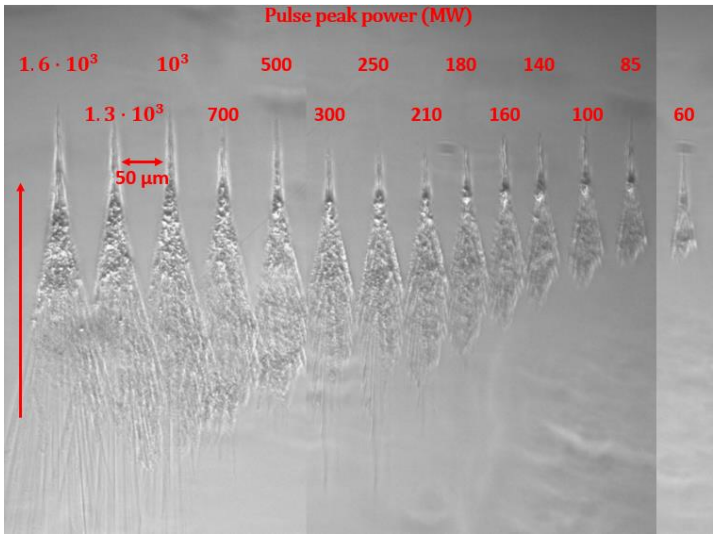

Figure 5.37. PCM image of the induced damage under 1030 nm femtosecond pulses at different pulse peak powers for the Corning 7980. The red arrow indicates the laser direction propagation.

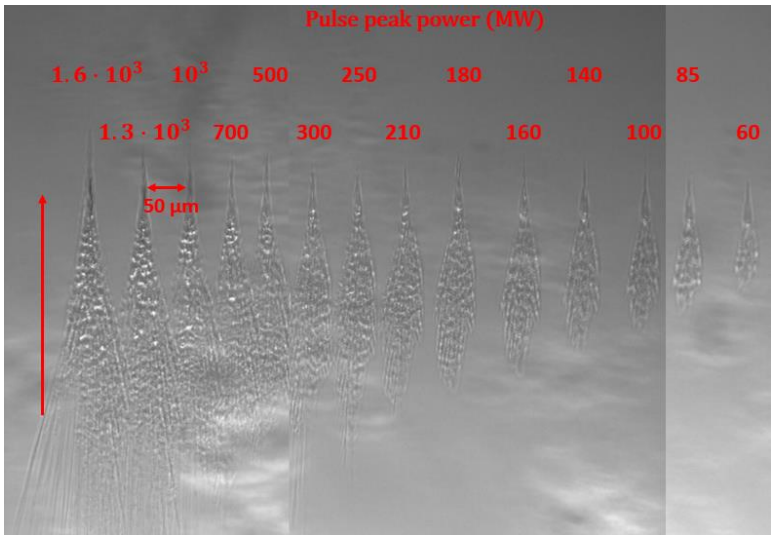

Figure 5.38. PCM image of the induced damage under 1030 nm femtosecond pulses at different pulse peak powers for the Herasil 1. The red arrow indicates the laser direction propagation.

Figures 5.36-5.38 show the damage along the laser direction propagation: the elongated trace left by the 1030 nm femtosecond laser is substituted by a wide region characterized by ruptures and fractures, likely caused by shock waves and other thermal effects at the all investigated pulse peak powers. No clear average refractive index is induced, since the images are characterized by the dark and clear colors, with respect to the background. The main difference among the investigated samples is in the dimension of the damaged area, which increases when increasing the OH content.

Also the investigation with the ARAMIS did not reveal big differences between the three samples. In Figure 5.39, which is representative of all the samples, we report the steady state PL (Figure 5.39 (a)) and Raman (Figure 5.39 (b)) post mortem characterization. The former reveals the same PL spectra as a function of the samples and of the used power: there is a strong band peaked at ~545 nm, reflecting that the whole investigated power range belongs to a Type II regime of interaction, with a small contribution due to the NBOHC. It is interesting to note that the NBOHC PL band was also measured in the traces where it was not observed during the online measurements. This difference could be related to the higher sensitivity of steady-state PL in comparison with the on-line PL during the laser exposure. As a further hypothesis, this finding

could be due to a systematic rearrangement of the matrix requiring a time longer than the online measurements, resulting in new NBOHC sites.

In addition, the Raman measurements did not detect differences between the samples, showing the same relation between the damages at the three used powers and the pristine sample, depicted in Figure 5.39 (b). The decreases of the main band around 400 cm^{-1} and of the D_2 line suggest a density reduction of the glass, according to the Type II regime of interaction.

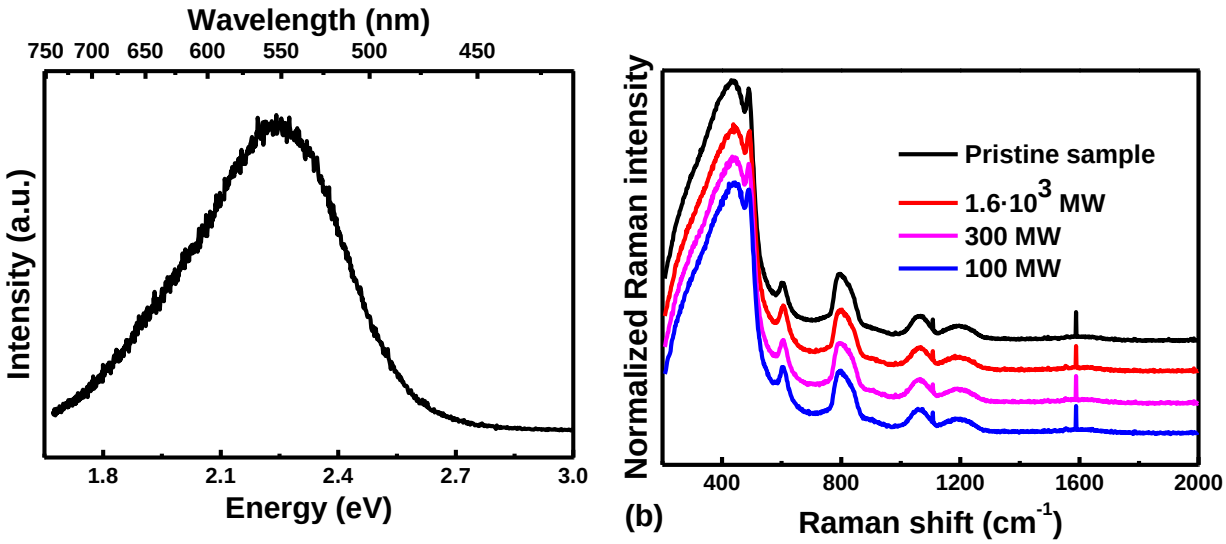

Figure 5.39. (a) Post mortem normalized PL spectra of the laser induced trace in the Corning 7980. (b) Comparison between the Raman spectra acquired in the pristine sample (black line), at $1.6 \cdot 10^3$ MW (red line), at 300 MW and at 100 MW (blue) observed in the Corning 7980.

5.3. Conclusion

In the first section, the above reported results highlight the laser wavelength effects on the amorphous silica exposure under high intensity femtosecond irradiation at 1030 nm (near-IR) and 343 nm (UV), being in experimental conditions able to write waveguides in the material [139]. By comparing the two set of wavelengths, we have observed more important structural modifications in the waveguides inscribed with UV laser pulses, leading also to stronger light guiding properties. Moreover, there is higher efficiency in the refractive index change induced by the UV laser: at lower pulse powers, higher positive refractive index changes are induced compared to the near-IR wavelength laser case. Different Type I/Type II thresholds were observed at the two different laser wavelengths.

Also the defect contribution to the total Δn is wavelength dependent: as shown by the thermal treatments, in the waveguides inscribed with the IR laser almost all the induced Δn is due to the generated defects, while for the UV waveguides an important contribution from the laser induced densification is observed.

The second section reports the PL induced by femtosecond laser as a function of the laser power and the sample chemical composition upon 1030 nm and 343 nm femtosecond laser pulses exposures. Under UV laser excitation, the sample chemical composition plays a role in the NBOHC response, manifesting two different scenario: i) intrinsic generation process, observed in the sample with low OH content, caused by the STX relaxation as consequence of a band-to-band multiphoton absorption process; ii) extrinsic process, observed in sample with relevant OH concentration, in which the NBOHC generation is driven by the OH breaking bond to have a transition to an intrinsic behavior at high doses.

Under 1030 nm femtosecond laser excitation, it is possible to conclude that the OH content plays an analogous role compared to the one observed with UV pulses. However, we observed two regimes of interaction as function of the laser pulse peak power: i) low pulse powers induce the ODC(II) generation, observed by the characteristic band at 2.7 eV; ii) high pulse powers, where the appearance of the NBOHC PL band is accompanied by a blue shift of the 2.7 eV band indicating the STX presence.

Chapter 6. Time-resolved pump-probe spectroscopy on point defects

In previous sections we have provided an overview on the color center generation under ionizing irradiation and femtosecond laser pulses. The purpose of this chapter is to clarify as much as possible the transient behaviors of the silica defects. This means to deepen our knowledge about the color center generation mechanisms, studying their behavior during and after the irradiation, as well as the study of the defect's photocycle. The latter, notwithstanding tens of years of research on the defect dynamics, still needs further studies to have a fine analysis of the whole photocycle under linear excitations, especially with an ultimate time resolution. The extremely short pulse duration allows to continuously improve the different pump-probe technique performances, leading to better investigation of the fast dynamics of numerous systems [110], [148], [241]–[244]. Nowadays, being the probe based on $\mathrm{fs} - \mathrm{ns}$ time scale regimes, it is possible to reconstruct the basic mechanisms at the origin of the structural modifications, which govern the decisive transformation phases and their final equilibrium state.

Pump/probe experiments in large bandgap insulators are made particularly difficult by the need to use tunable excitations in the UV range, which still today, remains a rather complex task from the experimental point of view. Our contribution will be exactly in this direction: the present investigation takes advantage from the coupling of femtosecond laser with an OPA, having the possibility to tune the excitation wavelength in a wide spectral range. The transient absorption (TA) measurements, becomes then an innovative tool to investigate the excited state absorption as a function of the laser pump wavelength. Furthermore, being in linear absorption conditions, we selectively excited the studied color center. As a case study, we apply this approach to TA measurements performed on the Non-Bridging-Oxygen-Hole-Center (NBOHC) [1], [3], [4], [40], [47]–[49] and Germanium-lone-pair-center (GLPC) [1], [4], [54], [91], [92], [240] under UV photo-excitation, following the femto-picosecond dynamics of these photoluminescent defects as a function of excitation wavelength from $230 - 320\ \mathrm{nm}$ in single-photon absorption conditions. The combination of our experiments allows clarifying the defects' photocycle, highlighting how state-of-the-art TA measurements with tunable UV excitation could represent an innovative tool to investigate such amorphous systems and the solid state in general. This approach is promising

in addressing unresolved issues regarding color centers in wide band-gap solids that often dominate their optical responses.

6.1. Transient absorption on NBOHC center

In the following section, we demonstrate how the experimental approach followed to perform transient pump-probe measurements allow us to follow the whole photoexcited dynamics, from hundreds of fs to ns, of the Non-bridging-Oxygen-Hole-Center, an archetypal defect in silica [1], [3], [4], [40], [47]–[49]. The interest in the NBOHC's dynamic study is fundamental because such defect represents a luminescent model system in dielectric materials, characterized by a very large Stokes shift (> 1 eV) [42], [44], [245], [246].

To our knowledge, this is the first attempts to investigate, in linear absorption condition, the photocycle of a color center embedded in a silica matrix, with a time resolution of hundreds of femtoseconds.

The study was performed in two steps: exploratory measurements, in order to probe which kind of signal, under UV excitation, characterizes the defect, and a deeper investigation, to study the TA response under different conditions. The former measurements were performed at the University of Palermo: part of my PhD was devoted to improve and adapt the already existent pump-probe setup in order to study the NBOHC's photocycle exciting at 266 nm fs laser. The latter were performed on the pump-probe setup in Saint-Etienne, optimized to reproduce the experimental condition used in Palermo and with the possibility to investigate the TA signal as a function of the laser power and the excitation wavelength. The combination of the experiments gives us the possibility to have new insight into the NBOHC's photocycle with an unprecedent time resolution, allowing us to provide a model able to explain the large Stokes shift which characterizes such defect.

6. 1.1 NBOHC: state of the art

Thanks to its optical properties, the oxygen dangling bond, commonly known as Non-Bridging-Oxygen-Hole-Center (NBOHC), is one of the most studied defects in amorphous silica. Its strong optical activity, in particular the intense and wide bands in the UV, makes NBOHC defect as a specific case which influences the transmission properties of silica in the UV and VUV spectral ranges.

It is pictured as an undercoordinated oxygen atom bounded to a single silicon atom, with an unpaired electron in the 2p non-bonding orbital and its structure is described as $\equiv Si - O \cdot$ (Figure 6.1). As already said in the first chapter, the NBOHC is identified by a well-known paramagnetic signal, allowing to clarify its structure: a hole localized in a nonbonding 2p orbital of a nonbridging oxygen [1], [3], [4], [40], [47]–[49]. Notwithstanding it is embedded in an amorphous matrix, the NBOHC is nearly characterized by a C_{3v} local symmetry.

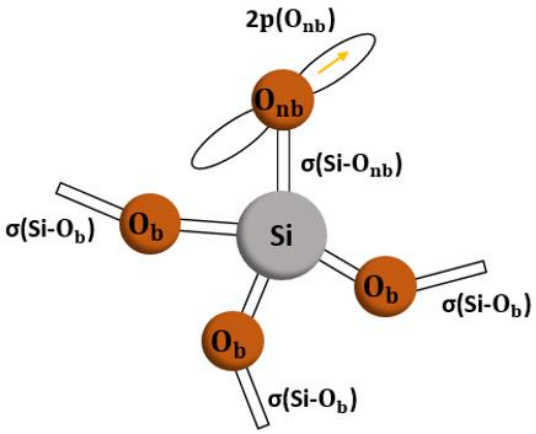

Figure 6.1. Schematic illustration of the NBOHC's structure embedded in a silica matrix.

The NBOHC generation is usually observed upon UV, γ-, X-rays, neutron and femtosecond laser irradiations. In α-quartz it is observed after high-energy irradiation by fast particles, usually neutrons, leading the material to amorphous micro-regions and microvoids. All these evidences support the hypothesis that NBOHC is peculiar to the glassy state, since it is not observed in α-quartz by a softer irradiation (like γ-rays) that would be incapable to create amorphous regions.

In literature, and coherently with the results of the present chapter, both the growth kinetics (the generation) and its stability depend on the silica material type (chemical composition and fabrication method) and on its environment (atmosphere or temperature).

Two different generation processes of NBOHC have been identified, starting from the pristine glass:

- An extrinsic process [41], [247], which consists in the radiolysis of the OH group (already described in equation 5.1) according to the following reaction:

$$\equiv Si - OH \rightarrow \equiv Si - O \cdot + H \tag{6.1}$$

  with the release of an atomic hydrogen. Since it was observed that the OH groups drive the absorption in silica by F_2 laser ($E_{laser} = 7.9$ eV), the break of the OH bond happens around ~ 8 eV [239]. Once the atomic hydrogen is generated, being extremely reactive, during the diffusion it leads to the formation of molecular hydrogen, SiH groups or recombines back with the NBOHC defect, thus restoring the OH bond by the inverse of reaction 6.1.

- The intrinsic process [41], [247] instead is due to the radiolysis of a strained $Si - O$ bond, according to the following reaction:

$$\equiv Si - O - Si \equiv \rightarrow \equiv Si - O \cdot + \cdot Si \equiv \tag{6.2}$$

  In this case, the NBOHC is generated with the correspondent intrinsic E´ defect, a dangling silicon with an unpaired electron in the hybridized sp^3 orbital $\equiv Si \cdot$.

The NBOHC optical properties are well-known:

- An asymmetric absorption band peaked at 2.0 eV, reported in Figure 6.2 (a), with a FWHM$\sim$ 0.17 eV, characterized by a low oscillator strength $f_{2.0\ eV} \approx 1.91 \cdot 10^{-4}$ [1], [3], [4], [39]–[42], [45], [245], [248].

- A wide and intense absorption bands in the UV, from 4.8 eV to 7.5 eV. The exact shape, reconstructed with the sum of five Gaussian bands (their spectral characteristics are listed in table 6.1), is reported in Figure 6.2 (b). The oscillator strength of the UV band is $\sim$200 times higher than that measured at 2.0 eV: $f_{4.8\ eV} \approx 0.03$ [1], [3], [4], [42], [45], [245], [246], [248].

Table 6.1. Parameters of five Gaussian functions, used to reconstruct the UV NBOHC's absorption band in silica. Values are taken from [42].

	G_1	G_2	G_3	G_4	G_5
Peak (eV)	4.706	5.474	6.085	6.635	7.29
FWHM (eV)	1.014	0.919	0.818	0.813	1.439

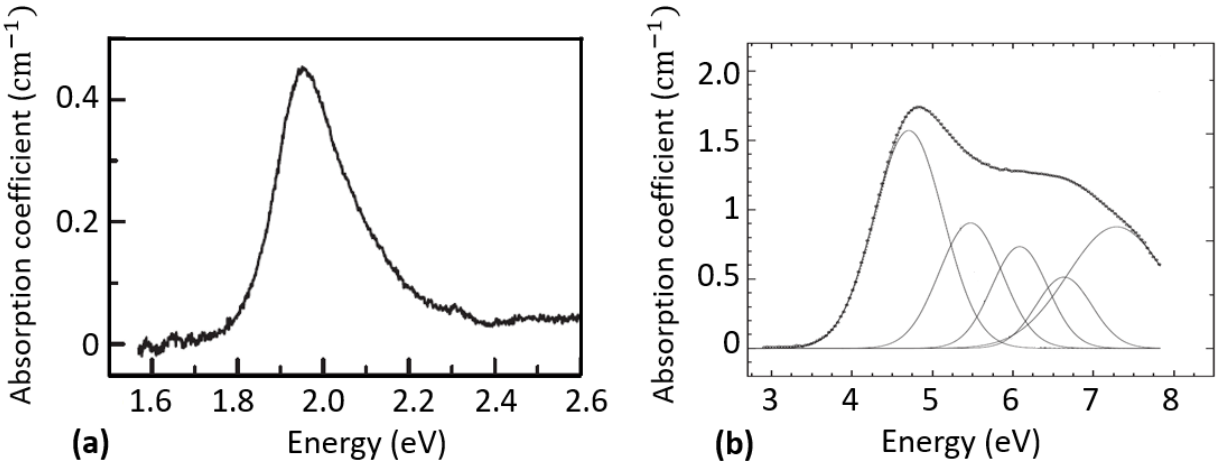

Figure 6.2. NBOHC optical absorption bands: (a) the 2.0 eV absorption band and (b) the UV wide band reconstructed with five Gaussians. Figure adapted from [42].

As concerns the luminescence properties, it is firmly established that the NBOHC is characterized by an asymmetric emission signal around 1.9 eV with FWHM of $\sim 0.1 \div 0.2$ eV. This luminescence is excited upon the above mentioned absorption bands, its decay kinetic slightly deviates from a purely exponential law and features a lifetime between $15 \div 20$ μs as highlighted in Figures 6.3 [248].

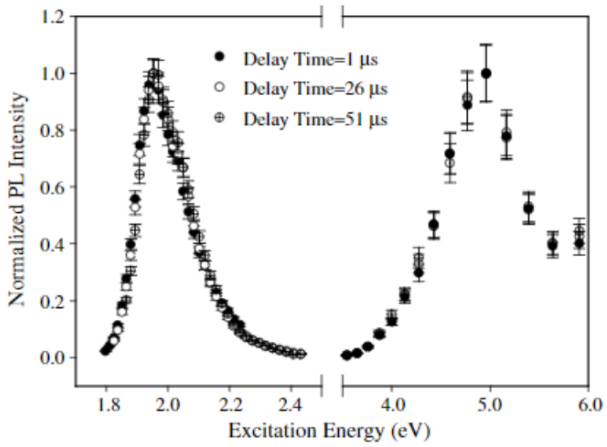

Figure 6.3. Integrated PL intensity as a function of the excitation energy measured in a sample containing NBOHC at three different delay times from the excitation pulse. The plotted curves are normalized to their maximum amplitude. Figure taken from [248].

Furthermore, it was established by synchrotron photoluminescence experiments that the NBOHC's PL at 1.9 eV could also be induced by band-to-band excitation with a mechanism in common with the self-trapped excitons [237], [249].

Different models are proposed to describe the NBOHC's excitation-emission process [47]–[49], supporting the hypothesis for which the absorption bands are due to charge transfer from orbitals localized at the defect site. In particular, the 2.0 eV peaked band is ascribed to an electron promotion to the half-filled 2p nonbridging oxygen (O_{nb}) non-bonding orbital from the Si-O_{nb} σ bond. The reverse forbidden transition gives rise to the 1.9 eV peaked PL band. In contrast, the UV excitation processes with a very large Stokes shift $\gtrsim 3$ eV, are not fully clarified yet. Among the most accredited hypotheses it is suggested a promotion of an electron from the deep of the valence band, composed of Si-O_b σ states, to the unpaired 2p (O_{nb}) non-bonding orbital, justifying the absorption bands in the UV range. The subsequent non-radiative relaxation in the valence band makes available an electronic state in the Si-O_{nb} σ bond, reproposing the same excited state upon

the 2.0 eV absorption, with the consequent PL at 1.9 eV. Since the involved transition requires fs-ps timescale, the most of the literature which is supporting the above-mentioned picture of the UV-excitation/1.9eV-emission is related to computational works, because of the lack of time resolved ultrafast experiments with such resolution timescales.

6. 1.2 Experimental setup

Experimental setup Palermo

The sample under test, already described in the third chapter, is a synthetic wet silica specimen Suprasil 1, $5 \times 5 \times 0.5\ \mathrm{mm}^3$ sized, supplied by Heraeus. In this sample NBOHC were produced by beta irradiation at the huge dose of $5 \times 10^9\ \mathrm{Gy(SiO_2)}$, using a Van de Graff electron accelerator (2.5 MeV), with an estimated concentration of $\sim 3.2 \times 10^{18}\ \mathrm{cm}^{-3}$ [245]. The excitation photon energy at 266 nm (4.66 eV) matches the NBOHCs absorption peak, as reported in Figure 6.4 (a); it is important to underline that the UV absorption band is probably affected by an absorption tail related to other UV absorbing point defects, mainly the E´ center characterized by an absorption band peaked at 5.8 eV [1], [3], [4]. In order to highlight how the UV fs laser excites the NBOHC, Figure 6.4 (b) shows the comparison between the steady state PL recorded under 325 nm (3.82 eV) continuous laser excitation (measure performed with the micro-Raman ARAMIS) and the PL excited by the 266 nm (4.66 eV) fs pulses, which is the pump radiation used in the transient absorption spectra. The close matching of the PL spectra, both centered at 1.9 eV, is a firm proof that our pump-probe system is able to investigate the ultrafast dynamics of the NBOHC's photocycle upon fs laser pulses.

The pump/probe setup (already described in chapter 3) is based on a 5 kHz Ti:sapphire femtosecond laser, with a pulse duration of ~50 fs, centered at 800 nm. Thanks to the extremely short pulse duration, the experimental resolution, defined by the XPM, is of the order of ~150 fs. The maximum delay available in this setup is 200 ps. Since the 266 nm (4.66 eV) pulses came from the generation of the third harmonic, it is possible to observe on the sample light from the 400 nm (3.1 eV) and the 800 nm (1.55 eV), the residuals of both the second harmonic and the fundamental, respectively. As highlighted in Figure 6.4, no absorption band is present both at 800 nm and 400 nm, then no particular influence should be ascribed to these wavelengths in case

they reach the sample (two photon absorption effects are indeed neglected at these energies, in comparison with the linear absorption studied in the following sections).

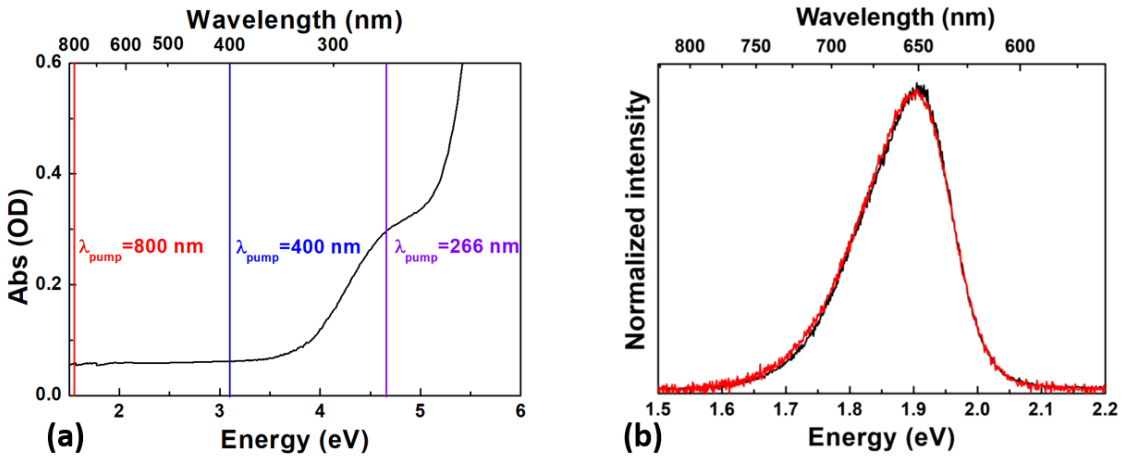

Figure 6.4. (a) Absorption spectrum of the Suprasil 1 β-irradiated sample, characterized by the NBOHC absorption band in the UV with the probable tail of the E´ center; vertical lines are related to the incoming light on the sample: 266 nm, 400 nm and 800 nm, respectively in violet, blue and red. (b) The PL of the sample: in black under the steady state irradiation at 325 nm (3.82 eV) obtained with the micro-Raman ARAMIS and in red upon irradiation with 266 nm (4.66 eV) fs pulses.

The beam, chopped at 500 Hz, reaches the sample with 20 nJ/pulse and a diameter of ~140 μm (probe beam diameter dimension ~60 μm). To improve the signal-to-noise ratio, every spectrum at fixed pump-probe delay results in the average of 100 spectra, exploring a delay window of 16 ps. The probed spectral region, defined by the available white light in our setup (Figure 3.30), is between ~400 nm and ~650 nm.

It is important to observe that no contribution to the total transient absorption comes from the pristine silica network, since in the not-irradiated Suprasil 1 sample there is no absorption band in the spectral range around the possible incoming light in the sample (Figure 6.5): at 266 nm, 400 nm and 800 nm.

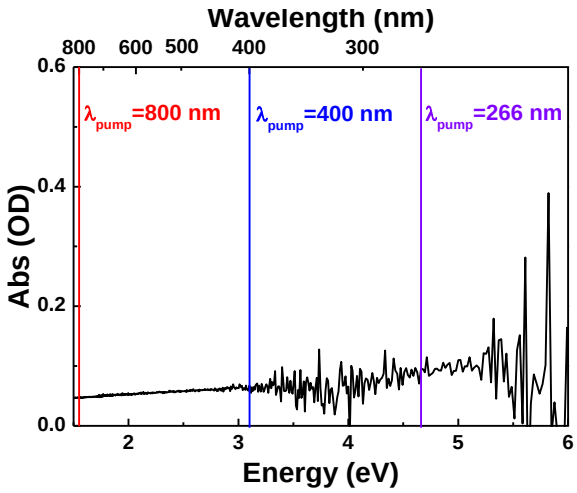

Figure 6.5. Suprasil 1 absorption spectra of a pristine not-irradiated sample; vertical lines are related to the incoming lights on the sample at: 266 nm, 400 nm and 800 nm, respectively in violet, blue and red.

Experimental setup Saint-Etienne

The pump/probe setup (reported in details in chapter 3) is based on a Yb:KGW femtosecond laser working at a repetition rate of 60 kHz, centered at 1030 nm. The PHAROS fs laser is coupled with an OPA delivering tunable fs-laser signals from 210 nm to 20 μm, allowing pump laser wavelength control. Since the PHAROS pulses have a duration of ~200 fs, the temporal resolution is ~400 fs. The maximum available pump-probe delay used in the experiment, is around ~8 ns.

The experiment was carried out by exciting the sample with femtosecond pulses in the UV range from 320 nm to 230 nm, at fixed energy per pulse of ~50 nJ/pulse, (Figure 6.6), following the transient absorption around the first NBOHC peak signal at 4.8 eV. It is important to note that the OPA efficiency is not the same at every chosen wavelength, delivering monochromatic beams at the output with different energies and beam sizes. For this reason, in order to compare the results from different pump wavelengths, it is necessary to measure the beam spot on the sample, varying the diameter from 80 μm to 120 μm (probe beam diameter ~80 μm), and correct the data for the laser intensity on the sample. Moreover, we control the pump power on the sample by the use of a filter, allowing studying the transient absorption signal as a function of the pump intensity. The transient absorption response was probed in two different spectral ranges:

- 550 ÷ 900 nm, generating the white light from the PHAROS fundamental;

- 400 ÷ 650 nm, generating the white light from the second harmonic of the PHAROS fundamental.

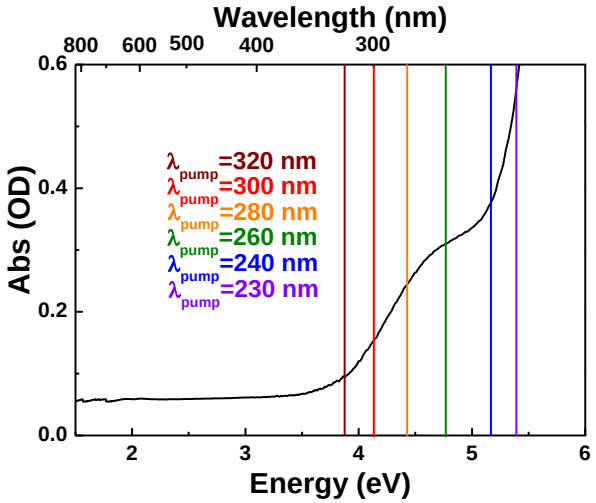

Figure 6.6. Absorption spectrum of the Suprasil 1 β-irradiated sample, characterized by the NBOHC absorption band in the UV with the probably tail of the E´ center; the vertical lines indicate the spectral positions of the exciting pump signals.

6. 1.3 TA measurements performed in Palermo

We first characterized the pristine Suprasil 1 sample through its pump-probe response under an excitation at 266 nm (4.66 eV) and at ~20 nJ pulse energy to highlight the TA signal contribution due to the color center of the as received matrix. The TA spectra at different pump-probe delays are reported in Figure 6.7. These responses are already corrected for white light group velocity dispersion.

Whatever the delay, no signal is detected in the studied pristine sample and over all the involved spectral range.

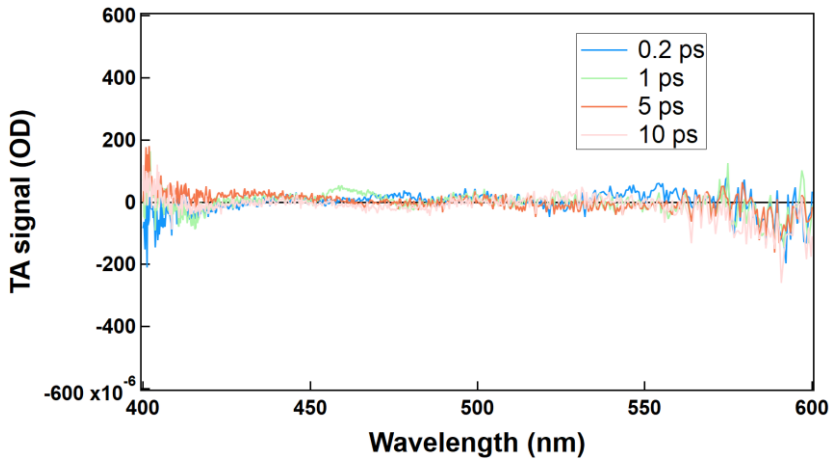

Figure 6.7. TA signal, as a function of the wavelength, of a not-irradiated Suprasil 1 sample at different pump-probe delays: light blue at 0.2 ps, green at 1 ps, orange at 5 ps and pink the 10 ps.

However, the recorded spectra on the β-irradiated sample, Figure 6.8, exhibit different responses as a function of the wavelength and the pump-probe delays. An SVD analysis was carried out on the raw date for noise contributions. The reported TA values are in a color scale. A wide band is detected, more intense in the blue part of the spectrum, whose shape changes as a function of the pump-probe delay. The delay times around zero value were cancelled because affected by the XPM (~150 fs width).

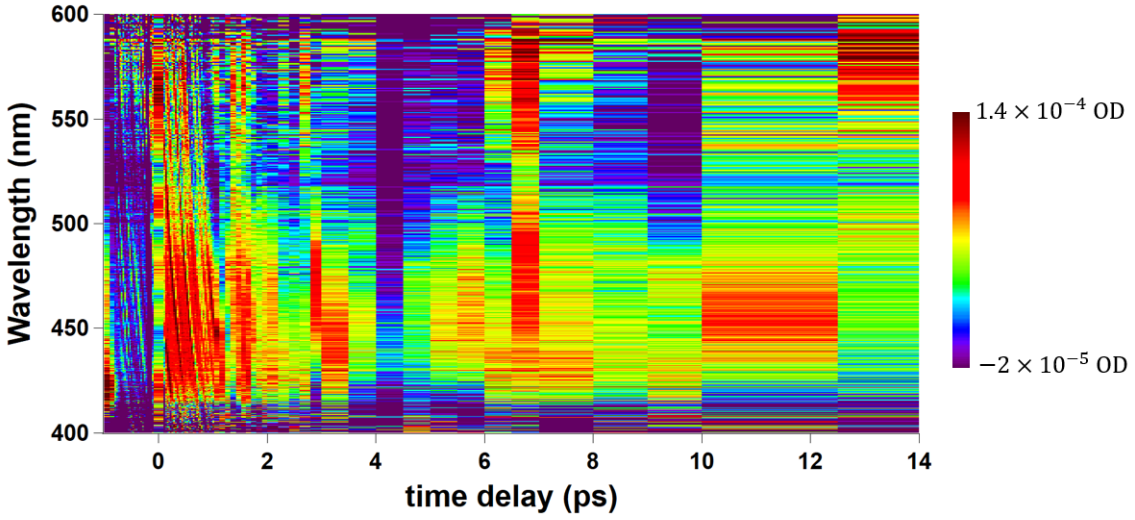

Figure 6.8. TA signal as a function of the wavelength and the pump-probe time delay in color scale.

More information could be gained studying the spectra at different time-delays. To this end, Figure 6.9 shows the comparison between spectra recorded at different pump-probe delays. The observed TA is characterized by:

- A continuous wide and unstructured band, dominating almost the whole investigated spectral range;
- A negative component for the earlier times after the pump pulse for wavelength lower than ~430 nm;
- No tail of the stimulated emission at 1.9 eV is observed in these experimental conditions, which is probably explained by the characteristically long decay NBOHC lifetime (~15 μs).

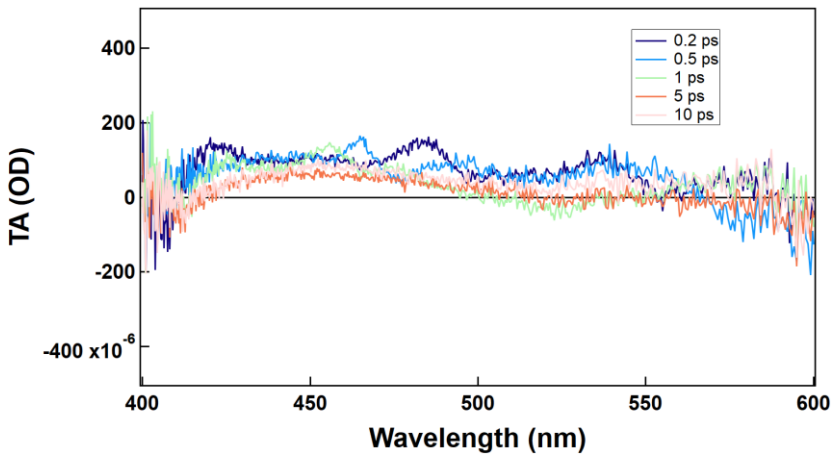

Figure 6.9. TA signal, as a function of the wavelength, of a β-irradiated Suprasil 1 sample at different pump-probe delays: blue at 200 fs, light blue at 0.5 ps, green at 1 ps, orange at 5 ps and pink the 10 ps.

Studying the single wavelength kinetic we can investigate the evolution of the spectra as function of the pump-probe delay. Moreover, we can even reconstruct the experimental time evolution using multi-exponential decay functions defined as follow:

$$\sum_{i=1}^{2} A_i e^{-t/\tau_i} + C \qquad (6.3)$$

characterizing the main timescales involved during the TA process. The fitting results are reported in Figures 6.10-6.12 for three wavelengths and the best-fit parameter sets are listed in table 6.2. At 410 nm we observed a very fast dynamics, $\tau \sim 0.1$ ps (which is a dynamic at the limit of the experimental sensibility), reaching a constant value for longer times. The dynamics at 450 nm and 520 nm are fitted with the same decay time, suggesting that the spectrum decreases equally from ~430 nm to ~600 nm. The corresponding decay times are: 0.7 ps and 5 ps and the last observed only in the kinetics at 450 nm is >> 16 ps (probably present also in the 520 nm dynamic, but with a value close to zero).

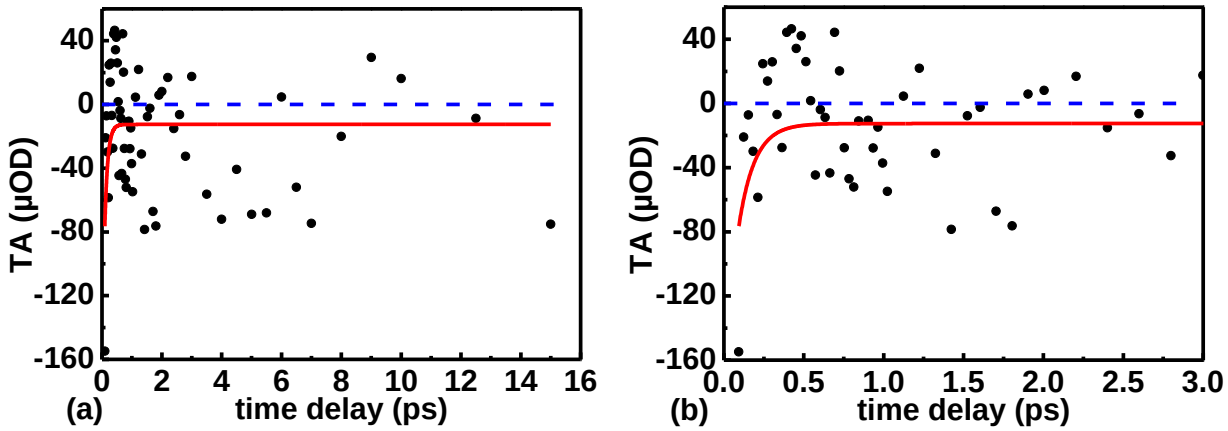

Figure 6.10. (a) Kinetic at 410 nm (3 eV) up to 16 ps and (b) the zoom up to 3 ps. The red curve is the best-fit function while the dashed blue line is an eyes guide for the zero value.

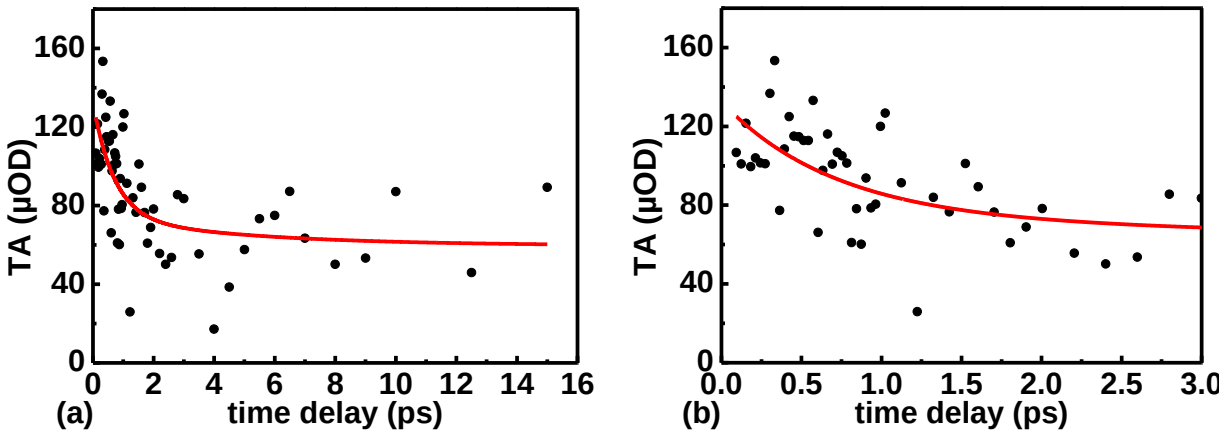

Figure 6.11. (a) Kinetic at 450 nm (2.8 eV) up to 16 ps and (b) the zoom up to 3 ps. The red curve is the best-fit function.

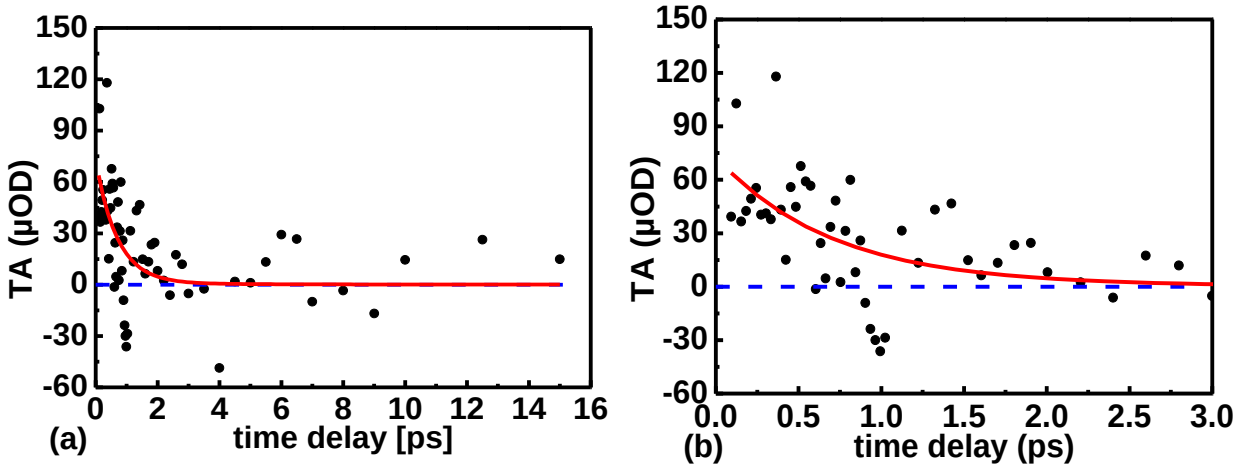

Figure 6.12. (a) Kinetic at 520 nm (2.4 eV) up to 16 ps and (b) the zoom up to 3 ps. The red curve is the best-fit function while the dashed blue line is an eyes guide for the zero value.

Table 6.2. Best-fit parameters used for the deconvolution of decay kinetics reported in Figures 6.10-6.12.

Parameters	410 nm	450 nm	520 nm
C	−13 μOD	60 μOD	
A_1	−160 μOD	60 μOD	70 μOD
τ_1	0.1 ps	0.7 ps	0.7 ps
A_2		15 μOD	9 μOD
τ_2		5 ps	5 ps

Up to now, we observed the pump-probe response of a pristine and a β-irradiated Suprasil 1 sample containing NBOHCs. The experiment was carried out pumping at 266 nm with ∼20 nJ/pulse. Our measurements reveal:

- No transient absorption in the pristine sample;
- A very broad and unstructured band distributed in the [430 nm - 600 nm] spectral range ;
- This broad band is characterized by at least three different kinetics: $\tau_1 < 1$ ps, $\tau_2 \sim 5$ ps and $\tau_3 \gg 16$ ps;
- A negative component for the earlier times after the excitation for wavelength lower than 430 nm.

The next step will be the comparison with analogous measurements on the same sample using the pump-probe setup in Saint Etienne, studying also the signal as a function of the laser intensity and the pumping wavelength. The goal will be to provide a model to describe all the observed features.

6. 1.4 TA measurements performed in Saint-Etienne

The first step of the pump-probe measurements performed in Saint-Etienne was the reproduction of analogous experimental conditions used in Palermo and compare the results. The experiment was carried out by exciting the sample with fs pulses at 266 nm (4.66 eV), at an average energy of ~50 nJ/pulse, probing with the UV/visible white light (400 ÷ 650 nm). The main difference between the two experimental stages is the laser repetition rate: and the 5 kHz with the first setup (Palermo) and 60 kHz for the second one (St-Etienne). The higher repetition rate allows to have more averaged spectra per unit of time, cleaning the sample from the noise.

The 2D map TA signal is reported in Figure 6.13 in color scale. The spectral shape reveals that the signal is composed of very broad and unstructured excited state absorption, covering the whole probed spectral range, between 650 nm (1.9 eV) and 380 nm (3.2 eV), thus suggesting an absorption process from/to a continuum of states. Even in this case no stimulated emission was observed at 1.9 eV. This signal rapidly decays over multiple time scales. The very noisy region centered at 532 nm (2.33 eV) is an artifact due to the residual 532 nm beam used to generate the 266 nm beam through the second harmonic generation process in the OPA. After the SVD correction were removed the data affected by this artifact noise (520-560 nm range). Moreover, all the TA measurements are corrected for white light group velocity dispersion.

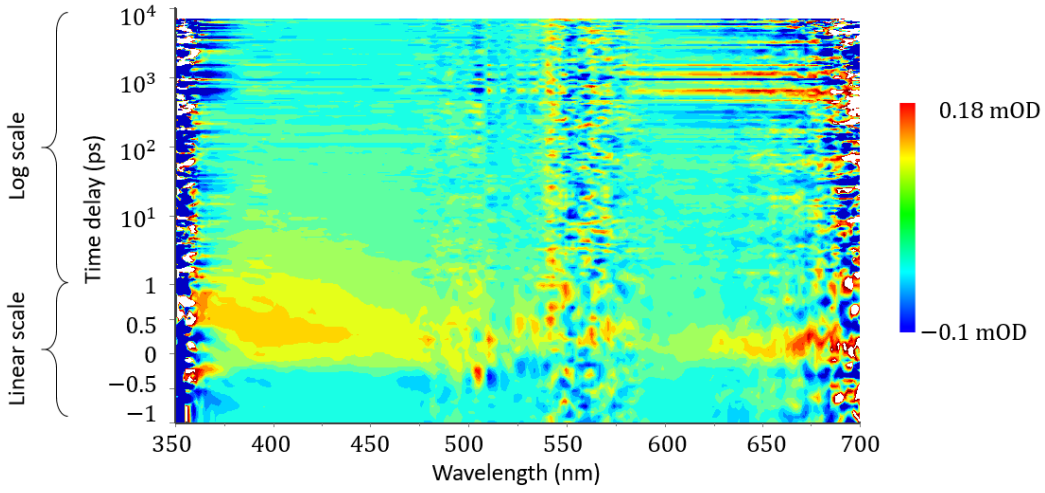

Figure 6.13. Two-dimensional time-wavelength plot of the TA signal measured in β-irradiated Suprasil 1 sample after photo-excitation with 200 fs laser pulses at 50 nJ/pulse at 266 nm (4.66 eV) in the whole investigated pump-probe delay window.

In order to compare these experiments with those performed in Palermo, we reported in Figure 6.14 a zoom up to 14 ps with the same color scale used in Figure 6.8.

Figure 6.15 (a) reports two TA spectra recorded after a delay of 1 ps and 10 ps respectively. While the recorded kinetic at 450 nm (2.8 eV) is reported in Figure 6.15 (b) including the fit curves obtained with equation 6.3, the best fit values being reported in table 6.3. The presence of four time scales, instead of three found in the kinetics measured in Palermo, is due to the longer investigated pump-probe delay window. All the features previously observed are confirmed in the present experiments, finding an excellent qualitative agreement between the two measurement sets. It is important to note that the XPM of the present setup is ~0.4 ps, making impossible the results comparison within this pump-probe delay, in particular the fast negative kinetic previously observed in the blue part of the investigated spectral range.

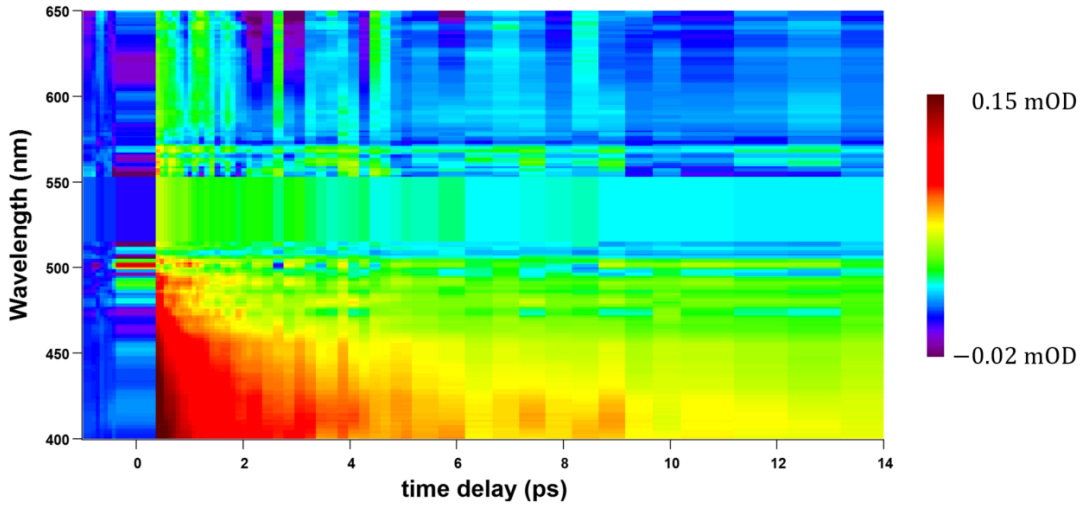

Figure 6.14. Two-dimensional time-wavelength plot of the TA signal measured in β-irradiated Suprasil 1 sample after photo-excitation with 200 fs laser pulses at 50 nJ/pulse at 266 nm (4.66 eV) from the beginning of the irradiation to a pump-probe delay of 14 ps.

The fitting routine evidences that the 60% of the amplitude decay is yielded by a sub-picosecond decay time around 0.7 ps, followed by two other decay times around ~10 ps and ~100 ps respectively. The constant value corresponds to a much slower time-decay compared to the timescale explored in these experimental conditions. The obtained values are perfectly coherent

with the kinetics measured in Palermo, as highlighted by the comparison of the normalized kinetics probed at 450 nm (2.8 eV) in Figure 6.16.

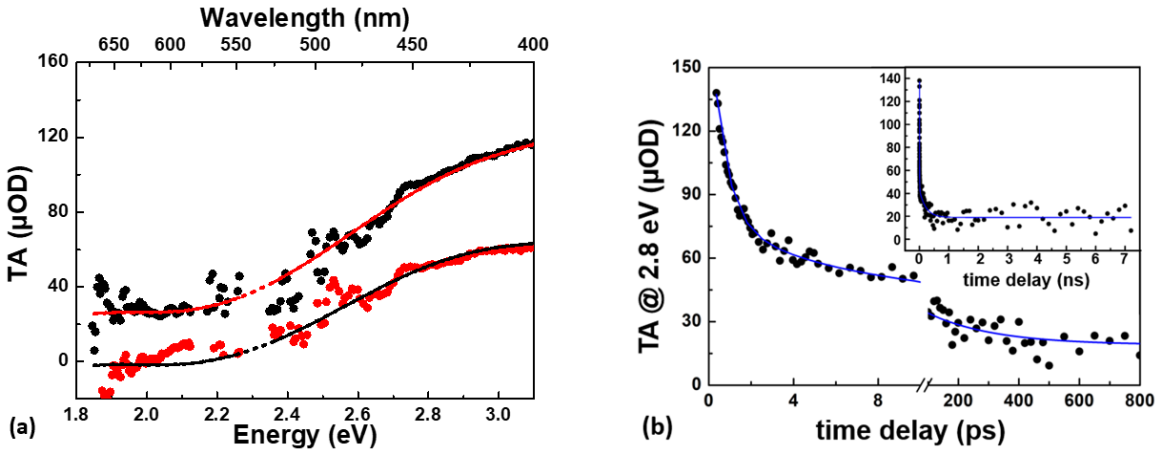

Figure 6.15. (a) TA spectra recorded at different pump-probe delays: 1 ps in black and 10 ps in red. Solid lines are a guide to the eyes, while the dashed ones between ~2.25 eV and ~2.4 eV are extrapolations. (b) TA kinetics probed at 2.8 eV (in black dots), as a function of pump-probe delay. The blue lines are the best-fit exponential decay curves. The panel (b) inset presents the kinetic at 2.8 eV in the whole investigated time delay window, showing the quality of the fit even for longer delays.

Table 6.3. Best-fit parameters used to reconstruct the experimental decay kinetic measured at 450 nm (2.8 eV).

Parameters	Value
C	20 μOD
A_1	100 μOD
τ_1	0.67 ps
A_2	40 μOD
τ_2	6.5 ps
A_3	20 μOD
τ_3	230 ps

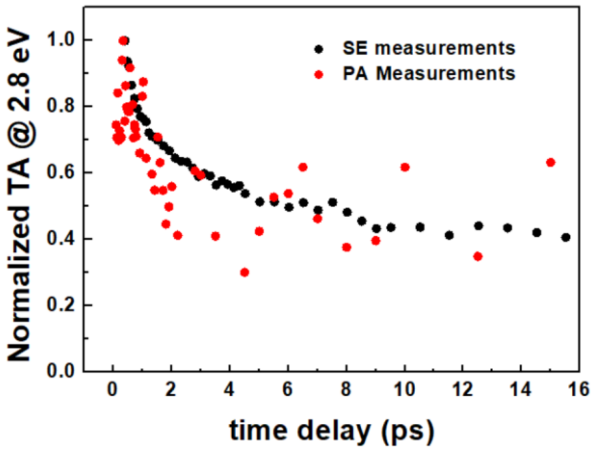

Figure 6.16. Comparison of the normalized kinetics, probed at 450 nm (2.8 eV) measured in Saint Etienne (black curve) and in Palermo (red curve).

Moreover, by comparing the extracted kinetics, the whole TA signal follows the same decay, despite the wide data dispersion in the red part of the investigated spectral range, probably because of a lack of photons in the IR part of the white light. Indeed, in Figure 6.17 (a) we reported the normalized decays at different wavelengths: the kinetics show the same time responses independently of the probed wavelengths. Consistently, we also find that the spectra maintain the same shape on varying the pump-probe delay time) as showed by the spectra normalization at different delays between pump and probe (Figure 6.17 (b), notwithstanding the wide dispersion in the infrared region. It is important to note that the signal rises instantaneously, within the time resolution of our experiment (~400 fs of width, defined by the cross-phase modulation). Therefore, we can conclude that the excited state responsible for the signal in Figure 6.15 (b) is already fully populated from photo-excitation.

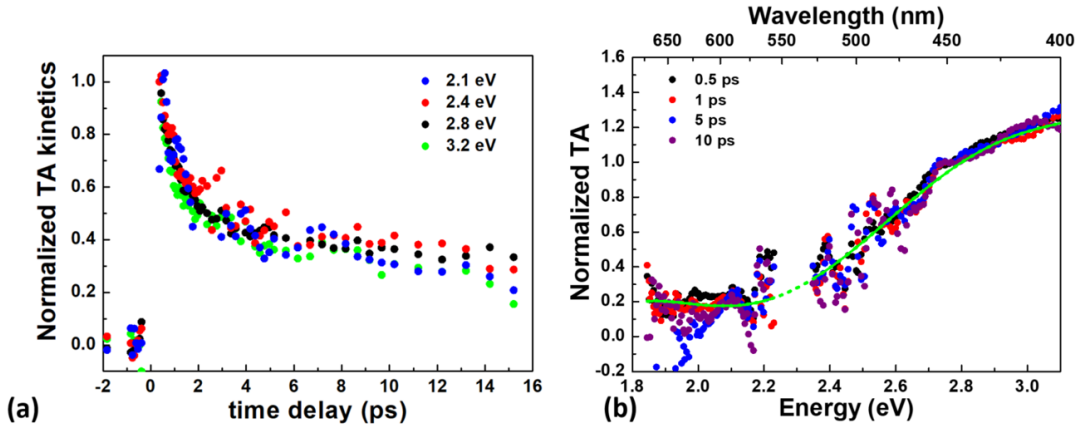

Figure 6.17. (a) Normalized kinetics at different energies: 2.1 eV are the blue dots, 2.4 eV the red dots, 2.8 eV the black dots and the green ones are at 3.2 eV. (b) Normalized transient absorption spectra measured at different delay times between the pump and the probe: 0.5 ps the black line, 1 ps in red, 5 ps the blue line and 10 ps the magenta one. The green solid line is a guide to the eyes, while the dashed one between ~2.25 eV and ~2.4 eV is an extrapolation.

For a more global view and a better investigation in the IR domain, we carried out the same experiment with the white light generated by the PHAROS fundamental signal, in the [550 ÷ 900] nm spectral range. Figure 6.18 reports the spectra acquired at 5 ps of pump-probe delay, the two responses are plotted without any data correction. It is evident that no new spectral feature is available in the IR range and the spectrum is basically the tail of the wide and unstructured band dominating the UV/visible region.

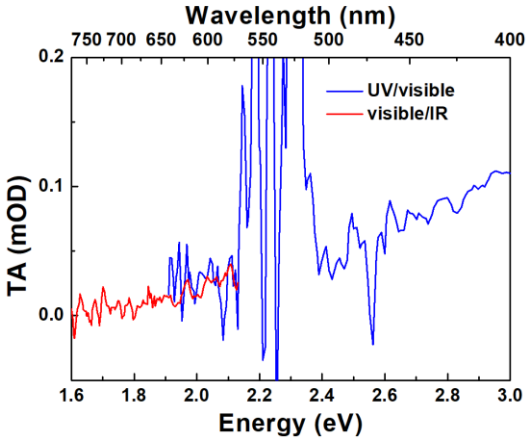

Figure 6.18. Comparison between the TA responses probing with a UV/visible white light (in blue) and with a visible/infrared whit light (red) at 5 ps of pump-probe delay. Since the 4.66 eV fs-pulse is generated by doubling a 2.33 eV fs-beam in the OPA, the residual component of green light affects the transient absorption spectra around 2.33 eV.

Since the purpose of the present chapter is the investigation on the NBOHC's photocycle under linear absorption condition, we have repeated the same experiment as a function of the pump intensity to verify the signal's linearity with the laser power, Figure 6.19 (a) reports the TA levels, probed at 450 nm (2.8 eV), as a function of the laser energy/pulse at different pump-probe delay times: the TA is linear at all the pump energies and at any given time, manifesting also the same kinetic as a function of the pump power (Figure 6.19 (b)). Then, all the previous experiments carried out at $\sim$50 nJ/pulse, with an intensity of $\sim 10^9$ W/cm^2, were performed under the same condition. It is important to stress that all the pump probe measurements, involving a linear excitation process, are directly linked to the investigated point defect, which is substantially different from the non-linear phenomena that involve the whole silica network.

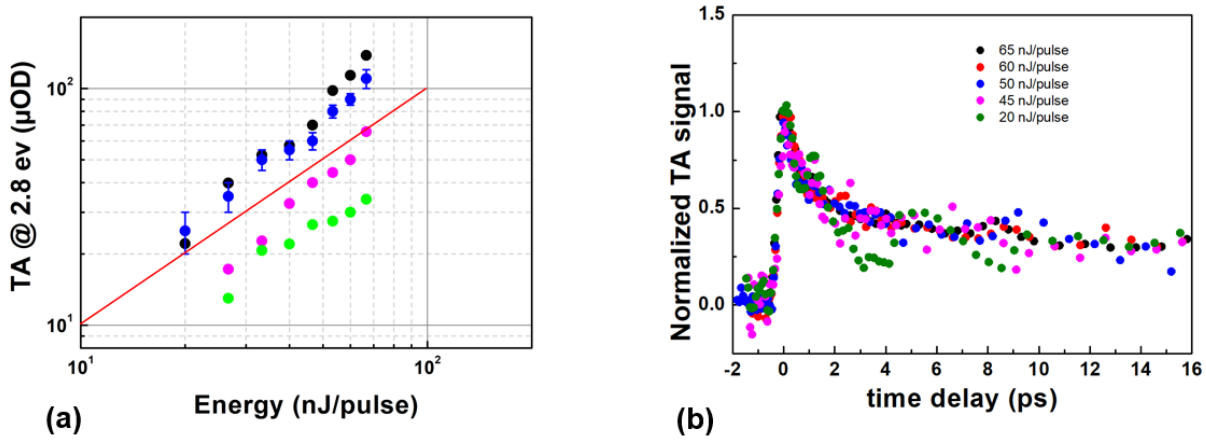

Figure 6.19. (a) TA measured at 2.8 eV with 0.7 ps (black), 5 ps (blue), 10 ps (magenta) and 100 ps (green) of delay as a function of the energy per pulse. The red line is a guide highlighting the linear dependence. The error bar is reported only in the 5 ps data set for the sake of clarity. (b) Normalized kinetics at 2.8 eV as a function of the pump energy/pulse.

To deeply characterize the TA signal, the same experiment was performed as a function of the exciting wavelengths, tuning the laser pulse between 230 nm (5.4 eV) and 320 nm (3.8 eV). Once the linear excitation regime is validated, it is possible to make a comparison between the TA signal, as a function of the exciting wavelength, and the steady state absorption spectra, correcting the pump-probe responses to the pump intensity for each wavelength. Moreover, because of the

strong absorption in the UV range (Figure 6.6), the sample is not uniformly illuminated by the pump photons. Then, to guarantee a linear dependence with the concentration of color centers we have corrected the TA spectra with the following factor:

$$C(E) = \frac{\alpha(E)d}{1 - e^{-\alpha(E)d}} \tag{6.4}$$

where α(E) is the absorption coefficient (cm^{-1}) and d is the sample thickness (cm). Figure 6.20 reports the comparison between the absorption spectrum (normalized to the optical density value at 4.8 eV) and the normalized TA signal, under different excitation wavelengths, keeping fixed the TA value probed at 450 nm (2.8 eV) and at 5 ps of pump-probe delay. From this comparison, the normalized TA signal matches quite well the NBOHC absorption spectrum profile, strongly supporting that the observed signal is determined by this defect's direct photo-excitation. Indeed, the normalized TA is nearly zero at wavelengths before the absorption band, reaching the maximum at ~4.8 eV and for energies higher than the first NBOHC's peak (the more intense among the five Gaussians of the NBOHC's bands in the UV).

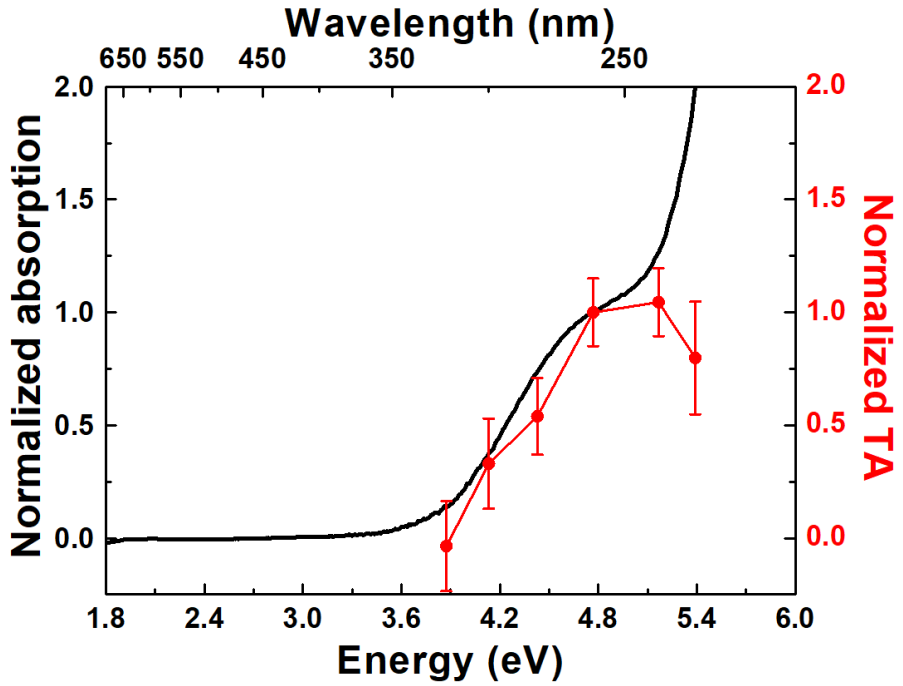

Figure 6.20. Normalized 2D spectra (in red dots) of the TA at 450 nm (2.8 eV) and 5 ps of delay as a function of the pumping wavelength overlapped on the normalized absorption spectra of the β-irradiated suprasil sample.

6. 1.5 NBOHC's photocycle

On the basis of the above illustrated observations, it is possible to hypothesize a model to describe the NBOHC photocycle, explaining the large Stokes shift under UV excitation. Indeed, as already proposed in literature, the UV absorption is caused by a charge transfer from a state into the valence band to the half-filled 2p atomic orbital of O_{nb}. An oversimplified NBOHC's model depicting the involved electronic states is reported in Figure 6.21. As illustrated, the promoted electron in the NBOHC's higher acceptor level, leaves a hole in the valence band. The remaining hole induces an absorption in a wide spectral range, coherent with that expected by an intra-band absorption in a solid-state system and explaining the broad observed ESA (Figure 6.9 and 6.15 (a)). After UV excitation, the electron in the $\sigma(Si\text{-}O_{nb})$ relaxes down to the VB filling the hole, in a sub-picosecond time scale, explaining the rapid 60% amplitude drop in the pump/probe signal. The further exponential decay contributions suggest that for a minority of NBOHC sites, this recombination results in a longer time scale, highlighting the appearance of site-to-site non-equivalent defect centers within the disordered silica matrix. Therefore, our data provide a direct estimation of the relaxation time for the excited NBOHCs, due to the electron transfer filling the hole in the VB. After the recombination process, the emissive transition at 1.9 eV is finally possible due to the transition from the 2p non-bonding orbital of O_{nb} to the σ bonding orbital of $Si\text{-}O_{nb}$.

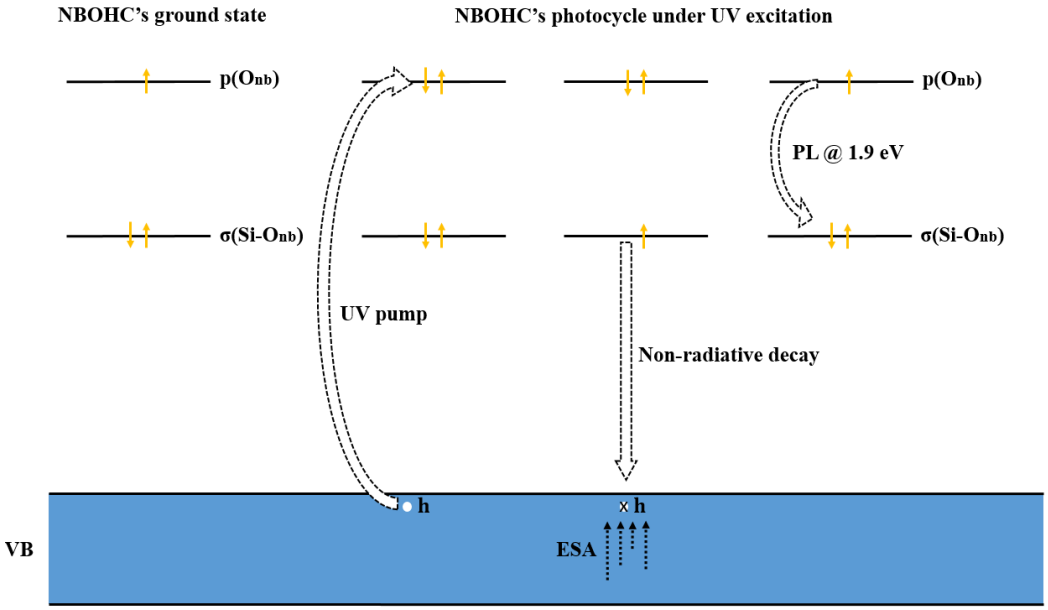

Figure 6.21. Model of the NBOHC's photocycle under UV excitation.

6.2. Transient absorption on GLPC

The second investigated point defect is a Ge-related center that plays an important role in the optical properties of Ge-doped silica [1], [4], [54], [88], [91], [92]. Indeed, the germanium presence in amorphous silica, both in bulk or in other silica-based systems such as optical fibers, leads to a higher photosensitivity of the glass and also to the breaking of the material symmetry making possible non linear optical phenomena such as SHG. Moreover, the existence of a wide variety of Ge-related defects changes the transmission properties of the silica. From the structural point of view, since the Ge atom is isoelectronic with Si, it could be substitutional in the bonding with four O atoms, or it could be under-coordinated giving rise to oxygen deficient centers (GeODC). Among the variety of Ge-related defects, in the present chapter we have studied the Germanium Lone Pair Center (GLPC), which is a well-known PL active defect. The focus of our experiments will be the investigation of the whole color center's photocycle, thanks to our approach in transient pump-probe measurements, giving us the possibility to follow the excitation/relaxation process from hundreds of fs to ns timescale.

The study was performed following the previously used procedure for the NBOHC photocycle: starting with exploratory measurements to highlight the GLPC pump-probe response under UV excitation, and a deeper investigation, devoted to the TA spectra under different conditions. Since the GLPC is characterized by an absorption band centered at $\sim$245 nm (5.1 eV), the experiment will be performed exciting around this absorption band, being in TA linear condition. Moreover, we have also the possibility to study the TA response as a function of the Ge concentration, having samples differing in terms of germanium contents (0.1%, 1% and 6% in weight, already described in chapter 3). The combination of these experiments provides us enough information to propose a model for the GLPC photocycle.

6. 2.1 GLPC's State of art

The germanium lone pair center (GLPC), also known as the twofold coordinated Ge, is the germanium substitutional variety of the ODC(II). Ge-doped amorphous silica-based materials are extensively used in a very wide application domain and the properties of many Ge related defects have been fully characterized in the last few years: the GLPC is one of the most studied center.

Its structure (Figure 6.22) is composed of an undercoordinated germanium atom bonded to two oxygen atoms and characterized by the presence of a lone pair, described as $=$ Ge: [1], [4], [54], [88], [91], [92]. Then, the GLPC is a diamagnetic defect, with a C_{2v} local symmetry.

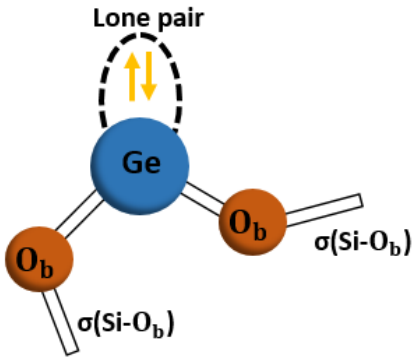

Figure 6.22. Schematic illustration of the GLPC's structure embedded in silica matrix.

The optical absorption bands related to the GLPC are [1], [4], [54], [88], [91], [92]:

- a band peaked at 5.1 eV, reported in Figure 6.23 (a), the so-called $B_{2\beta}$ band, with a FWHM$\sim$ 0.46 eV, and an oscillator strength $f_{2.0\ eV} \approx 0.12$.

- another band in the vacuum UV, centered around $\sim$7.6 eV, with an oscillator strength of the same order of the $B_{2\beta}$ band [250].

Upon excitation of these two absorption bands, two emissions are reported [1], [4], [54], [88], [91], [92]:

- A photoluminescence band, peaked at 4.2 eV, the α_E band, with a FWHM~0.44 eV and a lifetime that depends on temperature: $\tau \sim 1 \div 2$ ns at T=300 K; $\tau \sim 7 \div 8$ ns at T=10 K

- The second emission is peaked at 3.1 eV with a FWHM~0.42 eV, the so-called β band, it has a forbidden character consistently with a long lifetime $\tau \sim 100$ μs.

Moreover, some experimental studies highlight the existence of an absorption band around ~3.8 eV, caused by the direct light absorption from the ground state to the forbidden state with the 3.2 eV emission, with an oscillator strength of less than 10^{-3} [4].

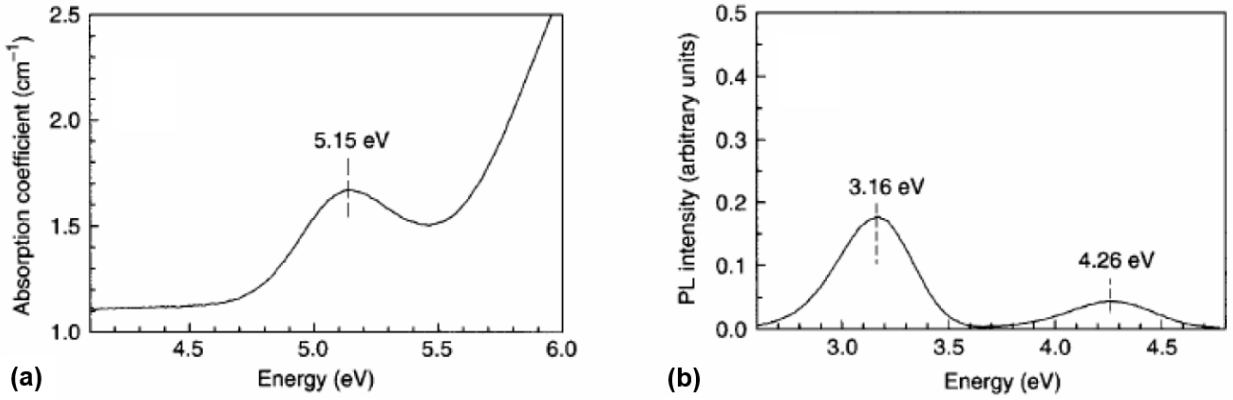

Figure 6.23. (a) GLPC absorption band peaked at 5.1 eV, also known as $B_{2\beta}$ band. (b) GLPC emission spectrum excited at ~5 eV. Figure adapted from [251].

According to the above mentioned spectroscopic features, it is possible to draw the GLPC electronic levels scheme, reported in Figure 6.24. The energetic levels correspond to a ground single electronic level, S_0, two excited single states at S_1 and S_2, related to the 5.1 eV and 7.6 eV absorption bands, and a triplet excited level T_1. The α_E emission is associated with the $S_1 \rightarrow S_0$ transition, inverse to the $S_0 \rightarrow S_1$ absorption, and is also excited by the $S_0 \rightarrow S_2$ excitation through an $S_2 \rightarrow S_1$ internal conversion (int); its lifetime of the order of the nanoseconds is consistent with the singlet-singlet permitted transition [92]. As already noted before, the 3.1 eV PL should be associated to a forbidden transition and, in agreement with that, such emission is linked to the $S_0 \rightarrow S_1$ (or $S_0 \rightarrow S_2$ with the addition of the $S_2 \rightarrow S_1$ internal conversion) by an $S_1 \rightarrow T_1$ intersystem crossing (ISC) with an associated relaxation time ~1 ns. Furthermore, it is commonly

accepted that nonradiative relaxation channel linked to the $S_1 \rightarrow S_0$ and $T_1 \rightarrow S_0$ can be neglected compared to the relaxation rate of the α_E band, the ISC and the β band [251].

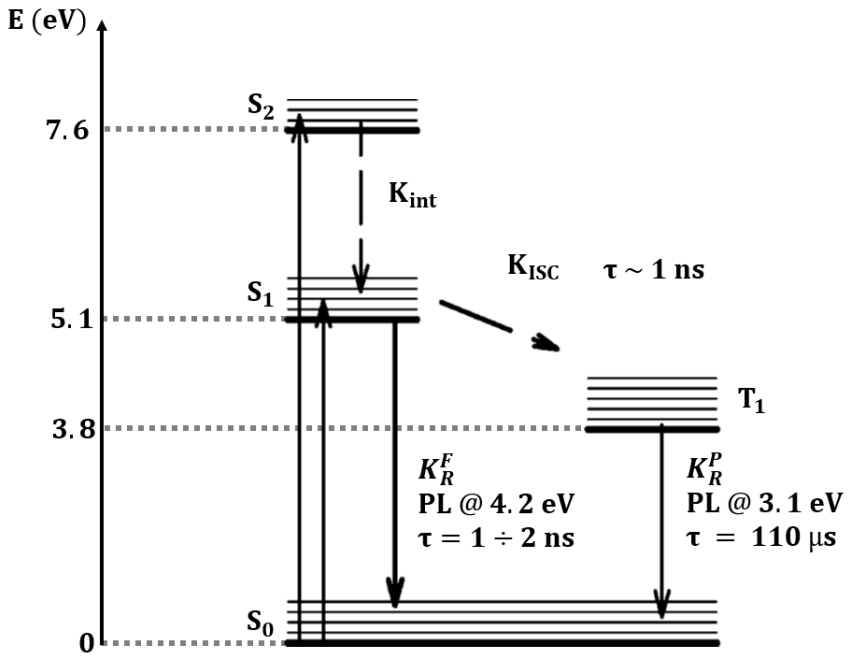

Figure 6.24. GLPC's energy level scheme. Both absorption and relaxation channels (continuous - radiative and dashed - no radiative) are evidenced by arrows. K_R^F and K_R^P are the emission rates of fluorescence and phosphorescence, respectively, while the K_{ISC} is the nonradiative phonon-assisted intersystem-crossing rate and K_{int} is the internal conversion rate. Figure adapted from [92].

6. 2.2 Transient absorption measurements on Ge-doped preform

The samples under test have been already described in chapter 3 with their corresponding absorption spectra:

- Ge-doped preform with 6% Ge-doped core and pure silica in the cladding, with a size of $4 \times 4 \times 0.67$ mm^3;
- 0.1 % uniformly Ge-doped sample, size of $3 \times 3 \times 0.92$ mm^3;
- 1 % uniformly Ge-doped sample, size of $4 \times 4 \times 0.77$ mm^3.

All the pump/probe measurements were performed with the PHAROS+OPA setup (reported in details in chapter 3), working at 60 kHz and centered at 1030 nm. Most details are identical to the experimental conditions reported for the pump-probe experiment on the NBOHC defect.

The samples were excited with femtosecond pulses in the UV range, at fixed energy per pulse of ~50 nJ/pulse, from 280 nm to 230 nm, following the transient absorption resonantly with the $B_{2\beta}$ band. Even in this case, the transient absorption response was probed in the UV/visible ($380 \div 650$ nm) and visible/near ($550 \div 900$ nm) spectral ranges.

The TA signal as a function of the pump-probe delay and the wavelength is reported in Figure 6.25 in color scale. The observed 2D map is composed of a broad band with a peak located between $460 - 480$ nm, that disappears within ~1 ns; moreover, in the blue part of the investigated spectral range a negative component is present.

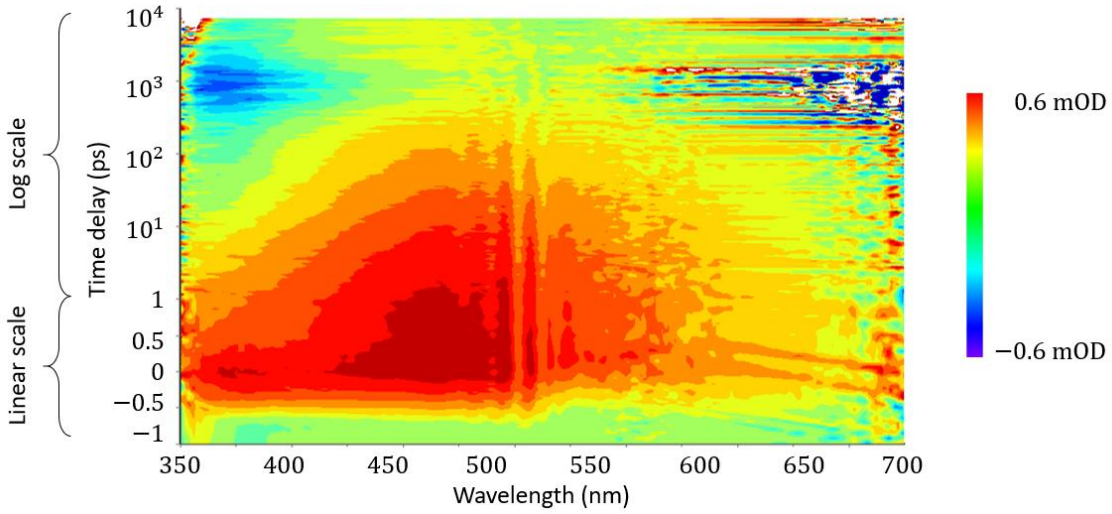

Figure 6.25. Two-dimensional time-wavelength plot of the TA signal measured in the 6% Ge-doped preform sample after photo-excitation with 200 fs laser pulses at 50 nJ/pulse at 245 nm (5.06 eV) in the whole investigated pump-probe delay window.

All these considerations are clearer in Figure 6.26, in which TA spectra at different delays are shown. The main band, which covers the whole investigated spectral range from 360 to 640 nm, is consistent with an ESA between not exactly localized electronic levels. In fact, notwithstanding a ~2.6 eV peaked absorption band is expected with respect to the $S_1 \rightarrow S_2$

transition, it is also known that a high germanium content decreases the bandgap. In particular, a bandgap ~7.1 eV was measured in a 5% doped sample [89], [252], which is less than the $S_0 \rightarrow S_2$ electronic transition. This energy band gap should be a maximum value of the possible bandgap of our 6% Ge-doped sample and, accordingly with this consideration, optical absorption spectra evidence an edge around 6.4 eV. Then we can assume that the wide main band has a contribution originating from a $S_1 \rightarrow$ CB transition, thus explaining the continuous of ESA observed. Moreover, it is possible to detect the rise of the negative component, reaching the maximum around ~1 ns after which it decreases (see the comparison between the light blue curve at 1 ns and the yellow one at 5 ns). This result evidences that the whole spectrum does not follow the same decay, then the post excitation relaxation depends on the wavelength.

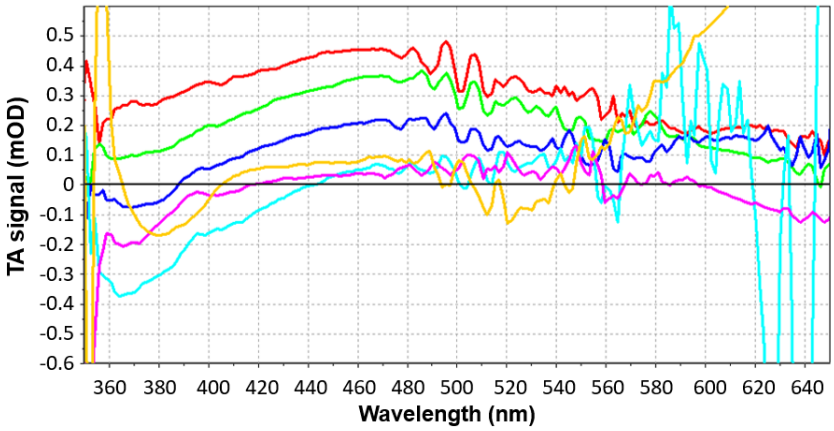

Figure 6.26. TA spectra recorded at different delays between the pump and the probe: 1 ps in red, 10 ps in green, 100 ps in blue, 1 ns in light blue, 3 ns in magenta and 5 ns in yellow.

Figure 6.27 shows TA kinetics recorded at different wavelengths: the comparison evidences that the UV component (370 nm) assumes negative values after ~10^2 ps and reaches a minimum at ~10^3 ps.

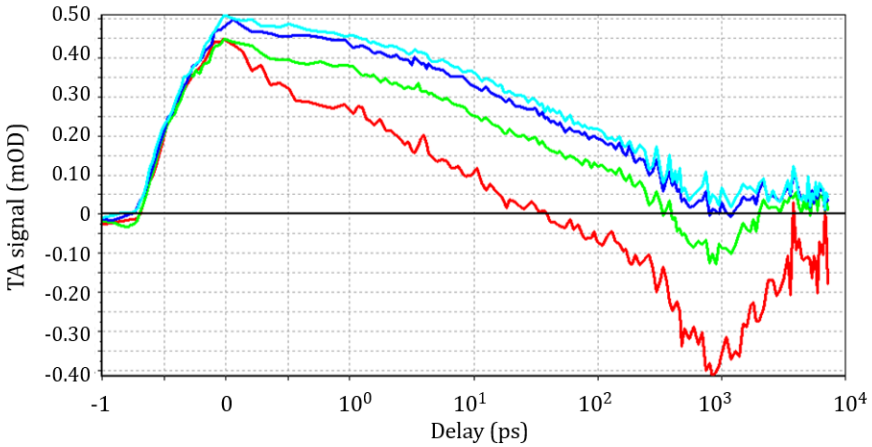

Figure 6.27. TA kinetics at different wavelengths: in red at 370 nm, in green at 420 nm, in blue at 450 nm and in light blue at 470 nm.

As already mentioned in chapter 2, the TA spectrum is the sum of three different components: a positive one that is the ESA, and two negatives which are the SE and the GSB. Since the GLPC has no absorption bands around $350 - 420$ nm, which could give rise to the GSB, it is reasonable to attribute such negative signal to a SE. Taking into account that the PL at 3.1 eV (400 nm) has a longer decay time ($\tau = 110$ μs) compared to the investigated time window, only the PL centered at 4.2 eV (decaying in few ns) could be the cause of this finding. Therefore, to shed light into negative values of TA after ~10^2 ps, we performed a fitting routing considering an exponential decay (with a negative amplitude) to determine the decay time τ of such a component. As reported in Figure 6.28, the best fit parameter $\tau = 1.46$ ns is in strong agreement with the characteristic decay time of the GLPC related 4.2 eV measured at room temperature (~293 K). So, what is measured in our TA experiments is the tail of the PL band centered at ~295 nm (4.2 eV).

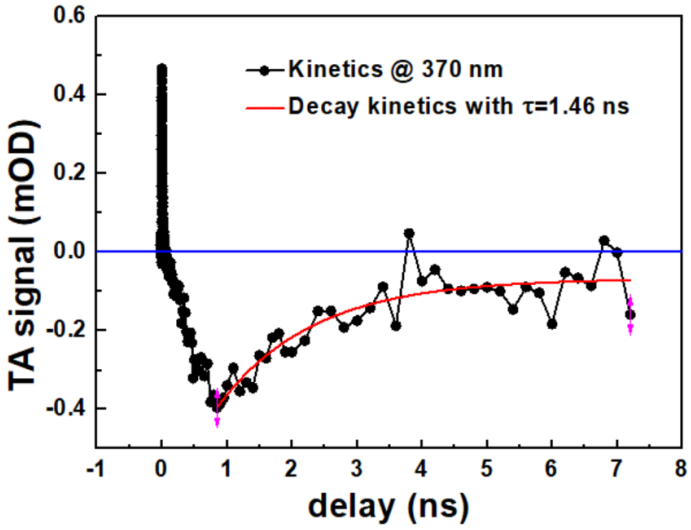

Figure 6.28. Decay time fitting of the negative component observed probing the GLPC TA response at 370 nm: in black the experimental data and in red the fit.

Changing the probing spectral domain, we extended the investigated spectral range to the IR domain: as reported in Figure 6.29 for spectra acquired at 5 ps of pump-probe delay, no new features are observed in the infrared, but only the tail of the UV/visible signal.

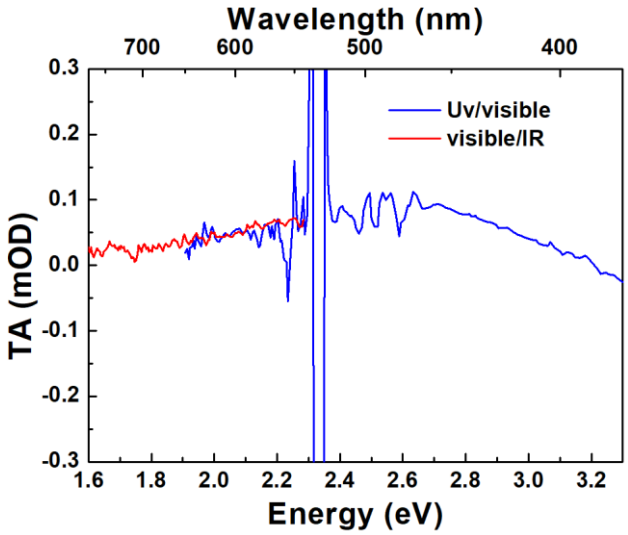

Figure 6.29. Comparison between the TA response probing with a UV/visible white light (in blue) and with a visible/infrared light (red), acquired at 5 ps of pump-probe delay.

To verify the signal's linearity with the pump pulse energy, we have performed TA experiments as a function of the laser pulse energy. Figure 6.30 reports the TA values, probed at 450 nm (2.8 eV) at a pump-probe delay of 5 ps; the results well evidence the linear dependence.

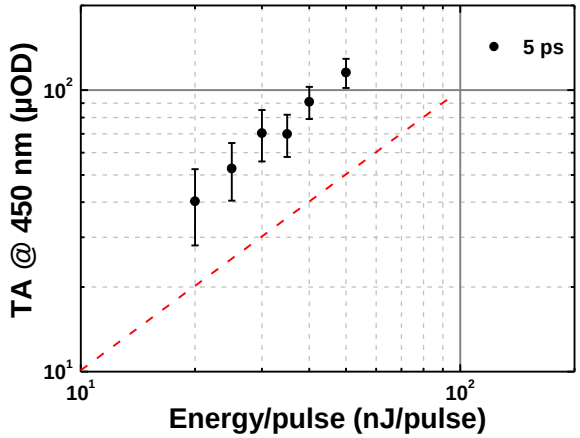

Figure 6.30. TA measured at 2.8 eV with 5 ps pump-probe delay as a function of the laser pulse energy. The red line is a guide for the reader highlighting the linear dependence.

The robustness of the consideration made above relies on the fact that we are exciting linearly (condition that was already proven) and selectively the GLPC. In order to highlight the last requirement, we have performed TA experiments at different pumping wavelengths, following the absorption band from 320 nm to 230 nm. Figure 6.31 reports the comparison between the GLPC absorption band and TA signal probed at 450 nm as a function of the pumping wavelength, both curves are normalized to their peak value and all the TA values are corrected for the laser fluence. The excellent agreement between the two data sets demonstrates that in our TA experiments we are selectively exciting the GLPC and then we are following its photocycle.

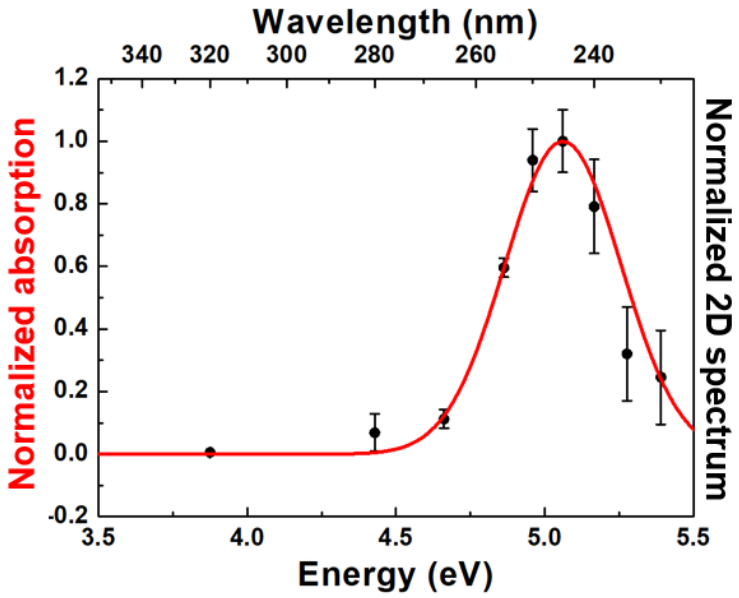

Figure 6.31. The normalized 2D spectra (in black dots) of the TA at 450 nm (2.8 eV) and 5 ps of delay as a function of the pump light overlapped on the normalized GLPC absorption band.

6. 2.3 GLPC's photocycle

All the carried out measurements give us the possibly to describe in details the GLPC's photocycle in the 6% Ge-doped preform sample. In particular we have observed:

- A wide band in the whole spectral range, suggesting a transition from the S_1 to the CB and the S_2 electronic level, which is degenerate with the CB;
- The tail of the PL band centered at 4.2 eV.

In order to have a complete picture of the relaxation process upon an excitation resonant with the 5.1 eV peaked band, we have performed a fitting routine following the same procedure done for the NBOHC defect, described by equation 6.3. The comparison between the kinetics evidences that all the spectra without the negative component follow the same kinetics, while in the UV part of the spectrum there is a further component to take into account the tail of the PL at 4.2 eV.

Following this hypothesis, the fitting is based on global parameters used to describe the decay components. The best-fit curves are reported in Figure 6.32 together with the TA kinetics recorded at different wavelengths, the best-fit parameters are listed in table 6.4.

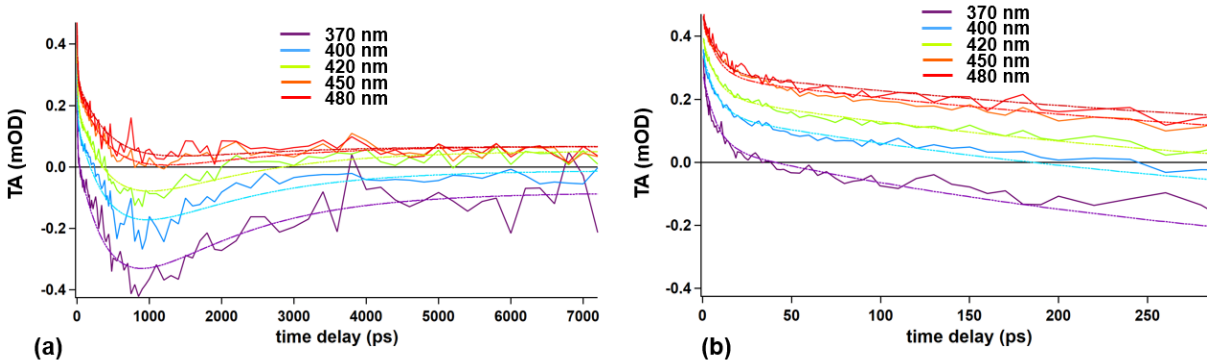

Figure 6.32. Global fitting of the different kinetics related to the GLPC's relaxation under 245 nm of pump excitation: (a) the kinetics in the whole pump-probe delay investigated window, (b) the zoom.

Table 6.4. Best fit parameters of the different kinetics as a function of the pump-probe delay.

	370 nm	**400 nm**	**420 nm**	**450 nm**	**480 nm**
$\mathbf{A_1}$ **(μOD)**	0.23	0.19	0.18	0.21	0.20
$\boldsymbol{\tau_1}$ **(ps)**	8	8	8	8	8
$\mathbf{A_2}$ **(μOD)**	0.71	0.56	0.48	0.23	0.23
$\boldsymbol{\tau_2}$ **(ps)**	400	400	400	400	400
$\mathbf{A_3}$ **(μOD)**	−0.57	−0.39	0.32		
$\boldsymbol{\tau_3}$ **(ps)**	1460	1460	1460		
C (μOD)	−0.09	−0.02	0.05	0.03	0.04

In these analysis we have four different time decays: 8 ps, 400 ps, 1460 ps and the last with a time scale much more longer than the probed one. The only relaxation time already justified is the decay component described by the third component (1-2 ns at RT), which takes into account the competition between the radiative ($S_1 \rightarrow S_0$) and non radiative ($S_1 \rightarrow T_1$) processes. Therefore, the GLPC model shown in Figure 6.24, based on previous studies on the defect's photocycle [90]–[92], [251], disagrees with our observation, since the only relaxation path considered is included in one of the observed kinetics. In particular it was assumed that the non-radiative relaxation

$S_1 \rightarrow S_0$ is negligible, while it is necessary to take into account only the radiative ones in the considered transition. This picture of the GLPC does not fit with the present measurements: indeed, from the TA signal as a function of the pump-probe delay, it is evident that the signal decays before the activation of the considered depopulation channel. In order to describe the relaxation characterized by a decay time of 8 ps and 400 ps, respectively, it is necessary to consider the nonradiative decay between the S_1 (electronic level resonant with the excitation pump wavelength) and the S_0 ground level, making this relaxation path not anymore negligible.

Moreover, it is possible to argue that the constant component is linked to the $T_1 \rightarrow T_2$ transition: indeed, few nanoseconds after the excitation, the S_1 level should be depopulated because of the different relaxation processes already described (nonradiative and radiative $S_1 \rightarrow S_0$ and the ISC $S_1 \rightarrow T_1$). For a longer time, the only electronic level able to absorb the probe light is the T_1 level, which is now populated by the ISC. A possible evidence of such a transition is provided by measurements with pump-probe negative delays: non zero TA signal for negative delays means that the sample is still excited in a time window comparable with the inverse of the laser repetition rate, in our case $\sim 20\ \mu s$ ($1/60$ kHz). Figure 6.33 reports the TA spectrum measured at ~ 10 ps of pump-probe delay. This hypothesis, in accordance with the forbidden $T_1 \rightarrow S_0$ transition characterized by a lifetime $\sim 110\ \mu s$, suggests that the $T_1 \rightarrow T_2$ absorption band is located in the UV so that in the investigated spectral range only the tail of this transition is observed.

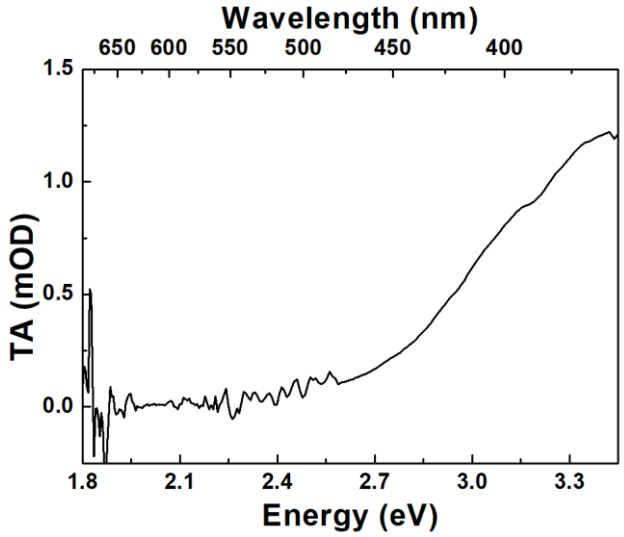

Figure 6.33. TA spectra measured at negative times: the positive signal could be due to the $T_1 \rightarrow T_2$ transition.

All these measurements allowed us to provide a model of the GLPC's photocycle that is reported in Figure 6.34. First, the GLPC is in the ground state. In a pump-probe delay window between ~ps and $\sim 10^2$ ps after the excitation resonant with the S_1 level, the transition from the S_1 to the CB is involved, giving rise the wide band detected in the whole investigated spectral range, with the nonradiative decay between S_1 and S_0. At larger pump-probe delay, the most relevant depopulation channels of the S_1 level are the radiative $S_1 \rightarrow S_0$ transition and the ISC between S_1 and T_1. At times longer than few ns, the $T_1 \rightarrow T_2$ transition is observed.

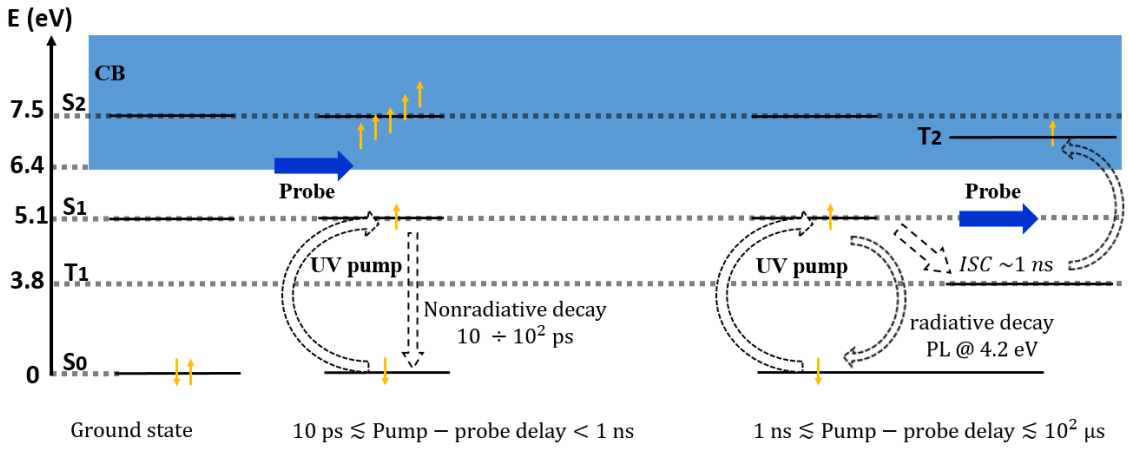

Figure 6.34. GLPC's photocycle in 6% Ge-doped preform.

Another interesting feature highlighted by the study of the pump-probe signal as a function of the exciting wavelength is the evidence of the different defect's energy dissipation to the slow vibration modes of the lattice. Indeed, after the electron's excitation, according to the Frank-Condon principle, and the thermalization (not observable with our resolution time), the energy in excess is dissipated in the lattice through slow modes. What we are observing is the cooling of the defect and the cooling is faster in correspondence of higher exciting wavelengths, redistributing the excess of stored energy. Figure 6.35 reports the normalized TA kinetics at 370 nm measured at different excitation wavelengths. It is evident that notwithstanding the three kinetics have the same initial value, after less than ~10 ps, the relaxation time is faster in accordance with the decrease of the excitation wavelength.

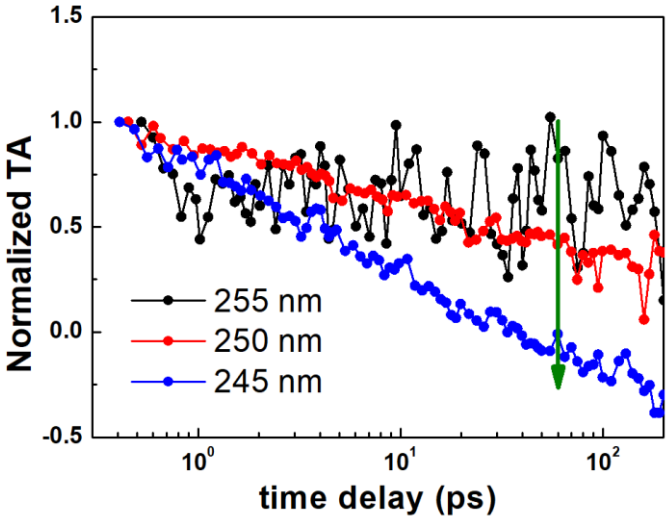

Figure 6.35. Normalized TA kinetics probed at 370 nm at different excitation wavelengths: in black 255 nm, in red 250 nm and in blue at 245 nm.

6. 2.4 Transient absorption measurements on 0.1% and 1% Ge-doped samples

As already mentioned above, the unstructured band that does not respect the $S_1 \rightarrow S_2$ expected transition is due by the high germanium content in the preform, making the bandgap lower than the $\Delta E = E_{S_2} - E_{S_0}$. In this case, the S_2 level is within conduction band. We carried out pump-probe measurements on samples containing 0.1% and 1% of germanium with a high GLPC content, to improve the signal. At these doping levels, the bandgap is still comparable with that of the amorphous silica, making possible the investigation of the ESA linked to the $S_1 \rightarrow S_2$ transition.

Figures 6.36 and 6.37 report the TA as a function of the wavelength and the pump-probe delays for the 1% and 0.1% Ge-doped samples, respectively.

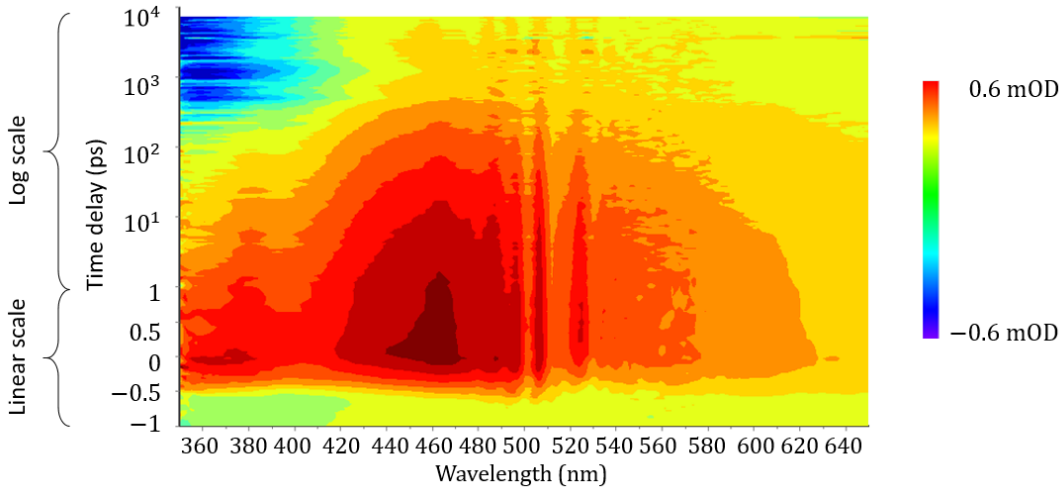

Figure 6.36. Two-dimensional time-wavelength plot of the TA signal measured in the 1% Ge-doped sample after photo-excitation with 200 fs laser pulses at 50 nJ/pulse at 245 nm (5.06 eV) in the whole investigated pump-probe delay window.

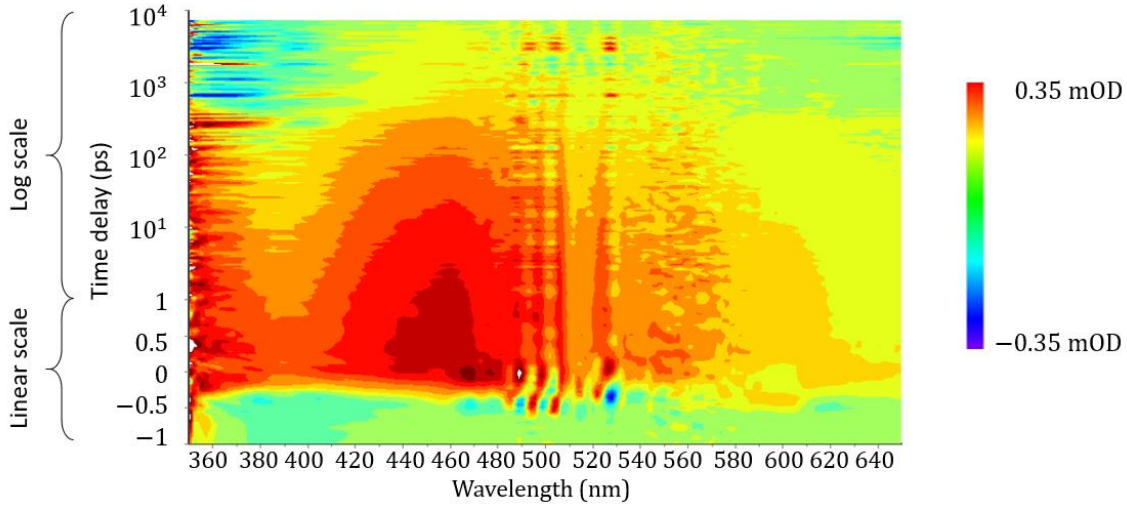

Figure 6.37. Two-dimensional time-wavelength plot of the TA signal measured in the 0.1% Ge-doped sample after photo-excitation with 200 fs laser pulses at 50 nJ/pulse at 245 nm (5.06 eV) in the whole investigated pump-probe delay window.

In Figures 6.38 and 6.39 we report the TA spectra at different pump-probe delays (left) and the kinetics at different wavelengths (right) for both samples, respectively.

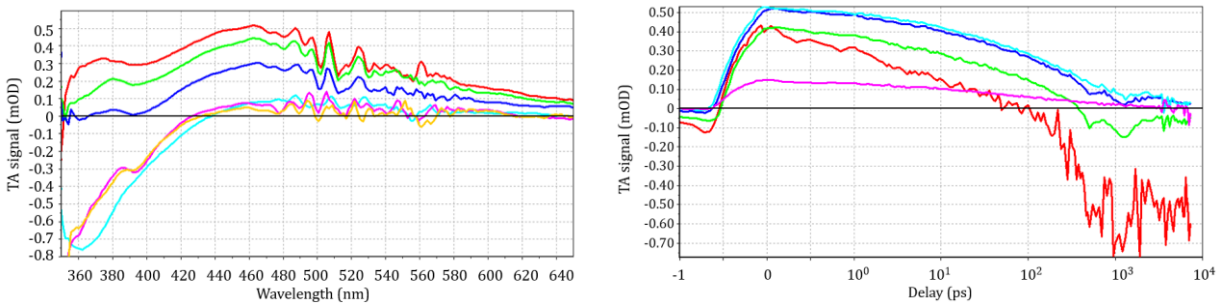

Figure 6.38. Left figure: TA spectra at different pump-probe delays measured in the 1% Ge-doped sample: 1 ps in red, 10 ps in green, 100 ps in blue, 1 ns in light blue, 3 ns in magenta and 5 ns in yellow. Right figure: TA kinetics at different wavelengths measured in the 1% Ge-doped sample: 390 nm in red, 420 nm in green, 450 nm in blue, 460 nm in light blue and 620 nm in magenta.

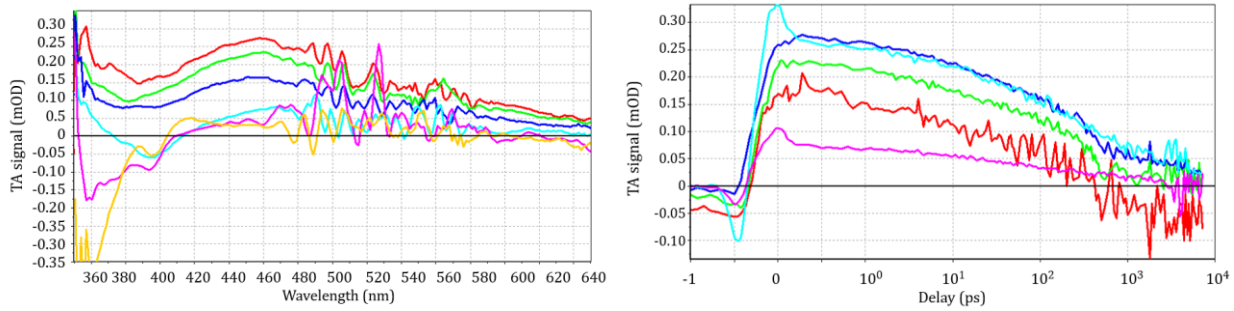

Figure 6.39. Left figure: TA spectra at different pump-probe delays measured in the 0.1% Ge-doped sample: 1 ps in red, 10 ps in green, 100 ps in blue, 1 ns in light blue, 3 ns in magenta and 5 ns in yellow. Right figure: TA kinetics at different wavelengths measured in the 0.1% Ge-doped sample: 390 nm in red, 420 nm in green, 450 nm in blue, 460 nm in light blue and 620 nm in magenta.

Both samples clearly exhibit an ESA band peaked at ~ 460 nm $(2.6 - 2.7$ eV), being in excellent agreement with the $S_1 \rightarrow S_2$ expected transition. In addition, even in these samples the tail of the 4.2 eV PL band is observed. Moreover, the kinetics report a single wavelength trend corresponding (albeit much more noises) to that already observed in the 6% Ge-doped preform, thus highlighting the same relaxation path followed by the excited electron. Indeed, by comparing

the global fitting routine on all the samples (Figure 6.40), the obtained decay times are consistent to each other, as reported in tables 6.5 and 6.6.

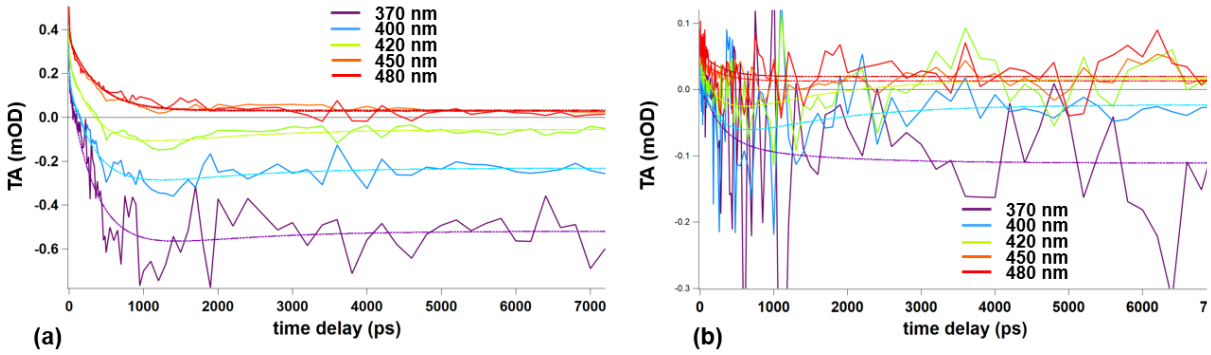

Figure 6.40. Global fitting of the different kinetics related to the GLPC's relaxation under 245 nm of pump excitation: (a) 1% Ge-doped sample and (b) 0.1% Ge-doped sample.

Table 6.5. Best fit parameters of the different kinetics as a function of the pump-probe delay related to the 1% Ge-doped sample.

	370 nm	**400 nm**	**420 nm**	**450 nm**	**480 nm**
$\mathbf{A_1}$ **(μOD)**	0.17	0.17	0.15	0.15	0.12
$\boldsymbol{\tau_1}$ **(ps)**	6	6	6	6	6
$\mathbf{A_2}$ **(μOD)**	0.86	0.59	0.49	0.33	0.32
$\boldsymbol{\tau_2}$ **(ps)**	370	370	370	370	370
$\mathbf{A_3}$ **(μOD)**	−0.19	−0.19	−0.1		
$\boldsymbol{\tau_3}$ **(ps)**	1300	1300	1300		
C (μOD)	−0.52	−0.23	−0.05	0.03	0.03

Table 6.6. Best fit parameters of the different kinetics as a function of the pump-probe delay related to the 0.1% Ge-doped sample.

	370 nm	400 nm	420 nm	450 nm	480 nm
$\mathbf{A_1}$ (μOD)	0.04	0.03	0.02	0.03	0.01
$\boldsymbol{\tau_1}$ (ps)	6	6	6	6	6
$\mathbf{A_2}$ (μOD)	0.10	0.13	0.13	0.03	0.04
$\boldsymbol{\tau_2}$ (ps)	350	350	350	350	350
$\mathbf{A_3}$ (μOD)	0.02	−0.09	−0.1		
$\boldsymbol{\tau_3}$ (ps)	1300	1300	1300		
C (μOD)	−0.11	−0.02	0.017	0.01	0.02

Also the comparison between the GLPC absorption band and the normalized TA signal, probed at 450 nm as a function of the pumping wavelength (analogously to Figure 6.31), provides an excellent agreement between these curves as Figure 6.41.

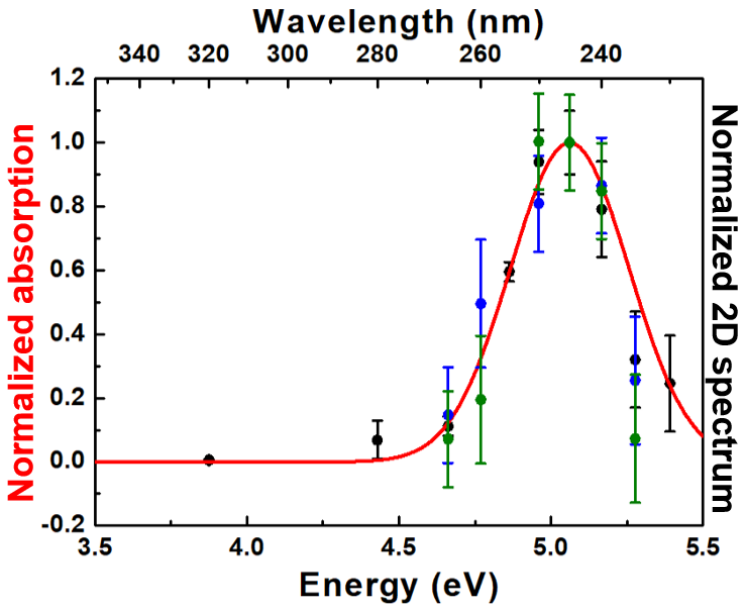

Figure 6.41. The normalized 2D spectra of the TA at 450 nm (2.8 eV) and 5 ps of delay as function of the pumping wavelength overlapped on the normalized theoretical GLPC absorption spectra (red line): black dots are related to the 6% Ge-doped sample, the blue to the 1% Ge-doped sample and the green dots to the 0.1% Ge-doped sample.

The combination of all the measurements reported in the investigated samples highlights that the same photocycle is observed, which is in agreement with GLPC's relaxation upon an excitation resonant with the $S_0 \rightarrow S_1$ transition. Indeed, in the less doped samples the electron's relaxation path is analogous to the photocycle reported in Figure 6.36 without the conduction band.

6.3. Conclusion

In the present chapter, we presented a new promising experimental approach adapted to investigate the pump-probe responses of color centers in transparent materials taking advantages from the possibility to excite in linear absorption regime and also at different exciting wavelengths. In order to the highlight the potential of such experimental method/tool, we carried out pump-probe measurements on two long-time studied point defects in amorphous silica, the NBOHC and the GLPC. For the first time, we characterized the transient absorption dynamics of such color centers, in single photon absorption conditions, exciting in the UV energy range and probing in the visible at different pump/probe ultra-short delays. The combination of these measurements sheds light into the defects' photocycle, clarifying the electronic relaxation.

Conclusions

In the present PhD thesis work, we have investigated the nature and the properties of metastable and stable point defects in a variety of pure and doped amorphous silica-based materials such as bulk glasses or optical fibers. In particular, our attention has been devoted to the characterization of the optical (absorption, luminescence) properties associated with the point defects either embedded in the pristine silica matrix or induced by radiations (X-rays or femtosecond laser), including their photocycle mechanisms. The dynamic nature of these three years of PhD, allowed me investigating various silica-based systems in very different experimental and extreme conditions, from the pulsed X-ray generator Asterix to the pump-probe experiments. In the following, I briefly summarize the key results acquired as well as the perspectives regarding my three main research topics:

- Nature and properties of the point defects at the origin of the steady state and pulsed X-ray radiation-induced attenuation in pure and doped optical fibers;
- Non-linear optical effects induced by femtosecond laser in various bulk silica glasses;
- Time-resolved pump-probe spectroscopy on point defects.

Origin of the steady state and pulsed X-ray radiation induced attenuation in silica-based optical fibers

Key results

On this research axis, we have reported the effects of ionizing X-rays, either pulsed or steady state, on the main classes of optical fibers [4]. Indeed, the investigated samples were selected to gain new knowledge about the impact on RIA of the dopants routinely employed in the fiber manufacturing: pure-silica, fluorine, germanium and phosphorous. Moreover, thanks to the close collaboration with iXblue through the LabH6, the compositions and manufacturing details

[79], [87], [163], [169] of all samples are known, facilitating the analysis of their radiation responses and the associated basic mechanisms. Our investigation aimed to characterize their radiation responses mainly in terms of RIA, focusing our attention on its origin in terms of induced defects, studying the loss kinetics during and after the irradiation. Furthermore, as the temperature strongly influences the fiber radiation response (mainly by varying the defect generation and bleaching rates), we compared the RIA levels at both liquid nitrogen temperature (LNT) and room temperature (RT). Our results allow us to better distinguish between the absorption bands of the different metastable defects responsible for the fiber darkening from the UV to near-infrared range [79], [80], [87]. Indeed, lowering the temperature slows down the defects' decay kinetics, better highlighting the contribution of the metastable defects to the global RIA. This study supplies a powerful access key to the defects' dynamics overcoming the complexity of time-resolved measurements. We explained the observed RIA in terms of induced defects, describing also the kinetics in agreement with a diffusion-controlled reaction. The most important result of the present investigation is a clearer description of the spectral attenuation features of the various canonical optical fibers at the two temperatures, resulting in a better understanding of the crucial role of the self-trapped holes (STHs) defects that are shown to affect the transmission properties of all types of optical fibers [78]–[80], [87]. Moreover, our approach also reveals a strong correlation between two not so well-known defects belonging to Germanium: the GeY and GeX centers [79]. Regarding the near-IR spectral range, the RIA origins in the PSC and F-doped samples still remain unresolved, and additional future studies are required to identify the defect(s) contributing to the attenuation in this spectra domain. The P-doped fibers also exhibit unknown contribution to the RIA at ~1.2 eV, suggesting the need of further experiments to reveal the involved defect(s).

Perspectives

The study of the RIA, in terms of induced defects' kinetics, is a powerful tool to investigate such systems, providing many information both from the qualitative and the quantitative points of view. Moreover, the possibility to perform low temperature measurements, gives us the access to the metastable defects not easily observable at RT. Such method allows pointing out the importance of STHs as intrinsic defects, and their influence on the RIA response of doped optical fibers. Furthermore, it is possible also to find correlations between defects for which a direct

investigation is difficult because of the overlap with other defects or because of the instability of such defects. In this framework, we also found a linear correlation between the behaviors of GeX and GeY centers. Further experiments are however needed to better understand the exact correspondence between those defects, clarifying the nature of their relationship: if they arise from the same precursor site and recombine together, or if the two observed absorption bands are indeed related to the same defect structure. It is also important to compare our results with the ones in ref. [95] under γ-ray steady state irradiation, in which an anti-correlation was observed between the intensities of the GeX and GeY absorption bands as a function of the temperature of irradiation.

Moreover, the systematic spectral analysis in terms of point defects has pointed out the lack of knowledge regarding the origins of the RIA in some spectral domains of practical importance in different optical fibers. Notwithstanding the fact that we were able to provide a quite good description in terms of defects for the Ge-doped optical fibers (both in continuous and pulsed X-rays irradiation), for the other classes of fibers the situation is different. Indeed, further investigations are necessary to explain the near-IR RIA in the PSC and F-doped optical fibers, even if some recent works are shedding light into it (see ref [202], [206]), as well as to find the P-related defect which absorbs the light around $\sim$1.2 eV.

Non-linear optical effects induced in silica by femtosecond laser

Key results

This chapter was focused on the characterization of the point defects generated by the interaction of silica with high intensity femtosecond laser pulses. In particular, we studied those interactions as a function of the experimental exposure conditions varying the laser wavelength, the deposited energy and the sample chemical composition. This investigation was stimulated by a number of works concerning the defects' generation under femtosecond laser which were not able to give a complete and satisfactory picture of the involved mechanisms [11], [13], [14], [72]. Indeed the first section [139], related to the waveguides inscription through femtosecond laser writing, highlights the higher efficiency of UV laser to induce structural permanent modifications leading to light guidance properties compared to IR laser. Moreover, I was able to show that the laser induced defects contribute to the total induced refractive index change Δn in the exposed

regions. Several selective thermal treatments were applied on our samples revealing a much more complex representation and panorama of induced defects than the one which is classically attributed to the inscribed waveguides in amorphous silica. The second section focused on the defects induced during the irradiation, highlighting how changing the laser wavelength and power affects the nature and concentration of the induced defects. This investigation was performed studying the online photoluminescence (PL) signatures assigned to the defects generated by femtosecond laser pulse irradiation. For a complete view about the silica interaction with such high intensity lasers, the PL response was also studied as a function of the sample's chemical composition, identifying different generation kinetics as a function of the hydroxyl content in the glasses.

Perspectives

Our work highlights the importance to characterize the induced defects to investigate the fs laser-silica interaction mechanisms, and more generally, the fs laser-matter interaction. Indeed, our measurements showed the complex panorama related to the induced defects, during and after, the fs laser irradiation. As pointed out by the two selective thermal treatments, not well attributed defects play an important role on the optical properties of the inscribed waveguides, such as their propagation losses, mode confinements and the induced refractive index change. Therefore, further experiments will be necessary to identify the defects involved in the processes occurring during the femtosecond exposure of silica glass: optical absorption measurements, time resolved photoluminescence and electron paramagnetic resonance (EPR) measurements. Those spectroscopic techniques could also shed light into the defect responsible to the PL band peaked at 545 nm [14], [226].

The goal of the second part of the chapter was to reveal the PL-active induced defects in the amorphous silica under fs laser irradiation. We have found that the nature and concentrations of the induced defects depend not only on the experimental irradiation conditions, but also on the chemical composition of the exposed sample, introducing extrinsic processes which could dominate their global response. Furthermore, it is important to stress that online measurements are fundamental in order to provide new and deeper information. Indeed, even if *in situ* techniques are complex, they are also more powerful than post mortem characterization because of their ability

to probe the metastable nature of most of the induced defects. Therefore, future experiments will be focused on the possibility to study the generation of point defects during the irradiation (not only PL-active defects), with fast resolution time, such as pump-probe measurements with a femtosecond probe pulse duration.

Time resolved pump-probe spectroscopy on point defects

Key results

The third and last section, is driven by the defect photocycle mechanisms and especially at the early first stages just after the femtosecond laser pulse. This section represents the state-of-art regarding the investigation on the point defects' photocycle in wide band gap materials. Indeed, pump/probe experiments in large bandgap insulators are nowadays still particularly difficult to perform. This analysis remains a rather complex task from the experimental point of view. Here we provide an innovative approach in addressing unresolved issues regarding color centers in wide band-gap solids. In order to highlight the potentialities of this method, we investigated the photocycle of two different and well-known defects, the NBOHC and the GLPC, going deeper in the dynamics of those defects with unprecedented time resolution. The combination of the experiments helps to clarify the defects' photocycle, highlighting how state-of-the-art transient absorption measurements with tunable UV excitation represent an innovative tool to investigate such amorphous systems and the solid state in general at ultimate time scales.

Perspectives

As already pointed out in chapter 6, our purpose is to provide an innovative experimental tool to investigate point defects. It is important to stress that such method has a general validity, and to show its potentialities, we have exploited it to study the photocycle of known silica-related defects. Indeed, thanks to our measurements, we have gained many and new information regarding the involved defects, being also the first to investigate the defects dynamics at femto-picosecond scale in linear absorption conditions. The success to explain the involved defects' photocycle highlights how such experimental approach could be useful not only studying the a-SiO_2 variety

of defects, but potentially, also the color centers embedded in the matrix of all types of wide band gap materials. This will be for sure the topic of future studies.

Conclusions

Dans le cadre de la présente thèse de doctorat, nous avons étudié la nature et les propriétés des défauts ponctuels métastables et stables dans une variété de matériaux à base de silice amorphe pure et dopée, tels que les verres massifs ou les fibres optiques. En particulier, nous nous sommes consacrés à la caractérisation des propriétés optiques (absorption, luminescence) de ces défauts ponctuels, qu'ils soient présents initialement dans la matrice de silice vierge, soit induits par des irradiation (rayons X ou laser femtoseconde), y compris leurs photocycles. La nature transverse de ces trois années de doctorat, m'a permis d'étudier différents systèmes à base de silice dans des conditions expérimentales extrêmes et très différentes, du générateur de rayons X pulsé Astérix aux expériences pompe-sonde. Dans ce qui suit, je résume brièvement les principaux résultats acquis ainsi que les perspectives concernant mes trois principaux thèmes de recherche:

- Nature et propriétés des défauts ponctuels à l'origine de l'atténuation induite par irradiation (RIA) sous irradiation X continue ou pulsée dans les fibres optiques pures et dopées;
- Effets optiques non linéaires induits par laser femtoseconde dans divers verres massifs de silice;
- La spectroscopie pompe-sonde à ultra-haute résolution temporelle sur les défauts ponctuels.

Origine de l'atténuation induite par irradiation X pulsée et continue dans les fibres optiques à base de silice

Résultats clés

Sur cet axe de recherche, nous avons rapporté les effets des rayons X ionisants, pulsés ou continus, sur les principales catégories de fibres optiques. En effet, les échantillons étudiés ont été sélectionnés pour acquérir de nouvelles connaissances sur l'impact sur la RIA des dopants

couramment utilisés dans la fabrication des fibres: silice pure, fluor, germanium et phosphore. De plus, grâce à l'étroite collaboration avec iXblue par l'intermédiaire du LabH6, les compositions et les détails de fabrication [2] – [6] de tous les échantillons sont connus, ce qui facilite l'analyse de leurs réponses radiatives et des mécanismes fondamentaux de l'interaction rayonnement matière. Notre investigation visait à caractériser leurs réponses aux rayonnements principalement en termes de RIA, en concentrant notre attention sur les défauts à l'origine de ces pertes induites, en étudiant les cinétiques d'évolution de la RIA pendant et après l'irradiation. En outre, comme la température influence fortement la réponse aux radiations des fibres (principalement en faisant varier les efficacités de génération et de guérison des défauts), nous avons comparé les niveaux de RIA à la température de l'azote liquide (LNT) et à celle ambiante (RT). Nos résultats nous permettent d'identifier plus facilement les bandes d'absorption des différents défauts métastables responsables de l'assombrissement transitoire de la fibre, depuis l'UV jusqu'au proche infrarouge [2], [3], [7], [11]. En effet, abaisser la température ralentit la cinétique de recombinaison de ces défauts métastables, ce qui permet de mettre plus facilement en évidence leur contribution à la RIA globale. Cette étude fournit un puissant outil d'analyse de la dynamique des défauts, surmontant la complexité des mesures à très grande résolution temporelle, et rendant possible l'étude des défauts possibles même avec une résolution temporelle de plusieurs dizaines de millisecondes. Nous avons ainsi pu expliquer la RIA observée en termes de défauts induits, en décrivant également leurs cinétiques via une réaction contrôlée par des processus de diffusion. Le résultat le plus important de notre étude est une description améliorée des propriétés d'atténuation spectrale des diverses fibres optiques canoniques aux deux températures, ce qui a permis de mieux appréhender le rôle crucial des défauts de type self-trapped holes (STH). Les STHs affectent les propriétés de transmission de tous les types de fibres optiques étudiées. De plus, notre approche révèle également une forte corrélation entre deux défauts peu étudiés du Germanium: les centres GeY et GeX. En ce qui concerne le domaine spectral proche de l'infrarouge, les origines de la RIA dans les échantillons dopés F et à cœur de silice pure restent encore à déterminer, et des études supplémentaires seront nécessaires pour identifier le(s) défaut(s) contribuant à l'atténuation dans ce domaine spectral. Les fibres dopées P présentent également une contribution inconnue à la RIA autour de $\sim$1.2 eV, ce qui impliquera de mener d'autres expériences pour révéler le (ou les) défaut(s) à l'origine de la RIA dans cette zone spectrale.

Perspectives

L'étude de la RIA, en termes de cinétique des défauts induits, est un outil puissant pour étudier ces systèmes, fournissant de nombreuses informations tant du point de vue qualitatif que quantitatif. De plus, la possibilité d'effectuer des mesures à basse température nous donne accès à l'observation des défauts métastables difficilement caractérisables à la température ambiante. Comme nous l'avons déjà vu dans les chapitres précédents, cette méthode permet de mettre en évidence l'importance des STH en tant que défauts intrinsèques, ainsi que leur influence sur la réponse en termes de RIA des fibres optiques dopées. En outre, il est également possible de trouver des corrélations entre des défauts pour lesquels il est difficile d'effectuer une investigation directe, en raison du recouvrement de leurs bandes d'absorption avec elles d'autres défauts ou de leur instabilité thermique. Dans ce cadre, nous avons également trouvé une corrélation linéaire entre les comportements des centres GeX et GeY. D'autres expériences sont cependant nécessaires pour mieux comprendre la nature de la relation entre ces défauts: comprendre s'ils proviennent du même site précurseur et se recombinent ensemble, ou si les deux bandes d'absorption observées sont effectivement liées à une structure unique de défaut. Il est également important de pouvoir expliquer simultanément nos résultats et ceux rapportés dans la réf. [95] sous γ irradiation continue, dans laquelle une anticorrélation a été observée entre les intensités des bandes d'absorption des défauts GeX et GeY en fonction de la température d'irradiation.

De plus, l'analyse spectrale systématique en termes de défauts ponctuels a mis en évidence les manques de connaissances concernant les origines de la RIA dans certains domaines spectraux d'importance pour les applications basées sur les fibres optiques. Malgré le fait que nous ayons pu fournir une assez bonne description en termes de défauts dopées au germanium en cœur (tant pour les irradiations continues que pulsées), pour les autres types de fibres optique, ce n'est pas encore le cas. En effet, des recherches additionnelles seront nécessaires pour expliciter les origines de la RIA mesurée dans le proche-IR pour les fibres optiques à cœur de silice pure et dopées et F, même si certains travaux récents offrent des pistes très intéressantes (voir réfs [202], [206]). De plus, il faudra aussi identifier la nature et les propriétés du défaut relatif au P qui absorbe la lumière autour de ~1.2 eV.

Effets optiques non linéaires induits dans la silice par laser femtoseconde

Résultats clés

Cette section était axée sur la caractérisation des défauts ponctuels générés par l'interaction de la silice avec des impulsions laser femtoseconde de haute intensité. En particulier, nous avons étudié ces interactions en fonction des conditions d'irradiation expérimentales en faisant varier la longueur d'onde du laser, l'énergie déposée et la composition chimique de l'échantillon. Cette recherche a été stimulée par un certain nombre de travaux antérieurs concernant la génération de défauts sous laser femtoseconde qui n'avaient pas pu donner une image complète et satisfaisante des mécanismes impliqués. La première partie de ces travaux, relative à l'inscription des guides d'ondes par laser femtoseconde dans la silice massive, souligne la plus grande efficacité du laser UV pour induire des modifications structurelles permanentes permettant d'accéder au guidage de la lumière par comparaison au laser IR. De plus, j'ai pu montrer que les défauts induits par le laser femtoseconde contribuent au changement total Δn de l'indice de réfraction induit dans les régions exposées. Plusieurs traitements thermiques sélectifs ont été appliqués sur nos échantillons, révélant un panorama des défauts induits beaucoup plus complexe que celui classiquement attribué aux guides d'ondes inscrits dans la silice amorphe. La deuxième section s'est concentrée sur les défauts induits pendant l'irradiation, en soulignant comment la modification de la longueur d'onde et de la puissance du laser affecte la nature et la concentration des défauts induits. Cette étude a été réalisée en étudiant *in situ* les signatures de photoluminescence (PL) attribuées aux défauts générés par les impulsions laser femtoseconde. Pour obtenir une vue complète de l'interaction de la silice avec ces lasers de haute intensité, la réponse de la PL a également été étudiée en fonction de la composition chimique de l'échantillon, en identifiant les différentes cinétiques de génération en fonction de la teneur en groupements hydroxyles des verres.

Perspectives

Nos travaux soulignent l'importance de caractériser les défauts induits pour étudier les mécanismes d'interaction laser fs-silice, et plus généralement, l'interaction laser fs-matière. En effet, nos mesures ont montré le panorama complexe lié aux défauts induits, pendant et après l'irradiation, par le laser fs. Comme l'ont montré les deux traitements thermiques sélectifs, certains

défauts méconnus jouent un rôle important sur les propriétés optiques des guides d'ondes inscrits, comme leurs pertes de propagation, le confinement des modes et le changement induit d'indice de réfraction. Par conséquent, d'autres expériences seront nécessaires pour identifier les défauts impliqués dans les processus se produisant lors de l'exposition femtoseconde du verre de silice telles que: mesures d'absorption optique, photoluminescence résolue en temps (TRL) et mesures de résonance paramagnétique électronique (RPE). Ces techniques spectroscopiques pourraient également permettre d'identifier le défaut responsable de la bande de photoluminescence dont le maximum d'intensité se situe à 545 nm.

L'objectif de la deuxième section était de révéler les défauts induits par l'activité PL dans la silice amorphe sous irradiation laser fs. Nous avons découvert que la nature et les concentrations des défauts induits dépendent non seulement des conditions d'irradiation expérimentales, mais aussi de la composition chimique de l'échantillon exposé, introduisant des processus extrinsèques qui peuvent parfois dominer leur réponse globale. En outre, il est important de souligner que les mesures *in situ* sont fondamentales pour fournir des informations nouvelles et plus approfondies. En effet, si ces techniques sont complexes, elles sont également plus puissantes que la caractérisation *post mortem* en raison de leur capacité à sonder la nature métastable de la plupart des défauts induits par le laser. Par conséquent, les expériences futures seront axées sur la possibilité d'étudier la génération de défauts ponctuels pendant l'irradiation (en ne se limitant pas aux défauts luminescents), avec un temps de résolution ultra-rapide rapide, comme avec les expériences pompe-sonde avec une durée d'impulsion de sonde femtoseconde.

Spectroscopie pompe-sonde résolue en temps sur les défauts ponctuels

Résultats clés

La troisième et dernière section, est dédiée à l'étude des mécanismes du photocycle des défauts et surtout à ses premiers stades, juste après l'impulsion laser femtoseconde. Cette section représente l'état de l'art concernant l'étude du photocycle des défauts ponctuels dans les matériaux à large bande interdite. En effet, les expériences pompe/sonde dans les isolants à large bande interdite sont encore aujourd'hui particulièrement difficiles à réaliser. Cette analyse reste une tâche

assez complexe du point de vue expérimental. Nous proposons ici une approche innovante pour résoudre les problèmes concernant l'étude des centres colorés dans les solides à large bande interdite. Afin de mettre en évidence les potentialités de cette méthode, nous avons étudié le photocycle de deux défauts différents et bien connus, le NBOHC et le GLPC, en approfondissant la dynamique de ces défauts avec une résolution temporelle sans précédent. La combinaison des expériences permet de clarifier le photocycle des défauts, en soulignant comment les mesures innovantes d'absorption transitoire avec une excitation UV accordable représentent un outil d'exception pour étudier ces systèmes amorphes et l'état solide en général à des échelles de temps ultimes.

Perspectives

Comme nous l'avons déjà souligné au chapitre 6, notre objectif est de fournir un outil expérimental innovant pour étudier les défauts ponctuels. Il est important de souligner que cette méthode a une validité générale, et pour montrer ses potentialités, nous l'avons exploitée pour étudier le photocycle de défauts connus relatifs à la silice. En effet, grâce à nos mesures, nous avons obtenu de nombreuses et nouvelles informations concernant les défauts en question, étant également les premiers à étudier la dynamique des défauts à l'échelle femto-picoseconde dans des conditions d'absorption linéaire. Le succès de l'explication du photocycle des défauts étudiés montre à quel point cette approche expérimentale pourrait être utile non seulement pour étudier la grande variété de défauts dans la silice amorphe, mais aussi, potentiellement, les centres colorés présents dans la matrice vitreuse de tous les matériaux à large bande interdite. Ceci sera certainement le sujet de futurs travaux.

Conclusioni

Nella presente tesi di dottrato, sono state investigate la natura e le properietà dei difetti di punto stabili e metastabili, in campioni di silice pura e/o drogati, sia massivi che in fibre ottiche. In particolare, la nostra attezione si è rivolta alla caratterizzazione delle proprietà ottiche (assorbimento e luminescenza) associate ai difetti di punto presenti nella matrice di silice o indotti dalla radiazione (raggi X o laser al femtosecondo), includendo lo studio dei meccanismi alla base dei loro fotocicli. La natura trasversale di questi tre anni di dottorato, mi hanno permesso di studiare diversi sistemi in diverse condizioni sperimentali, come l'irraggiamento X pulsato o misure pump-probe. Di seguito si riassumono brevemente i risultati chiave ottenuti, così come anche le prospettive future, legate ai tre principali argomenti di ricerca affrontati:

- la natura e le proprietà dei difetti di punto all'origine dell'attenuazione indotta da radiazione (RIA) X continua e pulsata in fibre ottiche in silice pure e drogate;
- Effetti non lineari di assorbimento di fotoni indotti dall'esposizione della silice a laser al femtosecondo;
- Spettroscopia pump-probe dei difetti di punto risolta in tempo.

Origine dell'attenuazione indotta da irraggiamento X continuo e pulsato in fibre ottiche in pura silice e dopate

Risultati

Su questo fronte di ricerca, abbiamo studiato l'effetto della radiazione X ionizzante, sia pulsata che continua, nei principali tipi di fibre ottiche. I campioni sono stati selezionati in modo da approfondire la conoscenza relativa all'effetto sulla RIA dei più comuni droganti di fibre ottiche: in pura silice, drogate con fluoro, germanio o fosforo. Inoltre, grazie alla collaborazione con la iXblue attraverso il LabH6, conosciamo nel dettaglio la composizione ed il processo di

fabbricazione di tutti i campioni, semplificando l'analisi della loro risposta alla radiazione ed i relativi processi base. La nostra ricerca ha l'obbietivo di caratterizzare la risposta alla radiazione principalmente in termini di RIA, focalizzando l'attenzione sulla sua origine in termini di difetti indotti, studiandone le perdite durante e dopo l'irraggiamento. In più, considerando che la temperatura influenza la risposta della fibra alla radiazione (principalmente variando il tasso di generazione e la vita media dei difetti), abbiamo confrontato la RIA misurata alla temperatura dell'azoto liquido (LNT) con quella misurata a temperatura ambiente (RT). I risultati ottenuti ci permettono di distinguire le bande di assorbimento dei diversi difetti metastabili responsabili dell'attenuazione della fibra dall'UV al vicino infrarosso. Infatti, abbassando la temperatura si rallenta la cinetica di decadimento dei difetti, evidenziando il contributo dei difetti metastabili rispetto alla RIA totale. Questo studio fornsce una potente chiave di accesso alla dinamica dei difetti superando la complessità di uno studio con bassa risoluzione temporale, misurando dinamica dell'ordine delle decine di millisecondi. Grazie a tale metodo di indagine, infatti, siamo in grado di spiegare la RIA in termini di difetti indotti, descrivendone le cinetiche corrispondenti in accordo con modelli di reazioni diffusion-controlled. Il risultato più importante ottenuto è una chiara descrizione delle bande di assorbimento nelle fibre studiate alle due diverse temperature, risultando in una migliore comprensione del ruolo cruciale dei self-trapped holes (STHs) che influenzano le propretà di trasmissione di tutti i tipi di fibre ottiche. Il nostro approccio, inoltre, rivela una forte correlazione tra due diffetti il cui comportamento non è ancora del tutto chiaro, appartenenti ai difetti associati al germanio: il GeX ed il GeY. Relativamente alla RIA nel vicino infrarosso, la sua origine nelle fibre in pura silice e drogate con il fluoro non è stata ancora compresa e per questo motivo futuri studi saranno focalizzati per identificare i diffetti (il difetto) responsabili/e dell'assorbimento in questo dominio spettrale. Anche le fibre dopate con il fosforo presentano un contributo sconosciuto della RIA a circa ~ 1.2 eV, stimonando ulteriori esperimenti per identificare i difetti (o il difetto) coinvolti/o.

Prospettive

Lo studio della RIA, in termini di difetti di punto, è uno strumento potente per investigare tali sistemi, fornendo importanti informazioni sia dal punto di vista qualitativo che quantitativo. La possibilità di effettuare misure a bassa temperatura, inoltre, ci da accesso ai difetti metastabili

non facilmente osservabili a RT. Come già visto nei capitoli precedenti, questo metodo permette di evidenziare l'importaza dei STHs come difetti intrinseci, e la loro influenza nella RIA delle fibre dopate e non. È anche possibile trovare correlazioni tra difetti per cui è difficile un'investigazione diretta, sia perchè in alcuni casi le bande di assorbimento si sovrappongono con quelle di altri difetti, sia perchè in altri casi possono rivelarsi non stabili. In questo contesto, abbiamo osservato una correlazione lineare tra il comportamento dei centri GeX e GeY. Futuri esperimenti saranno necessari al fine di stabilire la corrispondenza tra i due difetti, in modo da chiarire l'esatta natura di questa relazione: se essa derivi dal fatto che hanno lo stesso sito precursore e quindi possono ricombinarsi insieme, oppure se le due bande correlate siano relative allo stesso difetto. Sarà anche importante confrontare i nostri risultati con quanto osservato in ref. [95] sotto irraggiamento γ continuo, dove si ha un'anticorrelazione tra l'intensità delle bande di assorbimento dei centri GeX e GeY in funzione della temperatura.

Lo studio sistematico della RIA in termini delle bande di assorbimento dei difetti di punto, ha inoltre evidenziato delle lacune nella conoscenza delle origini della RIA in diversi domini spettrali e in vari tipi di fibre ottiche. Nonostante siamo stati in grado di fornire una buona descrizione, in termini di difetti, delle fibre drogate con il germanio (sotto irraggiamento X sia continuo che pulsato), nel caso delle altre fibre la situzione è differente. Sono necessarie, infatti, nuove indagini per spiegare la RIA nel vicino infrarosso delle fibre in silice pura e dopate con fluoro, anche se lavori recenti stanno facendo luce su questa RIA (ref. [202] [206]), come anche per spiegare l'assorbimento intorno a ∼1.2 eV delle fibre dopate con il fosforo.

Effetti non lineari di assorbimento di fotoni indotti dall'esposizione della silice a laser al femtosecondo

Risultati

Questa parte della tesi è rivolta alla caratterizzazione dei difetti di punto generati dall'interazione di laser al femtosecondo ad alta intensità con la silice. In particolare abbiamo studiato l'interazione, in funzione delle condizioni di esposizione, variando la lunghezza d'onda del laser, l'energia depositata e la composizione chimica dei campioni. Questo studio è stato

stimolato dai lavori relativi alla generazione di difetti di punto indotti da laser al femtosecondo, i quali non danno una completa e soddisfaciente descrizione dei meccanismi coinvolti. La prima parte dello studio evidenzia la maggiore efficienza del laser UV nell'indurre modifiche strutturali permanenti che permettono il guidaggio nella luce, rispetto ad un laser nell'IR. Inoltre è stato possibile mostrare che i difetti generati nella regione esposta al laser contribuiscono alla variazione indotta dell'indice di rifrazione Δn. Abbiamo inoltre effettuato dei trattamenti termici selettivi, che hanno rivelato un panorama di difetti indotti molto più complesso di quello generalmente associato all'iscrizione di guide d'onda in silice amorfa. La seconda parte è relativa ai difetti generati durante l'irraggiamento laser, evidenziando come la variazione della lunghezza d'onda del laser, della potenza e della composizione chimica dei campioni, influenza la natura e la concentrazione dei centri di colore indotti. Questo studio è stato codotto misurando la photoluminescenza (PL) online dei difetti generati dagli impulsi al femtosecondo. Per una completa caratterizzazione dell'interazione tra questo tipo di laser e la silice, la PL è stata studiata anche in funzione della composizione chimica dei campioni, identificando diverse cinetiche di generazione in funzione della quantità di gruppi idrossili.

Prospettive

Il nostro lavoro mette in luce l'importanza di caratterizzare i difetti indotti per studiare i meccanismi alla base dell'interazione tra laser al femtosecondo e la silice, e più in generale, tra i laser al femtosecondo e la materia. Infatti, le nostre misure mostrano un complesso panorama di difetti generati durante, e dopo, l'esposizione a questo tipo di laser. Come è stato dimostrato dai due trattamenti termici selettivi, i difetti non ancora individuati, giocano un ruolo importante nelle proprietà ottiche delle guide d'onda inscritte, come le loro perdite, il confinamento dei modi e il cambiamento indotto all'indice di rifrazione. Futuri esperimenti saranno necessari al fine di identificare i difetti coinvolti durante l'irraggiamento della silice: misure di assorbimento ottico, PL risolta in tempo e risonanza magnetica elettronica. Queste tecniche spettroscopiche potranno anche essere in grado di far luce sui difetti responsabili della banda PL piccata a $545\ nm$.

L'obbiettivo di questa ricerca è rivelare i difetti luminescenti indotti durante l'esposizione al laser al femtosecondo. Abbiamo osservato che la natura e le concentrazioni dei difetti dipendono non solo dalle condizioni sperimentali di irradggiamento, ma anche dalla composizione chimica

del campione, introducendo processi estrinseci che potrebbero dominare la loro risposta globale. É importante, inoltre, sottolineare che le misure online sono fondamentali per fornire nuove e più approfondite informazioni. Infatti, seppur complesse, le tecniche *in situ* sono più potenti rispetto allo studio post mortem, grazie alla loro capacità di sondare la natura metastabile della maggior parte dei difetti indotti. Pertanto, i futuri esperimenti saranno focalizzati sulla possibilità di studiare la generazione di difetti di punto durante l'esposizione (non solo difetti PL-attivi), con risoluzioni temporali molto brevi, come misurazioni pump-probe basate su probe con una durata dell'impulso dell'ordine dei femtosecondi.

Spettroscopia pump-probe dei difetti di punto risolta in tempo

Risultati

La terza e ultima sezione è relativa allo studio dei meccanismi del fotociclo dei difetti di punto negli istanti di tempo successivi all'impulso laser. Tale indagine rappresenta lo stato dell'arte per quanto riguarda lo studio del fotociclo dei difetti di punto in materiali ad alto band gap. Esperimenti pump-probe in isolanti ad alto bandgap sono ancora oggi particolarmente difficili da eseguire, in quanto particolarmente complessi dal punto di vista sperimentale. In questo contesto, siamo interessati a fornire un approccio innovativo relativo a questioni irrisolte, riguardanti i centri di colore nei solidi con ad alto band gap. Per evidenziare le potenzialità di questo metodo, abbiamo studiato il fotociclo di due diversi e ben noti difetti, l'NBOHC e il GLPC, studiandone la dinamica con una risoluzione temporale senza precedenti. L'insieme degli esperimenti effettuati aiuta a chiarire il fotociclo dei difetti, evidenziando come le misure di assorbimento transiente, accoppiate ad un'eccitazione UV tunabile, rappresentino uno strumento innovativo per indagare tali sistemi amorfi e, in generale, la fisica dello stato solido, su scale temporali molto brevi.

Prospettive

Come già sottolineato nel capitolo 6, il nostro scopo è fornire un approccio sperimentale innovativo per studiare i difetti di punto. È importante sottolineare che tale metodo ha una validità generale e, per mostrarne le potenzialità, lo abbiamo sfruttato per studiare il fotociclo di difetti noti legati alla silice. Mediante le nostre misure, infatti, abbiamo acquisito molte nuove informazioni sui difetti coinvolti, essendo anche i primi ad indagarne la dinamica su una scala dei femto-picosecondi, in condizioni di assorbimento lineare. Il successo nello spiegare il fotociclo osservato evidenzia come tale approccio sperimentale potrebbe essere utile non solo a studiare la varietà di difetti relativi a-SiO_2, ma potenzialmente, anche i centri di colore presenti in altri tipi di materiali ad alto band gap. Questo sarà sicuramente l'argomento di studi futuri.

List of related papers and communications

Papers

V. De Michele, A. Sciortino, F. Messina, M. Cannas, Aziz Boukenter, Emmanuel Marin, Sylvain Girard, and Youcef Ouerdane, "**Transient Absorption with fs Tunable Excitation Pump Reveals the Emission Kinetics of Color Centers in Amorphous Silica**", accepted in *Optics Letters*.

https://doi.org/10.1364/OL.420198

V. De Michele, Emmanuel Marin, Aziz Boukenter, M. Cannas, Sylvain Girard, and Youcef Ouerdane, "**Photoluminescence of Point Defects in Silicon Dioxide by Femtosecond Laser Exposure**", in *Phys. Status Solidi A (2021), 202000802*.

https://doi.org/10.1002/pssa.202000802

A. Morana, C. Campanella, J. Vidalot, **V. De Michele**, E. Marin, I. Reghioua, A. Boukenter, Y. Ouerdane, P. Paillet, and S. Girard, **Extreme Radiation Sensitivity of Ultra-Low Loss Pure-Silica-Core Optical Fibers at Low Dose Levels and Infrared Wavelengths**, *Sensors (2020), 20, 7254*.

https://doi.org/10.3390/s20247254

V. De Michele, C. Marcandella, J.Vidalot, P. Paillet, A. Morana, M. Cannas, A. Boukenter, E. Marin, Y. Ouerdane and S. Girard, **Origins of Radiation-induced Attenuation in Pure-Silica-Core and Ge-doped Optical Fibers under Pulsed X-ray Irradiation**, *Journal of Applied Physics (2020), 128, 103101*.

https://doi.org/10.1063/5.0014165

V. De Michele, A. Morana, C. Campanella, J. Vidalot, A. Alessi, A. Boukenter, M. Cannas, P. Paillet, Y. Ouerdane, and S. Girard, **Steady State X-Ray Radiation Induced Attenuation in Canonical Optical Fibers**, *IEEE Trans. Nucl. Sci. (2020), 67(7), 1650-1657*.

https://doi.org/10.1109/TNS.2020.2969717

S. Girard, **V. De Michele**, A. Alessi, C. Marcandella, D. Di Francesca, P. Paillet, A. Morana, J. Vidalot, C. Campanella, S. Agnello, M. Cannas, M. Gaillardin, E. Marin, A. Boukenter, and Y. Ouerdane, **Transient and Steady-State Radiation Response of Phosphosilicate Optical Fibers: Influence of H_2 Loading**, *IEEE Trans. Nucl. Sci. (2020), 67(1), 289-295*.

https://doi.org/10.1109/TNS.2019.2947583

V. De Michele, M. Royon, E. Marin, A. Alessi, A. Morana, A. Boukenter, M. Cannas, S. Girard, and Y Ouerdane, **Near-IR- and UV-femtosecond Laser Waveguides Inscription in Silica Glasses**, *Opt. Mater. Express (2019), 9(12), 4624-4633*.

https://doi.org/10.1364/OME.9.004624

(Invited review) S. Girard, A. Alessi, N. Richard, L. Martin-Samos, **V. De Michele**, L. Giacomazzi, S. Agnello, D. Di Francesca, A. Morana, B. Winkler, I. Reghioua, P. Paillet, M. Cannas, T. Robin, A. Boukenter and Y. Ouerdane, **Overview of Radiation Induced Point Defects in Silica-Based Optical Fibers**, *Reviews in Physics (2019), 4, 100032*.

https://doi.org/10.1016/j.revip.2019.100032

V. De Michele, C. Marcandella, D. Di Francesca, P. Paillet, A. Alessi, M. Cannas, Y. Ouerdane, A. Boukenter and S. Girard, **Pulsed X-ray Radiation Response of Solarization-Resistant Optical Fibers**, *Phys. Status Solidi A (2018), 1800487*.

https://doi.org/10.1002/pssa.201800487

S. Girard, P. Paillet, M. Trinzcek, C. Marcandella, A. Alessi, A. Morana, **V. De Michele**, A. Boukenter and Y. Ouerdane, **Influence of Self-Trapped Holes on the Responses of Fluorine-Doped Multimode Optical Fibers Exposed to Low Fluences of Protons**, *Phys. Status Solidi A (2018), 1800547.*

https://doi.org/10.1002/pssa.201800547

Proceedings

V. De Michele, A. Sciortino, F. Messina, M. Cannas, A. Boukenter, E. Marin, S. Girard, and Y. Ouerdane, **NBOHCs' photocycle revealed in synthetic silica by transient absorption measurements**, *The 22nd International Conference on Ultrafast Phenomena 2020*, F. Kärtner, M. Khalil, R. Li, F. Légaré, and T. Tahara, OSA Technical Digest (Optical Society of America, 2020), paper Tu4B.42.

V. De Michele, M. Royon, E. Marin, A. Alessi, G. Zhang, G. Cheng, R. Stoian, M. Cannas and Y. Ouerdane, **Laser Wavelength Effects on the Refractive Index Change of Waveguides Written by Femtosecond Pulses in Silica Glasses,** *Advanced Photonics 2018* (*BGPP, IPR, NP, NOMA, Sensor, Networks, SPPCom, SOF*), OSA Technical Digest (Optical Society of America, 2018), paper BM2A.5.

https://doi.org/10.1364/BGPPM.2018.BM2A.5

Communications

V. De Michele, M. Royon, E. Marin, A. Alessi, A. Morana, A. Boukenter, M. Cannas, S. Girard and Y. Ouerdane, **NIR- and UV-femtosecond Laser Waveguides Inscription in Silica Glasses**.

Conference on Radiation Effects in Insulators REI-20, Nur-Sultan (Kazakhstan).

V. De Michele, E. Marin, A. Alessi, A. Morana, A. Boukenter, M. Cannas, S. Girard and Y. Ouerdane, **Photoluminescence of Point Defects in Silicon Dioxide by Femtosecond Laser Exposure**.

FMR 2018: 9eme journées sur les Fibres Optiques en Milieu Radiatif, Saint Etienne (France).

V. De Michele, M. Royon, E. Marin, A. Alessi, G. Zhang, G. Cheng, R. Stoian, M. Cannas and Y. Ouerdane, **Laser Wavelength Effects on the Refractive Index Change of Waveguides Written by Femtosecond Pulses in Silica Glasses**.

OSA Advanced Photonics Congress: Bragg Gratings, Photosensitivity and Poling in Glass Waveguides & Materials conference, Zurich (Switzerland).

V. De Michele, C. Marcandella, D. Di Francesca, P. Paillet, A. Alessi, M. Cannas, Y. Ouerdane, A. Boukenter and S. Girard, **Pulsed X-ray Radiation Responses of Solarization-Resistant Optical Fibers**.

SiO_2 2018: 12th international symposium on SiO_2 advanced dielectrics and related devices, Bari (Italy).

V. De Michele, C. Marcandella, D. Di Francesca, P. Paillet, A. Alessi, Y. Ouerdane, A. Boukenter and S. Girard, **Transient Radiation Responses of Silica-Based Materials and Optical Fibers**.

FMR 2017: 8eme journees sur les Fibres Optiques en Milieu Radiatif, Mons (Belgium).

Poster Presentations

V. De Michele, A. Sciortino, F. Messina, M. Cannas, A. Boukenter, E. Marin, S. Girard**, NBOHCs' Photocycle Revealed in Synthetic Silica by Transient Absorption Measurements**.

The 22nd International Conference on Ultrafast Phenomena 2020 (Virtual event), Shanghai (China).

V. De Michele, A. Adriana, C. Campanella, J. Vidalot, A. Alessi, A. Boukenter, M. Cannas, Y. Ouerdane and S. Girard, **Characterization of the RIA Induced in Canonical Optical Fibers under Continuous X-ray Irradiation at Room and Liquid Nitrogen Temperatures**.

European Conference on Radiation and its Effects on Components & System (RADECS) 2019, Montpellier (France).

International Awards

BGPP student award: in recognition for the valuable contribution to the *Bragg Gratings, Photosensitivity and Poling in Glass Waveguides & Materials conference*, IFOS sponsor award, OSA advanced photonics Congress, Zurich (Switzerland).

References

[1] G. Pacchioni, L. Skuja, and D. L. Griscom, *Defects in SiO_2 and Related Dielectrics: Science and Technology*. Dordrecht: Springer Netherlands, 2000.

[2] R. A. B. Devine, *Physics and Technology of Amorphous SiO_2.* Boston: Springer US, 1988.

[3] L. Skuja, 'Optical properties of defects in silica', in *Defects in SiO2 and Related Dielectrics: Science and Technology*, G. Pacchioni, L. Skuja, and D. L. Griscom, Eds. Dordrecht: Springer Netherlands, 2000.

[4] S. Girard et al., 'Overview of radiation induced point defects in silica-based optical fibers', *Reviews in Physics* 4, 2019.

[5] S. Girard et al., 'Integration of optical fibers in radiative environments: Advantages and limitations', in *2011 2nd International Conference on Advancements in Nuclear Instrumentation, Measurement Methods and their Applications*, 2011.

[6] S. Girard et al., 'Radiation Effects on Silica-Based Optical Fibers: Recent Advances and Future Challenges', *IEEE Transactions on Nuclear Science* 60, 2013.

[7] R. Osellame, G. Cerullo, and R. Ramponi, Eds., *Femtosecond Laser Micromachining*, vol. 123. Berlin, Heidelberg: Springer Berlin Heidelberg, 2012.

[8] J. Cheng et al., 'A review of ultrafast laser materials micromachining', *Optics & Laser Technology* 46, 2013.

[9] S. S. Mao et al., 'Dynamics of femtosecond laser interactions with dielectrics', *Applied Physics A* 79, 2004.

[10] K. M. Davis, K. Miura, N. Sugimoto, and K. Hirao, 'Writing waveguides in glass with a femtosecond laser', *Optics Letters* 21, 1996.

[11] A. Zoubir et al., 'Laser-induced defects in fused silica by femtosecond IR irradiation', *Physical Review B* 73, 2006.

[12] D. G. Papazoglou, D. Abdollahpour, and S. Tzortzakis, 'Ultrafast electron and material dynamics following femtosecond filamentation induced excitation of transparent solids', *Applied Physics A* 114, 2014.

[13] W. J. Reichman, J. W. Chan, C. W. Smelser, S. J. Mihailov, and D. M. Krol, 'Spectroscopic characterization of different femtosecond laser modification regimes in fused silica', *Journal of the Optical Society of America B* 24, 2007.

[14] K. Mishchik et al., 'Ultrafast laser induced electronic and structural modifications in bulk fused silica', *Journal of Applied Physics* 114, 2013.

[15] H. Bach, N. Neurot, *The Properties of Optical Glass*, Heidelberg: Springer Berlin, 1998.

[16] W. H. Zachariasen, 'The atomic arrangement in glass', *Journal of the American Chemical Society* 54, 1932.

[17] E. Duval, A. Boukenter, and T. Achibat, 'Vibrational dynamics and the structure of glasses', *Journal of Physics: Condensed Matter* 2, 1990.

[18] P.-G. de Gennes, 'A simple picture for structural glasses', *Comptes Rendus Physique* 3, 2002.

[19] A. C. Wright, 'Neutron scattering from vitreous silica. V. The structure of vitreous silica: What have we learned from 60 years of diffraction studies?', *Journal of Non-Crystalline Solids* 179, 1994.

[20] D. L. Griscom, 'Defect structure of glasses', *Journal of Non-Crystalline Solids* 73, 1985.

[21] A. E. Geissberger and F. L. Galeener, 'Raman studies of vitreous Si O 2 versus fictive temperature', *Physical Review B* 28, 1983.

[22] A. Pasquarello and R. Car, 'Identification of Raman Defect Lines as Signatures of Ring Structures in Vitreous Silica', *Phyical Review Letters* 80, 1998.

[23] B. Hehlen, 'Inter-tetrahedra bond angle of permanently densified silicas extracted from their Raman spectra', *Journal of Physics: Condensed Matter* 22, 2010.

[24] F. N. C. Anyaegbunam and C. Augustine, 'A study of optical band gap and associated urbach energy tail of chemically deposited metal oxides binary thin films', *Digest Journal of Nanomaterials and Biostructures* 13, 2018.

[25] A. Gulino et al., 'A Novel Self-generating Liquid MOCVD Precursor for $Co_3 O_4$ Thin Films', *Chem. Mater.* 15, 2003.

[26] F. Bassani, U. M.Grassano, *Fisica dello Stato Solido*, Bollati Boringhieri, 2000.

[27] E. P. O'Reilly and J. Robertson, 'Theory of defects in vitreous silicon dioxide', *Physical Review B* 27, 1983.

[28] J. R. Chelikowsky and M. Schlüter, 'Electron states in α-quartz: A self-consistent pseudopotential calculation', *Physical Review B* 15, 1977.

[29] D. L. Griscom, 'A minireview of the natures of radiation-induced point defects in pure and doped silica glasses and their visible/near-IR absorption bands, with emphasis on self-trapped holes and how they can be controlled', *Physics Research International* 2013, 2013.

[30] D. L. Griscom, E. J. Friebele, K. J. Long, and J. W. Fleming, 'Fundamental defect centers in glass: Electron spin resonance and optical absorption studies of irradiated phosphorus-doped silica glass and optical fibers', *Journal of Applied Physics* 54, 1983.

[31] D. L. Griscom, 'Optical properties and structure of defects in silica glass', *Journal of the Ceramic Society of Japan* 99, 1991.

[32] L. Skuja, 'Optically active oxygen-deficiency-related centers in amorphous silicon dioxide', *Journal of Non-crystalline Solids* 239, 1998.

[33] Y. Toyozawa, '*Optical Processes in Solids*', Cambridge University Press, 2003.

[34] B. H. Bransden and C. J. Joachain, *Physics of Atoms and Molecules*, Longman Scientific & Technical, 1983.

[35] R. Salh, 'Defect related luminescence in silicon dioxide network: A review', in *Crystalline Silicon - Properties and Uses*, S. Basu, InTech, 2011.

[36] G. Buscarino, S. Agnello, and F. M. Gelardi, 'Delocalized Nature of the E'_{δ} Center in Amorphous Silicon Dioxide', *Physical Review Letters* 94, 2005.

[37] G. Buscarino, S. Agnello, and F. M. Gelardi, 'Si^{29} hyperfine structure of the E′α center in amorphous silicon dioxide', *Physical Review Letters* 97, 2006.

[38] S. Agnello, R. Boscaino, G. Buscarino, M. Cannas, and F. M. Gelardi, 'Structural relaxation of E'_{γ} centers in amorphous silica', *Physical Review B* 66, 2002.

[39] A. Morana et al., 'Origin of the visible absorption in radiation-resistant optical fibers', *Optical Material Express* 3, 2013.

[40] L. Skuja, K. Kajihara, M. Hirano, and H. Hosono, 'Oxygen-excess-related point defects in glassy/amorphous SiO2 and related materials', *Nuclear Instruments and Methods in Physics Research Section B: Beam Interactions with Materials and Atoms* 286, 2012.

[41] L. Vaccaro, M. Cannas, B. Boizot, and A. Parlato, 'Radiation induced generation of non-bridging oxygen hole center in silica: Intrinsic and extrinsic processes', *Journal of Non-Crystalline Solids* 353, 2007.

[42] L. Skuja, K. Kajihara, M. Hirano, and H. Hosono, 'Visible to vacuum-UV range optical absorption of oxygen dangling bonds in amorphous SiO_2', *Physical Review B* 84, 2011.

[43] L. Skuja, K. Kajihara, J. Grube, and H. Hosono, 'Luminescence of non-bridging oxygen hole centers in crystalline SiO_2', AIP Conference Proceedings 1624, 2014.

[44] L. Vaccaro, M. Cannas, V. Radzig, and R. Boscaino, 'Luminescence of the surface nonbridging oxygen hole center in silica: Spectral and decay properties', *Physical Review B* 78, 2008.

[45] M. Cannas, L. Vaccaro, and B. Boizot, 'Spectroscopic parameters related to non-bridging oxygen hole centers in amorphous-SiO_2', *Journal of Non-Crystalline Solids* 352, 2006.

[46] L. Skuja and B. Güttler, 'Detection of interstitial oxygen molecules in SiO_2 glass by a direct photoexcitation of the infrared luminescence of singlet O_2', *Physical Review Letters* 77, 1996.

[47] L. N. Skuja and A. R. Silin, 'A model for the non-bridging oxygen center in fused silica', *Physica Status Solidi (a)* 70, 1982.

[48] T. Suzuki, L. Skuja, K. Kajihara, M. Hirano, T. Kamiya, and H. Hosono, 'Electronic structure of oxygen dangling bond in glassy SiO_2 : The role of hyperconjugation', *Physical Review Letters* 90, 2003.

[49] T. Bakos, S. N. Rashkeev, and S. T. Pantelides, 'Optically active defects in SiO_2 : The nonbridging oxygen center and the interstitial OH molecule', *Physical Review B* 702004.

[50] T. Uchino, M. Takahashi, and T. Yoko, 'Model of oxygen-deficiency-related defects in SiO_2 glass', *Physical Review B* 62, 2000.

[51] H. Imai, K. Arai, H. Imagawa, H. Hosono, and Y. Abe, 'Two types of oxygen-deficient centers in synthetic silica glass', *Physical Review B* 38, 1988.

[52] H.-J. Fitting, 'How to make silica luminescent?', *Journal of Luminescence* 129, 2009.

[53] A. N. Trukhin and K. M. Golant, 'Peculiarities of photoluminescence excited by 157 nm wavelength F_2 excimer laser in fused and unfused silicon dioxide', *Journal of Non-Crystalline Solids* 355, 2009.

[54] Y. Sakurai, 'The 3.1 eV photoluminescence band in oxygen-deficient silica glass', *Journal of Non-Crystalline Solids* 271, 2000.

[55] A. N. Trukhin, J. Troks, and D. L. Griscom, 'Thermostimulated luminescence and electron spin resonance in X-ray- and photon-irradiated oxygen-deficient silica', *Journal of Non-Crystalline Solids* 353, 2007.

[56] B. Winkler et al., 'Correlations between structural and optical properties of peroxy bridges from first principles', *The Journal of Physical Chemistry C* 121, 2017.

[57] L. Skuja, K. Kajihara, M. Hirano, and H. Hosono, 'Oxygen-excess-related point defects in glassy/amorphous SiO2 and related materials', *Nuclear Instruments and Methods in Physics Research Section B: Beam Interactions with Materials and Atoms* 286, 2012.

[58] D. L. Griscom and M. Mizuguchi, 'Determination of the visible range optical absorption spectrum of peroxy radicals in gamma-irradiated fused silica', *Journal of Non-Crystalline Solids* 239, 1998.

[59] E. J. Friebele, D. L. Griscom, M. Stapelbroek, and R. A. Weeks, 'Fundamental defect centers in glass: the peroxy radical in irradiated, high-purity, fused silica', *Physical Review Letters* 42, 1979.

[60] A. H. Edwards and W. B. Fowler, 'Theory of the peroxy-radical defect in a-SiO_2', *Physical Review B* 26, 1982.

[61] K. S. Song and R. T. Williams, *Self-Trapped Excitons*, Heidelberg: Springer Berlin, 1993.

[62] H. Fujiwara, T. Suzuki, and K. Tanimura, 'Femtosecond time-resolved spectroscopy of the Frenkel-pair generation and self-trapped-exciton formation in KCl and RbCl', *Journal of Physics: Condensed Matter* 9, 1997.

[63] K. Kajihara, M. Hirano, L. Skuja, and H. Hosono, 'Frenkel defect process in amorphous silica', *Proceedings of SPIE* 8077, 2011.

[64] R. M. Van Ginhoven, H. Jónsson, and L. R. Corrales, 'Characterization of exciton self-trapping in amorphous silica', *Journal of Non-Crystalline Solids* 352, 2006.

[65] A. Shluger and E. Stefanovich, 'Models of the self-trapped exciton and nearest-neighbor defect pair in SiO_2', *Physical Review B* 42, 1990.

[66] A. J. Fisher, W. Hayes, and A. M. Stoneham, 'Structure of the self-trapped exciton in quartz', *Physical Review Letters* 64, 1990

[67] D. L. Griscom, 'Trapped-electron centers in pure and doped glassy silica: A review and synthesis', *Journal of Non-Crystalline Solids* 357, 2011.

[68] C. Itoh, K. Tanimura, and N. Itoh, 'Optical studies of self-trapped excitons in SiO_2', *Journal of Physics C: Solid State Physics* 21, 1988.

[69] K. Tanimura, C. Itoh, and N. Itoh, 'Transient optical absorption and luminescence induced by band-to-band excitation in amorphous SiO_2', *Journal of Physics C: Solid State Physic* 21, 1988.

[70] W. Joosen et al., 'Femtosecond multiphoton generation of the self-trapped exciton in α-SiO_2', *Applied Physics Letters* 61, 1992.

[71] A. N. Trukhin, 'Temperature Dependence of Luminescence Decay Kinetics of Self-Trapped Excitons, Germanium and Aluminium Centres in Crystalline Quartz', *Physica Status Solidi (b)* 143, 1987.

[72] N. Fukata, Y. Yamamoto, K. Murakami, M. Hase, and M. Kitajima, '*In situ* spectroscopic measurement of transmitted light related to defect formation in SiO2 during femtosecond laser irradiation', *Applied Physics Letters* 83, 2003.

[73] D. L. Griscom, 'Self-trapped holes in amorphous silicon dioxide', *Physical Review B* 40, 1989.

[74] D. L. Griscom, 'Self-trapped holes in pure-silica glass: A history of their discovery and characterization and an example of their critical significance to industry', *Journal of Non-Crystalline Solids* 352, 2006.

[75] P. F. Kashaykin, A. L. Tomashuk, M. Yu. Salgansky, A. N. Guryanov, and E. M. Dianov, 'Anomalies and peculiarities of radiation-induced light absorption in pure silica optical fibers at different temperatures', *Journal of Applied Physics* 121, 2017.

[76] A. L. Tomashuk et al., 'Role of Inherent Radiation-Induced Self-Trapped Holes in Pulsed-Radiation Effect on Pure-Silica-Core Optical Fibers', *Journal of Lightwave Technology* 37, 2019.

[77] S. Girard, D. L. Griscom, J. Baggio, B. Brichard, and F. Berghmans, 'Transient optical absorption in pulsed-X-ray-irradiated pure-silica-core optical fibers: Influence of self-trapped holes', *Journal of Non-Crystalline Solids* 352, 2006.

[78] Sylvain Girard et al., 'Influence of Self-Trapped Holes on the Responses of Fluorine-Doped Multimode Optical Fibers Exposed to Low Fluences of Protons', *Physica Status Solidi (a)* 216, 2019.

[79] V. De Michele et al., 'Origins of radiation-induced attenuation in pure-silica-core and Ge-doped optical fibers under pulsed x-ray irradiation', *Journal of Applied Physics* 128, 2020.

[80] V. De Michele et al., 'Pulsed X-ray radiation responses of solarization-resistant optical fibers', *Physica Status Solidi (a)* 216, 2019.

[81] P. V. Chernov et al., 'Spectroscopic manifestations of self-trapped holes in silica', *Physica Status Solidi (b)* 156, 1989.

[82] E. M. Dianov et al., ‘Spectroscopic manifestations of self-trapped holes in silica theory and experiment’, *Physica status solidi (b)* 156, 1989.

[83] A. V. Kimmel, P. V. Sushko, and A. L. Shluger, ‘Structure and spectroscopic properties of trapped holes in silica’, *Journal of Non-Crystalline Solids* 353, 2007.

[84] Y. Sasajima and K. Tanimura, ‘Optical transitions of self-trapped holes in amorphous SiO_2’, *Physical Review B* 68, 2003.

[85] J. Stone and G. E. Walrafen, ‘Overtone vibrations of OH groups in fused silica optical fibers’, *The Journal of Chemical Physics* 76, 1982.

[86] S. Girard et al., ‘Transient Radiation Responses of Optical Fibers: Influence of MCVD Process Parameters’, *IEEE Transactions on Nuclear Science* 59, 2012.

[87] Vincenzo De Michele et al., ‘Steady-State X-Ray Radiation-Induced Attenuation in Canonical Optical Fibers’, *IEEE Transactions on Nuclear Science* 67, 2020.

[88] V. B. Neustruev, ‘Colour centres in germanosilicate glass and optical fibres’, Journal of Physics: Condensed Matter 6, 1994.

[89] Y. Laudernet et al., ‘Ab initio molecular dynamics simulations of oxygen-deficient centers in pure and Ge-doped silica glasses: Structure and optical properties’, *Journal of Non-Crystalline Solids* 352, 2006.

[90] M. Cannas, M. Barbera, R. Boscaino, A. Collura, F. M. Gelardi, and S. Varisco, ‘Photoluminescence activity in natural silica excited in the vacuum-UV range’, *Journal of Non-Crystalline Solids* 245, 1999.

[91] S. Grandi, P. Mustarelli, S. Agnello, M. Cannas, and A. Cannizzo, ‘Sol-Gel GeO_2-doped SiO_2 glasses for optical applications’, *Journal of Sol-Gel Science and Technology* 26, 2003.

[92] S. Agnello et al., ‘Temperature and excitation energy dependence of decay processes of luminescence in Ge-doped silica’, *Physical Review B 68*, 2003.

[93] A. Cannizzo et al., ‘Relaxation processes of point defects in vitreous silica from femtosecond to nanoseconds’, *Applied Physics Letters* 93, 2008.

[94] P. F. Kashaykin et al., ‘Observation of radiation-induced absorption of self-trapped holes in Ge-doped silica fiber in near infrared range at reduced temperature’, *Journal of Non-Crystalline Solids* 496, 2018.

[95] P. F. Kashaykin et al., ‘New radiation colour centre in germanosilicate glass fibres’, *Quantum Electronics* 48, 2018.

[96] A. Alessi et al., ‘Gamma and x-ray irradiation effects on different Ge and Ge/F doped optical fibers’, *Journal of Applied Physics* 118, 2015.

[97] P. V. Chernov et al, ‘Spettroscopic manifestations of self-trapped holes’, *Physica Status Solidi (b)* 155, 1989.

[98] N. Shibata, M. Horigudhi, and T. Edahiro, ‘Raman spectra of binary high-silica glasses and fibers containing GeO_2, P_2O_5 and B_2O_3’, *Journal of Non-Crystalline Solids* 45, 1981.

[99] V. G. Plotnichenko, V. O. Sokolov, V. V. Koltashev, V. B. Sulimov, and E. M. Dianov, 'UV-irradiation-induced structural transformation in phosphosilicate glass fiber', Optics Letters *23*, 1998.

[100] D. Di Francesca et al., 'Qualification and calibration of single mode phosphosilicate optical fiber for dosimetry at CERN', *Journal Lightwave Technology* 37, 2019.

[101] S. Girard et al., 'Transient and steady state radiation response of phosphosilicate optical fibers: influence of H_2 loading', *IEEE Transactions on Nuclear Science* 67, 2020.

[102] S. Girard et al., 'Feasibility of radiation dosimetry with phosphorus-doped optical fibers in the ultraviolet and visible domain', *Journal of Non-Crystalline Solids* 357, 2011.

[103] C. Kittel, W. D. Knight, M. A. Ruderman, A. C. Helmholz, B. J. Moyer, *Berkeley Physics Course Vol. 1 - Solutions Manual to Mechanics*, McGraw-Hill Book Company, 1965.

[104] M. Born and E. Wolf, *Principles of Optics*, Pergamon Press, 1959.

[105] P. Lorrain and D. L. Corson, *Electromagnetic Fields and Waves*, W. H. Freeman and Company, 1987.

[106] C. J. F. Böttcher, *Dielectrics in static fields*, New York: Elsevier Scientific Pub. Co, 1973.

[107] P. V. Rysselberghe, 'Remarks concerning the Clausius-Mossotti Law', *The Journal of Physical Chemistry* 36, 1932.

[108] J. H. Crawford and L. M. Slifkin, *Point Defects in Solids: General and Ionic Crystals*, Boston: Springer US, 1972.

[109] D. Strickland and G. Mourou, 'Compression of amplified chirped optical pulses', *Optics Communication* 56, 1985.

[110] G. Mourou, 'The ultrahigh-peak-power laser: present and future', *Applied Physics B: Lasers and Optics* 65, 1997.

[111] G. Petite, P. Daguzan, S. Guizard, and P. Martin, 'Ultrafast processes in laser irradiated wide bandgap insulators', *Applied Surface Science* 109, 1997.

[112] A. Kaiser, B. Rethfeld, M. Vicanek, and G. Simon, 'Microscopic processes in dielectrics under irradiation by subpicosecond laser pulses', *Physical Review B* 61, 2000.

[113] B. Poumellec, M. Lancry, A. Chahid-Erraji, and P. G. Kazansky, 'Modification thresholds in femtosecond laser processing of pure silica: review of dependencies on laser parameters', *Optical Materials Express* 1, 2011.

[114] C. B. Schaffer, A. Brodeur, and E. Mazur, 'Laser-induced breakdown and damage in bulk transparent materials induced by tightly focused femtosecond laser pulses', *Measurement Science and Technology* 12, 2001.

[115] V. V. Temnov, K. Sokolowski-Tinten, P. Zhou, and A. El-Khamhawy, 'Multiphoton Ionization in Dielectrics: Comparison of Circular and Linear Polarization', *Physical Review Letters* 97, 2006.

[116] V. Nathan, S. S. Mitra, and A. H. Guenther, 'Review of multiphoton absorption in crystalline solids', *Journal of the Optical Society of America B* 2, 1985.

[117] A. Rosenfeld, M. Lorenz, R. Stoian, and D. Ashkenasi, 'Ultrashort-laser-pulse damage threshold of transparent materials and the role of incubation', *Applied Physics A: Materials Science & Processing* 69, 1999.

[118] D. Grojo et al., 'Exciton-seeded multiphoton ionization in bulk SiO_2', *Phys. Rev. B* 81, 2010.

[119] L. V. Keldysh, 'Behavior of non-metallic crystals in strong electric fields', *Soviet Physics JETP* 6, 1958.

[120] L. V. Keldysh, 'Ionization in the field of a strong electromagnetic wave', *Soviet Physics JETP* 20, 1965.

[121] B. C. Stuart, M. D. Feit, A. M. Rubenchik, B. W. Shore, and M. D. Perry, 'Laser-Induced Damage in Dielectrics with Nanosecond to Subpicosecond Pulses', *Physical Review Letters* 74, 1995.

[122] M. Shahmohammadi, *Ultrafast spectroscopy of wide bandgap semiconductor nanostructures*, PhD Thesis, EPFL Lausanne, 2015.

[123] L. Schlessinger and J. Wright, 'Inverse-bremsstrahlung absorption rate in an intense laser field', *Physical Review A* 20, 1979.

[124] R. W. Boyd, *Nonlinear Optics*, Academic Press/Elsevier, 2008 .

[125] J.-C. Diels and W. Rudolph, *Ultrashort laser pulse phenomena: fundamentals, techniques, and applications on a femtosecond time scale*, Academic Press/Elsevier, 2006.

[126] T. E. Itina, O. Utéza, N. Sanner, and M. Sentis, 'Interaction of femtosecond laser pulses with dielectric materials: insights from numerical modelling', *Journal of Optoelectronics and Advanced Materials* 12, 2010.

[127] R. Darkins and D. M. Duffy, 'Modelling radiation effects in solids with two-temperature molecular dynamics', *Computational Materials Science* 147, 2018.

[128] B. Rethfeld, D. S. Ivanov, M. E. Garcia, and S. I. Anisimov, 'Modelling ultrafast laser ablation', *Journal of Physics D: Applied Physics* 50, 2017.

[129] B. H. Christensen, K. Vestentoft, and P. Balling, 'Short-pulse ablation rates and the two-temperature model', *Applied Surface Science*. 253, 2007.

[130] N. Singh, 'Two-temperature model of non-equilibrium electron relaxation: A review', *Internation Journal of Modern Physics B* 24, 2010.

[131] E. Carpene, 'Ultrafast laser irradiation of metals: Beyond the two-temperature model', *Physical Review B* 74, 2006.

[132] B. Chimier *et al.*, 'Damage and ablation thresholds of fused-silica in femtosecond regime', *Physical Review B* 84, 2011.

[133] A. Alessi *et al.*, 'Confocal-micro-luminescence characterization of femtosecond laser irradiated silica and borosilicate glasses', *Nuclear Instruments and Methods in Physics Research Section B: Beam Interactions with Materials and Atoms* 435, 2018.

[134] C. B. Schaffer, A. O. Jamison, and E. Mazur, 'Morphology of femtosecond laser-induced structural changes in bulk transparent materials', *Applied Physics Letters* 84, 2004.

[135] R. Taylor, C. Hnatovsky, and E. Simova, 'Applications of femtosecond laser induced self-organized planar nanocracks inside fused silica glass', *Laser & Photonics Review*. 2, 2008.

[136] S. Richter *et al.*, 'Laser induced nanogratings beyond fused silica-periodic nanostructures in borosilicate glasses and ULE™', *Optical Materials Express* 3, 2013.

[137] E. G. Gamaly et al., 'Laser matter interaction in the bulk of a trasparent solid Confined microexplotion and void formation', *Physical Review B* 73, 2006.

[138] H.-B. Sun et al., 'Generation and Recombination of Defects in Vitreous Silica Induced by Irradiation with a Near-Infrared Femtosecond Laser', *The Journal of Physical Chemistry B* 104, 2000.

[139] V. De Michele *et al.*, 'Near-IR- and UV-femtosecond laser waveguide inscription in silica glasses', *Optical Material Express* 9, 2019.

[140] G. M. Barrow, *Introduction to Molecular Spectroscopy*, McGraw-Hill Book Company, 1962.

[141] WARD'S DataHub, B*eer-Lambert law: Measuring percent transmittance of solutions at different concentrations*, WARD'S Science, 2012.

[142] D. J. Griffiths, *Introduction to Quantum Mechanics*, Prentige Hall, 1994.

[143] A. Smakula, 'Über erregung und entfärbung lichtelektrisch leitender alkalihalogenide', *Zeitschrift für Physik* 59, 1930.

[144] D. R. Vij, Ed., *Luminescence of Solids*. Boston: Springer US, 1998.

[145] J. R. Lakowicz, *Principles of fluorescence spectroscopy*, New York: Springer, 2010.

[146] C. Ruckebusch, M. Sliwa, P. Pernot, A. de Juan, and R. Tauler, 'Comprehensive data analysis of femtosecond transient absorption spectra: A review', *Journal of Photochemistry and Photobiology C: Photochemistry Reviews* 13, 2012.

[147] G. Cerullo and S. De Silvestri, 'Ultrafast optical parametric amplifiers', *Review of Scientific Instruments* 74, 2003.

[148] R. Berera, R. van Grondelle, and J. T. M. Kennis, 'Ultrafast transient absorption spectroscopy: principles and application to photosynthetic systems', *Photosynth Research* 101, 2009.

[149] HARPIA ultrafast spectroscopic system user's manual, Light Conversion.

[150] C. Rulliere, *Femtosecond Laser Pulses*, Springer, 2003.

[151] H. Abramczyk, *Introduction to laser spectroscopy*, Amsterdam: Elsevier, 2005.

[152] R. R. Alfano, *The Supercontinuum Laser Source*, Springer, 2016.

[153] H. Chen, Y. Weng, and J. Zhang, 'Noncollinear optical parametric amplifier based femtosecond time-resolved transient fluorescence spectra: characterization and correction', *Journal of the Optical Society of America B* 26, 2009.

[154] ORPHEUS collinear optical parameter amplifier of white light continuum user's manual, Light Conversion.

[155] M. Lorenc, M. Ziolek, R. Naskrecki, J. Karolczak, J. Kubicki, and A. Maciejewski, 'Artifacts in femtosecond transient absorption spectroscopy', *Applied Physics B: Lasers and Optics* 74, 2002.

[156] I. H. M. van Stokkum, D. S. Larsen, and R. van Grondelle, 'Global and target analysis of time-resolved spectra', *Biochimica et Biophysica Acta - Bioenergetics* 1657, 2004.

[157] R. B. Miles, W. R. Lempert, and J. N. Forkey, 'Laser Rayleigh scattering', *Measurement Science and Technology*. 12, 2001.

[158] D. A. Long, *The Raman Effect: A Unified Treatment of the Theory of Raman Scattering by Molecules*, New York: Wiley, 2002.

[159] Y. Kim *et al.*, 'Endoscopic imaging using surface-enhanced Raman scattering', *European Journal of Nanomedicine* 9, 2017.

[160] F. Zernike, 'How I Discovered Phase Contrast', *Science* 121, 1955.

[161] https://www.microscopyu.com/techniques/phase-contrast/introduction-to-phase-contrast-microscopy.

[162] N. Richard *et al.*, 'Coupled Theoretical and Experimental Studies for the Radiation Hardening of Silica-Based Optical Fibers', *IEEE Transactions on Nuclear Science* 61, 2014.

[163] S. Girard *et al.*, 'Radiation Effects on Silica-Based Preforms and Optical Fibers—I: Experimental Study With Canonical Samples', *IEEE Transactions on Nuclear Science* 55, 2008.

[164] S. Girard *et al.*, 'Radiation Effects on Silica-Based Preforms and Optical Fibers-II: Coupling *Ab initio* Simulations and Experiments', *IEEE Transactions on Nuclear Science* 55, 2008.

[165] https://photonics.ixblue.com/labcom/labh6.

[166] https://photonics.ixblue.com

[167] S. Girard et al., 'Radiation-induced defects in fluorine-doped silica-based optical fibers: Influence of a pre-loading with H_2', *Journal of Non-Crystalline Solids* 355, 2009.

[168] A. Alessi *et al.*, 'Radiation Effects on Aluminosilicate Optical Fibers: Spectral Investigations From the Ultraviolet to Near-Infrared Domains', *Physica Status Solidi (a)* 216, 2019.

[169] D. Di Francesca, *Role of Dopants, Interstitial O_2 and Temperature in the Effects of Irradiation on Silica-based Optical Fibers*, PhD Thesis, Université Jean Monnet Saint-Etienne, 2015.

[170] R. Brückner, ‘Properties and structure of vitreous silica. I’, *Journal of Non-Crystalline Solids* 5, 1970.

[171] https://www.heraeus.com/en/hca/imprint_hca.html.

[172] L. Vaccaro, M. Cannas, and R. Boscaino, ‘Luminescence features of nonbridging oxygen hole centres in silica probed by site-selective excitation with tunable laser’, *Solid State Communications* 146, 2008.

[173] G. Raboisson, P. Eyl, M. Roche, C. Malaval, and A. Johan, ‘Asterix, a high intensity x-ray generator’, *7th Pulsed Power Conference*, Monterey (USA), 1989.

[174] A. Johan, B. Azais, C. Malaval, G. Roboison, and M. Roche, ‘Asterix, un nouveau moyen pour la simulation des effets de debit de dose sur l'electronique’, *Annales de Physique* 14, 1989.

[175] S. Girard, J. Baggio, A. Boukenter, and Y. Ouerdane, ‘Vulnerability Analysis of Optical Fibers for Laser Megajoule Facility: Preliminary Studies’, *IEEE Transactions on Nuclear Science* 52, 2005.

[176] S. Girard et al., ‘Spectroscopic study of γ-ray and pulsed x-ray radiation-induced point defects in pure-silica-core optical fibers’, *IEEE Transactions on Nuclear Science* 52, 2005.

[177] S. Girard et al., ‘Growth and Decay Kinetics of Radiation- Induced Attenuation in Bulk Optical Materials’, *IEEE Transactions on Nuclear Science* 65, 2018.

[178] S. Girard *et al.*, ‘Recent advances in radiation-hardened fiber-based technologies for space applications’, *Journal of Optics* 20, 2018.

[179] Agilent Cary UV-Vis-NIR Supplies Quick reference guide, Agilent Technologies.

[180] PHAROS High Power and Energy Femtosecond Laser datasheet, Light Conversion.

[181] G. Raciukaitis, M. Grishin, R. Danielius, J. Pocius, and L. Giniunas, ‘High repetition rate ps- and fs-lasers for micromachining’, in *International Congress on Applications of Lasers & Electro-Optics*, Scottsdale (USA), 2006.

[182] Y. Cheng *et al.*, ‘Control of the cross-sectional shape of a hollow microchannel embedded in photostructurable glass by use of a femtosecond laser’, *Optics Letters* 28, 2003.

[183] M. Ams, G. D. Marshall, D. J. Spence, and M. J. Withford, ‘Slit beam shaping method for femtosecond laser direct-write fabrication of symmetric waveguides in bulk glasses’, *Optics Express* 13, 2005.

[184] M. Royon, Ingénierie de verres de silice: influence de pré-traitements sur la variation d'indice de réfraction de guides d'ondes photo-inscrits par laser femtoseconde, PhD Thesis, Université Jean Monnet Saint Etienne, 2018.

[185] Aramis Raman Instrumentation with Intelligent Automation, HORIBA.

[186] W. Becker, *The bh TCSPC handbook*, Becker & Hickl GmbH, 2017.

[187] OBR - Overview and Applications, Luna.

[188] V. M. Gordienko, F. V. Potemkin, and P. M. Mikheev, 'Evolution of a femtosecond laser-induced plasma and energy transfer processes in a SiO_2 microvolume detected by the third harmonic generation technique', *JETP Letters* 90, 2009.

[189] S.-H. Cho, H. Kumagai, and K. Midorikawa, 'In situ observation of dynamics of plasma formation and refractive index modification in silica glasses excited by a femtosecond laser', *Proceedings SPIE* 4830, 2016.

[190] K. I. Popov, C. McElcheran, K. Briggs, S. Mack, and L. Ramunno, 'Morphology of femtosecond laser modification of bulk dielectrics', *Applied Physics Letters* 84, 2004.

[191] Andor Kymera 193i specifications, Oxford Instruments.

[192] Solstice ace high energy, industrial one box ultrafast amplifier datasheet, Spectra Physics.

[193] Mai Tai short pulse ultrafast oscillator datasheet, Spectra Physics.

[194] K. C. Kao, 'Dielectric-fibre surface waveguides for optical frequencies', *Proceedings IEEE* 113, 1966.

[195] J. L. Bourgade *et al.*, 'New constraints for plasma diagnostics development due to the harsh environment of MJ class lasers', *Review of Scientific Instruments* 75, 2004.

[196] M. Benabdesselam *et al.*, 'Performance of Ge-doped optical fiber as a thermoluminescent dosimeter', *IEEE Transactions on Nuclear Science* 60, 2013.

[197] D. A. Krohn, T. W. MacDougall, and A. Mendez, 'Fiber Optic Sensors: Fundamentals and Applications' *Society of Photo-Optical Instrumentation Engineers*, 2014.

[198] H. Hartog, *An Introduction to Distributed Optical Fibre Sensors*, CRC Press, 2017.

[199] S. Girard *et al.*, 'Radiation Effects on Silica-Based Preforms and Optical Fibers-II: Coupling *Ab initio* Simulations and Experiments', *IEEE Transaction Nuclear Science* 55, 2008.

[200] B. Brichard *et al.*, 'Radiation-hardening techniques of dedicated optical fibres used in plasma diagnostic systems in ITER', *Journal of Nuclear Materials* 329, 2004.

[201] S. Girard *et al.*, 'Combined high dose and temperature radiation effects on multimode silica-based optical fibers', *IEEE Transaction on Nuclear Science* 60, 2013.

[202] P. F. Kashaykin *et al.*, 'Radiation induced attenuation in pure silica polarization maintaining fibers', *Journal of Non-Crystalline Solids* 508, 2019.

[203] A. Alessi *et al.*, 'Influence of the Manufacturing Process on the Radiation Sensitivity of Fluorine-Doped Silica-Based Optical Fibers', *IEEE Transactions on Nuclear Science* 59, 2012.

[204] S. Girard et al., 'Radiation-induced defects in fluorine-doped silica-based optical fibers: Influence of a pre-loading with H2', *Journal of Non-Crystalline Solids* 355, 2009.

[205] K. Nagasawa, M. Tanabe, and K. Yahagi, 'Gamma-Ray-Induced Absorption Bands in Pure-Silica-Core Fibers', *Japanese Journal of Applied Physics* 23, 1984.

[206] A. Morana *et al.*, 'Extreme Radiation Sensitivity of Ultra-Low Loss Pure-Silica-Core Optical Fibers at Low Dose Levels and Infrared Wavelengths', *Sensors* 20, 2020.

[207] D. L. Griscom, 'Fractal kinetics of radiation-induced point-defect formation and decay in amorphous insulators: Application to color centers in silica-based optical fibers', *Physical Review B* 64, 2001.

[208] S. Girard, J. Baggio, and J. Bisutti, '14-MeV neutron, γ-ray, and pulsed x-ray radiation-induced effects on multimode silica-based optical fibers', *IEEE Transactions on Nuclear Science* 53, 2006.

[209] M. Malinauskas et al., 'Ultrafast laser processing of materials: from science to industry', *Light: Science & Applications* 5, 2016.

[210] D. G. Papazoglou and S. Tzortzakis, 'In-line holography for the characterization of ultrafast laser filamentation in transparent media', *Applied Physics Letters* 93, 2008.

[211] S. Richter et al., 'Nanogratings in fused silica: Formation, control, and applications', *Journal of laser applications* 24, 2012.

[212] V. R. Bhardwaj et al., 'Optically Produced Arrays of Planar Nanostructures inside Fused Silica', *Physical Review Letters* 96, 2006.

[213] J. Hernandez-Rueda, J. Clarijs, D. van Oosten, and D. M. Krol, 'The influence of femtosecond laser wavelength on waveguide fabrication inside fused silica', *Applied Physics Letters* 110, 2017.

[214] M. Royon et al., 'X-ray preconditioning for enhancing refractive index contrast in femtosecond laser photoinscription of embedded waveguides in pure silica', *Optical Material Express* 9, 2019.

[215] A. Saliminia, N. T. Nguyen, S. L. Chin, and R. Vallée, 'Densification of silica glass induced by 0.8 and 1.5 μm intense femtosecond laser pulses', *Journal of Applied Physics* 99, 2006.

[216] J. W. Chan, T. R. Huser, S. H. Risbud, and D. M. Krol, 'Modification of the fused silica glass network associated with waveguide fabrication using femtosecond laser pulses', *Applied Physics A: Materials Science & Processing* 76, 2003.

[217] K. Hirao and K. Miura, 'Writing waveguides and gratings in silica and related materials by a femtosecond laser', *Journal of Non-Crystalline Solids* 239, 1998.

[218] S. Gross, N. Riesen, J. D. Love, and M. J. Withford, 'Three-dimensional ultra-broadband integrated tapered mode multiplexers: Three-dimensional ultra-broadband integrated tapered mode multiplexers', *Laser & Photonics Reviews* 8, 2014.

[219] N. Jovanovic *et al.*, 'Starlight demonstration of the Dragonfly instrument: an integrated photonic pupil-remapping interferometer for high-contrast imaging: Starlight demonstration of Dragonfly', *Monthly Notices of the Royal Astronomical Society* 427, 2012.

[220] S. Gross and M. J. Withford, 'Ultrafast-laser-inscribed 3D integrated photonics: challenges and emerging applications', *Nanophotonics* 4, 2015.

[221] Y. Shimotsuma, P. G. Kazansky, J. Qiu, and K. Hirao, 'Self-Organized Nanogratings in Glass Irradiated by Ultrashort Light Pulses', *Physical Review Letters* 91, 2003.

[222] I. M. Burakov *et al.*, 'Spatial distribution of refractive index variations induced in bulk fused silica by single ultrashort and short laser pulses', *Journal of Applied Physics* 101, 2007

[223] V. V. Temnov, K. Sokolowski-Tinten, P. Zhou, A. El-Khamhawy, and D. von der Linde, 'Multiphoton Ionization in Dielectrics: Comparison of Circular and Linear Polarization', *Physical Review Letters* 97, 2006.

[224] V. De Michele *et al.*, 'Laser wavelength effects on the refractive index change of waveguides written by femtosecond pulses in silica glasses', in *Advanced Photonics 2018 (BGPP, IPR, NP, NOMA, Sensors, Networks, SPPCom, SOF)*, Zurich, 2018, p. BM2A.5, doi: 10.1364/BGPPM.2018.BM2A.5.

[225] A. Saliminia, J.-P. Bérubé, and R. Vallée, 'Refractive index-modified structures in glass written by 266 nm fs laser pulses', *Optics Express* 20, 2012.

[226] K. Mishchik, *Transformation photo-assistée de diélectriques pour l'optique par laser `a impulsions ultra-brèves: études des mécanismes microscopiques*, PhD Thesis, Université Jean Monnet Saint Etienne, 2012.

[227] M. Lancry *et al.*, 'Nanogratings formation in multicomponent silicate glasses', *Applied Physics B* 122, 2016.

[228] C. Fan, 'Directional Writing Dependence of Birefringence in Multicomponent Silica-based Glasses with Ultrashort Laser Irradiation', *Journal of Laser Micro/Nanoengineering* 6, 2011.

[229] Y. Zhang et al., 'Femtosecond laser-inscribed fiber interface Mach–Zehnder interferometer for temperature-insensitive refractive index measurement', *Optics Letters* 43, 2018.

[230] D. M. Krol, 'Femtosecond laser modification of glass', *Journal of Non-Crystalline Solids* 354, 2008.

[231] G. S. Henderson, D. R. Neuville, B. Cochain, and L. Cormier, 'The structure of GeO_2–SiO_2 glasses and melts: A Raman spectroscopy study', *Journal of Non-Crystalline Solids* 355, 2009.

[232] J. W. Chan, T. Huser, S. Risbud, and D. M. Krol, 'Structural changes in fused silica after exposure to focused femtosecond laser pulses', *Optics Letters* 26, 2001.

[233] M. Leon *et al.*, 'Neutron Irradiation Effects on the Structural Properties of KU1, KS-4V and I301 Silica Glasses', *IEEE Transactions on Nuclear Science* 61, 2014.

[234] D. Di Francesca *et al.*, 'Resonance Raman of oxygen dangling bonds in amorphous silicon dioxide: Resonance Raman of oxygen dangling bonds', *Journal of Raman Spectroscopy* 48, 2017.

[235] M. Lancry, B. Poumellec, A. Chahid-Erraji, M. Beresna, and P. G. Kazansky, 'Dependence of the femtosecond laser refractive index change thresholds on the chemical composition of doped-silica glasses', *Optics Material Express* 1, 2011.

[236] L. Skuja, 'Isoelectronic series of twofold coordinated Si, Ge, and Sn atoms in glassy SiO_2: A luminescence study', *Journal of Non-Crystalline Solids* 149, 1992.

[237] F. Messina, L. Vaccaro, and M. Cannas, 'Generation and excitation of point defects in silica by synchrotron radiation above the absorption edge', *Physical Review B* 81, 2010.

[238] G. L. Tan, M. F. Lemon, D. J. Jones, and R. H. French, 'Optical properties and London dispersion interaction of amorphous and crystalline SiO_2 determined by vacuum ultraviolet spectroscopy and spectroscopic ellipsometry', *Physical Review B* 72, 2005.

[239] K. Kajihara, L. Skuja, M. Hirano, and H. Hosono, 'Formation and decay of nonbridging oxygen hole centers in SiO2 glasses induced by F_2 laser irradiation: *In situ* observation using a pump and probe technique', *Applied Physics Letter* 79, 2001.

[240] I. Reghioua *et al.*, 'Study of point defects in as-drawn and irradiated Ge-doped optical fibers using cathodoluminescence', *IOP Conference Series: Material Science and Engineering* 169, 2017.

[241] S. Guizard, P. Martin, G. Petite, P. D'Oliveira, and P. Meynadier, 'Time-resolved study of laser-induced colour centres in SiO_2', *Journal of Physics: Condensed Matter* 8, 1996.

[242] A. Sciortino *et al.*, 'The interaction of photoexcited carbon nanodots with metal ions disclosed down to the femtosecond scale', *Nanoscale* 9, 2017.

[243] T. Balciunas, A. Melninkaitis, G. Tamosauskas, and V. Sirutkaitis, 'Time-resolved off-axis digital holography for characterization of ultrafast phenomena in water', *Optics Letter* 33, 2008.

[244] Y. Hayasaki, S. Fukuda, S. Hasegawa, and S. Juodkazis, 'Two-color pump-probe interferometry of ultra-fast light-matter interaction', *Scientific Reports* 7, 2017.

[245] L. Vaccaro, M. Cannas, and R. Boscaino, 'Luminescence features of nonbridging oxygen hole centres in silica probed by site-selective excitation with tunable laser', *Solid State Communications* 146, 2008.

[246] M. Cannas and F. M. Gelardi, 'Vacuum ultraviolet excitation of the 1.9 eV emission band related to nonbridging oxygen hole centers in silica', *Physical Review B* 69, 2004.

[247] L. Vaccaro, *Electronic and vibrational properties of the Non Bridging Oxygen Hole Center in the bulk and at the surface of silica*, PhD Thesis, Università degli Studi di Palermo, 2009.

[248] M. Cannas, V. Lavinia, and B. Roberto, 'Time resolved photoluminescence associated with non-bridging oxygen hole centers in irradiated silica', *Nuclear Instruments and Methods in Physics Research Section B: Beam Interactions with Materials and Atoms* 266, 2008.

[249] A. Paleari, F. Meinardi, S. Brovelli, and R. Lorenzi, 'Competition between green self-trapped-exciton and red non-bridging-oxygen emissions in SiO2 under interband excitation', *Communications Physics* 1, 2018.

[250] G. Pacchioni and R. Ferrario, 'Optical transitions and EPR properties of two-coordinated Si, Ge, Sn and related H (I) , H (II) , and H (III) centers in pure and doped silica from *ab initio* calculations', *Physical Review B* 58, 1998.

[251] H. S. Nalwa, *Silicon-Based Materials and Devices*, Academic Press, 2001.

[252] J. Nishii, K. Fukumi, H. Yamanaka, K. Kawamura, H. Hosono, and H. Kawazoe, 'Photochemical reactions in GeO_2-SiO_2 glasses induced by ultraviolet irradiation: Comparison between Hg lamp and excimer laser', *Physical Review B* 52, 1995.

Phénomènes optiques transitoires liés aux défauts ponctuels dans la silice pure et dopée

L'objectif de cette thèse de doctorat est de mettre en évidence les propriétés et mécanismes relatifs aux défauts transitoires, en étudiant leurs mécanismes de génération dans la silice amorphe pure ou dopée par des rayons X ou des impulsions laser femtoseconde de haute intensité. Nous sommes concentrés sur leurs propriétés optiques, en caractérisant l'ensemble du photocycle associé aux défauts impliqués dans les processus d'interaction entre le rayonnement et la matière. Nous étudions les verres massifs et les fibres optiques, à l'aide de différentes techniques spectroscopiques, afin d'évaluer l'impact des défauts induits dans les matériaux à large bande interdite. Le premier chapitre offre une vue d'ensemble de la silice, avec une attention particulière sur la génération de défauts sous irradiation ionisante et par photo-ionisation non-linéaire. Le chapitre 2 est consacré aux concepts à la base des phénomènes observés au cours de cette thèse, en présentant les techniques expérimentales utilisées pour étudier les échantillons sélectionnés. Le chapitre 3 décrit nos échantillons ainsi que les différentes installations et dispositifs expérimentaux exploités tout au long de ces trois années de travail. Le chapitre 4 passe en revue les principaux résultats de nos recherches sur les origines de l'atténuation induite par des irradiations X continues ou pulsées dans les différentes catégories de fibres optiques. Le chapitre 5 se focalise sur notre caractérisation des processus d'interaction entre la silice amorphe et les impulsions laser femtoseconde de haute intensité. Pour cela, nous avons combiné l'étude post mortem des guides d'ondes femtoseconde inscrits dans la silice massive avec la caractérisation *in situ* des défauts instables se recombinant juste après l'irradiation. Le dernier chapitre, le chapitre 6, présente une nouvelle approche expérimentale très prometteuse que nous avons mis en place afin d'étudier le photocycle d'un défaut dans des conditions d'absorption linéaire et avec une résolution temporelle sub-picoseconde. Notre méthode tire parti de la possibilité d'accorder, dans une large gamme spectrale, la longueur d'onde d'excitation dans les mesures d'absorption transitoire (TA). Comme exemple du potentiel de cette approche, nous discutons des photocycles des défauts photoluminescents NBOHCs (Non-Bridging Oxygen Hole Centers) et GLPC (Germanium Lone Pair Center) sous photo-excitation ultraviolette, en suivant leur dynamique femto-picoseconde en fonction de la longueur d'onde d'excitation dans des conditions d'absorption à un photon.

Fenomeni Ottici Transienti in Silice Pura e Drogata Legati a Difetti di Punto

L'obiettivo della presente tesi di dottorato è quello di far luce sul comportamento dei difetti transitori, studiando i meccanismi alla base della loro generazione in silice pura e drogata, esposta a radiatione X ionizzante e ad impulsi laser al femtosecondo ad alta intensità. Ci siamo concentrati sulle proprietà ottiche, caratterizzando l'intero fotociclo associato al difetto coinvolto nei processi di interazione tra la radiazione e la silice. Sono stati studiati sia campioni massivi che fibre ottiche, con differenti tecniche spettroscopiche, al fine di valutare l'influenza dei difetti indotti nei materiali caratterizzati da alto band gap. Il primo capitolo offre una panoramica sulla silice, con particolare attenzione alla generazione dei difetti esposti a radiazione ionizzante e fotoionizzazione non lineare. Il capitolo 2 è dedicato ai principi alla base dei fenomeni osservati lungo questa tesi di dottorato, introducendo i concetti teorici legati alle tecniche sperimentali utilizzate per studiare i campioni selezionati. Il capitolo 3 descrive i nostri campioni così come le varie strutture e gli apparati sperimentali utilizzati in questi tre anni di lavoro. Il capitolo 4 passa in rassegna i principali risultati del nostro studio sulle origini dell'attenuazione indotta da radiazioni X pulsata e continua in diverse classi di fibre ottiche. Il capitolo 5 si concentra sulla caratterizzazione dei processi di interazione tra la silice amorfa e gli impulsi laser al femtosecondo ad alta intensità. A tal fine, abbiamo combinato lo studio post mortem delle guide d'onda inscritte utilizzando laser al femtosecondo con la caratterizzazione *in situ* dei difetti instabili che decadono subito dopo l'esposizione al laser. L'ultimo capitolo, il capitolo 6, presenta un nuovo e promettente approccio sperimentale per studiare il fotociclo del difetto in condizioni di assorbimento lineare e con una risoluzione temporale sotto il picosecondo. Il nostro metodo sfrutta la possibilità di variare in maniera continua, in un ampio intervallo spettrale, la lunghezza d'onda di eccitazione nelle misure di assorbimento transiente. Come esempio del beneficio di questo approccio, presentiamo lo studio dei fotocicli del Non-Bridging-Oxygen-Hole-Center e del Germanium-Lone-Pair-Center sotto foto-eccitazione ultravioletta, seguendo la dinamica nella scala temporale dei femto-picosecondi di questi difetti fotoluminescenti, in funzione della lunghezza d'onda di eccitazione e in condizioni di assorbimento a singolo fotone.

Transient Optical Phenomena Related to Point Defects in Pure and Doped Silica

The goal of the present PhD thesis is to shed light into the transient defect's behavior, studying their generation mechanisms in pure or doped amorphous silica, upon ionizing X-rays and high intensity femtosecond laser pulses. We focused on their optical properties, characterizing the whole photocycle associated with the defect involved in the radiation matter interaction processes. Both bulk glasses and optical fibers are investigated, with a variety of spectroscopic techniques, to evaluate the impact of the induced defects in wide-band gap materials. The first chapter offers an overview on the silica glass, with particular attention in the defect generation under ionizing irradiation and through non-linear photoionization. Chapter 2 is devoted to the concepts at the basis of the phenomena observed along this PhD thesis, introducing the experimental techniques used to investigate the selected samples. Chapter 3 describes our samples as well as the various experimental facilities and setups exploited along these three years of work. Chapter 4 reviews the main results of our investigation about the origins of the pulsed and steady state X-ray radiation-induced attenuation in different classes of optical fibers. Chapter 5 focuses on our characterization of the interaction processes between amorphous silica and high intensity femtosecond laser pulses. For this, we combined *post mortem* investigation of femtosecond inscribed waveguides with *in situ* characterization of the unstable defects recovering just after the irradiation. The last chapter, chapter 6, presents a new and promising experimental approach to study the defect's photocycle under linear absorption conditions and with a sub-picosecond time resolution. Our method takes advantage from the possibility to tune, in a wide spectral range, the excitation wavelength in transient absorption (TA) measurements. As example of the benefit of this approach, we discuss the photocycles of the Non-Bridging-Oxygen-Hole-Center and of the Germanium-Lone-Pair-Center under ultraviolet photo-excitation, following the femto-picosecond dynamics of these photoluminescent defects as a function of excitation wavelength in single-photon absorption conditions.